CHARGED CURRENT QUASI-ELASTIC MUON NEUTRINO INTERACTIONS IN THE BABY MIND DETECTOR

SVEN-PATRIK HALLSJÖ

SUBMITTED IN FULFILMENT OF THE REQUIREMENTS FOR THE DEGREE OF
Doctor of Philosophy

SCHOOL OF PHYSICS AND ASTRONOMY

COLLEGE OF SCIENCE AND ENGINEERING
UNIVERSITY OF GLASGOW

University of Glasgow | School of Physics & Astronomy

SEPTEMBER 2018

Abstract

The T2K long-baseline neutrino experiment in Japan is designed to study neutrino oscillations, to determine the mixing angles and mass-squared difference of the neutrino mass eigenstates and, potentially, to discover CP violation in neutrinos by comparing neutrino to antineutrino oscillations. In the near detector complex 280 m downstream of the production target at the Japanese Particle Accelerator Research Centre (J-PARC), the WAGASCI experiment will measure the ratio of cross sections from neutrinos interacting with a water and scintillator targets, in order to constrain neutrino cross sections essential for the T2K neutrino oscillation measurements. A prototype Magnetised Iron Neutrino Detector, called Baby MIND, has been constructed at CERN and will act as a magnetic spectrometer behind the main WAGASCI target. The Baby MIND spectrometer was installed between February and March 2018 in the near detector complex, behind WAGASCI and is able to measure the charge and momentum of the outgoing muon from neutrino charged current interactions inside the WAGASCI target, to be able to perform full neutrino event reconstruction. Baby MIND collected data in the reverse horn focussed antineutrino beam between April and May 2018. In this thesis, the Baby MIND spectrometer is described in detail along with the performance from initial beam tests performed with the Proton Synchrotron (PS) charged particle beam at the T9 test beam facility at CERN. The test beam was used to perform measurements of track reconstruction efficiency and charge reconstruction efficiency, using dedicated reconstruction programmes, SaRoMaN and SAURON. The software environment used to perform event reconstruction in the complex detector geometry of Baby MIND is described in this thesis. Furthermore, a machine learning multi-variate analysis was used to perform particle identification between muons and hadrons, allowing for a pure selection of muons in the test beam. NuSTORM is a novel type of neutrino beam from the decay of muons in a storage ring. This type of facility produces well defined beams of ν_μ and $\bar{\nu}_e$ neutrinos. A study is performed in the thesis to determine the expected sensitivity of measuring neutrino interactions in a fully active scintillator neutrino target, with a magnetised iron detector downstream. This analysis also benefited from an identification of the different event types by using a machine learning multi-variate approach. Finally, results are presented on charged current quasi-elastic neutrino and antineutrino interactions in iron reconstructed with the Baby MIND detector during the 2018 neutrino data taking at J-PARC.

"We are just an advanced breed of monkeys on a minor planet of a very average star. But we can understand the Universe. That makes us something very special." – Stephen W. Hawking

Acknowledgements

I wish to dedicate this thesis to my mathematics teacher Ulf Rydmark without whom I would not have studied physics.

Thank you Professor Paul Soler, my supervisor, for giving me this great opportunity and your help in completing this thesis. Your support these last few days has been invaluable.

To Professor Christophe Clément, thank you for showing me the world of particle physics and your support.

A big thank you to my wife and my family who always support me through all of my endeavours and made Scotland an even better place.

Thank you to all of my friends around the world who managed to support me when moving abroad and helped keep me sane throughout all of these years.

To all of my colleagues in Baby MIND, CERN neutrino platform and WAGASCI, thank you. This was an amazing project and we couldn't have done it without each other. A special thank you to Etam, Kenji, Saba and Aleksandr (Sascha) who really made everything fall into place. Without you I would not have managed.

To my other colleagues, Dana, Gesine, Hanna, John, Lars and Sarah. I'm not sure I would have managed past day one without your help, fika, our discussions and trips to the pub.

Thank you IT-guys, David Crooks, Gareth Roy, Sam Skipsey, Gordon Stewart, for handing the great ScotGRID bakeoff, providing advice and discussing crazy implementation of software.

Finally I would like to thank my funding agency, the European Union's Horizon 2020 research and innovation programme, for funding my research and part of the Baby MIND project through WP08 under AIDA2020.

Glasgow, September 2018
Sven-Patrik Hallsjö

Declaration

The research results presented in this thesis are the product of my own work unless otherwise stated. Appropriate references are provided when results of third parties are mentioned.

Chapters 1 and 2 are reviews of neutrino physics with descriptions of the current theory and experimental results. The review was carried out by the author with references to established literature and articles produced by experiments. Chapter 3 contains a description of the Baby MIND and WAGASCI detectors. This contains results from the Baby MIND and WAGASCI collaborations together and much has been developed by numerous collaborators. Much of the work with the design and both scintillators and magnets was started before I joined the Baby MIND collaboration, however I was heavily involved in the construction, validation and test beam. Details regarding the construction and test beam were presented by the author at the NuPhys2016 [1, 2] and NuFact17 [3] conferences. The WAGASCI detector was fully developed before I joined the WAGASCI detector and all work has been referenced to the appropriate colleagues. The simulation software described in chapter 4 was already developed to some degree at the group at the University of Glasgow. This software was further developed to provide a framework which could be used for the Baby MIND collaboration. The main part of my work in the collaboration was to lead the simulation and reconstruction efforts using a heavily modified version of this initial software. The specific functionality that was added and maintained have been described and was in part presented presented by the author at NuFact17 [3]. Over the course of this thesis a new framework was developed which is all of my own work. In chapter 5 the test beam studies are described. I was part of the data taking and software development, however much of the credit of the hardware results and the specifics of the data taking goes to my collaborators. The data analysis and usage of the reconstruction software was my own work. The test beam data were collected in the summer of 2016 and 2017 and presented at NuFact17 [3]. Chapter 6 and 7 present NuSTORM and J-PARC beam studies on neutrino interactions. The various neutrino spectra and data taking from J-PARC was provided by the collaboration however the studies are entirely my own work. The data was collected between March and May 2018 and was in part presented by the author at NuFact18.

The research presented here was not submitted for another degree in any other department or university.

Sven-Patrik Philip George Hallsjö

Table of Contents

List of Tables

List of Figures

Chapter 1

Introduction to Neutrino Physics

1.1 Research Goals

The research in this thesis describes the construction of a prototype Magnetized Iron Neutrino Detector (Baby MIND) at the European Organization for Nuclear Research (CERN), its performance to reconstruct charged particle interactions and determine their charge, carried out at a test beam at CERN, and the measurement of neutrino interactions with the WAGASCI detector, carried out at the neutrino beam line at the Japan Proton Accelerator Research Complex (J-PARC). Before describing the research carried out in detail, this first chapter contains a short introduction to neutrino physics.

1.2 Neutrino discovery

While measuring radioactive beta decay, in the first two decades of the 20th century, from bombarding beryllium with alpha particles from polonium, physicists discovered what was then an anomaly. At the time it was thought that beta decay occurred as a two-body process in which a neutron (n) decays to a proton (p) and electron (e^-). If this were the case, the energy of the proton and electron should be discrete and add up to the energy of the neutron. However, experiments showed that the electron had a continuous spectrum of energy values, violating the energy conservation law, as seen in figure 1.1 [4]. In order to solve this anomaly, a third particle, the neutrino (ν), was postulated by Wolfgang Pauli [5] and then incorporated into the beta decay by Enrico Fermi [6]. The neutrino was postulated as a neutral particle with mass of less than 1% of the proton mass and a spin of 1/2. For consistency, the particle produced in the beta decay is relabelled as the electron antineutrino, $\bar{\nu_e}$, in order to conserve lepton number. The addition of another particle changed the decay to $n \rightarrow p + e^- + \bar{\nu_e}$ and introduced the weak interaction model, as seen in figure 1.2.

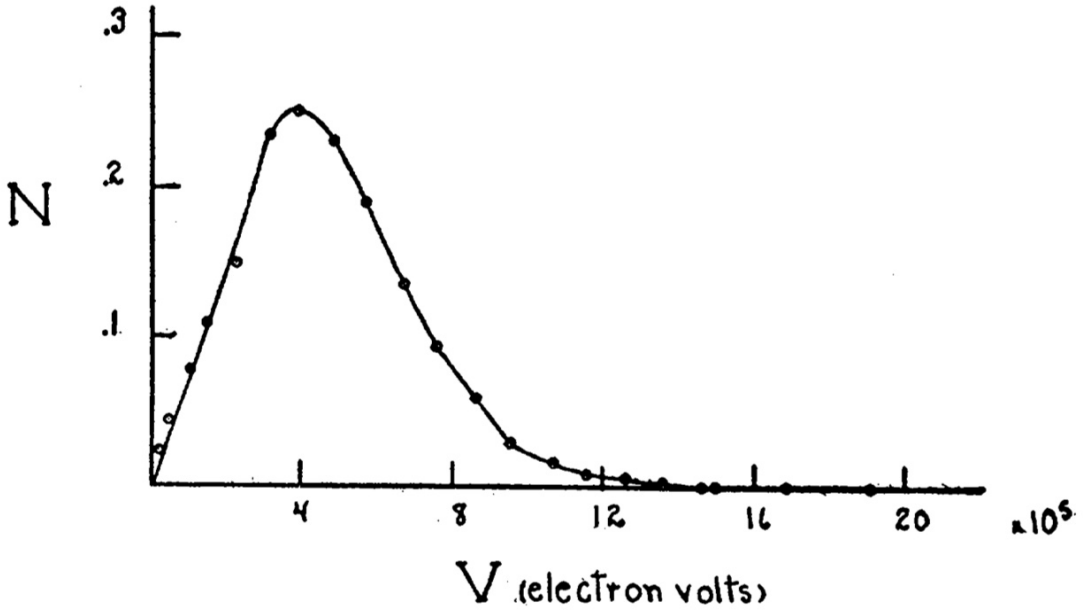

Figure 1.1: The kinetic energy spectrum of the emitted electron from beta decay from a Radium-E source [7]. If no antineutrino were emitted a single electron volt(s) value would be expected.

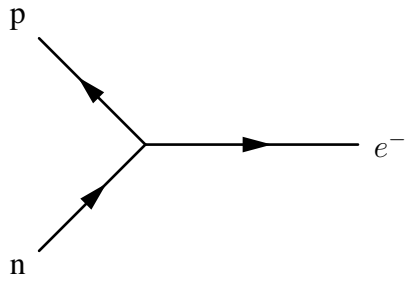

(a) The initially assumed beta decay

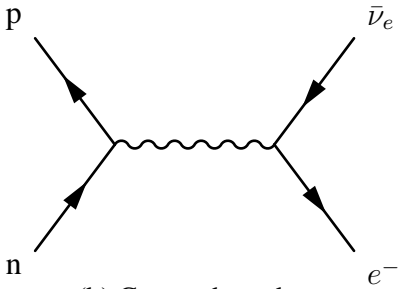

(b) Correct beta decay

Figure 1.2: Feynman diagrams showing beta decay.

It would take another twenty years until the neutrino was experimentally discovered by the Savannah river reactor experiment in 1956 [8] where neutrinos from a nuclear reactor were detected in 300 litres of liquid scintillator and cadmium. Fredrick Reines was awarded the Nobel prize in 1995 for his leading role in this experiment.

After the discovery of the electron neutrino (ν_e), several neutrino experiments were performed and led to the discovery of two other neutrino types/flavours, the muon neutrino (ν_μ) and the tau neutrino (ν_τ) [9, 10, 11].

1.3 Standard Model

The Standard Model of particle physics (SM) categorizes all the fundamental particles that have been discovered experimentally, the mathematics of their properties and how they interact [12, 13].

1.3.1 Quantum Electrodynamics

To describe neutrino interactions it is worth building a theory to try to describe the processes involved. Starting with the spin generalized and relativistic version of the Schrödinger equation for spin $\frac{1}{2}$ objects, the Dirac equation is given by:

$$\sum_{\mu}(i\gamma^{\mu}\partial_{\mu} - m)\psi(x) = 0 \tag{1.1}$$

where m is the rest-mass of the particle, $\psi(x)$ is a spinor, γ^{μ} are the so-called Dirac matrices and the sum over μ is often removed using the Einstein notation requiring summation over repeated indices. It should also be noted that this equation only applies to fermions, half-integer spin particles.

As with all quantum mechanical equations this allows us to define $\psi(x)$ as a quantum field or state.

After taking Lorentz-invariance into account the Dirac Lagrangian can be written as:

$$\mathcal{L} = \bar{\psi}(i\gamma^{\mu}\partial_{\mu} - m)\psi \tag{1.2}$$

where the Euler-Lagrange equation for $\bar{\psi}$ reproduces the Dirac equation.

The Lagrangian is so far correct, however from a physical point of view the equation also needs to be invariant under a phase shift, the so-called gauge transformation $\psi \rightarrow e^{i\theta(x)}\psi$. This requires the addition of an extra term to remove the terms that prevent gauge invariance, providing the full Dirac Lagrangian as:

$$\mathcal{L} = \bar{\psi}(i\gamma^{\mu}\partial_{\mu} - m)\psi - q\bar{\psi}\gamma^{\mu}\psi\epsilon_{\mu} \equiv \mathcal{L}_{Dirac}, \tag{1.3}$$

with ϵ_{μ} being a new field which must be gauge invariant and q a conserved quantity, a numerical constant.

There is now a mathematical framework to describe quantum states or particles in a vacuum, and for a particle interacting with an electromagnetic field by combining $\mathcal{L}_{Dirac}$ with the classical $\mathcal{L}_{Maxwell} = \frac{-1}{4}F_{\mu\nu}F^{\mu\nu}$ with $F^{\mu\nu} = \partial^{\mu}A^{\nu} - \partial^{\nu}A^{\mu}$ where A_{μ} is the electromagnetic vector potential, a four-vector combination of the electric potential and magnetic potential.

This produces the following Lagrangian:

$$\mathcal{L} = \mathcal{L}_{Dirac} + \mathcal{L}_{Maxwell} = \bar{\psi}(i\gamma^\mu\partial_\mu - m)\psi - q\bar{\psi}\gamma^\mu\psi\epsilon_\mu - \frac{1}{4}F_{\mu\nu}F^{\mu\nu}. \tag{1.4}$$

There is nothing preventing us from choosing our previous field ϵ as the electromagnetic vector potential A and choosing q as the electron charge e to produce the experimentally verified Lagrangian for quantum and electromagnetic interactions or Quantum ElectroDynamics (QED):

$$\mathcal{L}_{QED} \equiv \bar{\psi}(i\gamma^\mu\partial_\mu - m)\psi - e\bar{\psi}\gamma^\mu\psi A_\mu - \frac{1}{4}F_{\mu\nu}F^{\mu\nu}. \tag{1.5}$$

This can be simplified by introducing the gauge covariant derivative $D_\mu \equiv \partial_\mu + ieA_\mu$ and the slash notation as $\not{D} = \gamma^\mu D_\mu$. This produces the simplified QED Lagrangian as:

$$\mathcal{L}_{QED} = \bar{\psi}(i\not{D}_\mu - m)\psi - \frac{1}{4}F_{\mu\nu}F^{\mu\nu}. \tag{1.6}$$

1.3.2 Weak interactions

Based on the experiments relating to β-decay, Fermi hypothesised that the Lagrangian for weak interactions should be similar to the QED Lagrangian. To handle the observed differences, a constant G_F is added to replace the electron charge, and the mass term is removed. The assumption was made that the neutrinos were massless. QED contains the covariant multiplier γ^μ meaning that it transforms as a vector, which was confirmed by experiments. The transformation structure of weak interactions was not known and, a priori, anything could be mathematically possible. However, the absence of Fierz interference terms, parity violation and the Goldhaber helicity experiment [14] made it clear that the interactions had to transform as vectors and axial vectors giving the term $\gamma^\mu - \gamma^\mu\gamma^5 = \gamma^\mu(1 - \gamma^5)$ and also providing the theory with its name: V-A theory [15].

This produced a Lagrangian in the form of

$$\mathcal{L} = \frac{G_F}{\sqrt{2}}J_L \cdot J_H \tag{1.7}$$

with J_L as the current describing interactions with leptons and J_H describing interactions with hadrons (up and down quarks instead of protons and neutrons). The Fermi constant G_F was also added to substitute the electron charge. The currents were initially of the form:

$$J_L = \bar{\psi}_e(x)\gamma^\mu(1 - \gamma_5)\psi_\nu(x) \tag{1.8}$$

containing only the electron, and then expanded by adding more terms containing future

particles. For the hadrons it could either be written for quarks as:

$$J_H = \bar{\psi}_u(x)\gamma^\mu(1-\gamma_5)\psi_d(x) \tag{1.9}$$

or for protons and neutrons as:

$$J_H = \bar{\psi}_p(x)\gamma^\mu(g_V - g_A\gamma_5)\psi_n(x) \tag{1.10}$$

where g_V and g_A are constants relating to strong interactions and have to be determined experimentally along with G_F.

1.3.3 Glasgow-Weinberg-Salam Theory

V-A theory works well in practice but does not create a Gauge theory connecting to an underlying field, such as QED does. It is also based on the interacting particles not having mass which does not explain the observed masses of the weak interaction particles, W bosons. There is also no explanation for any neutral current interactions which were observed in 1973 [16] and introduced a massive Z boson. Group theory describes that any unitary group $U(N)$ has N^2-1 generators. The special unitary groups $SU(N)$ were investigated to include interactions mediated by other bosons, in analogy with the $SU(1)$ group that successfully describes QED.

Glashow-Weinberg-Salam (GWS) took the success of the V-A theory and modified it to make a Gauge theory, Quantum Flavour Dynamics (QFD) with massive intermediate vector bosons W and Z, basing it on the SU(2) group [17, 18, 19]. It was also easy to see that QFD and QED could be unified as an SU(2) group and it could be made invariant under U(1) by adding an extra term. By choosing this constant term correctly QFD and QED were unified into the Electroweak theory.

The experiment by Goldhaber, Grodzins, and Sunyar concluded that neutrinos only exist in a left-handed chiral state, meaning that momentum and spin are oppositely aligned [14]. They also concluded that antineutrinos only exist in the right-handed state. In the initial or unexpanded SM, [20], only fermions which have both chiral states have mass through the Brout-Englert-Higgs mechanism [21]. At the time this led to the definition of the neutrino as a massless particle, however in subsection 1.6 it will be shown that neutrino oscillations require at least one of the neutrinos to have mass. This indicates that the SM needs to be extended to account for this new physics.

The work by GWS will now be briefly detailed. Since experiments require 3 bosons and interaction modes, one can start with a simple field and make it SU(2). Initially the Lagrangian can naively be taken as that of a complex scalar field coupled to the electromagnetic field (and

itself) as:

$$\mathcal{L} = -\frac{1}{4}F_{\mu\nu}F^{\mu\nu} + |D_\mu\phi|^2 - V(\phi) \tag{1.11}$$

where D_μ is the covariant derivative from QED, $D_\mu = \partial_\mu + ieA_\mu$ and a potential V will be discussed shortly as a way of adding mass to the theory.

Following the procedure performed to produce QED and requiring gauge invariance implies that the covariant derivative needs to be changed, requiring a field for each of the so-called generators or each of the bosons. This requires 3 new fields aside from the QED/photon field. This changes the covariant derivative in the following way,

$$D_\mu = \partial_\mu - igS^a_\mu\frac{\sigma^a}{2} - \frac{1}{2}g'A_\mu \tag{1.12}$$

where g' is now the new coupling to the photon field and g is the coupling to our new fields S^a_μ, while σ^a are the Pauli matrices with a the index that can take the values 1, 2 and 3.

At this stage there are enough fields to produce the bosons required, however, there needs to be a way of making all but the photon field massive.

V is chosen in a way such that it produces a massive Goldstone boson [22] and so that it is also gauge invariant. This gives V as:

$$V(\phi) = -\mu^2\phi^*\phi + \frac{\lambda}{2}(\phi^*\phi)^2 \tag{1.13}$$

where μ is a parameter. If $\mu^2 < 0$ it will produce a massive boson, this is also a way of producing a massive photon in QED, however if $\mu^2 > 0$ then a spontaneous symmetry breaking is produced and ϕ can be split into a real and complex part where the real part will have mass but the complex will not. Essentially this breaks down the $SU(2) \times U(1)$ to a $U(1)$ theory. Therefore it produces one massless vector boson (the photon field A), three massive vectors boson fields (the S fields) and a vacuum expectation value v related to the physical Higgs scalar.

The potential can be chosen, within the symmetry breaking as the Higgs potential [21]:

$$\langle\phi\rangle = \frac{1}{\sqrt{2}}\begin{pmatrix}0\\v\end{pmatrix} \tag{1.14}$$

The mass related to each of these fields arises from the $|D_\mu\phi|^2$ term in the Lagrangian. This can be explicitly seen, using the Higgs potential and $\phi^*|D_\mu\phi|^2\phi$. Using the fact that the potential is a constant and cancelling signs produces:

$$V(\phi) = \begin{pmatrix}0 & v\end{pmatrix}(gS^a_\mu\frac{\sigma^a}{2} + \frac{1}{2}g'A_\mu)(gS^{b\mu}\frac{\sigma^b}{2} + \frac{1}{2}g'A^\mu)\begin{pmatrix}0\\v\end{pmatrix} \tag{1.15}$$

Using the properties of Pauli matrices this can be rewritten as:

$$V(\phi) = \frac{1}{2}\frac{v^2}{4}\{g^2(S_\mu^1)^2 + g^2(S_\mu^2)^2 + (-gS_\mu^3 + g'A_\mu)^2\} \tag{1.16}$$

These results can be modified to show how mass is added to fermions as well.

The terms corresponding to the factors g and g' can be combined to produce four different field combinations that result in bosons with different masses, three are massive bosons and one is massless:

$$W^\pm = \frac{1}{\sqrt{2}}(S_\mu^1 \mp S_\mu^2) \tag{1.17}$$

$$Z_\mu = \frac{1}{\sqrt{g^2+g'^2}}(gS_\mu^3 - g'A_\mu) \tag{1.18}$$

$$\gamma_\mu = \frac{1}{\sqrt{g^2+g'^2}}(g'S_\mu^3 + gA_\mu). \tag{1.19}$$

The masses for the bosons are $m_W = g\frac{v}{2}$, $m_Z = \sqrt{g^2+g'^2}\frac{v}{2}$ and $m_\gamma = 0$. By defining a weak mixing angle, the Weinberg angle, a relationship between these fields can be defined as:

$$\begin{pmatrix} Z \\ \gamma \end{pmatrix} = \begin{pmatrix} \cos(\theta_W) & -\sin(\theta_W) \\ \sin(\theta_W) & \cos(\theta_W) \end{pmatrix} \begin{pmatrix} S^3 \\ A \end{pmatrix} \tag{1.20}$$

where $\cos(\theta_W) = \frac{g}{\sqrt{g^2+g'^2}}$ and $\sin(\theta_W) = \frac{g'}{\sqrt{g^2+g'^2}}$. This also provides a relationship between the W and Z masses, as $m_W = m_Z\cos(\theta_W)$. To also ensure that QED is properly included in this theory the terms in front of the γ-field must be equal to the electron charge providing the following relationship: $e = g\sin(\theta_W) = g'\cos(\theta_W)$

This allows the final interaction Lagrangian to be written as:

$$\begin{aligned} \mathcal{L}_{int} = {} & i\frac{g}{\sqrt{2}}[j_\mu^{(+)}W^{\mu-} + j_\mu^{(-)}W^{\mu+}] \\ & + i[g\cos\theta_W j_\mu^{(3)} - g'\sin\theta_W j_\mu^{(Y/2)}]Z^\mu \\ & + i[g\sin\theta_W j_\mu^{(3)} + g'\cos\theta_W j_\mu^{(Y/2)}]\gamma^\mu \end{aligned} \tag{1.21}$$

or simplified as

$$\begin{aligned} \mathcal{L}_{int} = {} & i\frac{g}{\sqrt{2}}[j_\mu^{(+)}W^{\mu-} + j_\mu^{(-)}W^{\mu+}] \\ & + i[g\cos\theta_W j_\mu^{(3)} - g'\sin\theta_W j_\mu^{(Y/2)}]Z^\mu \\ & + ie[j_\mu^{(3)} + j_\mu^{(Y/2)}]\gamma^\mu \end{aligned} \tag{1.22}$$

where $j_\mu^{(a)}$ are the different currents for each of the interactions. As an example, for the

interaction between an electron and a neutrino, a purely weak interaction, the currents are written as:

$$j_\mu^{(W+)} = \frac{1}{2}\bar{\nu}_e\gamma_\mu(1-\gamma_5)e \tag{1.23}$$

$$j_\mu^{(W-)} = \frac{1}{2}\bar{e}\gamma_\mu(1-\gamma_5)\nu_e \tag{1.24}$$

$$j_\mu^{(Z)} = \frac{1}{2}\bar{\nu}_e\gamma_\mu(1-\gamma_5)\nu_e - \frac{1}{2}\bar{e}\gamma_\mu(1-\gamma_5)e + 2\sin^2\theta_W\bar{e}\gamma_\mu e \tag{1.25}$$

$$j_\mu^{(3)} = 0 \tag{1.26}$$

$$j_\mu^{(Y/2)} = 0. \tag{1.27}$$

Comparing the formula for $j_\mu^{(Z)}$ from the electroweak theory above, and from V-A theory, $j_\mu^{(Z)} = \frac{1}{2}\bar{\nu}_e\gamma_\mu(1-\gamma_5)\nu_e + \bar{e}\gamma_\mu(g_V - g_A\gamma_5)e$, provides a relation between the g_V and g_A and the Weinberg angles as $g_V = -\frac{1}{2} + 2\sin^2\theta_W$ and $g_A = -\frac{1}{2}$. Given that the currents for both W and Z are non-zero, the electrons and neutrinos should have interactions through all three bosons. Looking in detail it can be seen that both of the W currents couple antineutrino to electron or vice-versa but the Z current only couples the particles to themselves. This means that the W currents carry charge and thus are named charged-current interactions compared to the Z current where this is not the case and have been named neutral-current interactions.

Finally, to produce the full Standard Model requires the strong interaction QCD which will not be described in this thesis, and details can be found in [23] among others.

The particles in the SM, shown in figure 1.3, can be split into two different types, fermions and gauge bosons, characterised by their half-integer and integer spin. Fermions can be further split depending on whether they experience strong interactions or not, with quarks undergoing strong interactions and having fractional charge, and leptons that do not see the strong force and have integer charge. Gauge bosons are the force mediators for the particle interactions while the Higgs boson is the only scalar, spin 0, particle in the SM, responsible for symmetry breaking and giving mass to all particles [21], see figure 1.3.

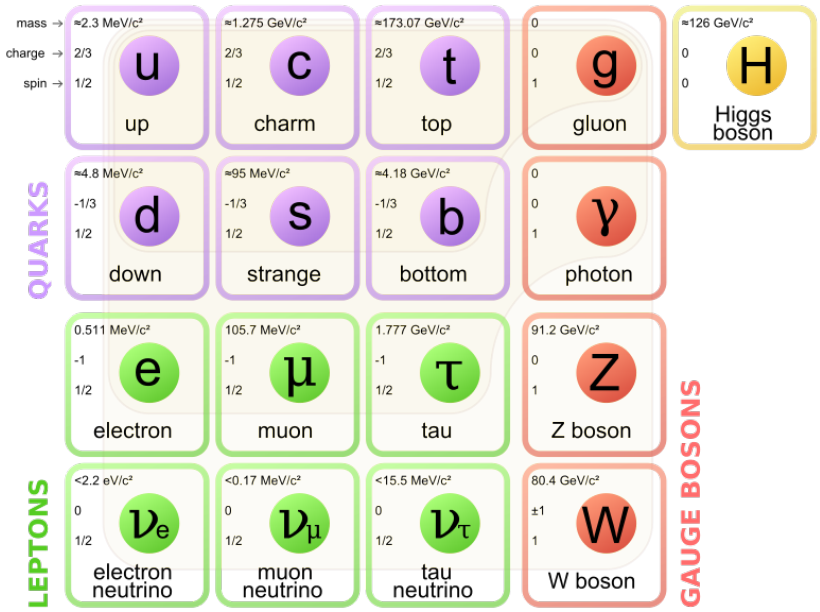

Figure 1.3: The Standard Model of particle physics where the three first columns of the figure represent the three generations, starting with the first. [24]

1.4 Neutrino interactions

Neutrino interactions are split into two different types depending on which boson mediates the interaction. Charged Current (CC) interactions change the final state quarks or leptons by one unit of electric charge and are mediated by the W^+ and W^- bosons while Neutral Current (NC) interactions do not change the charge and are mediated by a Z^0 boson. To look at possible interactions of neutrinos described in the Standard Model of particle physics, one needs to look at the quantum field theory description of the interactions, as was described in section 1.3 and details can be found in, among others [25, 26].

1.4.1 Neutrino-electron interactions

Neutrinos interact with electrons by Charged Current and Neutral Current interactions. Since electrons are fundamental particles, their interactions are point-like.

When it comes to neutrino and electron interactions, experimentally only the following have been observed:

$\nu_x e \rightarrow \nu_x e$ with the Lagrangian given by:

$$\mathcal{L} = -\frac{G_F}{\sqrt{2}} \left[\bar{\nu_x}\gamma_\alpha(1-\gamma_5)\nu_x\right] \left[\bar{e}\gamma_\alpha(g_V - g_A\gamma_5)e\right] \tag{1.28}$$

with the constants as defined previously, including the Fermi constant G_F, the Weinberg

angle θ_W and where g_V and g_A are constants relating to strong interactions from V-A theory. $\nu_x e \to \nu_e x$, with the Lagrangian given by:

$$\mathcal{L} = -\frac{G_F}{\sqrt{2}} \left[\bar{\nu_x}\gamma_\alpha(1-\gamma_5)x\right] \left[\bar{\nu_e}\gamma_\alpha(1-\gamma_5)e\right]. \tag{1.29}$$

The cross sections are calculated by first calculating the interaction amplitude by using the initial and final states to evaluate the Lagrangian. This amplitude can then be related to a derivative of the cross-section which can be integrated to provide the final cross section. The details can be found in [25].

The various processes involving an electron as an initial state with their calculated cross sections can be seen in table 1.1 where the variable s is the Mandelstam variable, $s = (p_{\nu_\mu} + p_e)^2 = 2m_e E_{\nu_\mu}$.

Table 1.1: Neutrino interactions with electrons.

Type	Process	Cross-section
CC interaction	$\nu_\mu + e^- \to \mu^- + \nu_e$	$\frac{G_F^2 s}{\pi}$
CC+NC Scattering	$\nu_e + e^- \to \nu_e + e^-$	$\frac{G_F^2 s}{4\pi}\left[(2\sin^2\theta_W - 1)^2 + \frac{4}{3}\sin^2\theta_W\right]$
CC+NC Scattering	$\bar{\nu_e} + e^- \to \bar{\nu_e} + e^-$	$\frac{G_F^2 s}{4\pi}\left[\frac{1}{3}(2\sin^2\theta_W + 1)^2 + 4\sin^2\theta_W\right]$
NC Scattering	$\nu_\mu + e^- \to \nu_\mu + e^-$	$\frac{G_F^2 s}{4\pi}\left[(2\sin^2\theta_W - 1)^2 + \frac{4}{3}\sin^2\theta_W\right]$
NC Scattering	$\bar{\nu_\mu} + e^- \to \bar{\nu_\mu} + e^-$	$\frac{G_F^2 s}{4\pi}\left[\frac{1}{3}(2\sin^2\theta_W - 1)^2 + 4\sin^2\theta_W\right]$
Neutrino pair production	$e^+ + e^- \to \nu_e + \bar{\nu_e}$	$\frac{G_F^2 s}{12\pi}\left[\frac{1}{2} + 2\sin^2\theta_W + 4\sin^4\theta_W\right]$
Neutrino pair production	$e^+ + e^- \to \nu_\mu + \bar{\nu_\mu}$	$\frac{G_F^2 s}{12\pi}\left[\frac{1}{2} - 2\sin^2\theta_W + 4\sin^4\theta_W\right]$

To make it simpler for calculations and visualization these interactions have been plotted as Feynman diagrams in figure 1.4, figure 1.5 and figure 1.6.

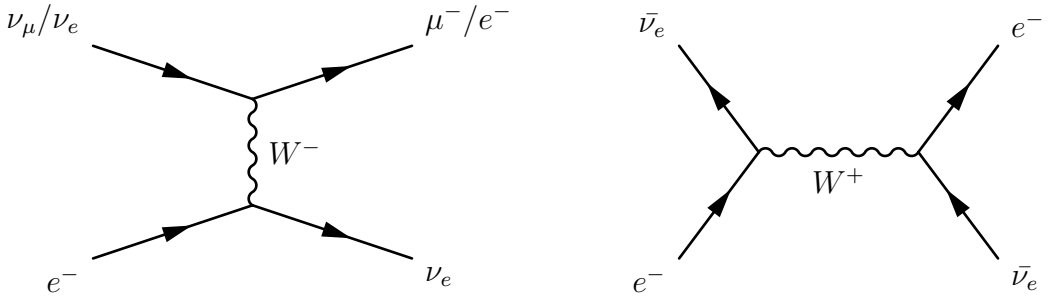

Figure 1.4: Charged current interaction between neutrinos and electrons.

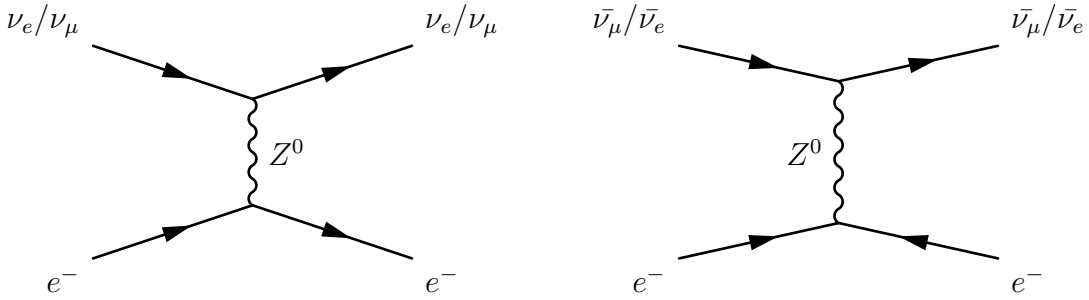

Figure 1.5: Neutral current interaction between neutrinos and electrons.

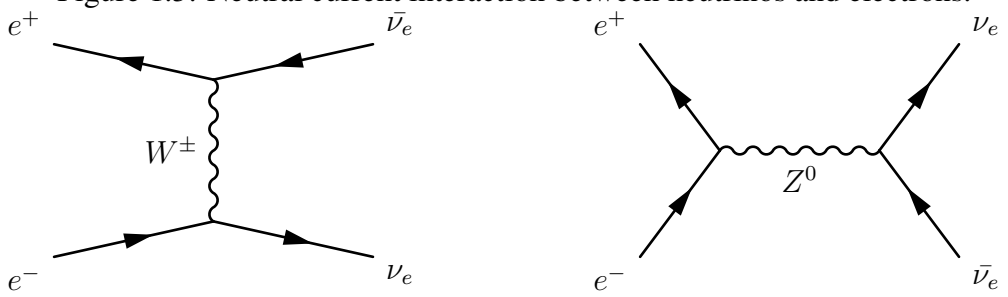

Figure 1.6: Neutrino pair production.

1.4.1.1 Comparing neutrino interactions to QED

It is interesting to compare the probability for Charged Current and Neutral Current interactions with the equivalent QED or electromagnetic interactions. In figure 1.7 a comparison is made between QED and a weak interaction with the same initial and final states. Calculating the cross-sections when $E << M_Z$ the following quotient is produced: $\frac{\sigma_{Weak}}{\sigma_{QED}} \approx (\frac{s}{M_Z^2})^2$ where s is the square of the center of mass energy and M_Z is the mass of the Z-boson. Currently the Z-boson mass is $91.1876\ GeV$ [23] but since s varies it is hard to give a value to the quotient. For the energy range where $E << M_Z$ this quotient varies from $0.01 \rightarrow 0.1225$. With the current values, QED is approximately 100 times more likely to occur than a weak interaction.

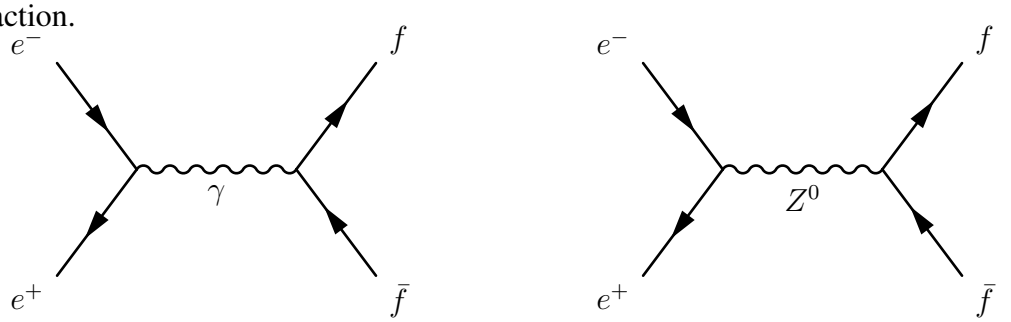

Figure 1.7: The QED and the weak contributions to electron-positron scattering with any quark or lepton pair in the final state.[1]

Consider the CC and NC examples in figure 1.8, with electrons and muon neutrinos, so that

[1] If $f = e^-$ a T-channel diagram has to be added as well.

the final states can be distinguished. The cross sections of both can be written as:

$$\sigma_{CC}(\nu_\mu e^-) \approx \frac{G_F^2 s}{\pi} \tag{1.30}$$

$$\sigma_{NC}(\nu_\mu e^-) \approx \frac{G_F^2 s}{\pi}\left[(-\frac{1}{2}+\sin^2\theta_W)^2+\frac{1}{3}\sin^4\theta_W\right], \tag{1.31}$$

where G_F, s and θ_W are defined above. This gives a relation between CC and NC as:

$$\frac{\sigma_{CC}}{\sigma_{NC}} = \left[(-\frac{1}{2}+\sin^2\theta_W)^2+\frac{1}{3}\sin^4\theta_W\right]^{-1} \approx 11. \tag{1.32}$$

With the current value of θ_W CC is approximately 11 times more likely to occur than NC.

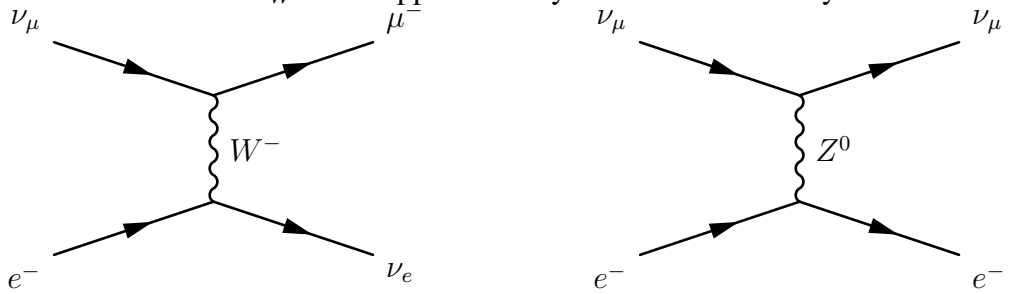

Figure 1.8: Feynman diagrams, CC (Left) and NC (Right) with the same initial states.

1.4.2 Neutrino-quark scattering

Moving away from electrons into quarks one has to take into account that quarks are always bound in a hadron, and thus do not exist in a free state.

Neutrino-quark interactions can be understood in two different ways. Inverse beta-decay where a proton interacts with an antineutrino producing a positive lepton and neutrino, $\bar{\nu}_{e/\mu} + p \rightarrow e^+/\mu^+ + n$, can be seen as an interaction where the full hadron interacts and only changes its weak charge instead of interacting with each quark separately. The interacting particle, the proton, changes into another baryon, the neutron. However, at higher energies neutrinos interact with the constituent quarks inside the nucleons, dissociating them through hadronisation into multiple hadrons.

1.4.2.1 Quasi-elastic interactions

Quasi-elastic scattering of neutrinos with nucleons is the process in which the (anti)neutrino interacts with the proton or neutron as a whole. This requires extra factors to model the nucleon as a whole, compared to the electron which was seen as point-like. The cross section

is given as:

$$\sigma(\bar{\nu_e} + p \rightarrow e^+ + n) = \frac{G_F s}{\pi} \times \cos^2\theta_C \times \xi_{mass} \times (g_V^2 + 3g_A^2) \tag{1.33}$$

with corrections for charged current quark mixing transition from u to d quark $(\cos^2\theta_C)$, a mass suppression factor:

$$\xi_{mass} = \frac{1 - m_{final}^2}{s} = \frac{2m_p\delta E}{(m_n + m_e)^2 + 2m_p\delta E}, \tag{1.34}$$

where $\delta E = E_\nu - E_\nu^{min}$ and where E_ν^{min} is the threshold energy $E_\nu^{min} \approx E_\nu - \frac{(m_n+me)^2 - m_p^2}{2m_p^2}$ for the interaction, and proton form factors $g_V^2 + 3g_A^2$ [27].

It is also interesting to note that apart from inverse beta-decay, which is a CC interaction, a quasi-elastic NC interaction can also happen $\nu_\mu + p \rightarrow \nu_\mu + p$ which knocks off the proton but does not change it.

1.4.2.2 Deep inelastic scattering

If the neutrino has an energy of around or above 1 GeV there is enough energy that the neutrino can break up the nucleon and interact with the quarks as if they were free particles. It becomes quite difficult to calculate the cross section for these interactions as it depends on the final particle(s) as well as understanding the so-called form factors relating the quarks to the proton. The cross-section for such a process can be written as

$$\sigma(\nu + h \rightarrow l + X) = \sum_q \int dx \sigma(\nu + q(x) \rightarrow l + X) q_h(x), \tag{1.35}$$

where we have convoluted each quark interaction cross section with an appropriate parton distribution function $q_h(x)$ which has to be determined experimentally to take combined interactions and the quark density into account. Writing this using the differential cross section provides the structure factors xF_1, F_2 and xF_3:

$$\frac{d\sigma^{\nu,\bar{\nu}}}{dxdy} \propto \left[y^2 2xF_1(x, Q^2) + (2 - 2y - \frac{M_T xy}{E})F_2(x, Q^2) \pm y(2 - y)xF_3(x, Q^2) \right], \tag{1.36}$$

with M_T as the target particle mass, $y = \frac{E - E_\mu}{E}$ is the inelasticity, Q^2 is the W boson negative four-momentum squared and $x = \frac{Q^2}{2M(E - E_\mu)}$ is the Feynman scaling variable.

DIS comes with both charged current and neutral current modes as $\nu_\mu + p \rightarrow \mu^- + X$ or $\nu_\mu + p \rightarrow \nu_\mu + X$.

More details can be found in [27].

1.4.2.3 Resonant interactions

Between the elastic and inelastic region is an area associated with pion production through the excitation of baryon resonances, $\nu_i + N \rightarrow l + N^*$ where the nucleus further decays $N^* \rightarrow \pi + N'$. Two examples with delta particles can be seen below.

$$\nu_\mu + N \rightarrow \mu^- + \Delta^{++} \rightarrow \mu^- + p + \pi^+ \tag{1.37}$$

$$\nu_\mu + N \rightarrow \mu^- + \Delta^{+} \rightarrow \mu^- + n + \pi^+ \tag{1.38}$$

Using the Rein and Sehgal model put forward in [28] the differential cross section can be written as

$$\frac{d\sigma}{dQ^2 dW} = \frac{1}{32 M_T E^2} \frac{1}{2} \sum_{spins} |T(\nu N \rightarrow l N*)|^2 \Gamma(W - M_T), \tag{1.39}$$

where W is the combined mass $W^2 = (M_T + m_\pi)^2$. The function $\Gamma(W - M_T)$ is defined as

$$\Gamma(W - M_T) = \frac{1}{2\pi} \frac{\Gamma_0}{(W - M_T)^2 + \Gamma_s^2/4}, \tag{1.40}$$

with more details in [28].

1.5 Missing neutrinos

The sun generates energy principally through the proton-proton chain reaction [29]. In this chain, electron neutrinos are produced through proton-proton interactions and beta decay processes.

$$\mathrm{H}^+ + \mathrm{H}^+ \longrightarrow {}^2\mathrm{H} + \mathrm{e}^+ + \nu_e. \tag{1.41}$$

The proton-proton interaction has the highest flux, $6.1 \times 10^{10} cm^{-2} sec^{-1}$ but produces neutrinos at very low energies ($< 0.4 MeV$) making them difficult to detect. Further on in this chain a boron decay,

$${}^8\mathrm{B} \longrightarrow {}^4\mathrm{He} + {}^4\mathrm{He} + \nu_e \tag{1.42}$$

produces electron neutrinos with energies up to 18 MeV, however the fluxes are much lower than proton-proton interactions, $3.2 \times 10^6 cm^{-2} sec^{-1}$. Neutrinos in this energy can be used in inverse-beta decay transforming chlorine into argon.

$$\nu_e + {}^{37}\mathrm{Cl} \longrightarrow {}^{37}\mathrm{Ar} + e^-. \tag{1.43}$$

The amount of argon can then be counted by measuring X-rays from the decaying argon isotope. The number of ^{37}Ar atoms decaying over a period of time (typically one month)

is related to the neutrino flux from the sun. The Homestake experiment used this technique and ran from 1970 until 1994 with a goal to measure the flux of electron neutrinos. They measured the flux of electron neutrinos and found only around 1/3 of the expected value from the theoretical model of the nuclear reactions in the core of the sun [30].

These results shocked the neutrino physics community by suggesting that there was something fundamentally wrong in the understanding of the neutrino, either in the interactions or in the solar model. There were various solar experiments which confirmed the solar neutrino model [29] implying that something was wrong in our understanding of neutrinos. At the same time, measurements were performed at several other detectors, Sudbury Neutrino Observatory (SNO) [31], Kamiokande [32] and Super-Kamiokande [33] all in agreement with a smaller flux. The SNO experiment measured neutral current interactions of solar neutrinos and verified that the total flux of neutrinos was correctly predicted by the solar model, but simultaneously measured that the flux of electron neutrinos was depleted, thereby showing that the electron neutrinos had transformed to another flavour. One of the possible explanations for the deficit was neutrino oscillations proposed by Bruno Pontecorvo [34].

The oscillation model is in good agreement with experimental values and was verified at SNO and Super-Kamiokande resulting in the award of the 2015 Nobel Prize in Physics to Arthur B, McDonald and Takaaki Kajita [35]. The results of these experiments paved the way for physics beyond the Standard Model.

1.6 Neutrino mass and oscillation in vacuum

While looking at an analog of neutral kaon mixing for neutrinos Bruno Pontecorvo, in 1957, developed the concept of neutrino-antineutrino transitions [34]. Even though to date no matter-antimatter oscillation had been observed, the concept formed the foundation of lepton mixing, which was developed by Maki, Nakagawa, and Sakata [36] and refined into a neutrino flavour oscillation model by Bruno Pontecorvo. They managed to show that neutrino mixing is a natural outcome of adding neutrino mass to a gauge theory [34].

The relation between the flavour and mass eigenstates can be expressed as,

$$|\nu_\alpha\rangle = \sum_i U^*_{\alpha i} |\nu_i\rangle \, , |\bar{\nu_\alpha}\rangle = \sum_i U_{\alpha i} |\bar{\nu}_i\rangle \tag{1.44}$$

where $|\nu_\alpha\rangle$ is a neutrino state with a fixed flavour, α is one of $\{$e,μ,$\tau\}$ and $|\nu_i\rangle$ is a neutrino state with a fixed mass. U is the Pontecorvo-Maki-Nagawa-Sakata (PMNS) matrix in

equation (1.45),

$$U = \begin{pmatrix} c_{12} & s_{12} & 0 \\ -s_{12} & c_{12} & 0 \\ 0 & 0 & 1 \end{pmatrix} \begin{pmatrix} 1 & 0 & 0 \\ 0 & c_{23} & s_{23} \\ 0 & -s_{23} & c_{23} \end{pmatrix} \begin{pmatrix} c_{13} & 0 & s_{13}e^{-i\delta_{CP}} \\ 0 & 1 & 0 \\ -s_{13}e^{i\delta_{CP}} & 0 & c_{13} \end{pmatrix} \times \begin{pmatrix} 1 & 0 & 0 \\ 0 & e^{i\phi_2} & 0 \\ 0 & 0 & e^{i\phi_3} \end{pmatrix} \tag{1.45}$$

where $s_{ij} = \sin\theta_{ij}$ and $c_{ij} = \cos\theta_{ij}$ with θ_{ij} the three mixing angles and δ_{CP}, ϕ_2 and ϕ_3 are complex phases. The parameters ϕ_2 and ϕ_3 are only non-zero if neutrinos are their own antiparticles, denoted as Majorana, which is still unknown at the time of writing [23]. This would be an interesting result as it would imply a splitting with the relation to the Higgs field. The three first matrices are denoted the Dirac part of the PMNS matrix and the final fourth matrix is the Majorana term which only has imaginary terms when neutrinos are Majorana particles.

The probability of finding a neutrino in a specific time-dependent state is related to the mass states through the PMNS matrix elements and the time-evolution operator. The PMNS matrix introduces a rotation in the space of mass eigenstates. The derivations of the oscillation probability for two-neutrino and three-neutrino oscillations can be found in the literature [20]. The three neutrino flavour state shown in equation 1.44 evolves as a function of time as:

$$|\nu_\alpha(t)\rangle = \sum_i e^{-iE_i t} U_{\alpha i} |\nu_i\rangle \tag{1.46}$$

which gives the probability of flavour evolution as

$$P_{\nu_\alpha \to \nu_\beta}(t) = |\langle \nu_\beta | \nu_\alpha \rangle|^2 \quad = \sum_{i,j} \left| U_{\alpha i} U^*_{\beta i} U \alpha j^* U_{\beta j} \right| \cos[(E_i - E_j)t - arg(U_{\alpha i} U^*_{\beta i} U \alpha j^* U_{\beta j})] \tag{1.47}$$

$$E_\alpha = \sqrt{\vec{p}^2 + m_i^2} \approx |\vec{p}| + \frac{m_i^2}{2\,|\vec{p}|}. \tag{1.48}$$

If one has a beam of neutrinos in an initial flavour state $|\nu_\alpha\rangle$, the probability to find the neutrinos changing to flavour state $|\nu_\beta\rangle$, after a distance x, is given by

$$P_{\nu_\alpha \to \nu_\beta}(x) = |\langle \nu_\beta | \nu_\alpha \rangle|^2 \quad = \sum_{i,j} \left| U_{\alpha i} U^*_{\beta i} U \alpha j^* U_{\beta j} \right| \cos \left[\frac{2\pi x}{L_{ij}} - arg(U_{\alpha i} U^*_{\beta i} U^*_{\alpha j} U_{\beta j}) \right], \tag{1.49}$$

where the approximate energy-momentum relationship of equation 1.48 has been taken into account, where the oscillation length is given by $L_{ij} = \frac{4\pi|\vec{p}|}{|m_i^2 - m_j^2|} = \frac{4\pi|\vec{p}|}{|\Delta m_{ij}^2|}$ and $\vec{p}$ is the three-momentum of the neutrinos in the initial beam.

It is worth noting that the equation can be simplified assuming only oscillation between two flavours:

$$P_{\nu_\mu \to \nu_y}(x) = \sin^2(2\theta_{\mu y}) \sin^2 \left(\frac{1.27 \Delta m^2_{\mu y} x}{E_\nu} \right) \tag{1.50}$$

where 1.27 is a dimensionless constant when Δm^2 is given in units of eV^2, x in meters and E_ν is in MeV.

It is also worth noting that in the full three-flavour description the equation contains the δ_{CP} phase and shows a relation between δ_{CP} and the other angles:

$$P(\nu_\mu \to \nu_e) = P1 + P2 + P3 + P4 \tag{1.51}$$

$$P1 = \sin^2 \theta_{23} \sin^2 2\theta_{13} (\frac{\Delta_{13}}{B_\pm})^2 \sin^2 \frac{B_\pm L}{2} \tag{1.52}$$

$$P2 = \cos^2 \theta_{23} \sin^2 2\theta_{12} (\frac{\Delta_{12}}{A})^2 \sin^2 \frac{AL}{2} \tag{1.53}$$

$$P3 = J \cos \delta_{CP} (\frac{\Delta_{12}}{A})(\frac{\Delta_{13}}{B_\pm}) \cos \frac{\Delta_{13} L}{2} \sin \frac{AL}{2} \sin \frac{B_\pm L}{2} \tag{1.54}$$

$$P4 = \mp J \sin \delta_{CP} (\frac{\Delta_{12}}{A})(\frac{\Delta_{13}}{B_\pm}) \sin \frac{\Delta_{13} L}{2} \sin \frac{AL}{2} \sin \frac{B_\pm L}{2} \tag{1.55}$$

where the following variables have been defined

$$\Delta_{ij} = \frac{\Delta m^2_{ij}}{2E_\nu} \tag{1.56}$$

$$A = \sqrt{2} G_F n_e \tag{1.57}$$

$$B_\pm = |A \pm \Delta_{13}| \tag{1.58}$$

$$J = \cos \theta_{13} \sin 2\theta_{12} \sin 2\theta_{13} \sin 2\theta_{23} \tag{1.59}$$

and where $\pm$ denotes neutrinos or antineutrinos. G_F is the Fermi constant, n_e is the electron density, L is the distance travelled and E_ν is the neutrino energy. If J, the Jarlskog determinant, were to be zero there would be no CP violating term involved. This means that non-zero measurements of θ_{12}, θ_{13} and θ_{23} are required to see an effect of δ_{CP}.

The mass-squared difference between neutrino mass states $\left|m_i^2 - m_j^2\right|$ has to be non-zero for there to be neutrino oscillations, so at least one of the neutrinos must have non-zero mass which currently is not explained through the Standard Model. Furthermore, if the elements of the PMNS matrix $U_{\alpha i}$ are all real then $arg(U_{\alpha i}U^*_{\beta i}U^*_{\alpha j}U_{\beta i}) = 0$ and the CP-violating phase $\delta_{CP} = 0$. The current experimental focus lies with trying to measure values for all these parameters. Current values of the neutrino masses can be found in table 1.2.

Looking at the oscillation probability in equation (1.49) two main classes of experiments for neutrino oscillations can be devised. Finding a distance x to the source where $P_{\nu_\alpha \to \nu_\alpha}(x) < 1$, it is possible to look at so-called disappearance of the beam by comparing the expected neutrino flux to the observed. For the disappearing flavour there must be a probability, $P_{\nu_\alpha \to \nu_\beta}(x) > 0, \alpha \neq \beta$ for another flavour to appear. The second kind of experiment, denoted as appearance, is based on looking for interaction products which are impossible without oscillations. An example of this would be to see a positron from a muon neutrino beam. More on this can be found well described in [20] and examples of different detectors will be discussed in chapter 2. As a rule of thumb the distance of propagation L has to be on the order of km for the neutrino energy ranges between MeV to GeV. This means that oscillations will have a small effect on short scale neutrino interactions measured close to the source.

Charge conjugation and parity (C and P, CP) symmetry states that physics should be the same for particles and anti-particles while the spatial coordinates are inverted. If δ_{CP} is non-zero implying CP symmetry is violated it would imply a difference between the rate of neutrino and antineutrino oscillations which could be responsible for the matter-antimatter asymmetry of the early universe. Current best-fit values (at 90% confidence limit) have $\delta_{CP} = -1.79 \pm 1.42$ for normal mass ordering (if $m_1 < m_2 < m_3$) and $\delta_{CP} = -1.41 \pm 0.68$ for inverted mass ordering (if $m_3 < m_1 < m_2$) both rejecting the null hypothesis for δ_{CP} at the 90% confidence limit [37].

Table 1.2 provides the current mass limits for neutrinos, note that currently there is no lower limit since it is only known that at least two of the neutrinos must have mass.

Particle	95% CL upper mass limits (MeV)
ν_e	$< 2 \cdot 10^{-3}$
ν_μ	< 0.19
ν_τ	< 18.2

Table 1.2: Current upper neutrino mass limits [23].

1.7 CP-violation, baryogenesis and leptogenesis

According to the Big Bang theory, matter and anti-matter were created in equal amounts [38]. Through observations of the universe, much more matter has been found compared to anti-matter. This constitutes one of the major unsolved problems in physics, where is all the anti-matter? There has currently not been any sign of an annihilation horizon, where matter and anti-matter interact, nor has there been any sign of this in the cosmic background radiation [38]. One direct measurement was AMS-01, (Alpha Magnetic Spectrometer),which measured the ratio of anti-helium to helium in the universe to be of the order of 10^{-6} [39].

The follow-up experiment, AMS-02, which is operational in the International Space Station, confirmed these results and measured the antibaryon component of the universe to be $\sim 10^{-9}$ less that of baryons [40]. Current models account for a difference between baryons and anti-baryons of $\sim 10^{-20}$, thus a factor of 10^{11} too small to explain the observed difference [41]. This implies that there must be a yet unknown process to account for the difference [42].

There exist two approaches to explain the matter asymmetry of the universe. The first is baryogenesis which studies possible mechanisms to enhance the baryon-antibaryon asymmetry, and the second is leptogenesis, in which violation of charge and parity symmetry (CP-violation) in leptons translates into a baryon asymmetry. Leptogenesis will be covered in this thesis as it relates to neutrinos. It should also be added that there are theories which explain baryogenesis through leptogenesis.

If neutrinos violate CP by their oscillations being different for neutrinos and antineutrinos, this could explain the matter anti-matter imbalance that has been observed. CP-violation exists in the Standard Model but it cannot explain the observed difference [25], and measurements of the CP-violation in neutrino oscillations have not yet been able to show any conclusive results [43].

Andrei Sakharov proposed three necessary conditions that any baryon-generating interaction, which would produce matter antimatter imbalance, must satisfy [44]. These conditions are:

- Baryon number violation.
- C-and CP-violation.
- Deviation from thermal equilibrium.

The first condition is very important in that it relates the cosmological models with models in particle physics. It also gives us a way to produce an excess of baryons over anti-baryons, as long as there is no reverse interaction, hence requiring the charge symmetry (C) violation. CP-violation is needed to counteract the balancing as well, and finally the universe must

be out of thermal equilibrium to get around charge, parrity and time (CPT) symmetry. As briefly mentioned previously the second condition is fulfilled in the SM, but not enough, and the third can always be satisfied.

In [27] a number of viable scenarios for baryogenesis are briefly discussed, for instance Grand Unified theories, heavy Majorana neutrinos and supersymmetry.

1.8 Introduction to explaining neutrino masses

The problem with neutrino masses is that we only see left-handed neutrinos. The standard way for fermions to obtain a mass through interaction with the Higgs field is through a three point interaction involving a left-handed fermion, a right-handed fermion, and the Higgs field. With no right-handed neutrinos, one cannot create a mass term after symmetry breaking in the conventional way. This leaves the exact mechanism by which neutrinos acquire mass a mystery. When the SM was created neutrinos were assumed to be massless since they were only left-handed. There are three main reasons why the neutrino mass must be zero in the SM:

- There is no renormalizable operator which allows for a neutrino mass without introducing either an additional Higgs particle or by introducing right-handed neutrinos, neither of which have currently been observed.
- The current Higgs is an $SU(2)_L$ doublet, thus it requires fermions to have both chiral states to provide mass. It could be possible to introduce further Higgs particles which do not require this.
- There are no right-handed neutrinos. Right-handed neutrinos could be introduced which would allow the current Higgs or any other current mechanism to provide mass. This is because the right-handed neutrino will be modeled as a singlet state in the extended-SM.

There are different ongoing searches to find all categories of solutions, higher-order operators (non-renormalizable), other Higgs particles (Non $SU(2)_L$ doublets) and right-handed neutrinos.

In this thesis the focus will be on introducing right-handed neutrinos. There are two main mass terms both related to the Higgs mechanism, the so-called Dirac term and the Majorana term.

Naively introducing right-handed neutrinos makes an assumption that neutrinos and antineutrinos are distinct particles, however, since the neutrino is electrically neutral, this does not have to be the case.

Introducing right-handed neutrinos introduces particles which will not interact in the SM since the electroweak interaction model only couples to left handed neutrinos. Thus right-handed neutrinos are often denoted sterile neutrinos and only interact through gravity. This introduces sterile neutrinos as a possible candidate for dark matter [45, 46].

The main problems with this description is both that no right-handed neutrinos have been detected and that the observed neutrino mass measurement requires a weaker coupling to the Higgs field for neutrinos compared to the other leptons.

Dirac neutrinos could be experimentally verified by finding that neutrinos are distinct particles with respect to the antineutrinos or by finding both right-handed neutrinos and left-handed neutrinos as different particles.

Removing the assumption that neutrinos and antineutrinos are distinct allows for a simplified model. Right-handed neutrinos have to be produced to conserve lepton number. Majorana mass also has no equivalent for other leptons and could explain why the neutrino mass is so small. Majorana neutrinos would allow neutrinoless double beta decay [47] as an experimental verification.

1.9 Summary

In this chapter, the history of the neutrino, the introduction of neutrinos into the Standard Model and a brief theory of neutrino interactions have been introduced. Current issues with massive neutrinos, neutrino oscillations and the nature of the neutrino, whether the neutrino is a Dirac or a Majorana particle, remain as open questions and are also presented in this chapter.

Chapter 2

Neutrino experiments

2.1 Introduction

Since the discovery of the neutrino in 1956 by Reines and Cowan [8] a multitude of neutrino experiments have tried to measure the properties of the different neutrino flavours. Since the Homestake experiment, many other experiments have been run to measure neutrino oscillations and the mass of neutrinos. A detailed description of these experiments is outside of the scope of this thesis, however in this section a description of the main types of experiments and milestones will be presented.

Neutrino experiments are split into four different categories based on their primary neutrino source. Each type features its own advantages and issues. The experiment types are those that detect:

- Atmospheric neutrinos
- Solar neutrinos
- Accelerator neutrinos
- Reactor neutrinos.

Each will be described briefly before examples are given.

2.2 Atmospheric neutrino experiments

As mentioned in section 1.5 neutrinos at low energy ranges (< 18 MeV) are produced through nuclear interactions in stars. There are other cosmological phenomena which produce neutrinos, and some searches are looking for signs of new physics in these signals.

The Earth is constantly bombarded by cosmic-ray particles from space. When they hit the atmosphere, these high-energy protons interact with air molecules to produce showers of pions, which subsequently decay to muons and muon-neutrinos. This process is similar to that used to produce neutrino beams from particle accelerators. Early observations of atmospheric neutrinos were contradictory, with some experiments observing approximately the expected ratio while others saw significantly fewer muon-neutrinos than expected, similar to the missing solar neutrinos. This became known as the Atmospheric Neutrino Anomaly. This was a measurement performed by Super-Kamiokande and confirmed, together with the Homestake experiment, the existence of neutrino oscillations [33, 30].

The atmospheric neutrinos are produced from cosmic-rays interacting through nuclear interactions producing pions which decay into muons, electrons and neutrinos through the following interactions:

$$\pi^{\pm} \rightarrow \mu^{\pm}\nu_{\mu}(\bar{\nu_{\mu}}) \tag{2.1}$$

$$\mu^{\pm} \rightarrow e^{\pm}\bar{\nu_{e}}\nu_{\mu}(\nu_{e}\bar{\nu_{\mu}}). \tag{2.2}$$

The neutrinos produced have an energy that can be in the GeV to PeV range. However, it is impossible to control the source and difficult to get many events due to the low fluxes expected from cosmic rays.

Looking at the two flavour oscillation formula:

$$P_{\nu_{\mu}\rightarrow\nu_{y}}(L) = \sin^2(2\theta_{\mu y}) \sin^2 \frac{[1.27\Delta m^2_{\mu y} L]}{E_{\nu}} \tag{2.3}$$

these experiments are able to measure the direction angle (θ), to extract the distance the neutrino has travelled L, and the energy (E_{ν}) of the neutrino to extract the mixing angle $\theta_{\mu y}$ and the mass-squared difference $\Delta m^2_{\mu y}$. Given the current experimental values, these experiments are best suited to look for θ_{23} and $|\Delta m^2_{32}|$.

2.2.1 Historical experiments

In the beginning of the 1960s the Kolar Gold Fields (KGF) experiment, in a mine near Kolar (India), was the first experiment to record atmospheric neutrinos by detecting inelastic

neutrino events in the large amount of rock covering the experiment producing two distinct muon tracks through charge current interactions $\nu + N \rightarrow N' + \mu$ [48]. These results were used to estimate the neutrino induced muon interaction flux.

At the same time a similar experiment in the E.R.P. Mines in South Africa reproduced the results and improved some of the measurements [49].

2.2.2 NUSEX

The NUSEX detector, installed in the Mont Blanc tunnel, collected data between June 1982 and 1988 and was a cube 3.5 m^3 consisting of 134 iron plates with plastic streamer tubes interlaced between the different iron plates providing 150 tons of instrumented mass (see figure 2.1). One of the main results from NUSEX was that they did not observe any difference in the rate of electron and muon neutrinos as seen in figure 2.2, in contradiction with the Kamiokande experiment [50, 51].

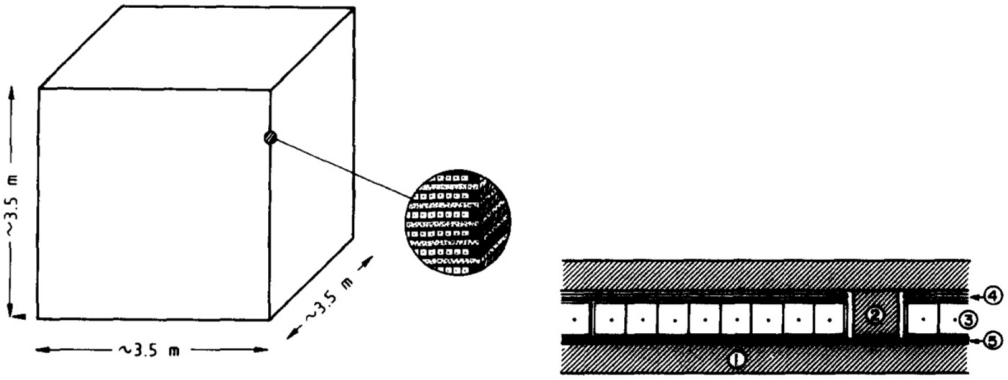

Figure 2.1: A sketch of the NUSEX detector with various parts highlighted [50].

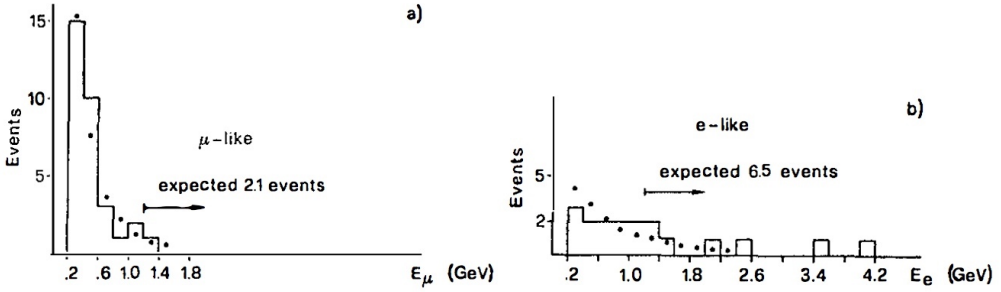

Figure 2.2: Data compared to Monte Carlo for 50 neutrino events in the NUSEX detector and showing consistency within errors [51].

2.2.3 KamiokaNDE

The Kamioka Nucleon Decay Experiment (KamiokaNDE) was a 3000 ton water Cherenkov detector installed in the Kamioka mine in Japan, 1000 m under the top of a mountain (figure 2.3). The goal of the detector, which began operation in 1983, was to study and search for nucleon decay. Cherenkov light is emitted when a particle travels faster than the speed of light inside a medium. This creates a shock wave similar to the sonic boom that is visible in nuclear reactors as a bluish light. In KamiokaNDE the Cherenkov light was detected using 1000 large PhotoMultiplier Tubes (PMTs) [52].

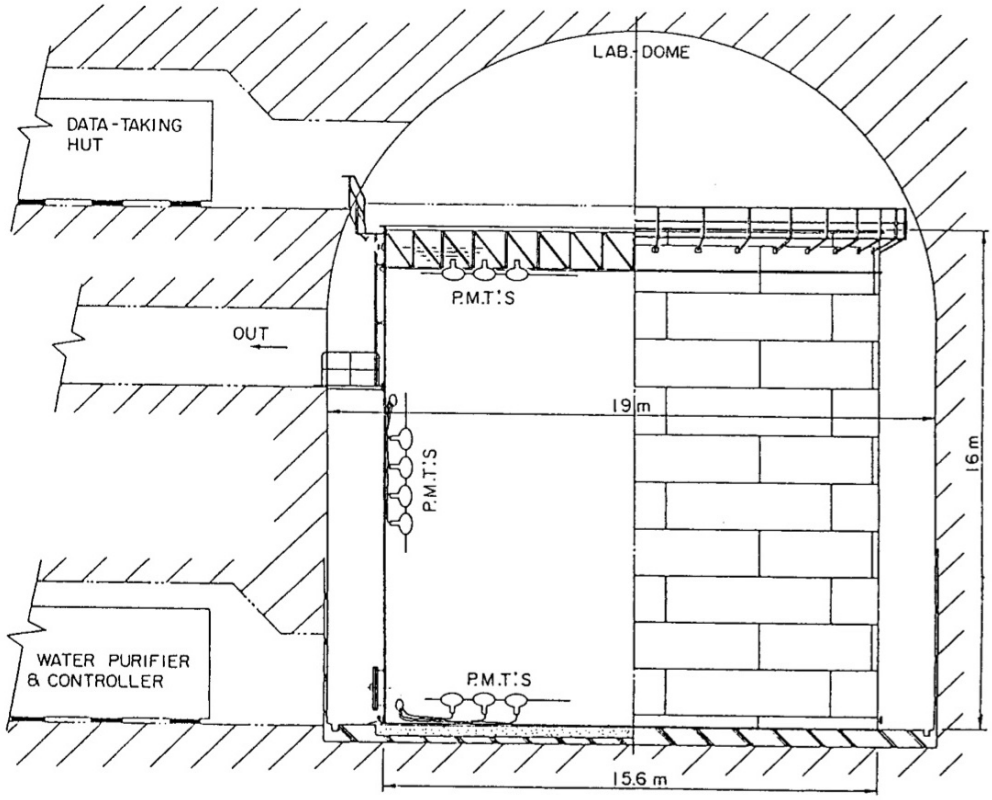

Figure 2.3: Schematic image of the KamiokaNDE detector. [52].

KamiokaNDE found an anomaly between the expected number of ν_μ and ν_e atmospheric neutrinos, which was the first hint that possibly atmospheric neutrinos were oscillating (figures 2.4 and 2.5.

2.2.4 IMB

The Irvine- Michigan-Brookhaven (IMB) groups built a 8 kiloton water Cherenkov detector 600 m under the Morton Salt Mine in Cleveland which began data taking in 1986. The design

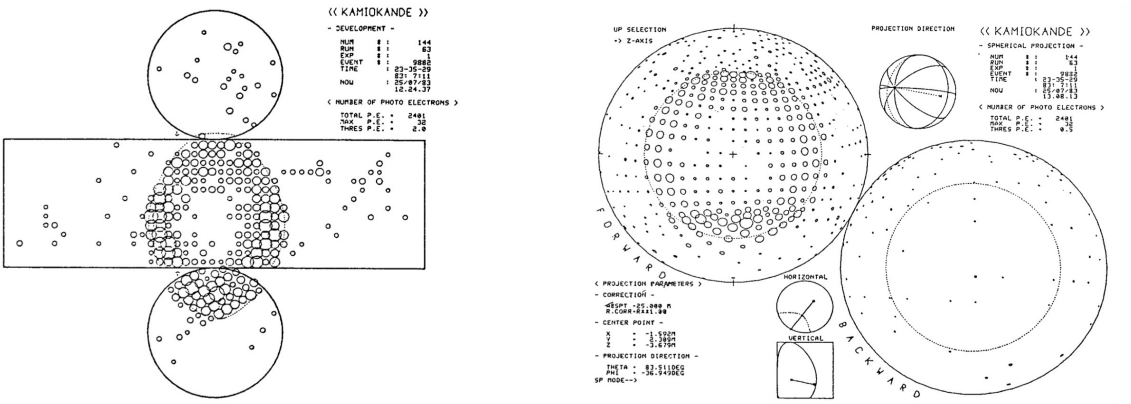

Figure 2.4: A sample event showing Cherenkov rings in KamiokaNDE produced by a muon event [52].

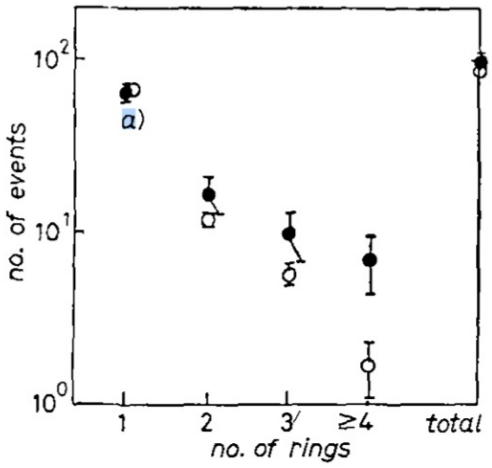

Figure 2.5: Comparing ring multiplicity distributions between data (black) and simulations (white) in KamiokaNDE [53].

was similar to KamiokaNDE and also observed the anomaly between ν_μ and ν_e atmospheric neutrino rates [54].

2.2.5 Super-KamiokaNDE

Super-KamiokaNDE (Super-K) [55], a water Cherenkov detector located 1 km underground also in the Kamioka mine in Japan and began operations in 1996. The detector consists of a cylindrical stainless steel tank holding 50 ktons of ultra-pure water (figure 2.7. Super-K performed the first experimental observation that the neutrino has non-zero mass [33] and also managed to detect strong evidence of muon neutrino oscillation to tau neutrinos from the analysis of atmospheric neutrinos interacting in the water target (see figure 2.6). The

deviation from unity is evidence for the discovery of neutrino oscillations and the lines show the expected shape for oscillation from muon neutrinos to tau neutrinos [33]. It also shows that electron-like events have no significant variation in length over neutrino energy whereby muon-like events are about half of the expected rate at large values of length over neutrino energy.

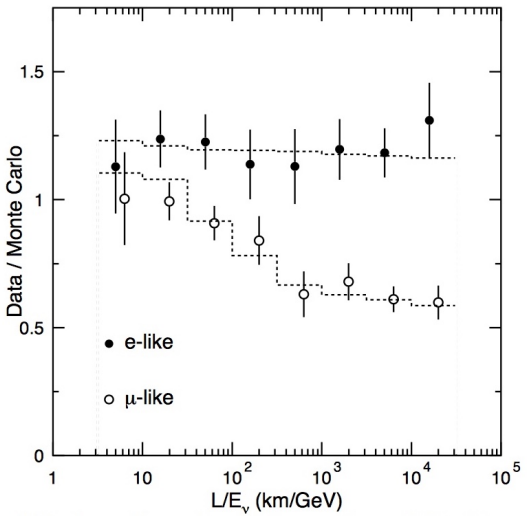

Figure 2.6: Comparison of the ratio of data vs Monte Carlo vs length over neutrino energy for fully contained atmospheric electron-like and muon-like events in the Super-K detector [33].

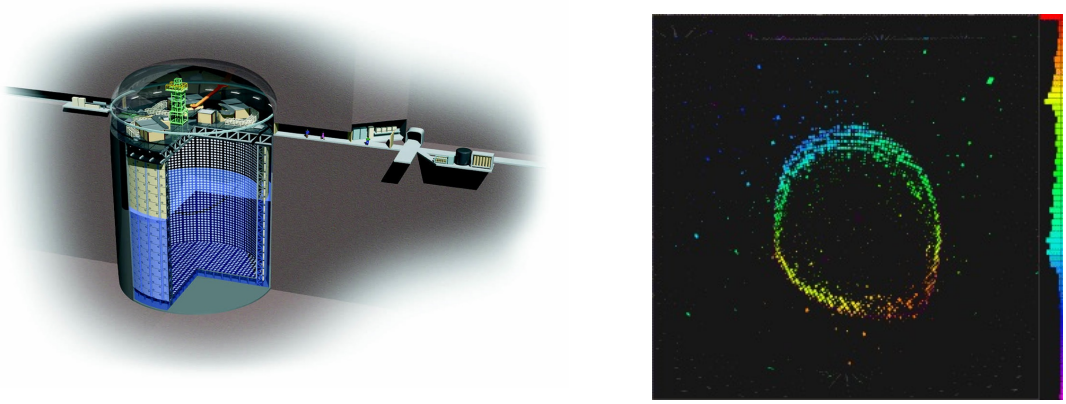

Figure 2.7: Left) A schematic of the Super-K detector., Right) Event recorded in Super-K.

2.2.6 MACRO

The Monopole, Astrophysics and Cosmic Ray Observatory (MACRO) detector (figure 2.8) was a combination of liquid scintillation counters, limited streamer tubes and nuclear track detectors which allowed it to search for signs of magnetic monopoles, as well as being able to

operate as a neutrino detector and search for other phenomena. Data was taken between 1995 until 2000 and by measuring neutrino induced muons, the MACRO experiment managed to aid in the discovery of atmospheric neutrino oscillation [56].

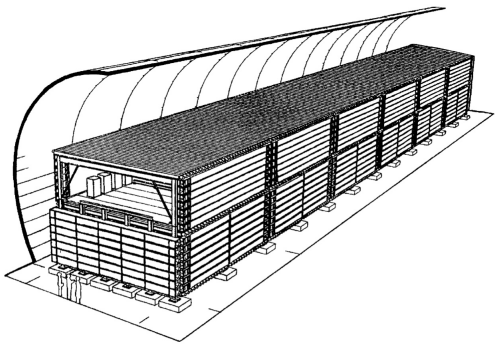

Figure 2.8: Schematic of the MACRO detector [57].

2.3 Solar neutrino experiments

The mechanism for neutrino generation in the sun was briefly discussed in subsection 1.5. Solar neutrinos are interesting for both allowing a unique way of probing the internal solar reactions as well as providing a very long baseline for neutrino oscillations. Solar neutrino experiments are sensitive to θ_{12} and Δm^2_{12}.

2.3.1 Super-KamiokaNDE

Super-KamiokaNDE, as described in subsection 2.2.5 was sensitive enough to measure solar neutrinos with improved sensitivity. It was able to confirm the reduction of the solar electron neutrino flux $(2.38 \pm 0.05(stat)^{+0.16}_{-0.15}) \times 10^6\ cm^{-2}s^1$, and determine the solar neutrino parameters to be $\tan^2\theta = 0.40$ and $\Delta m^2 \pm 6.03 \times 10^5$ eV^2 [58].

2.3.2 SNO

The Sudbury Neutrino Observatory (SNO) [31] was built to make a definite measurement of solar neutrinos following the measurements taken by the Homestake experiment [30]. The observatory recorded data from 19999 to 2006. It utilized PMT (Photo Multiplier Tubes) to measure Cherenkov radiation produced by neutrino interactions in the detector's 1000 ton ultra-pure heavy water (D_2O) volume (figure 2.9). The whole detector is placed 2 km underground to minimise background interactions. The larger depth of this experiment reduces the cosmic ray and atmospheric neutrino background seen by this detector and careful selection of materials used inside the detector reduced the threshold for solar neutrino interactions with respect to Super-K. The experiment has a unique ability to separate the reactions between electron neutrino charge current $\nu_e + d \rightarrow p + p + e^-$ (CC), neutral current interactions $\nu_x + d \rightarrow n + p + \nu_x$ (NC) with all flavours of neutrinos and with electron scattering $\nu_x + e^- \rightarrow \nu_x + e^-$ (ES). The neutrino flux observed through CC reactions could be compared to that of the ES and NC to provide evidence for a neutrino flavour change regardless of the predictions of solar modes.

The experiment clearly showed a significant difference in flux between CC interactions, only available with electron neutrinos compared to expected and compared to the NC and ES interactions. The result can be seen in figure 2.10.

The experiment is currently replacing the heavy water with liquid scintillator and renaming itself as SNO+ [60] to carry out a programme to search for double-beta decay.

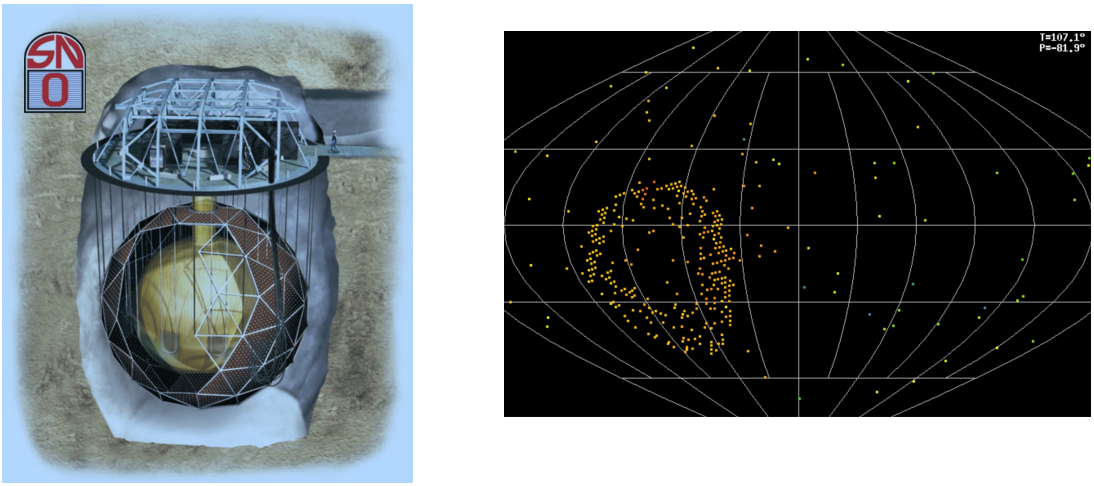

Figure 2.9: Left) A schematic drawing of the SNO detector [31], Right) Cherenkov light recorded from a muon created by interaction of an atmospheric neutrino in the heavy water.

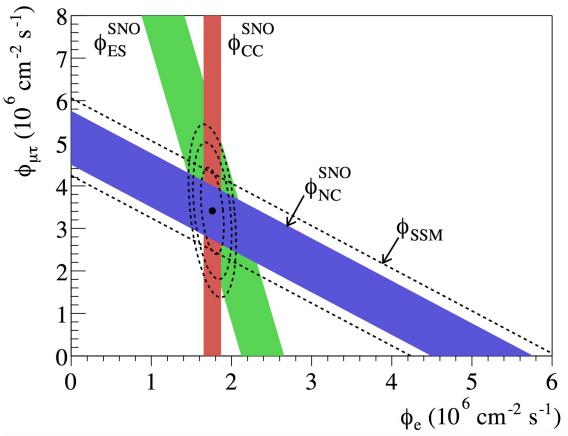

Figure 2.10: The flux of solar neutrinos of μ or τ flavour vs flux of electron neutrinos measured in SNO from the three reactions, CC in red, ES in green and NC in blue.The diagonal dashed lines show the prediction from the Standard Solar Model. The coloured bands intersect at the fit values for all fluxes indicating that they are consisted with neutrino flavour transformation with no distortion in the solar neutrino energy spectrum [59].

2.3.3 Borexino

Borexino is a liquid scintillator detector with very small radioactive contamination background, making it more sensitive to low energy solar neutrinos than the SNO and Super-K water Cherenkov detectors, but it lacks the ability to determine the direction of the incoming neutrino, since scintillation light is isotropic. The low radioactive background is achieved by containing the detector within shielding material and utilizing ultra pure materials [61]. The scintillating light is then read out by PMTs uniformly distributed around the active volume seen in figure 2.11.

The experiment started data taking in May 2007 and is still ongoing. It has the goal of making

very precise measurements of solar neutrino fluxes as well as setting limits on charge non conservation, limits on sterile neutrinos and measuring neutrinos emanating from the core of the earth (geoneutrinos).

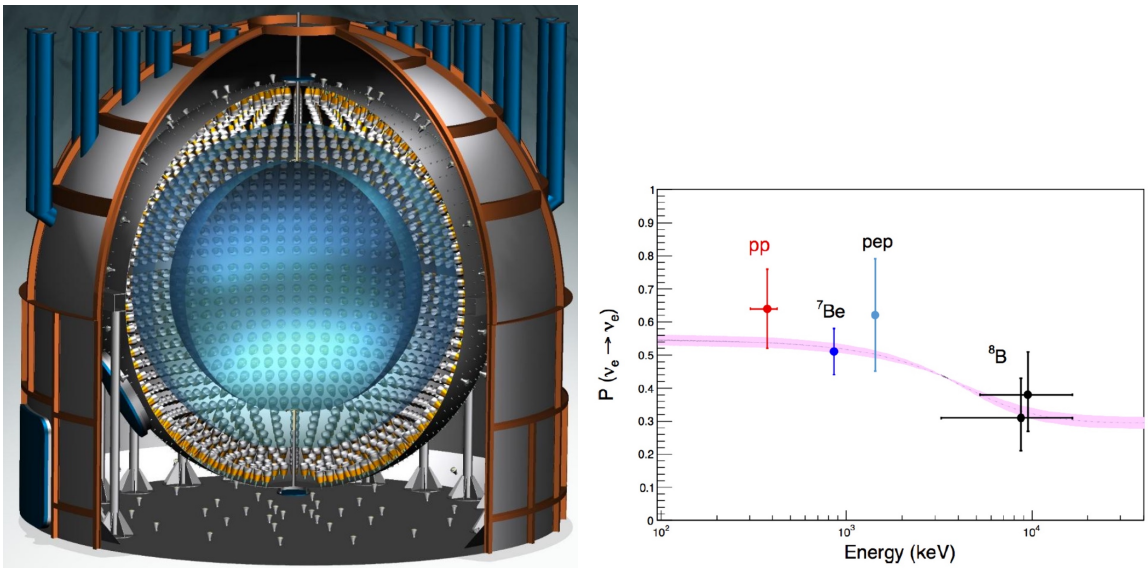

Figure 2.11: (Left) Schematic of the Borexino experiment [61]. (Right) Electron neutrino survival probability as a function of neutrino energy measured by the Borexino experiment from different production channels predicted by the standard solar model [61].

2.4 Accelerator neutrino experiments

Currently accelerator facilities can produce muon and electron neutrinos as well as antineutrinos from accelerated protons. Protons are accelerated in a particle accelerator and directed at a target where the protons interact with the target material, producing a large number of secondary pions (among other particles). Shaped magnetic fields, so-called focusing horns, are used to select out pions of the preferred charge (positive for a neutrino beam, negative for an antineutrino beam) in a specific momentum range and focus them into a collimated beam. The beam is directed into a long decay volume, where the pions decay into muons and (anti)neutrinos. At the end of the decay volume there is a large mass of material which absorbs all the particles except the neutrinos. This provides a nearly pure beam of muon-neutrinos (or muon-antineutrinos if negatively charged pions are selected). There is some inevitable contamination from antineutrinos in the neutrino beam or neutrinos in the antineutrino beam and from electron-neutrinos, mostly because the original pion beam also includes some kaons and muons, which can decay to produce electron-neutrinos. The main difference between accelerator-based neutrino experiments from the other types is that the beam composition is relatively well known. The energy range is higher than for reactor neutrinos. For oscillation experiments, the beam composition is generally measured using a near detector to determine any oscillation component at a far detector.

The advantages of accelerator neutrinos are that the energy range is well known and can be quite well tailored to the desired measurement and the flux is large compared to other methods. However the energy distribution will be quite wide because of the decay processes involved. It is also hard to produce a clean beam without background, for example, muon neutrinos without electron neutrinos. However, for oscillation experiments this can be desirable, see subsection 2.7. Based on current experimental values these experiments are sensitive for θ_{23} and Δm^2_{23}.

2.4.1 Historical experiments

The European Organization for Nuclear Research (CERN) Dortmund Heidelberg Saclay Warsaw (CDHSW) [62] experiment was designed to study neutrino interactions in iron using the CERN SPS neutrino beam line. The experiment consisted of two similar detectors at different distances from the interaction vertex 130 m and 885 m [62]. The detectors were designed to combine the functions of a muon spectrometer and a hadron calorimeter. It consisted of 19 toroidal magnetised iron modules, with an average field of 1.65 T, separated from each other by wire drift chambers. The total detector mass was 1250 tons. A liquid hydrogen tank was placed in front of the experiment to study neutrino interactions in hydrogen. This is one of the first Magnetised Iron Neutrino Detectors (MIND).

The CHARM Collaboration (CERN-Hamburg-Amsterdam-Rome-Moscow Collaboration) proposed to study neutrino-nucleon and neutrino-electron interactions as well as muon polarisation. It took data from 1978 to 1991 and was comprised of a fine-grained target calorimeter made up of 78 subunits each surrounded by a frame of magnetized iron for muon identification and spectrometry [63].

The CCFR (University of Chicago, Columbia University, Fermilab, and the University of Rochester) detector installed at Fermilab consisted of an 18 m long 690 ton neutrino target calorimeter and followed by an iron toroid spectrometer. The calorimeter was made up of 168 iron plates, each 3m $\times$ 3m $\times$ 5.1cm, with liquid scintillation counters spaced between every two plates and drift chambers spaced every four plates. It provided among other things, precision measurements for neutrino-nucleon scattering [64]. The experiment was continued and became the NuTeV experiment which expanded results using the same detector and measured structure functions from deep inelastic scattering and electroweak parameters [65, 66]. CCFR took data from 1979 to 1988, NuTeV started in 1996 and continued until 2003.

2.4.2 NOMAD

The Neutrino Oscillation Magnetic Detector (NOMAD) [67], also using the CERN SPS neutrino beam line, searched for $\nu_\mu \rightarrow \nu_\tau$ oscillation by detecting τ appearance [68] between 1995 and 1998. Its goals were to measure the momenta of charged particles and identify and measure electrons, photons and muons. By the detector design it was also possible to look for $\nu_\mu \rightarrow \nu_e$ oscillation [69]. Compared to the modular design of CDHS, NOMAD had drift chambers and other sub-detectors contained inside a dipole magnet at 0.4 T (figure 2.12).

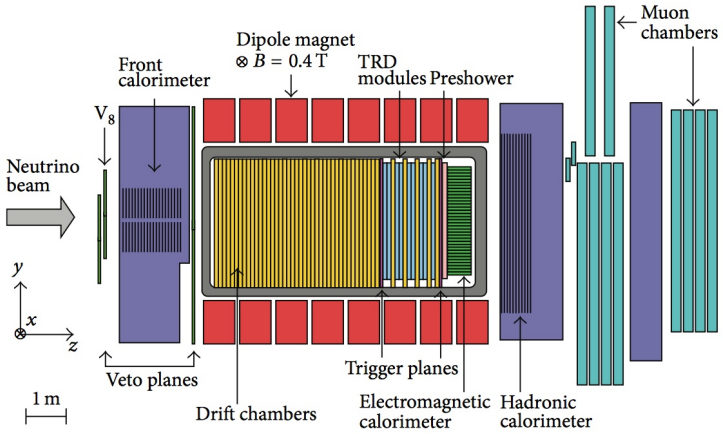

Figure 2.12: A sideview of the NOMAD detector [70].

2.4.3 K2K

After the success of Super-Kamiokande, the High Energy Accelerator Research Organization (KEK) to Kamiokande (K2K) experiment [71] was created with the main difference of using a well understood muon neutrino beam pointing at the Super-Kamiokande detector at a distance of 250 km. It was the first long-baseline neutrino oscillation measurement to observe the disappearance of muon neutrinos into tau neutrinos and found results of mass difference and mixing angle obtained that were consistent with Super-Kamiokande.

K2K, the set up seen in figure 2.13, ran from 1999 to 2004 and used a neutrino beam with a wide spectrum peaked at 1 GeV based on a 12 GeV proton synchrotron beam interacting with an aluminium target and focused through two horns and allowed to decay in a 200 m long decay pipe. This created a 98% pure muon neutrino beam with around 1% contamination of anti muon neutrinos and around 1% electron and anti-electron neutrinos. Understanding the beam composition is required for looking at ν_μ disappearance. To do this a 1-kiloton water Cherenkov near detector, a scaled-down version of Super-Kamiokande, was used to measure the neutrino spectrum which is then extrapolated using Monte Carlo simulated data to predict the neutrino spectrum at Super-Kamiokande.

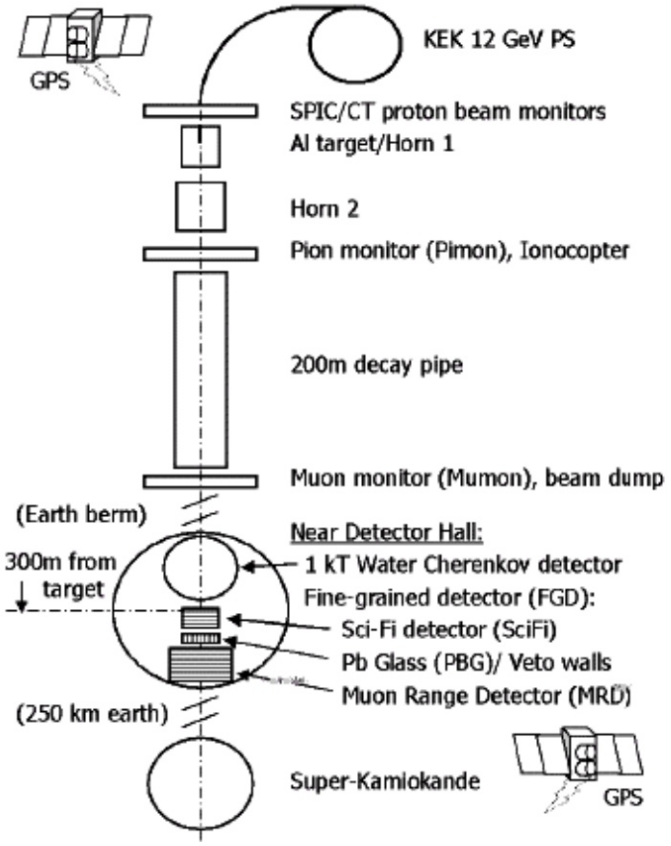

Figure 2.13: A schematic view of the K2K experiment [72].

2.4.4 MINOS, NOvA and MINERvA

The Main Injector Neutrino Oscillation Search (MINOS) [73] is a muon neutrino disappearance experiment, consisting of two magnetised spectrometers, one near (1 km from the target) and one far detector (735 km from the target), and using the NuMI [74] beam at Fermilab. The experiment took data from 2005 to 2012.

The two detectors have been designed to be as similar as possible to minimize any systematic errors in comparing the observed neutrino spectra in the two detectors. They are both constructed of planes with two magnetised steel plates with layers of scintillator in between, to measure the charge and momentum of charged particles and to allow their discrimination. The far detector is composed of 486 octagonal plates with a diameter of 8 meters and total length of 30 meters providing a total mass of 5400 tons. The near detector contains only 282 planes, slightly squashed octagonal planes at 3.8 meters $\times$ 4.8 meters. MINOS showed results consistent with Super-Kamiokande and the K2K experiments such as observation of ν_μ disappearance, measurements of the mixing angle and the mass squared difference.

After MINOS the next step using the NuMI [74] beam is the NOvA [75] experiment, which is an electron neutrino appearance experiment and hopes to be able to determine the mass hierarchy of neutrinos with initial results published in [76].

The MINERvA (Main INjector ExpeRiment ν-A) experiment [77] also uses the NuMI [74] beam to study neutrino-nucleus scattering to improve models of neutrino-nucleus scattering to reduce systematic uncertainties in results from oscillation experiments.

2.4.5 T2K

After the success of K2K, the T2K experiment [78] started data taking in 2010. This is a long-baseline neutrino oscillation experiment with a more powerful beam from the Japanese Proton Accelerator Research Complex (J-PARC) facility at Tokai to Super-Kamiokande, at a distance of 295 km, with a near detector inside an underground hall in Tokai, at a distance 280 m from the target, see figure 2.15.

The neutrino beam comes from an initial 30 GeV/c proton beam which impinges onto a graphite target embedded inside a magnetic horn. After the target the secondary beam is passed through two magnetic horns and focused into a decay volume before passing the beam dump. From here there is ≈ 180 meters of soil until hitting the near detector hall. This means that the near detector is traversed by neutrinos with an expected flux as seen in figure 2.14, and by muons from neutrino interaction in the soil upstream of the near detector. The magnetic horn can be tuned to provide a neutrino spectrum, forward mode, or anti-neutrino spectrum, reverse mode, by charge selecting the primary particles from the proton interaction.

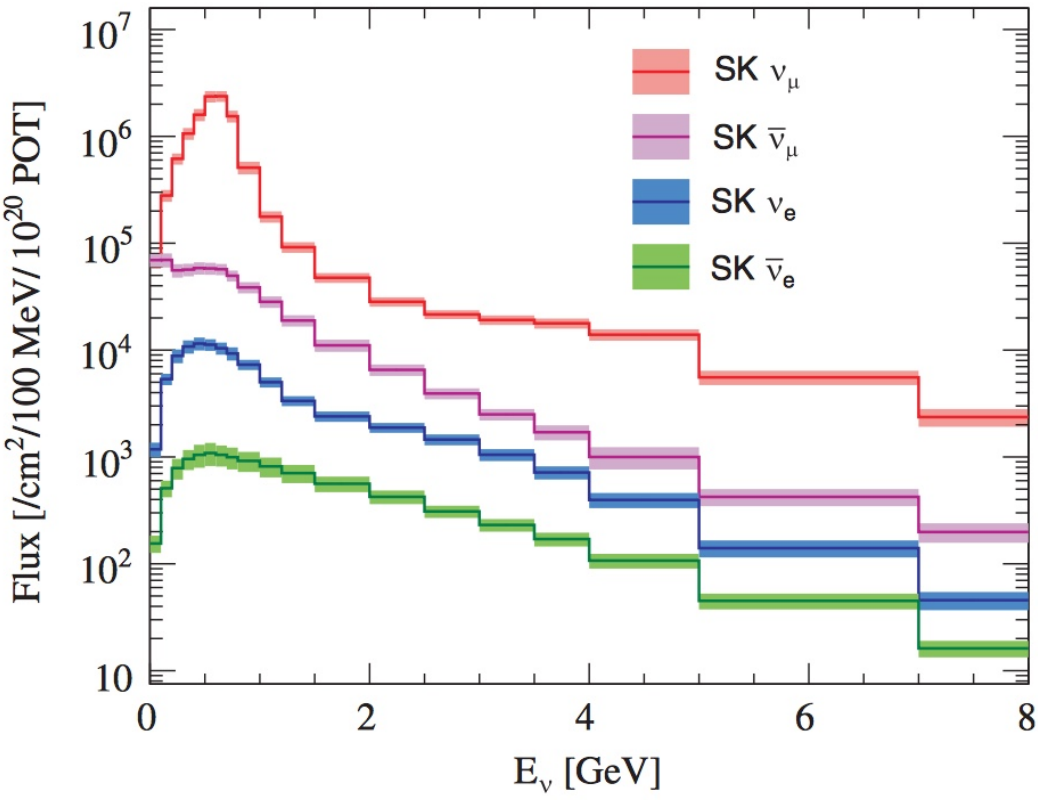

Figure 2.14: Simulated unoscillated expected neutrino fluxes for various flavours at the Super-K position for a forward horn current focussed beam, with expected systematic errors plotted as bands before applying the near detector data [78].

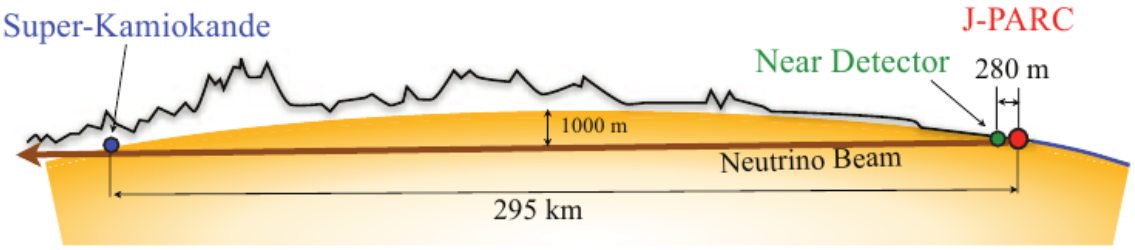

Figure 2.15: A schematic view of the T2K experiment, including the near detector site ND280 and Super-K [78].

The near detector hall contains two main experiments, an on-axis experiment INGRID [79] (figure 2.16) and the off-axis (2.5°) ND280 detector [80] (figure 2.17) both used to reduce model uncertainty and systematic uncertainty in the Super-Kamiokande analysis.

The experiment wants to improve our understanding of the neutrino oscillation parameters. T2K was able to successfully observe the appearance of muon to electron neutrino oscillations and find evidence that the third mixing angle θ_{13} is not zero.

The combined analysis shows the sensitivity of the experiment to the CP violating phase δ_{CP} (figure 2.16), the measurements of neutrino mixing parameters obtained by T2K (figure 2.19) and the effect of the measurement of θ_{13} as a function of the value of δ_{CP} (figure 2.20). This is still an ongoing experiment with ongoing analyses.

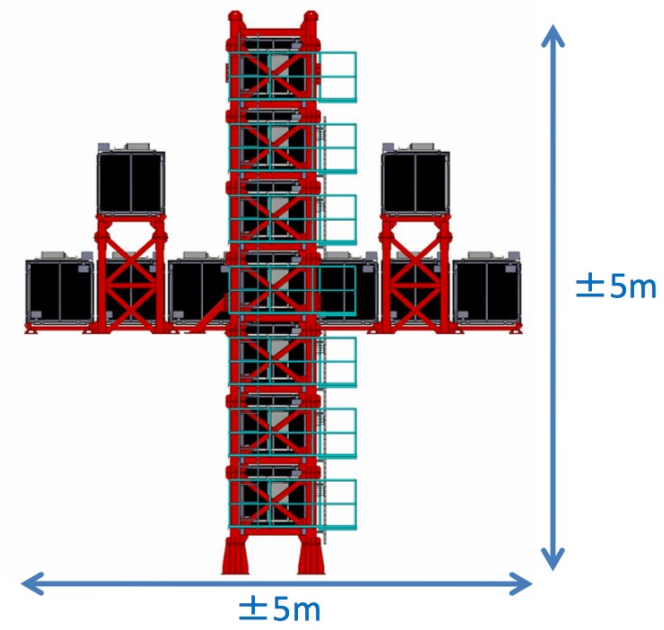

Figure 2.16: The INGRID on-axis near detector. the center of the cross, with two overlapping modules, corresponds to the designed neutrino beam center [79].

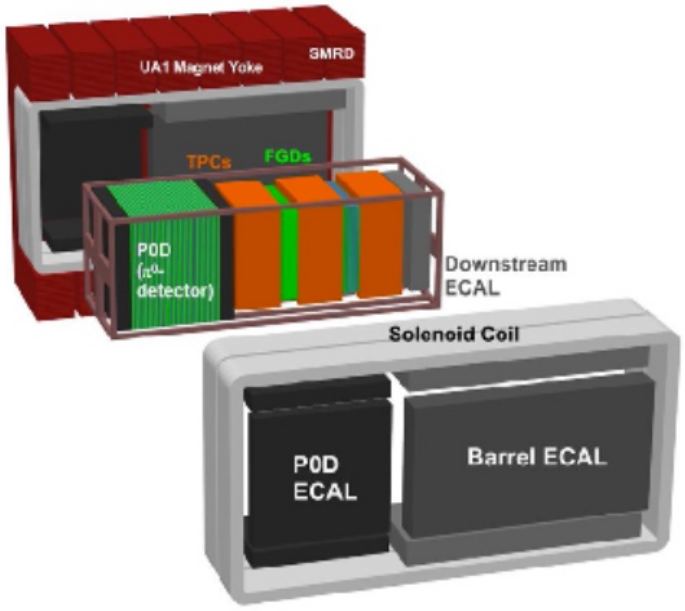

Figure 2.17: An exploded view of the ND280 detector [80].

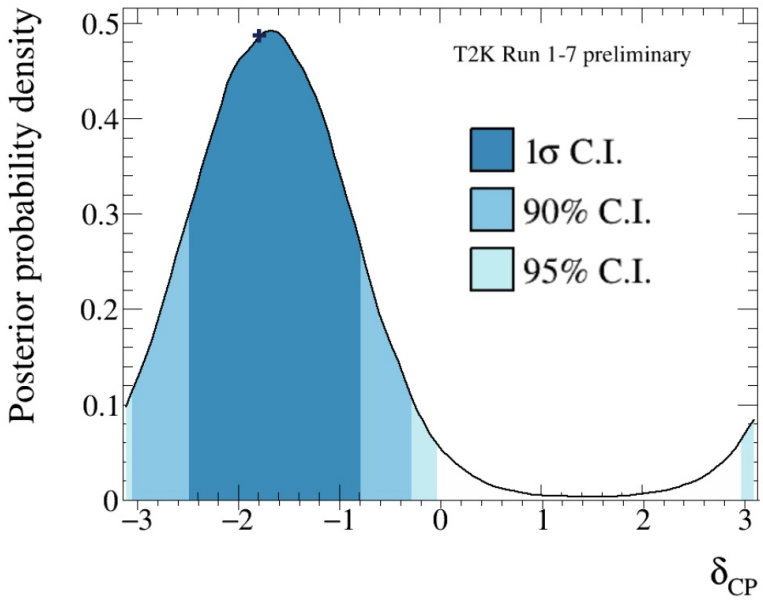

Figure 2.18: Posterior probability density on δ_{CP}, where the cross represent the best-fit [81].

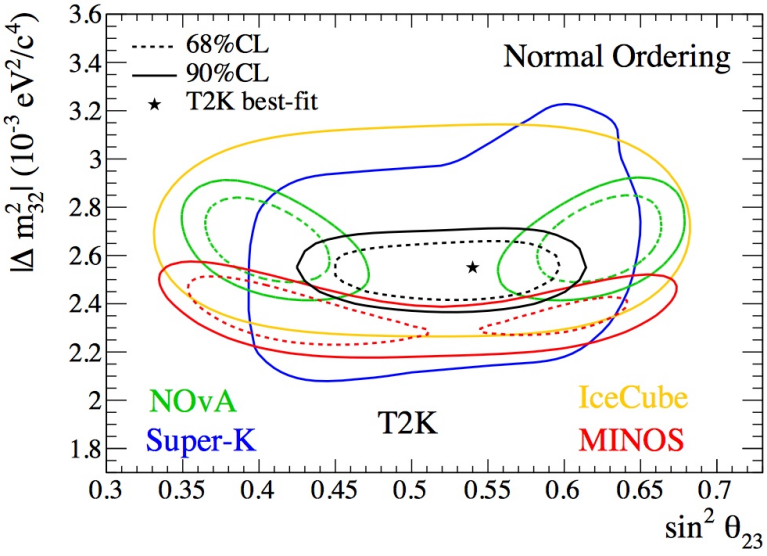

Figure 2.19: The 90% and 68% confidence levels in the $\sin^2\theta_{23}, \Delta m^2_{32}$ space from T2K compared to other experiments, assuming normal ordering of neutrino masses [81].

One of the main sources of systematic error for T2K is caused by the difference of the target material and acceptance between the ND280 near detector (hydrocarbon) and the far detector water Cherenkov detector [83] motivating further studies and upgrades to ND280.

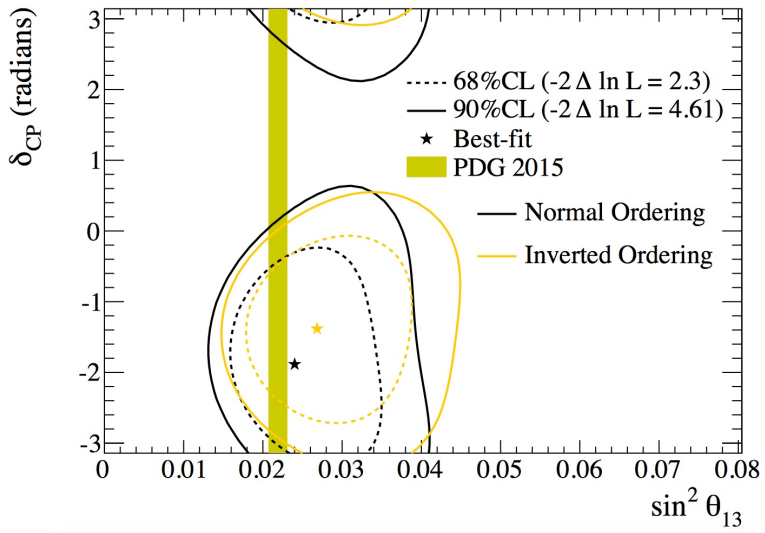

Figure 2.20: The 68% and 90% confidence regions in the $\delta_{CP} - \sin^2\theta_{13}$ plane as the dashed and continuous lines for the normal (black) and inverted (red) mass ordering. The best-fit point is shown by a star for each mass ordering hypothesis. The 68% confidence region of $\sin^2\theta_{13}$ from reactor experiments is shown by the yellow vertical band [82].

2.5 Reactor neutrino experiments

Nuclear reactors are very intense sources of low energy neutrinos. Through beta-decay channels electron antineutrinos are produced with well known energy spectra and low background. Compared to other neutrino sources the energy range is limited to below 9 MeV/c, (see figure 2.21) as well as a sharp cut off at 1.8 MeV/c required for inverse beta decay to occur. The low energy range means that oscillation experiments must be performed with a short baseline since equation 1.50 provides the same probability by decreasing both the momentum and baseline.

Beta-decay is also relatively easy to detect as the positron deposits its kinetic energy in the scintillator and annihilates with an electron and generates two photons. These two photons and the deposited energy causes a so-called prompt signal a few nanoseconds after the neutrino event. The ejected neutron thermalises and produces a delayed signal about 20 ms later, which is a very clear signature of a neutrino event.

The low energy range also means that experiments based on reactor neutrinos can only search for $\bar{\nu_e}$ disappearance since the produced neutrinos do not have enough energy to produce muons or taus and any neutral current interaction will be very difficult to distinguish from background. Based on the current values, neutrino reactor experiments are well suited to determine θ_{12} and Δm^2_{12} as well as θ_{13} and Δm^2_{13}.

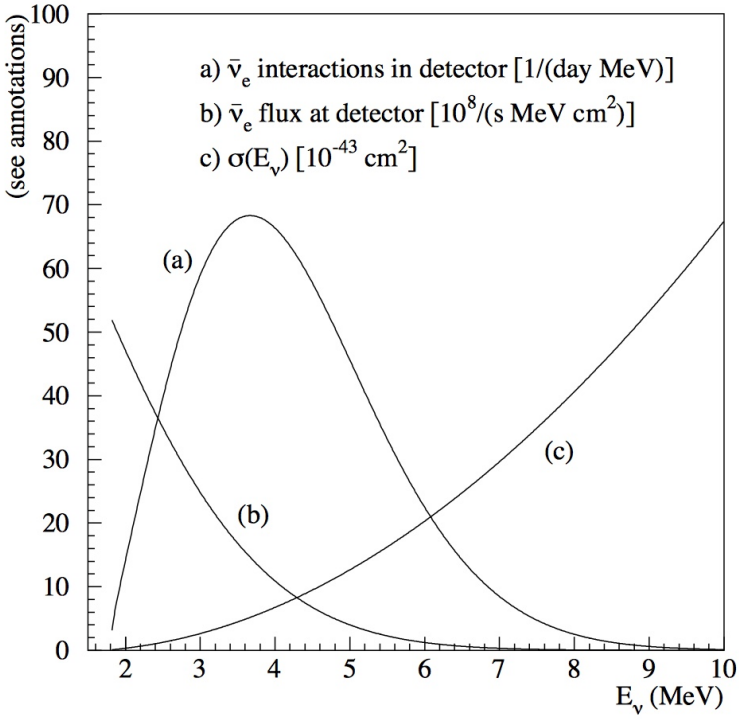

Figure 2.21: Energy spectrum of $\bar{\nu_e}$, the inverse beta decay cross section and interaction spectrum of detected inverse beta decay events [84].

2.5.1 KamLAND

After the completion of the KamiokaNDE experimental run, the site was used to install the Kamioka Liquid Scintillator Antineutrino Detector (KamLAND) in 2002. KamLAND, seen in figure 2.22, looks specifically for neutrino oscillations by looking at electron antineutrinos emitted from distant reactors [85] by using a 1 kton liquid scintillator volume encased in oil.

The majority of the neutrino events are from 26 reactors within the distance range of 138-214 km providing a good baseline to see oscillations by measuring distortions of the expected neutrino energy spectrum. The spectrum and results can be seen in figure 2.23.

KamLAND showed that electron antineutrinos oscillate in the same way as the electron neutrinos from the sun and the results produce the same mixing angle and mass squared difference. These results confirm the oscillation parameters between electron and muon neutrinos in a completely independent way. The experiment also set a constraint on the value of θ_{13} before this was conclusively measured by Daya Bay [86].

2.5.2 Daya Bay

The Daya Bay experiment's main result and goal was to make a conclusive measurement of θ_{13}. The experiment measured θ_{13} to be non-zero with more than 5σ significance [87] in

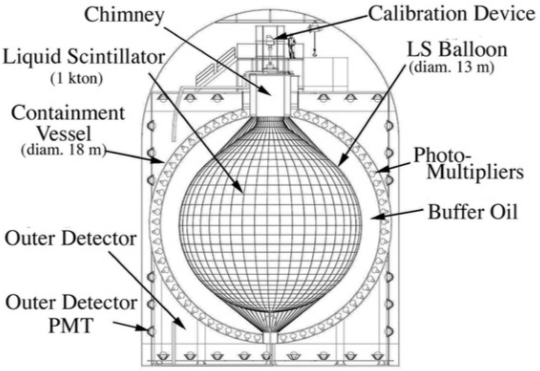

Figure 2.22: Schematic diagram of the KamLAND detector [85].

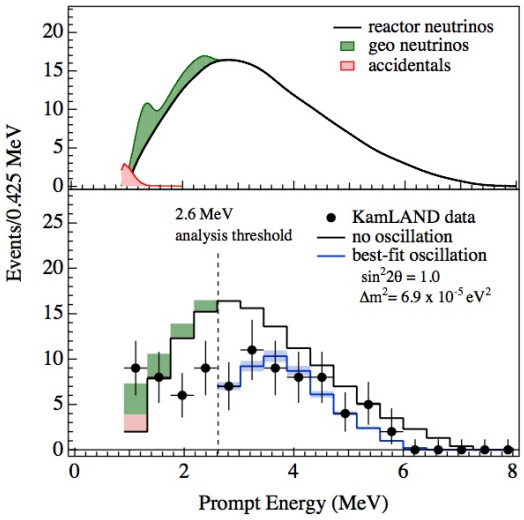

Figure 2.23: Top panel: Expected reactor $\bar{\nu}_e$ energy spectrum. Lower panel: Energy spectrum of the observed events along with the the no-oscillation spectrum and best-fit spectrum [85].

2012.

The Daya Bay Reactor Neutrino Experiment is a facility consisting of eight identical gadolinium-doped liquid scintillator detectors placed in underground experimental halls at three locations around the Daya Bay area in China, which detect antineutrinos from six different nuclear reactor cores of thermal energy 2.9 GW_{th} (figures 2.22 and 2.23). The flux-weighted baselines from the reactors to the three locations are 470 m and 576 m (two at a near location) and 1648 m, at a far location.

This layout allows for maximum sensitivity and the ability to reduce systematic uncertainties due to uncertainties in reactor power levels. It also allows for cross-calibration of the detectors since they are all identical. Each detector is a segmented gadolinium-doped liquid scintillator detector using PMTs to read out photons produced through inverse beta-decay and annihilation. The experiment has been taking data since 2011, and was the first experiment to measure a non-zero value for the neutrino mixing angle θ_{13} with more than 5σ significance [87]. The search for electron-antineutrino disappearance is dependent on the θ_{13} mixing angle. The probability for antineutrino disappearance is given by

$$P(\bar{\nu}_e \rightarrow \bar{\nu}_e) \approx 1 - \sin^2(2\theta_{13}) \sin^2 \left(\frac{1.27 L(m) \Delta m^2_{31}(eV^2)}{E_{\bar{\nu}}(MeV)} \right). \tag{2.4}$$

The reduction in the reactor antineutrino flux is used to determine the value of θ_{13}. Further measurements have improved on the original results, and now θ_{13}

is the most accurately measured mixing angle of the neutrino sector [88, 89]: $\sin^2 2\theta_{13} = 0.0841 \pm 0.0027(stat) \pm 0.0019(syst)$ and the effective neutrino mass-squared difference is $\Delta m^2_{ee} = (2.50 \pm 0.06(stat) \pm 0.06(syst)) \times 10^{-3}$ eV^2.

Figure 2.24: Layout of the Daya Bay experiment [87].

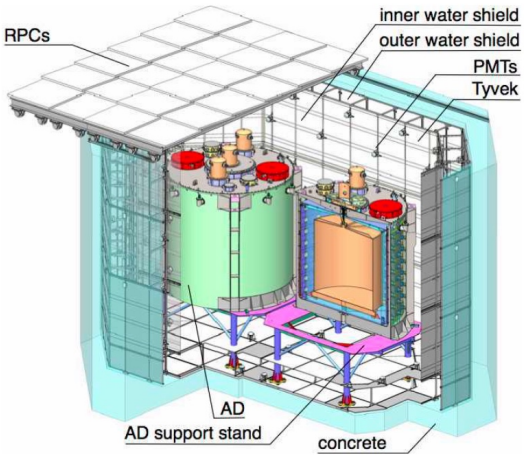

Figure 2.25: Near site layout of the Daya Bay detector with surrounding structure [87].

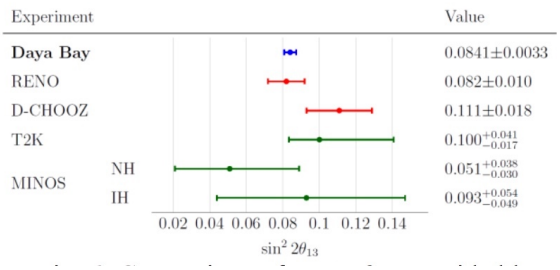

Figure 2.26: Comparison of $\sin^2 2\theta_{13}$ measurements from various experiments, taken from [87].

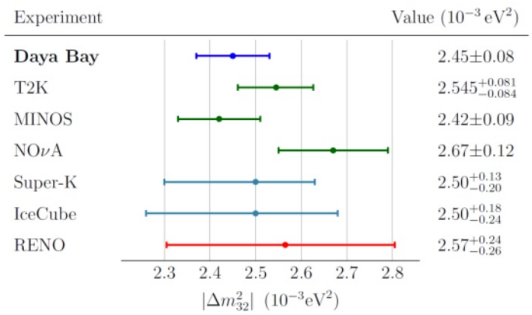

Figure 2.27: Comparison of $|\Delta m^2_{32}|$ measurements from various experiments, taken from [87].

2.5.3 RENO

The Reactor Experiment for Neutrino Oscillation (RENO), started taking data in 2011 and used two identical detectors placed at a near and far site. The detectors are liquid scintillator detectors with 16.5 tons of gadolinium-doped scintillator. It measures neutrinos generated by six nuclear reactors each spread out perpendicular from a base line setting the detectors

at 294 m and 1383 m from the center of the base line, see figure 2.28. RENO measured $|\Delta m^2_{32}| = (2.61 \pm 0.16 \pm 0.09) \times 10^{-3} eV^2$ and $\sin^2(2\theta_{13}) = 0.086 \pm 0.006 \pm 0.005$ using the data in figure 2.29 and confirmed the results from the Daya Bay experiment [90, 91].

Figure 2.28: Layout of the RENO detectors, yellow and reactors in red. The six reactors are equally spaced in a 1280 m span [90, 91].

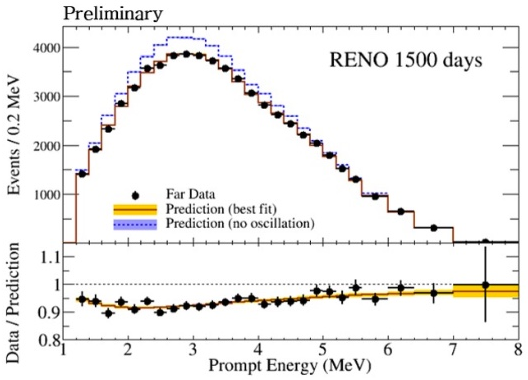

Figure 2.29: Top panel: Measured energy spectrum with data on best fit and no oscillation models. Lower panel: Ratio of data over no-oscillation prediction [90, 91].

2.5.4 Double Chooz

The Double Chooz experiment [92, 93] began in 2004 and used anti-neutrinos produced in two nuclear cores from a nuclear power station to measure the neutrino mixing angle θ_{13} as well as showing that these detectors can be used to ensure non-proliferation [94, 95]. The experiment included two liquid scintillator detectors at a distance of 280 m and 1050 m, both consisting of photo-multiplier tubes (PMT) inside a scintillating volume shielded from cosmic radiation (figure 2.30). The disappearance spectrum from Double Chooz is seen in figure 2.31 [96].

2.5.5 JUNO

The Jiangmen Underground Neutrino Observatory (JUNO) [97] is a 20 kton liquid scintillator detector currently under construction and aiming to start data taking in 2020, seen in both figure 2.32 and figure 2.33. It has as one of its primary aims to determine the mass hierarchy, i.e. the sign of the mass splitting between the m_2 and m_3 mass eigenstates by using reactor neutrinos and inverse beta-decay with an improved energy resolution compared to previous

Figure 2.30: Overview of the Double Chooz experimental site [94].

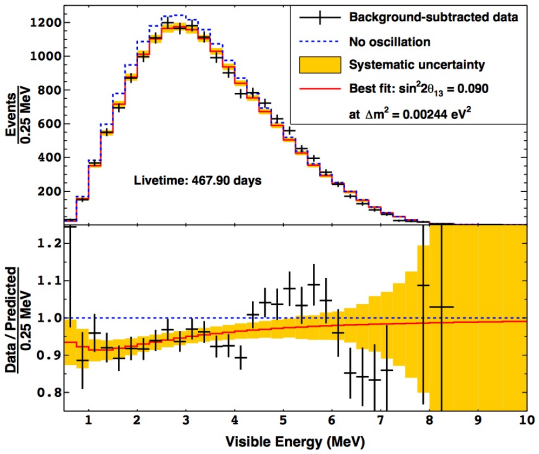

Figure 2.31: Top panel: Measured energy spectrum with data on best fit and no oscillation models. Lower panel: Ratio of data over no-oscillation prediction [96].

experiments [97]. It will use the Daya Bay set of reactors as a source of antineutrinos and results from the Daya Bay experiment to reduce systematic errors from the reactor.

Figure 2.32: Location of the JUNO site with distances to the nearby reactors, Yangjiang and Taishan at both 53 km as well as Daya Bay at 215 km away. [97].

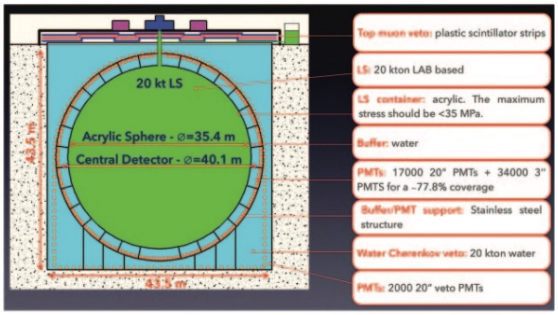

Figure 2.33: Schematic view of the JUNO detector [97].

2.6 Future neutrino oscillation experiments

2.6.1 DUNE

LBNF/DUNE[98], seen in figure 2.35, is a new experiment currently under construction, with the goal of discovering CP violation in neutrinos with more than 5σ sensitivity. DUNE

will perform an electron neutrino appearance measurement with a high-powered neutrino beam from Fermilab and a 40 kton liquid argon detector at a distance of 1300 km, in the Homestake mine in South Dakota. A full physics study with its expected performance is presented in [99]

The main goals are to perform precision measurements of neutrino oscillations to determine δ_{CP} to 5σ or better, to determine the neutrino mass ordering, seen in figure 2.34, and to measure the octant of the mixing angle θ_{23} all with improved precision.

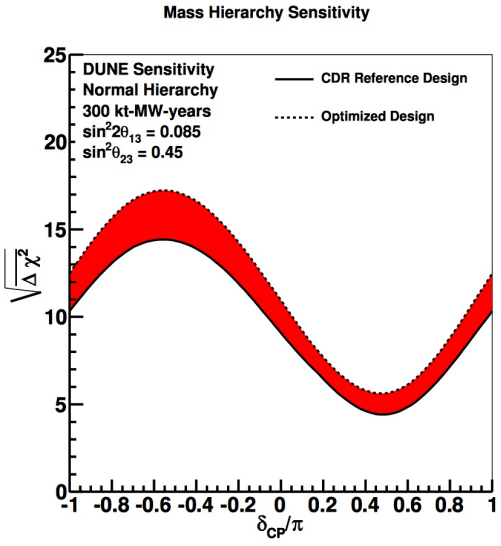

Figure 2.34: Estimated significance of the mass hierarchy discrimination metric as a function of values for δ_{CP} [98].

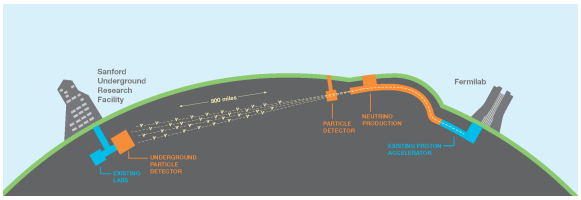

Figure 2.35: Schematic view of the DUNE detectors [98].

2.6.2 Hyper-K

The Hyper-Kamiokande Experiment (Hyper-K) [100] builds on the T2K-experiment [78] by improving the neutrino beam at JPARC, and expanding the water Cherenkov detector by a factor of 10 to a fiducial volume of 500 ktons (figures 2.36 and 2.37). Hyper-K aims to improve the sensitivity for δ_{CP} and to discover CP violation by observing a non-zero value of δ_{CP} with a sensitivity of 5σ. It also aims to measure $\Delta\delta < 18°$, determine the mass hierarchy with more than 3σ sensitivity and measure θ_{23} with sufficient accuracy to determine whether it is non-maximal.

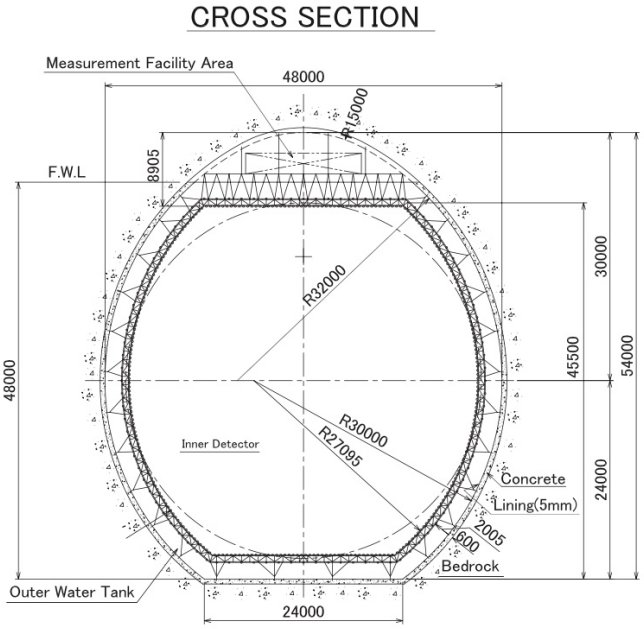

Figure 2.36: Cross section view of the Hyper-Kamiokande detector [100].

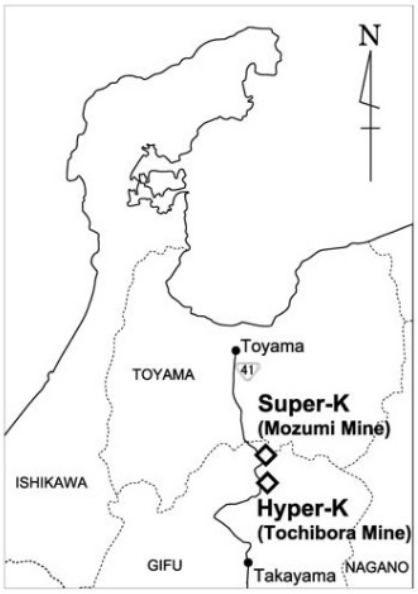

Figure 2.37: A map showing the proposed candidate site [100].

2.7 Neutrino Factory

The Neutrino Factory (NuFACT) is a novel concept for a neutrino accelerator which will produce a high-intensity (1000 times higher than previously attained) and a high-energy beam (up to 15 GeV [101]). Unlike previous experiments it will produce a two flavour, electron and muon, neutrino beam through a muon decay ring. The neutrino factory has the capacity to improve the precision of neutrino oscillation measurements, since the neutrino beam from the decay of muons can be determined with high accuracy. The beam produces one bunch of μ^+ and one bunch of μ^-, so the facility can make measurements of ν_μ and $\bar{\nu_e}$ and $\bar{\nu_\mu}$ and ν_e simultaneously. A large 100 kton Magnetised Iron Neutrino Detector (MIND) at a distance of 2000 km is used to perform a measurement of a wrong-sign muon signature that would be the signal for $\nu_e \rightarrow \nu_\mu$ and $\bar{\nu}_e \rightarrow \bar{\nu}_\mu$ oscillations to perform a measurement of δ_{CP}, with an expected accuracy of $\Delta\delta_{CP} \sim 5^\circ$ [102]. A schematic of the facility is shown in figure 2.38 showing the full accelerator chain. The full chain starts by producing muons and pions from a proton beam on target. Pions are then captured in a strong solenoid magnetic field surrounding the target. The bunches are sent through the so-called front end containing a phase rotation and an ionisation cooling channel before being re-accelerated to enter the muon storage ring. Before entering the ring the muons are charge separated and go into the storage ring in counter-rotating directions. The muons decay continuously over about 70 turns of the circuit into the following modes with branching ratios:

$$\mu^- \rightarrow e^- + \bar{\nu_e} + \nu_\mu, \approx 100\% \tag{2.5}$$

$$\mu^- \rightarrow e^- + \bar{\nu_e} + \nu_\mu + \gamma, < 1\% \tag{2.6}$$

$$\mu^- \rightarrow e^- + \bar{\nu_e} + \nu_\mu + e^+ + e^-, < 1\%. \tag{2.7}$$

The energy spectrum and composition of the neutrino beam is well known as the decays only produce two different neutrino flavours. It is important to note that a μ^+ beam will produce $\bar{\nu}_\mu$ and ν_e neutrinos and a μ^- beam will produce ν_μ and $\bar{\nu}_e$ neutrinos. Thus for a μ^- beam any electron neutrinos or muon anti-neutrinos discovered must have been produced through oscillation. To be able to distinguish muons from anti-muons at a detector, a magnetic field is required, motivating the design of any considered detector. Currently there are proposals for NuFACT to be constructed at CERN [102], ESS [103] and FERMILAB [104], where it is also seen as a step toward a full muon collider experiment. The expected precision of δ_{CP} is shown in figure 2.39.

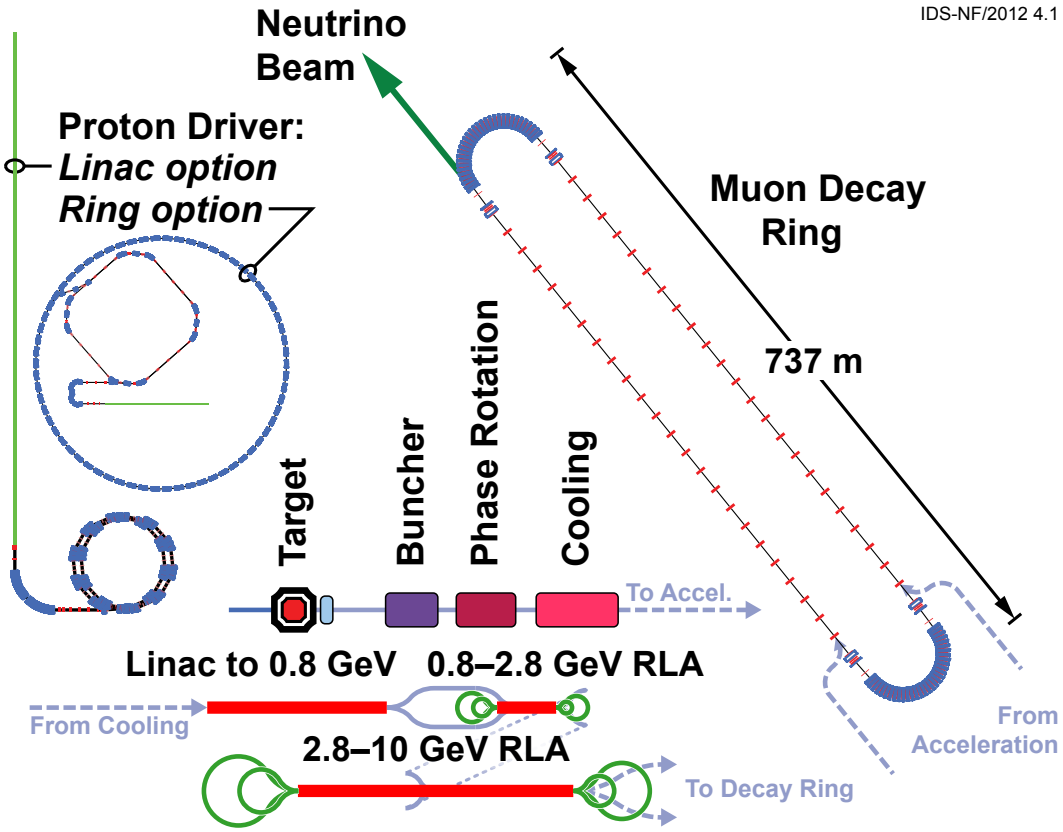

Figure 2.38: Schematic diagram of the Neutrino Factory [101].

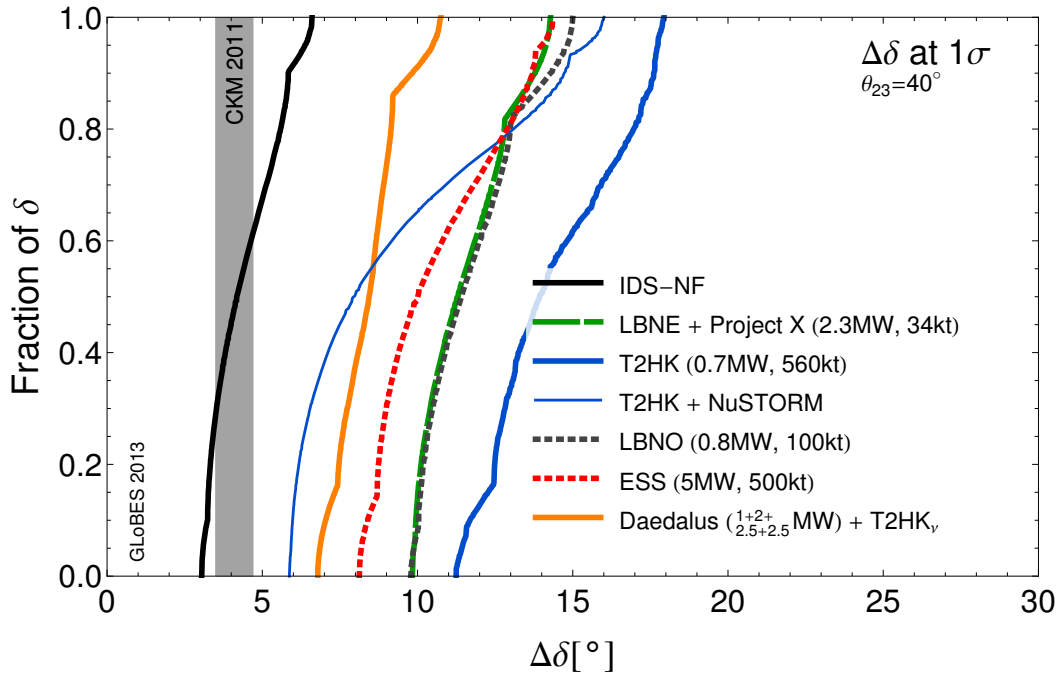

Figure 2.39: Expected precision for a measurement of the δ_{cp} at a Neutrino Factory compared to alternate neutrino oscillation facilities [101].

2.7.1 NuSTORM

The Neutrino Factory is a complex and expensive facility which requires new technology to be realised. To overcome this, a staged approach has been suggested, where each stage would be delivering physics [101]. The first stage in this plan is named NuSTORM (Neutrinos from Stored Muons) with a schematic shown in figure 2.40. The NuSTORM beam is designed to inject 5 GeV/c pions into a muon storage ring, and the ring is designed to store 3.8 GeV/c muons. Compared to the full neutrino factory, NuSTORM is expected to have some pions and kaons for the first pass in the storage ring providing some contamination in the final beam, which can also be used to perform physics measurements, producing both neutrinos and anti-neutrinos for both muon and anti-muon modes and thus a near detector is required to measure the flux of both.

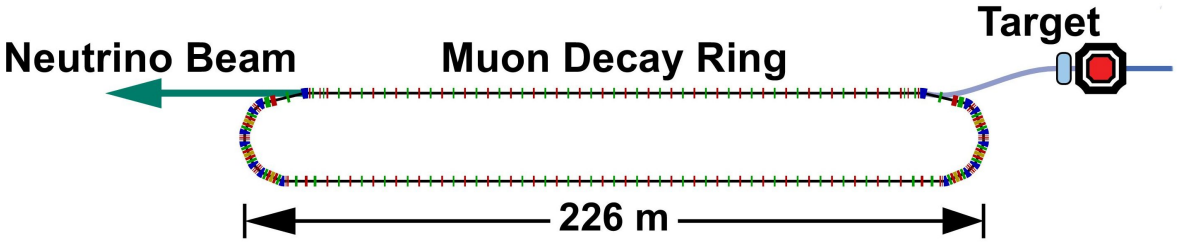

Figure 2.40: A schematic of a NuSTORM facility [101].

For both NuFACT and NuSTORM [105] the detector type proposed will be a large Mag-

netised Iron Neutrino Detector (MIND) type similar to the ones used in CDHSW [62] and MINOS [73, 106]. This type of detector, with magnetized steel plates and scintillation plates, is well suited to provide large mass for neutrino experiments and is able to provide momentum measurements by using range and curvature calculations as well as providing charge identification. A MIND type detector has been selected as the baseline detector for a neutrino factory [107, 108] and for NuSTORM, since it is the cheapest and most effective way of producing a large magnetized volume. This has provided the motivation for creating a prototype detector to perform a number of studies.

2.8 Additional experiments

There is a lot of interesting physics being performed to understand the parameters of neutrino oscillations as well as also finding a complete theory to describe how neutrinos have mass. Aside from this there are interesting experiments where muon detectors are being used for tomography. One example of this is trying to find chambers in the pyramids which provides a non-intrusive way of searching [109]. Another interesting aspect comes from doing precise measurements of nuclear reactors, to be used for non-proliferation [110] and perhaps even to search for nuclear submarines in a noisy environment where conventional techniques may not work [111].

2.9 Summary

In this chapter, a history and summary of neutrino experiments measuring neutrino oscillations is presented. These experiments have been able to determine the mixing angle and mass-squared differences of the different eigenstates. Future experiments aim to uncover the remaining questions, such as a measurement of CP violation, the neutrino mass hierarchy between m_2 and m_3 and whether θ_{23} is non-maximal. New experiments, such as DUNE and Hyper-K are being planned to make these measurements. Further in the future a neutrino factory could be the ultimate neutrino facility to explore CP violation in the neutrino sector with the best possible accuracy in δ_{CP}. A Magnetised Iron Neutrino Detector (MIND) is required at a neutrino factory, motivating a prototype detector, called Baby MIND.

Chapter 3

The Baby MIND and WAGASCI detectors

3.1 Baby MIND/NP05

The prototype Magnetized Iron Neutrino Detector (Baby MIND) [112] was designed with the aim to study muon charge identification efficiencies and momentum reconstruction in order to get estimates for a future Neutrino Factory, discussed in this section. The Baby MIND project was launched as a prototyping activity within the European Commission-funded AIDA-2020 project. The particle charge is essential for the oscillation measurements since wrong-sign muons are the neutrino oscillation signal. During the design process a secondary aim was added, to measure the momentum and charge of muons from neutrino interactions in water and hydrocarbon targets at the J-PARC T59 WAter-Grid-SCIntilator-detector (WAGASCI) experiment, further discussed in section 3.2.

The Baby MIND collaboration is comprised of around 46 scientists from 10 different institutions, and is part of the CERN Neutrino Platform as experiment NP05 [113] and is as of 2018 fully integrated into WAGASCI and in turn T2K.

3.1.1 Motivation

The Baby MIND aims to show that MIND type detectors are viable to use for muon charge identification at low momenta (< 1 GeV/c) and also to show how well the charge can be identified for charged current interactions from neutrinos produced at a Neutrino Factory [102] beam. A secondary motivation is to act as a platform to develop a new iron magnetisation scheme, and to test new electronics, scintillation fibres and the data acquisition system for future experiments. Additionally the experiment aims to compare simulations from

GEANT4 [114] to data taken by the detector at a test beam to be able to verify the properties of muon interactions in momentum ranges of 0.5 to 10 GeV/c. Separating and identifying particles of different charges requires a magnetic field, and to perform identification at low momenta a high uniform field has to be created in a large volume and preferably without fully stopping the particles which are being identified. The main difficulty that arises is to magnetise the volume in an inexpensive and simple manner.

In essence, one has to balance the requirements of magnetising a large non-magnetic volume containing low density material (such as gas, scintillator or liquid argon), with the convenience and reduced cost of magnetising iron plates, which can achieve uniformly high magnetic fields with modest currents, but stops low-momentum particles.

For the Baby MIND design a novel approach was chosen to use thin high permeability magnetised ARMCO [115] steel plates in an arrangement to optimize charge identification while minimising the number of steel plates interspersed with scintillator modules. The optimal design was adapted due to limiting constraints such as construction time, size of the ND280 shaft [78] and design costs. An added advantage of magnetising each steel plate separately is the possibility of a fully modular design leading to the Baby MIND being able to be set in any configuration with an appropriate support frame. The use of magnetised steel modules instead of requiring the use of an all encompassing magnet, simplifies the magnetic design, lowers the cost and allows for a more uniform field. The direct disadvantages of this is the momentum resolution which is limited by multiple Coulomb scattering and difficulty of performing track reconstruction, discussed further in section 4.6.

The CERN Neutrino Platform approved Baby MIND as experiment NP05 in December 2015 and construction started in August 2016 and finished in June 2017 [116].

During the development of the detector it was proposed to use Baby MIND as a muon spectrometer downstream of the WAGASCI experiment (T59) at J-PARC, which uses neutrinos from the T2K beamline, to provide charge and momentum of outgoing muons from neutrino charged current interactions. Baby MIND was installed in the ND280 pit at J-PARC in early 2018.

3.1.2 Magnet modules

The magnetised volume for the Baby MIND consists of a total of 33 uniform steel modules with a simple dipole magnetic field orientation as well as being modular and cheaper than the alternatives. An overview of the magnetic field is seen in figure 3.1 with two open slots in order to cover the entire plate with coils carrying currents in opposite directions. The flux return is designed to have an identical magnetic volume to the main dipole sections of the steel plate, so it contains the stray fields and reduces power dissipation outside of the plates

compared to a single conducting coil wound on the surface of each individual plate. Each module consists of ARMCO steel with two slits to allow aluminium coils to be wrapped around the steel (25 turns) and two side caps to allow for the magnetic flux return. The field is split into three parts where the field is 1.5 T but with opposite orientation as can be seen in figure 3.1. Because of this simple design, the field lines are contained in the steel and have negligible stray fields of less than 15 mT, with a good uniformity, < 3 % confirmed by Hall probe measurements, in the area of interest (seen as red in the figure 3.1). This provides a bending direction either up or down depending where the particle passes and its charge. The magnet module dimensions are $3500 \times 2000 \times 30$ mm^3, with the field oriented along the $x-$direction (right) and bending with respect to the $z-$axis (into the figure). Simulations show the magnetic field map to be very uniform over this central tracking region covering an area of 2800×2000 mm^2, where the field component in the $x-$direction dominates with respect to the field in the other orthogonal directions. The magnet modules were constructed at CERN through the CERN Neutrino Platform [117].

Test results on the 33 modules show all to achieve the required field of 1.5 T for a current of 140 A, with a total power consumption of 11.5 kW.

3.1.3 Scintillator modules

In the Baby MIND, particle hits are detected by scintillating bars which provide both horizontal and vertical position information. There are a total of 18 scintillator modules, where each scintillator module is constructed from 95 horizontal bars for each of the two horizontal planes, $3000 \times 31 \times 7.5$ mm^3, and 16 vertical bars, $1950 \times 210 \times 7.5$ mm^3 for two planes of vertical bars each providing a total size of the scintillator module as $3000 \times 1950 \times 30$ mm^3. Since the vertical information is important for curvature, smaller bars are used to provide a better position resolution. The bars are arranged in 4 planes, of horizontal, vertical, vertical, horizontal, with an overlap between planes to achieve close to 100% hit efficiency for minimum ionizing muons [1]. INR Moscow built and designed the scintillator bars, providing a good light yield, figures 3.2 and 3.3, regardless of where the bar is hit. The bars are polystyrene based, 1.5%PTP, 0.01% POPOP and held together mechanically within an aluminium support frame. The bars contain a groove within which are embedded Kurarray wavelength-shifting (WLS) fibers (200 ppm, S-type, diameter 1.0 mm) and contain a reflective coating of 50 to 100 μm thickness, chemically etched on the surface. The connectors are custom made using Eljen EJ-500 optical cement. A schematic view of the horizontal bars can be seen in figure 3.2 and the vertical bars in figure 3.3.

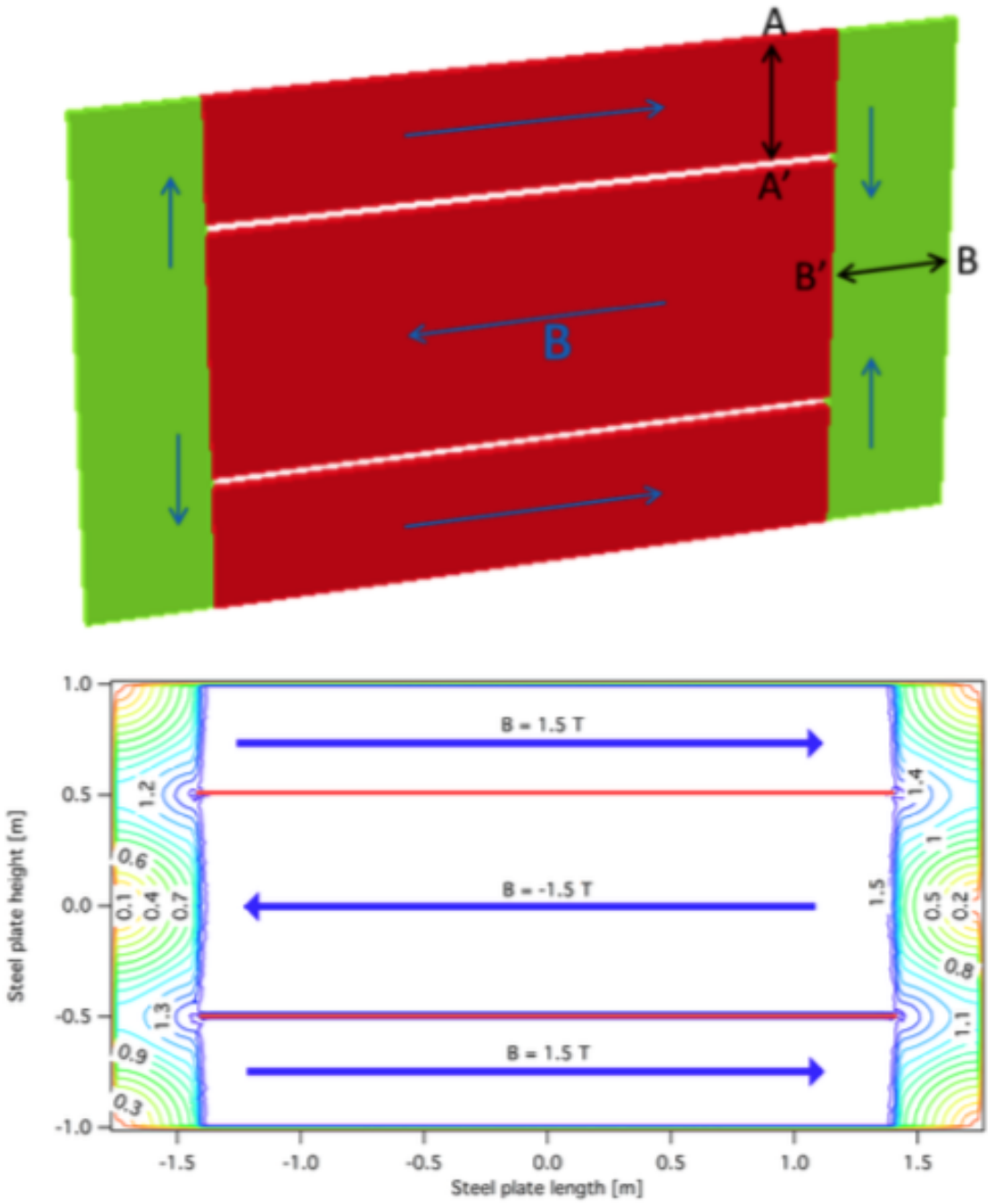

Figure 3.1: (Top) Schematic view of the magnet module. (Bottom) A contour plot of the magnet module, with the fiducial areas of interest showing magnetic field uniformity of $< 3\ \%$ in the areas of interest confirmed by Hall probe measurements. Figures, courtesy of Etam Noah.

3.1.4 Layout

Design constraints came from the need for Baby MIND to operate at both CERN and J-PARC on a relatively short time scale. The installation at J-PARC has driven the overall design with the requirement to lower segments of detector elements through a narrow shaft down to

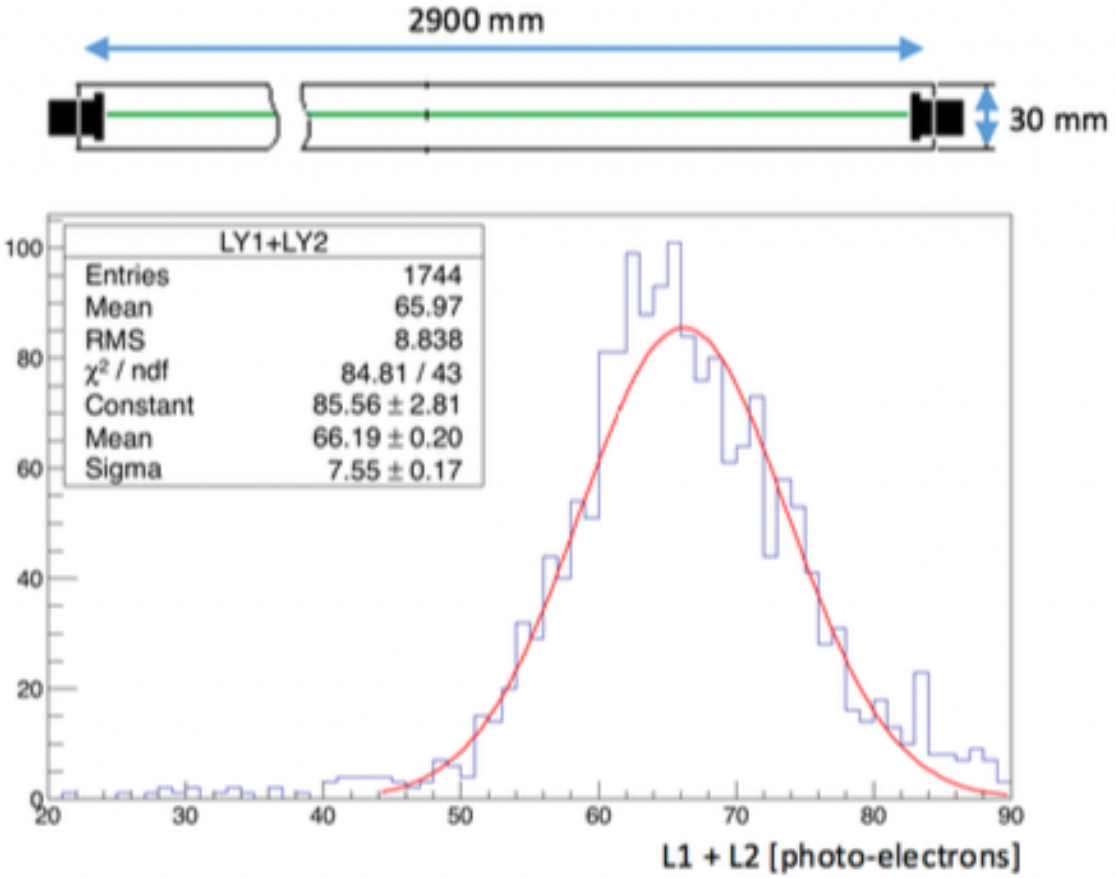

Figure 3.2: Schematic view of the horizontal bar and light yield curves [118] where the y-axis represents number of bars recorded. The blue histogram represent data for each of the horizontal bars and the red curve represents the best Gaussian fit to the data.

the lowest floor of the ND280 building pit at J-PARC. The magnetisation scheme for Baby MIND was designed by Alex Dudaeev and his magnet team at CERN and was developed within the CERN Neutrino Platform framework as a direct result of this constraint.

Previous magnetised iron detectors, discussed in chapter 2, have been in the kiloton range. Baby MIND is comparatively small weighing only 65 t. A schematic overview of the detector can be seen in figure 3.4, showing the full detector composed of 18 scintillator modules, and 33 magnetised ARMCO steel plates, referred to as magnet modules. The full detector is around 4 meters in length with a height of around 2 meters and width of 3.5 meters. The chosen layout of the detector for the test beam is divided into four blocks with block 1 containing three sub-blocks and block 4 containing two sub-blocks. The gaps between sub-blocks in block 1 have been added to improve the low momentum reconstruction using a lever-arm approach, discussed further in section 4.6.

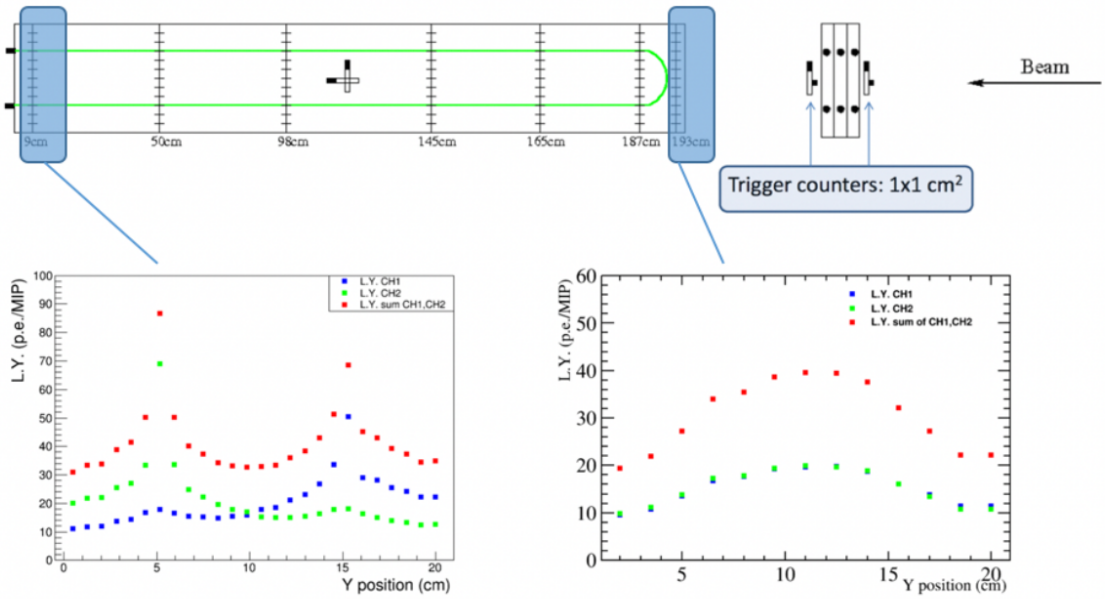

Figure 3.3: Schematic view of the vertical bar and light yield curves performed for hits at the near and far end of the vertical bar [118].

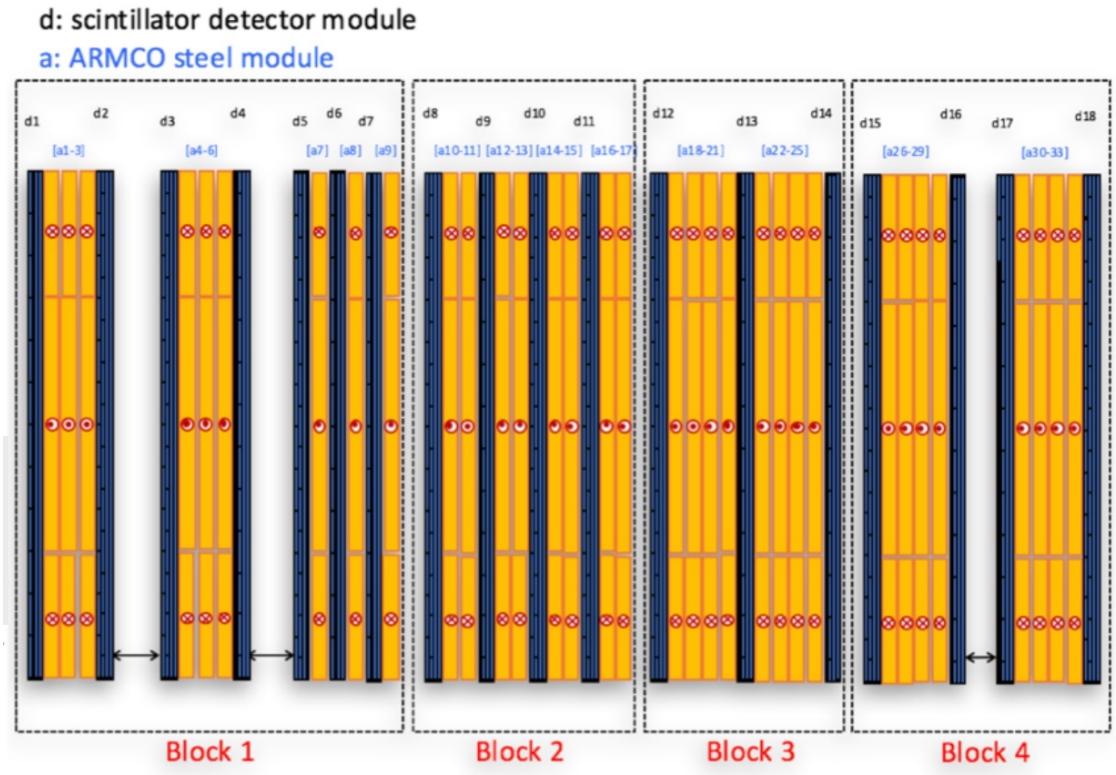

Figure 3.4: The test beam Baby MIND design, in yellow the magnet modules and in blue the scintillator modules. The red dots and x refer to the magnetic field direction.

3.1.5 Electronics

The scintillating fibres present in the bars are read out using Hamamatsu MPPC (Multi Pixel Photon Counters). Compared to PMTs these use a lower voltage, less current and are compatible with magnetic fields. This provides a small size, and simple electronics for the modules. The MPPCs are custom made S12571-025C (and derived S10943-5796), a size of 1×1 mm^2 (65% fill factor) and 25 μm cell size. The operating voltage is ≈ 67.5 V with photon detection efficiency (PDE) 35%, gain 5×10^5 and dark counts of typically 100 kcps. The MPPC signals, sampled at 400 MHz, are powered (HV/LV) and read out by custom made Front-End Boards (FEBs), seen in figure 3.5, designed for 96 channels using CITIROC ASICs [119]. The MPPC signals are connected through a 5 m extension coaxial cable bundle containing up to 32 photosensor signals. The purpose is to decouple the FEBs from the scintillator modules, which improves accessibility to FEBs and their long term maintainability. These rack mounted FEBs have been designed by Geneva University containing 3×32 channel connectors, i.e. three CITIROC ASICs with 32 channels each. The FEBs are installed in mini-crates which can connect up to seven FEBs via readout/slow control on USB3 and/or Gigabit using a backplane seen in figure 3.6. Data is sent from the mini-crates to Data acquisition (DAQ) computers via USB3 and passed on to a final computer located in a control room. The full readout chain can be seen in the block diagram in figure 3.7.

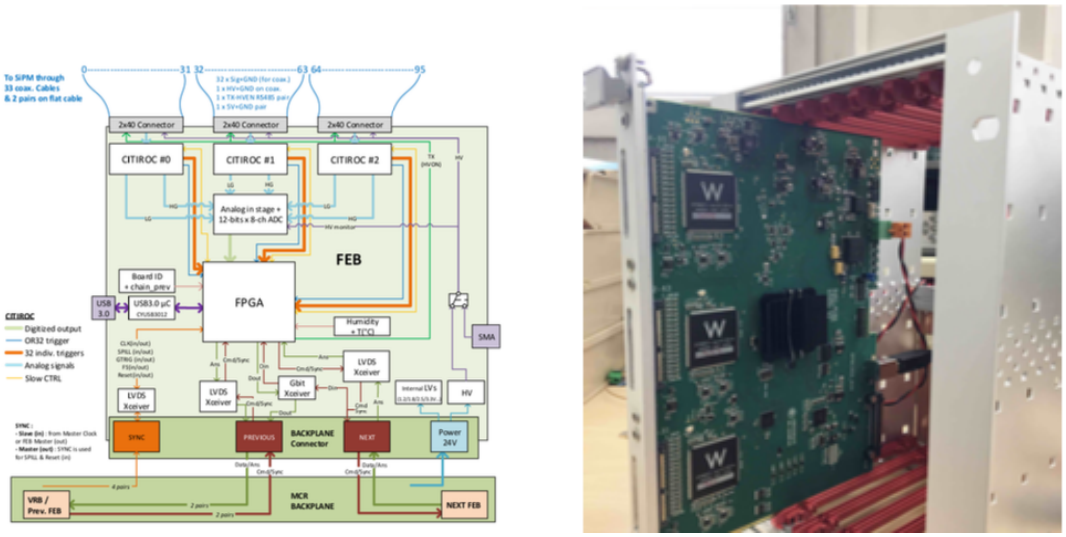

Figure 3.5: (Left) Schematic view of FEB layout. (Right) An image of the FEB in one of the racks. Figures, courtesy of Yannick Favre.

3.1.6 Construction and test beam

The CERN Neutrino Platform approved Baby MIND as experiment NP05 in December 2015 and construction started in August 2016 and finished in June 2017. During the development

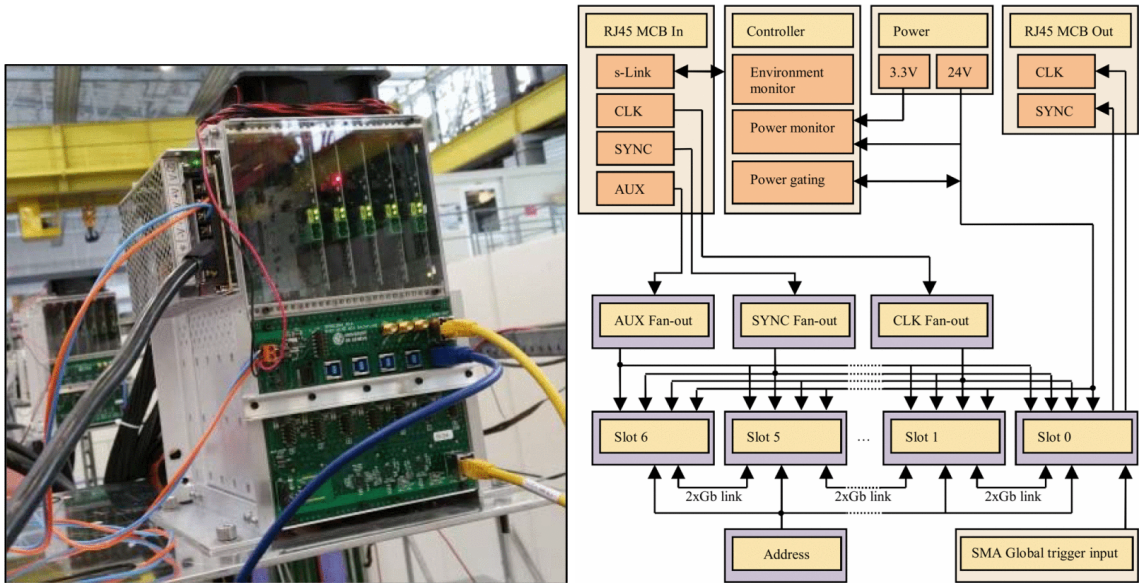

Figure 3.6: (Left) Front-end electronics mini-crate installed on the detector. (Right) Block diagram representing the backplane. Figures from [120]

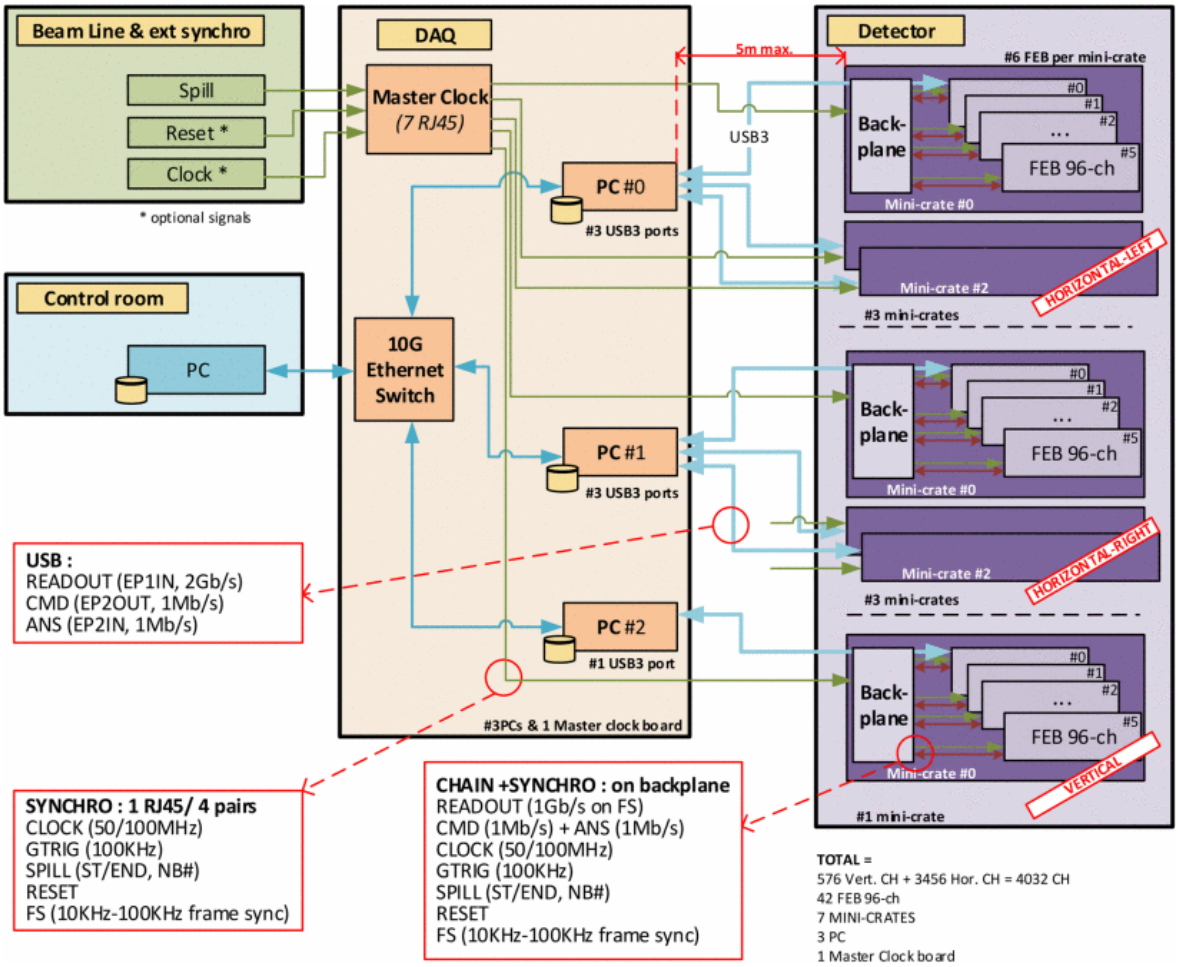

Figure 3.7: Readout block for the Baby MIND electronics. Figure from [120]

of the detector it was proposed to use Baby MIND as a muon spectrometer downstream of the WAGASCI experiment (T59) at J-PARC, using neutrinos from the T2K beamline, to provide charge and momentum of outgoing muons from neutrino charged current interactions. The installation and commissioning of the detector in J-PARC took place at the beginning of 2018, with commissioning of the detector with neutrinos from the beam at J-PARC between March and May 2018.

3.2 WAGASCI/T59

The new WAter-Grid-SCIintilator-detector (WAGASCI) at the J-PARC neutrino beam line will measure the difference in cross sections from neutrinos interacting with water and with scintillator targets, in order to constrain neutrino cross sections in oxygen and carbon, essential for the T2K neutrino oscillation measurements. It follows a similar approach to the one used for iron scintillator cross-sections in the INGRID detector [78].

Baby MIND will act as a magnetic spectrometer behind the main WAGASCI target. Baby MIND was installed behind the WAGASCI at J-PARC in the beginning of 2018 to measure the charge and momentum of the outgoing muon from neutrino charged current interactions, to enable full neutrino event reconstruction in WAGASCI.

3.2.1 Motivation

The WAGASCI experiment (T-59) at J-PARC on the T2K beamline aims to improve measurements of the ratio of neutrino interaction cross-sections on water and carbon. This is required to reduce systematics due to nuclear effects in water, currently the dominant systematic uncertainty in the T2K neutrino oscillation analyses [78]. With planned upgrades to the T2K experiment and a planned follow-up project HyperK [100], there is a strong motivation to reduce the systematic uncertainties. The aim is for T2K to improve the level of systematic precision to 4%.

WAGASCI proposes to test a new three-dimensional (3D) grid-type detector, composed of plastic scintillator and water, to improve on the current understanding of nuclear effects in neutrino interactions. The WAGASCI collaboration states that the detector will be able to measure this cross-section to a level of 3% systematic uncertainties in the 1 GeV/c energy region with a generic MIND [121]. Using WAGASCI as a near detector, in the ND280 building, combined with the Cherenkov detector, provides knowledge of the ratio of neutrino interaction cross-sections in water and plastic scintillator. Due to the WAGASCI being both small and not including any magnets, it is impossible to reconstruct charge or momentum for incoming particles. By including the Baby MIND detector to provide reconstruction

downstream, this obstacle is overcome. The size of the Baby MIND is particularly well suited for the WAGASCI experiment providing excellent acceptance for forward secondaries from interactions in the upstream WAGASCI water and carbon targets. During operation with the WAGASCI experiment, Baby MIND is referred to as the Muon Range Detector (MRD). The layout can be seen in figure 3.8.

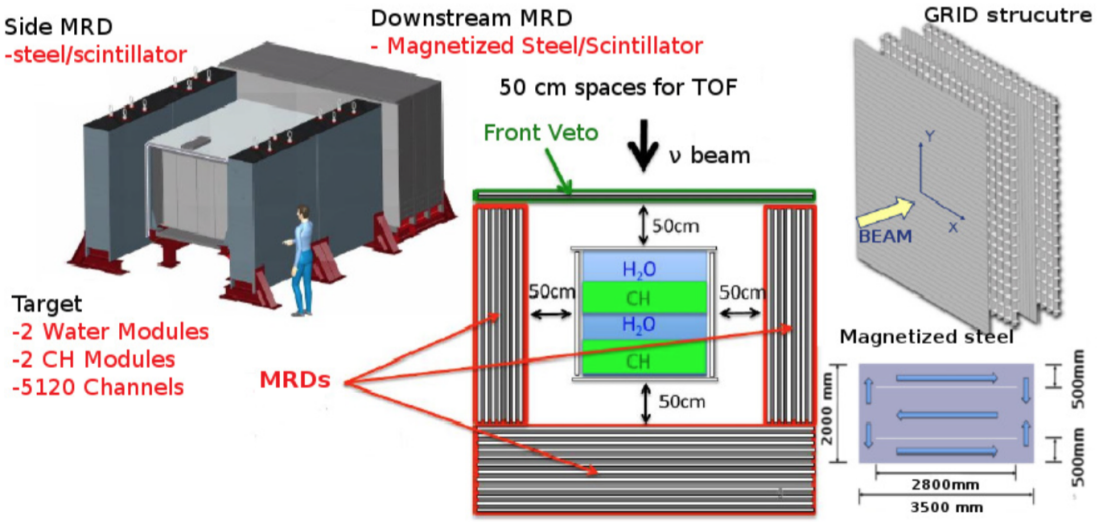

Figure 3.8: The basic structure of the WAGASCI detector including one of the possible designs for the MIND plates. The MIND detector is denoted as Downstream MRD [121].

3.2.2 Layout

There are two main elements of the WAGASCI detector, the central part is a neutrino interaction target which contains water and hydrocarbon, the target is surrounded by muon range detectors (MRDs). The target itself has scintillator bars in different orientations. The current layout includes a layer of horizontally stacked bars, followed by a 3D grid, then a layer of vertically stacked bars and another 3D grid, repeated twice providing a total of 8 planes. The 3D grid, seen in figure 3.9, is made of thin scintillator bars of $1000 \times 25 \times 3$ mm^3 put together to forms a mesh, as can be seen in figure 3.10. The 3D structure is currently filled with water, which forms the target in which to study neutrino interactions. This design maximizes the fraction of target material and also provides good particle tracking capabilities allowing one to reconstruct tracks emerging at large angles with respect to the neutrino beam direction. The WAGASCI detector will collect data with both polarities of T2K focusing horn system. The WAGASCI modules are mainly composed of 1280 plastic scintillator bars and a surrounding stainless steel tank. One WAGASCI module consists of 16 scintillator tracking planes, where each plane is an array of 80 scintillator bars fixed within a frame. The 40 bars,

called parallel scintillators, are placed perpendicularly to the beam, and the other 40 bars, called lattice scintillators, are placed in parallel to the beam within the hollow cuboid lattice.

WAGASCI has the possibility of being operated both with water-in and water-out providing either a fiducial volume of the module of 188 kg and the mass ratio of scintillator bars to water as 1 : 4 or a fiducial volume of 47 kg and the mass fraction of scintillator bars as 100%.

In conjunction with WAGASCI there is also the INGRID proton module, seen in figure 3.11, and an INGRID module with iron and scintillator, seen in figure 3.12. The proton module consists entirely of scintillator bars, which act as a hydrocarbon target, read out using the same electronics as the Interactive Neutrino GRID (INGRID) [122]. The experiment also includes a full INGRID module, which is a non-magnetised muon range detector comprised of scintillator bars interlaced with iron. The fully installed module chain, without the Baby MIND, can be seen in figure 3.13 and the full computer model sketch with the proton module, WAGASCI module, INGRID module and Baby MIND is observed in figures 3.14 and 3.15. By combining and taking measurements with all of these different modules as targets, measurements can be made on inclusive and exclusive differential cross sections of the charged current neutrino and antineutrino interactions with water and hydrocarbon. This will in turn make it possible to reduce one of the most significant sources of uncertainties of the T2K experiment [78].

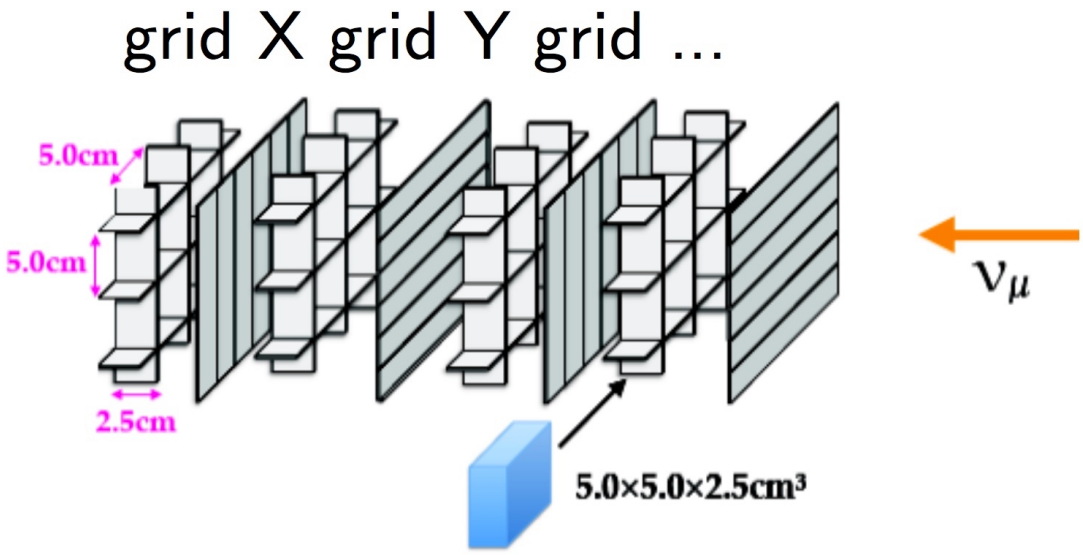

Figure 3.9: The structure of the WAGASCI detector with scintillator bars either horizontally or vertically with a structure to support each the boxes. Figure, courtesy of Akihiro Minamino.

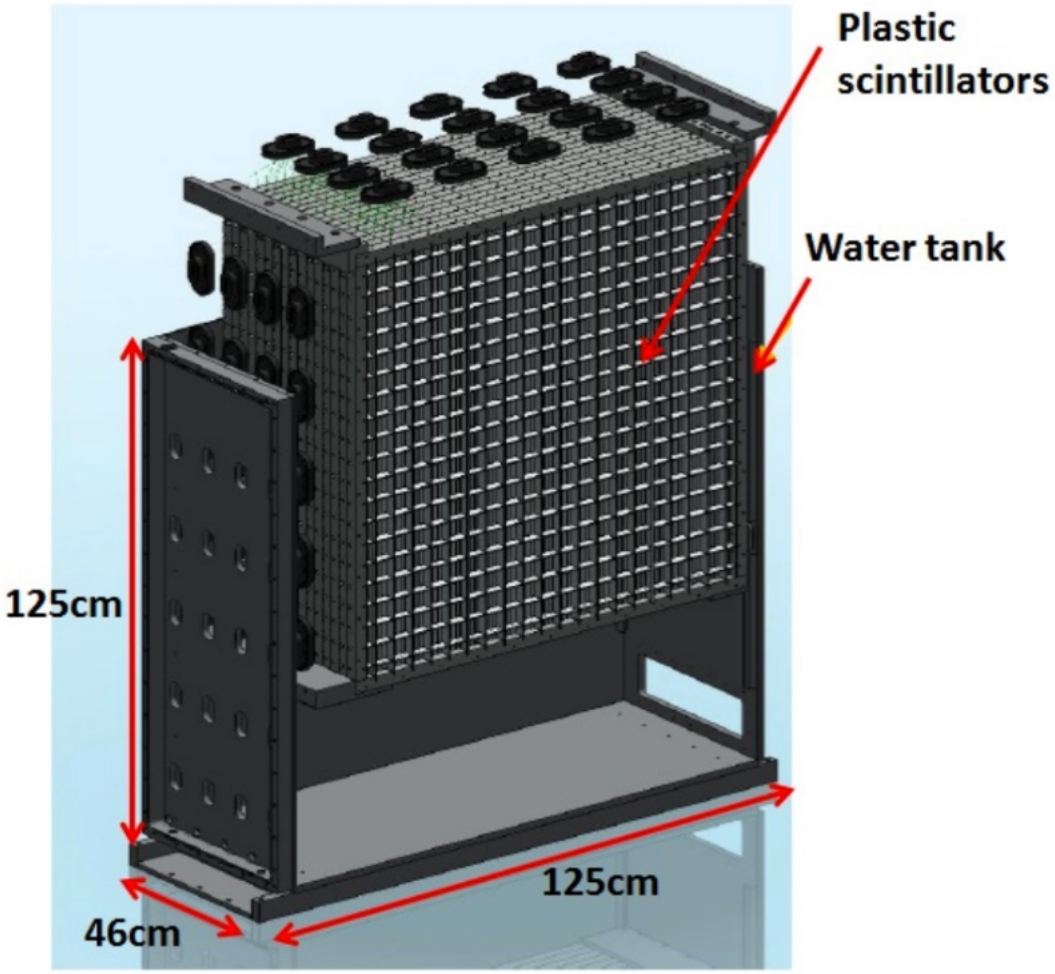

Figure 3.10: An illustration of the full WAGASCI module [123].

3.2.3 WAGASCI and INGRID electronics

Scintillator bars are used as active elements in the WAGASCI detector and INGRID modules. The bars are similar to those in Baby MIND as they also use WLS fibres to transport light to Hamamatsu MPPCs. The performance of the scintillator bars was measured with a 600 MeV positron beam. The average light yield was found to be 10-18 photo-electrons (p.e.) and the detection efficiency was better than 99% for the whole region of scintillator, with a threshold set to 1.5 p.e. The detector performance of the water-in WAGASCI module was checked during the beam operation in 2017.

The Silicon PM Integrated Read-Out Chip (SPIROC) was adopted as the front-end electronics of the WAGASCI modules. SPIROC is a 36-channel auto-triggered front-end ASIC, and is produced by OMEGA/ IN2P3 [125]. It not only contains an analog signal processing section such as amplification and shaping of the waveform, but contains a digital signal

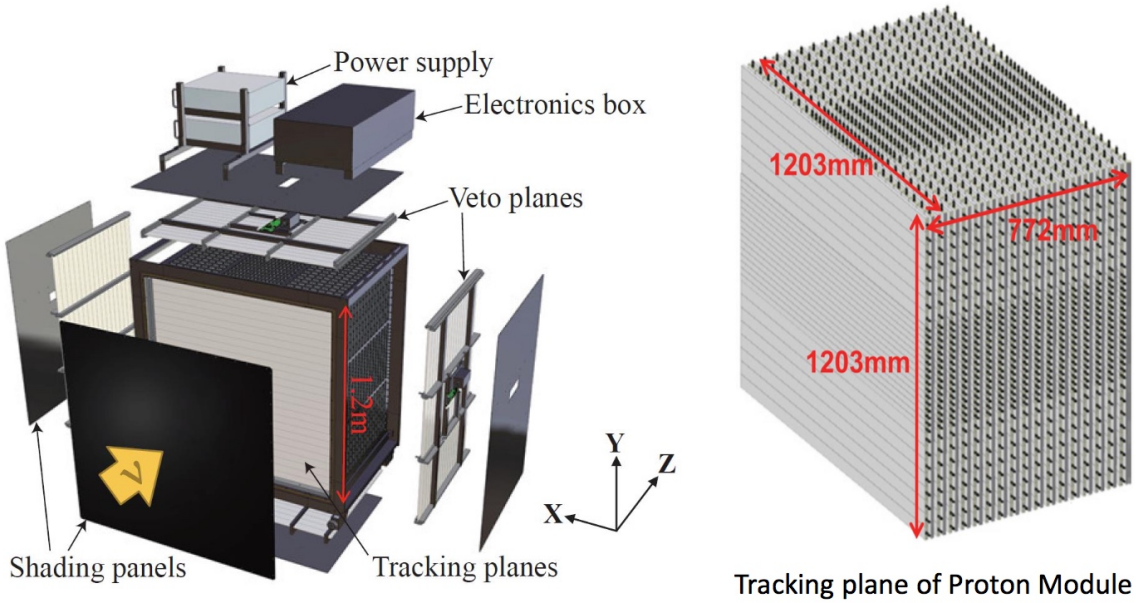

Figure 3.11: An illustration of the INGRID proton module [124].

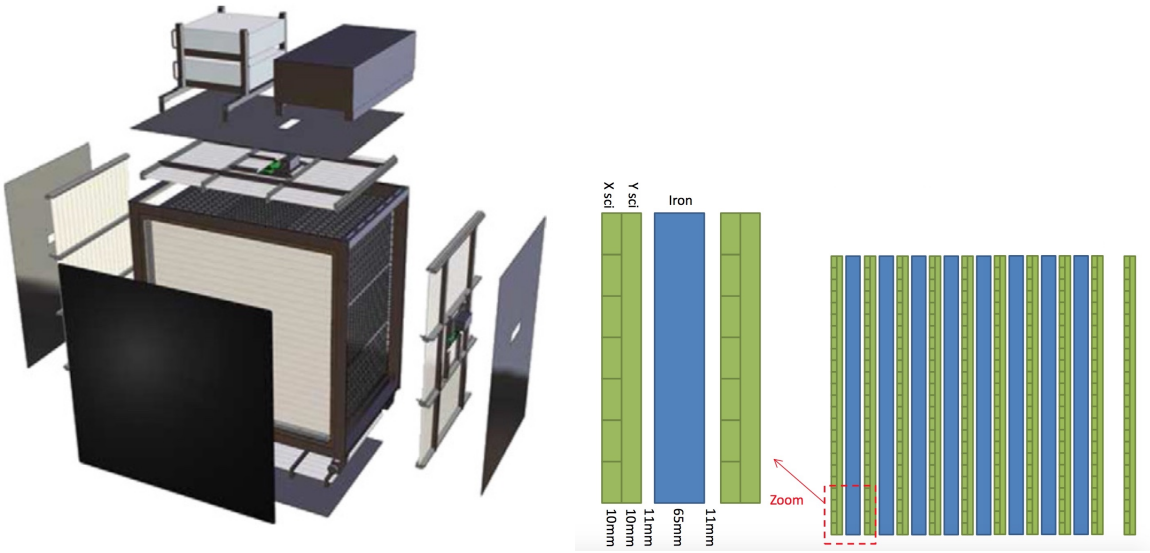

Figure 3.12: An illustration of the INGRID module [124].

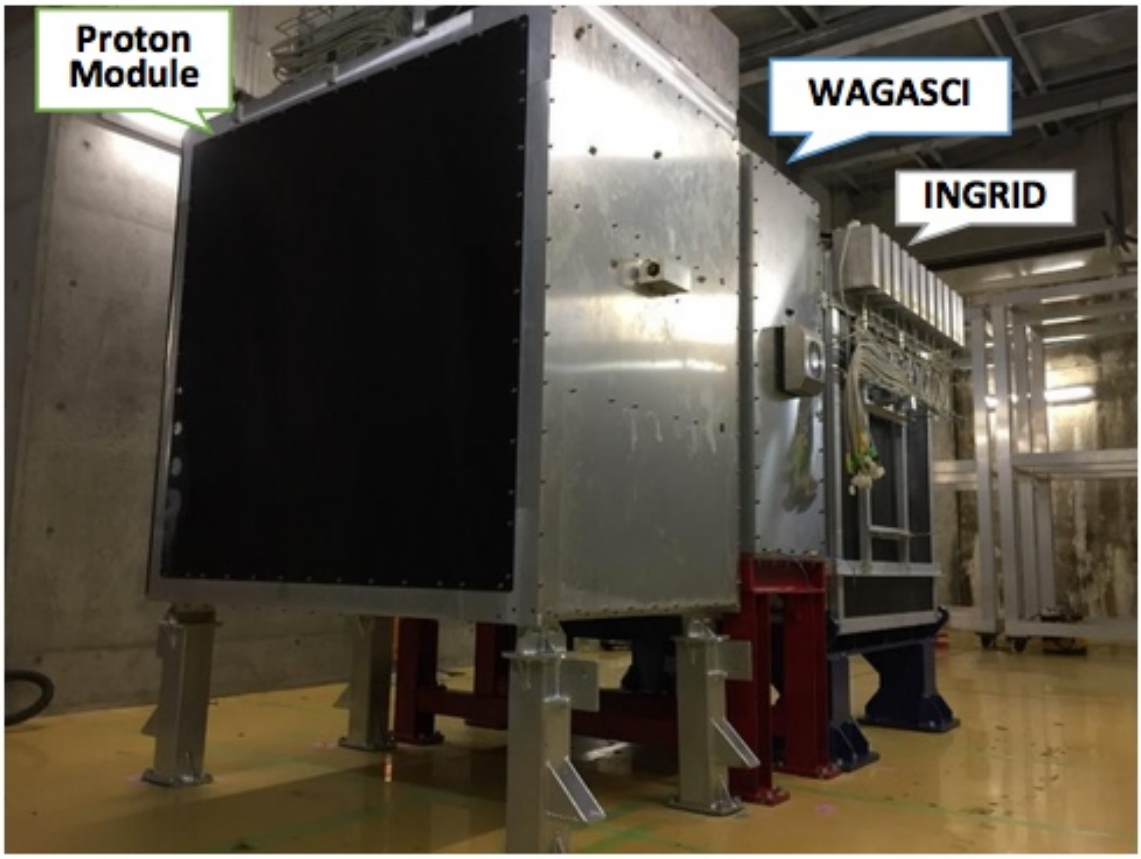

Figure 3.13: A photo of the fully installed WAGASCI module with the INGRID and INGRID proton modules at the B2 floor at J-PARC. Figure, courtesy of Akihiro Minamino.

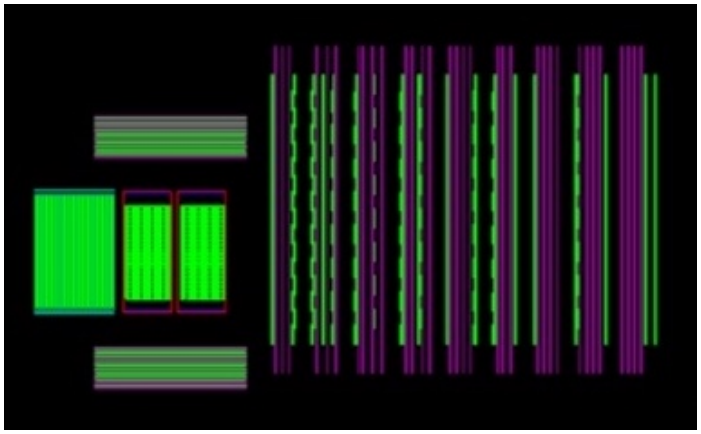

Figure 3.14: An image showing the B2 floor layout at J-PARC with (from left) INGRID proton module, WAGASCI, INGRID module and Baby MIND. The side MRDs are in gray.

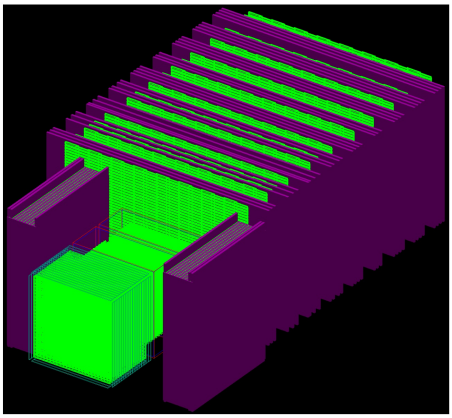

Figure 3.15: Axonometric view of the B2 experimental layout.

processing parts such as auto-trigger and timing measurement. The charge of the MPPC signal is sampled by a track-and-hold circuit. A front-end electronics board Active Sensor Unit (ASU), has been developed with the SPIROC2D chip, which is the latest version of SPIROC. Each readout board is designed to control a 32-channel array MPPC, and 40 of the ASU boards are aligned on the module surface. The data acquisition system used for this detector, including back-end boards, has been developed for prototypes of ultra-granular calorimeters for the International Linear Collider (ILC), and is independent of the T2K DAQ system. To synchronize the DAQ system to the J-PARC neutrino beam, the pre-beam trigger and beam trigger are sent to the clock control card. The beam trigger signals are converted from optical signals to NIM signal in a dedicated NIM module on the B2 floor. In addition, the spill-number information is delivered with 16-bit ECL level signals, and converted to an Ethernet frame by an FPGA evaluation board to be directly sent to the DAQ PC.

3.2.4 MRD and Baby MIND

The WAGASCI detector requires a muon tracker to measure the momentum and charge of outgoing muons to identify the neutrino interaction and calculate the neutrino cross-section. As mentioned above, Baby MIND provides this role placed after the main target. There are also two much smaller muon range detectors (MRDs) on either side of the target to measure background muons from other sources or which have been produced from the neutrino beam but will miss the target or Baby MIND. These side MRDs can only provide momentum measurements for contained particles and they cannot provide charge information and will thus only be used as an extra veto plane for acceptance measurements. The layout and

position of the side MRDs can be seen in figure 3.8.

3.3 Summary

In this chapter the Baby MIND and WAGASCI detectors have been presented as well as a description of their current status.

Chapter 4

SaRoMaN simulation and software

4.1 Introduction

The software environment used for Baby MIND is the Simulation and Reconstruction of Muons and Neutrinos (SaRoMaN) software suite which is a comprehensive software for MIND/nuSTORM detectors and has been developed at the University of Glasgow over several iterations [108, 126, 2]. The software has been expanded to be able to model and simulate a generic detector with limitations in the current implementation of the reconstruction. It includes a complete range of functionality for simulating single particle beams through GEANT4 [114], or neutrino beams, through GENIE [127], including geometry design, digitisation and reconstruction through RecPack [128]. The software suite is also shipped with several analysis code examples written in ROOT [129]. It has been created exploiting software engineering and object-oriented techniques and implemented in the C++ and Python programming languages. The software is accessible on request from `https://lspace.ppe.gla.ac.uk`.

4.2 General structure

The SaRoMaN software's main design goals have been to promote modularity, provide a single point of entry for the design and input variables and to simplify usage. With this in mind, the SaRoMaN software is split into four main parts which can be replaced or altered independently of the others as long as the input/output flow is conserved. The parts are denoted, wrapper, simulation, digitisation and reconstruction with the main flow regulated by the wrapper seen in figure 4.1 and a more detailed view in figure 4.2. Each part will be discussed further below.

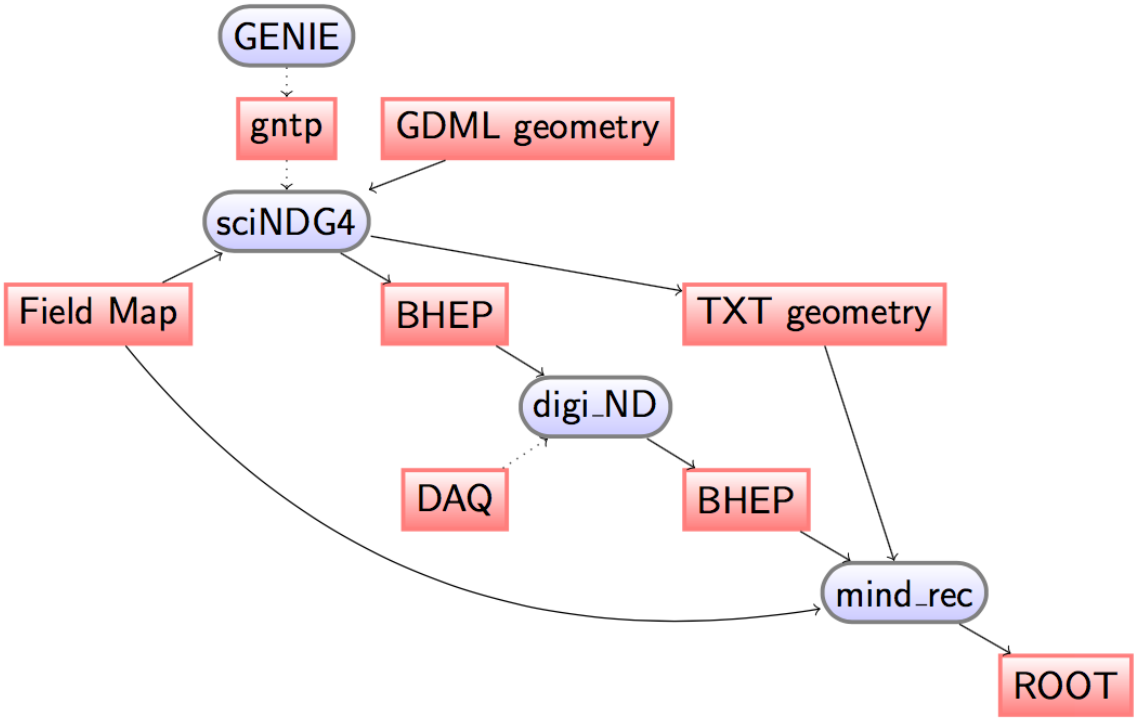

Figure 4.1: Code flow of the SaRoMaN software suite all controlled and handled through a wrapper.

4.3 Wrapper

To simplify the installation, compilation and usage of the other parts in the SaRoMaN suite, a wrapper has been developed in the Python programming language. This wrapper, aside from the above, handles all input variables, file names, writing of configuration files, standardisation of magnetic field maps and geometry, and data flow between the other parts.

To simplify operation for the user, all of the installation, compilation and running are handled through simple command line inputs with the option of more advanced commands being issued through the use of the Python wrapper class. After installation, SaRoMaN can be run with some default parameters, a full run diagram can be seen in figure 4.3.

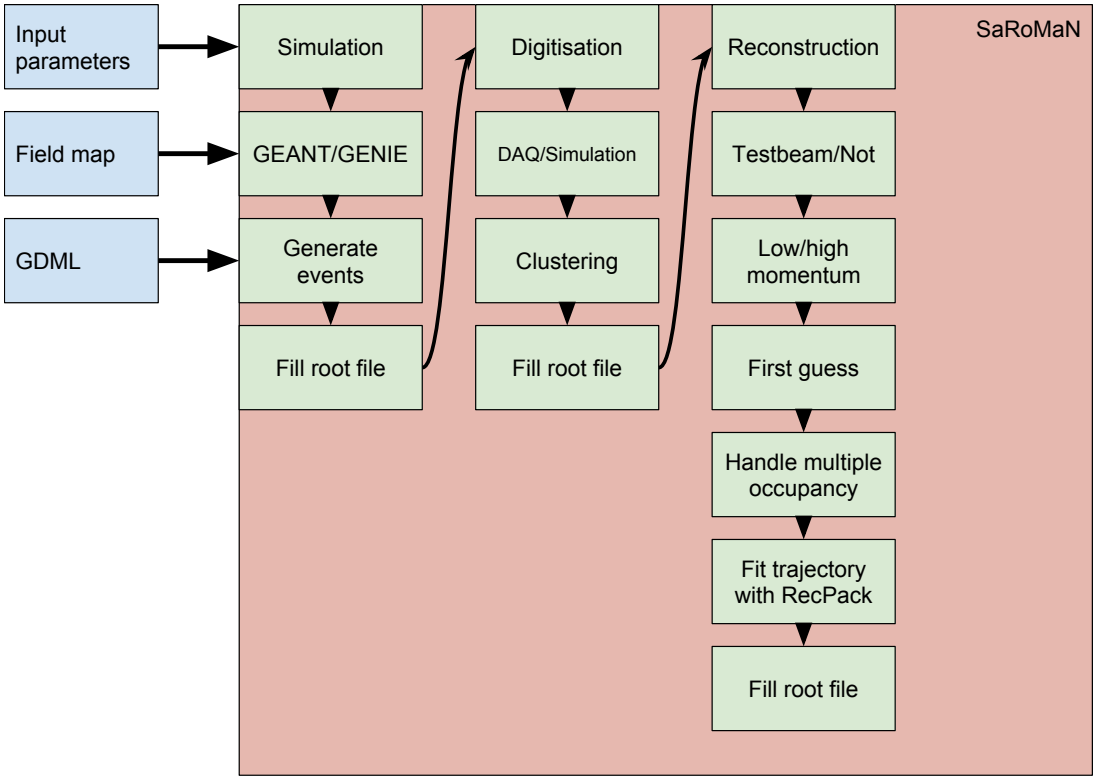

Figure 4.2: Code structure of the SaRoMaN software suite all controlled and handled through a wrapper.

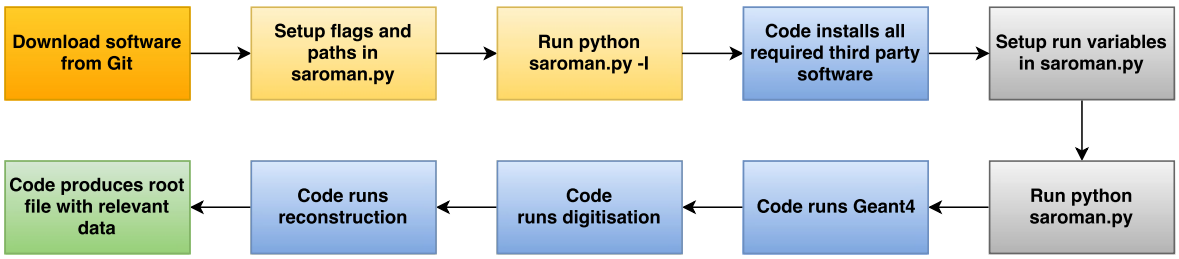

Figure 4.3: Example of how to run a default simulation.

4.4 Simulation

Simulations are used to test and model how particles will interact with a detector model and what scintillator hits can be expected. The outputs from the simulation include the position of the hit on a bar, the location of a bar, the time of the hit and the amount of energy that was deposited. For the studies performed in SaRoMaN, well tested physics models are used in GEANT4; however, the option exists to add new physics and to test new theoretical models.

The simulation comes with two different modes, neutrino or “single particle”. For neutrino mode, GENIE is first run to generate the neutrino events. The data from these events are run

through GEANT4, which includes details of the detector geometry and materials, to create the response of the detector to the particle hits. In the single particle mode, GENIE is not invoked, and one can choose to run with a beam of charged particles of a single species, which are also passed onto GEANT4 that simulates the response of the detector.

A unique feature is that SaRoMaN uses a single geometry definition for the whole framework, written in the Geometry Description Markup Language (GDML) [130] which is interpreted in GEANT4 and is passed as a simplified .txt file to the reconstruction, which simplifies any changes of the geometry. This GDML file can be used to describe simple detectors, such as a monolithic scintillator module, as well as the full Baby MIND and even any combination of several of these put together in any layout. It is also possible to generate a GDML file from computer-aided design (CAD) software to get all of the constructional details of the detector.

4.5 Digitisation

Digitisation is the emulation of the signals expected to be produced by the detector hardware. It needs to handle the response of the electronics and describe the expected output signals, based on input hits in the detector. Any electrical system can be described as providing an output based on the response function of the system and the input signal. The digitisation is based on a description of the response function of the detector for the simulated input.

This is currently done in a simplified way by smearing data with different Poisson or Gaussian distributions to take into account the stochastic nature of the production of the expected signals, as well as handling events which are distinguished by a large time difference. For the Baby MIND detector the algorithms take the horizontal and vertical bar hits and clusters them together to construct x, y and z positions along with the energy deposition and time to produce physical hit points. The full program flow can be seen in figure 4.4.

As a way to simplify the integration and implementation, the data acquisition (DAQ) used for the different test beams have been implemented in the digitisation as well. In this mode, real data is given as input and only the clustering takes place. Due to the usage of a single geometry, a token simulation has to be run in this mode as well to properly construct the geometry.

To ensure that all further analysis is performed properly, the output of the digitisation is identical, whether it was simulated or read out through the DAQ.

One of the most difficult design features of Baby MIND is combining hits from both vertical and horizontal bars. It is possible to get hits which cannot be combined without ambiguity. Figure 4.5 contains an illustration of two sets of simultaneous hits in the vertical and horizon-

tal bars. Think of two separate particles, the first one producing the green hits and the second the red hits. Given that the bars only return that they were hit, not the actual position on the bar that was hit it is not possible to distinguish the green hits from the red hits, they would produce the same data. The current method is for the digitisation to create both hits at all times and these hits are then handled by the reconstruction where they can be distinguished by looking at the pattern recognition and the track reconstruction.

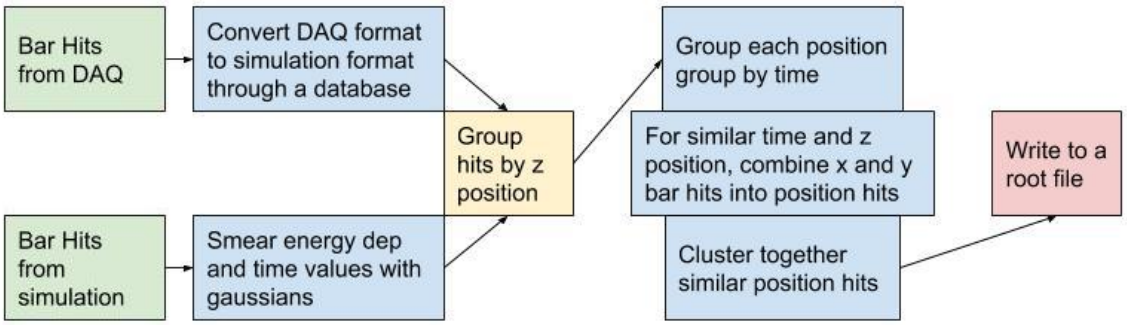

Figure 4.4: Program flow for the digitisation.

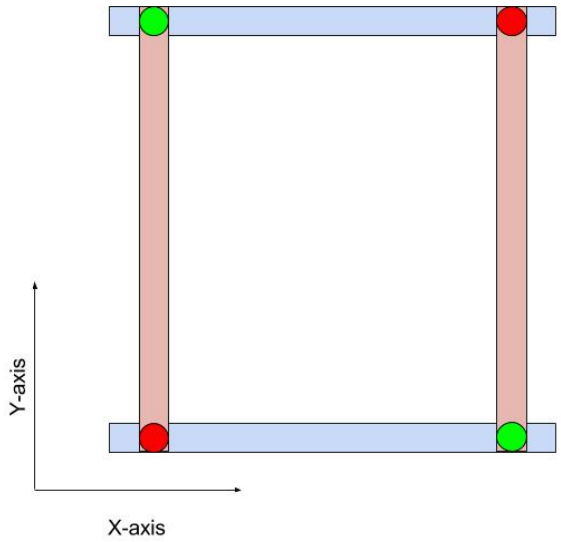

Figure 4.5: Illustration of the difficulty in combining hits in vertical and horizontal bars when there are two or more hits in each bar.

4.5.1 Simulated data

The digitisation is provided with a .root file [129] containing all of the information from the simulation. Given that the data is assumed to be analysed offline, the first task is to separate any hits into event time windows, where hits can be seen as coming from the same particle. The main difficulty is to allow for the particle to fully traverse the detector and to

allow a delay in electronics response within the time window. This provides a number of hits in several time bins, denoted as events, without being able to filter the events by using the position information.

After the timing clustering, so-called 3D space points are created by combining the vertical and horizontal bar hits for a specific module. These 3D points are combined to provide an x, y and z coordinate. For each bar, coincidence and overlaps are taken into account, as mentioned previously, by creating all of the possible space points allowed by the combination of hits. A clustering algorithm is used to combine the energy, position and hit time of multiple hits, to create one or several clusters each with a discrete position.

The final step in the digitisation is to smear the value of the deposited energy and hit time based on measured values of propagation time through the scintillator bars, given the simulated hit position and not only the bar position.

4.5.2 Data acquisition

The current data acquisition (DAQ) framework for the Baby MIND detector is based on the event building being carried out offline, meaning it is processed both after and away from the acquisition to combine the information from multiple FEBs and to create full events offline.

For simplicity, the DAQ converts the acquired data into the same format as expected from a simulation so that the digitisation can be used in the same way. The main difference is that the smearing is only used for simulated data.

In this simplified version of the data acquisition system written for the Baby MIND test beam, the data is stored in different data files specific for each FEB. In the future, the DAQ shall be adapted to merge the data from each FEB, but this was not possible for the test beams. The data from each FEB has channel number, hit time and hit amplitude. The first step is to convert the data into space-positions, using either the vertical or horizontal bar position information and $z-$position. This is carried out by using a database which correlates the FEB and channel number with the knowledge of the physical layout of the detector. The second step is to ensure that each hit position has a corresponding time and amplitude. Step three is to cluster all of the hits in specific time slots, which are equivalent to the event time windows. When this is achieved, several low level filters are performed, to ensure that an event has enough hits to produce at least four 3D space positions in a time slot. After these steps, the data is equivalent to the data produced by a simulation and is processed in the same manner by the reconstruction.

4.6 Reconstruction

The reconstruction takes the digitised hit data and assembles tracks and vertices. The main physics parameters are the momentum as well as the charge of the particle. The main problems occur when there are overlapping hits with multiple occupancy per bar. In this situation, it is difficult to distinguish between valid hits and to extract the momentum of the track and its charge. The first problem is handled by removing and adding hits and using a χ^2 analysis through a Kalman fitter package, RecPack [128], to find the best trajectory that fits all hits. The second problem is solved through various algorithms to estimate the charge and momentum using different fits.

For simplicity, the reconstruction currently contains a mode denoted as " test beam" where it does nothing more than writes out the input data into a final .root file.

4.6.1 Structure

The reconstruction software has been structured to ensure that the software is as modular as possible. It is currently based on the Kalman fitter package known as RecPack [128] to provide both a framework and back bone for handling track objects. It is still used since it was the first Kalman filter implementation, however, SaRoMaN would benefit from using a bespoke Kalman fitter implementation to ensure its maintenance and reliability, as RecPack is no longer maintained and its documentation is lacking.

A Kalman fitter is given an underlying model of the trajectory, in our case knowing that particles travel as helices, and a model of the detector as well as other known inputs to the system to form an estimate of the different possible states of the system in a way that is better than using only a single measurement. This is particularly well suited in particle physics where random noise is given through multiple scattering. It can also take into account the energy loss through different materials and keeps track of the varying magnetic field. The measurements can be used in different parts of the detector to estimate both how the particle has and will continue its propagation. Compared to other models, a Kalman fitter has no underlying assumption about the errors being Gaussian.

In high energy physics one frequently faces the problem of modeling the evolution of a dynamic system from a set of experimental measurements. Most reconstruction programs use similar methods. However, in general they are reimplemented for each specific experimental setup. Some examples are fitting algorithms (i.e. Kalman Filter), equations for propagation, random noise estimation (i.e. multiple scattering), model corrections (i.e. energy loss, inhomogeneous magnetic field, and physics measurements.), model conversion, etc. Similarly, the data structure (measurements, tracks, vertices, etc.), which can be generalised as well,

depends on the particular implementation. The motivation for using RecPack is due to the combination of these properties into a simple software package.

SaRoMaN has been split into a number of phases: it first initialises the fitter and then it uses an initial pattern classification to choose reconstruction mode. Currently particles and showers are identified, but only muon-like particles are reconstructed. In this identification, a track is produced along with any off-track hits. Finally, the fitter performs a final charge and momentum estimate on the track and tries to fit more tracks to the off-track hits. If this is a neutrino sample, proton/neutron tracks are only built if it finds an initial muon track.

The test beam mode ignores the event classification and uses the fitter to pass information from input through to the final root file.

The reconstruction has been split into several minor tasks.

- Handling data: Pushing the input data into a final root file.
- Track building / pattern recognition, given an event, (a time window) can we build a track from this?
- Fitting, with a candidate track, is it possible to add more hits to the track and make it longer? Is it possible to find secondary tracks? Also, is it possible to estimate the momentum and charge of the track?

4.6.2 Pattern recognition

The pattern recognition tries to estimate if the event is muon-like or not. It starts by looking at the number of hits for a given event. There are currently two main limitations to a track being fitted in SaRoMaN:

- At least 4 hit modules are required to do any form of charge estimation or track building.
- At least 10 hit modules are required to perform a Kalman fit.

Outside of these limitations, currently only muon track fitting has been implemented. The general assumption is that each event will contain at least one muon track followed by other secondary tracks. If this is not the case the event is discarded. The event filtering is performed very simply by assuming anything that is not a shower is a muon. Single hits here refer to separable space points, meaning that for each $z-$position there is only one unique hit. The aim of the pattern recognition is to find as many tracks with single hits as possible. In the pattern recognition, tracks are built up from so-called track stubs of at least four single hits.

As soon as a track stub is created other hits can be added onto the track stub to create a final track using a χ^2 fit as a metric for evaluating which hits to add. This χ^2 analysis is run through the Kalman fitter and requires an initial charge and momentum guess. This means that the best suitable hits are added to the track stub with the remaining hits saved for use in finding secondary tracks. This initial Kalman fitter produces a track with an estimate of the momentum and charge which is further used in the final fitting.

The program flow can be seen as taking in an event consisting of a number of hits and returning a number of tracks along with hits which could not be fitted into any track. Each returned track contains only single hits as well as a momentum and charge estimate. The latter two are then improved by the fitter.

4.6.3 Fitting

The fitter's main job is to build tracks and to estimate the momentum and charge of that track. There are two modes, one main mode for events with more than nine hits are passed into the Kalman fitter RecPack. When it is not possible to perform a helical fit and for any track with more than three hits, a self implemented lever-arm approach is used. In both cases RecPack is used to build the tracks, however the momentum and charge reconstruction has to be split depending on the possibility of a helical fit or not. The full helix equation (equations 4.1-4.3 and 4.4-4.6) has a total of nine parameters and takes ten measurements to be fully fitted.

$$x(t) = a\cos(bt + c) + d \tag{4.1}$$

$$y(t) = e\sin(ft + g) + h \tag{4.2}$$

$$z(t) = kt \tag{4.3}$$

The helix can be related to physical quantities as:

$$x(\phi) = x_0 + d_p\cos\phi_0 + \frac{\alpha}{\kappa}(\cos\phi_0 - \cos(\phi_0 + \phi)) \tag{4.4}$$

$$y(\phi) = y_0 + d_p\sin\phi_0 + \frac{\alpha}{\kappa}(\sin\phi_0 - \cos(\phi_0 + \phi)) \tag{4.5}$$

$$z(\phi) = z_0 + d_z - \frac{\alpha}{\kappa}\tan\lambda\phi \tag{4.6}$$

where $\vec{X} = (x_0, y_0, z_0)$ is the arbitrary helix pivot point, d_p is the distance from the helix to the pivot point in the xy plane, ϕ_0 is the azimuthal angle from the pivot point with respect to the helix center, κ is the signed reciprocal transverse momentum, d_z is the distance of the helix from the pivot point in the z direction, and $\tan\lambda$ is the dip angle. The deflection angle ϕ is measured from the pivot point and specifies the position of the charged particle on the

helical track. The variable κ can be used to relate to the transverse particle momentum, p_T to the magnetic field as

$$\kappa = Q/p_T \tag{4.7}$$

$$\rho = \alpha/\kappa \tag{4.8}$$

where Q is the particle charge, ρ being the signed radius of the helix, and $\alpha \equiv 1/cB$ being a magnetic-field-dependent constant with c as a constant and B the magnetic field strength. The full particle momentum can be obtained as:

$$\vec{p} = -\frac{Q}{\alpha}\frac{d\vec{X}}{d\phi} = \frac{1}{|\kappa|}\begin{pmatrix} -\sin(\phi_0+\phi) \\ cos(\phi_0+\phi) \\ tan\lambda \end{pmatrix}. \tag{4.9}$$

In practice, this fit also takes both energy loss in the detector and multiple scattering into account when calculating the χ^2 values used to fit the parameters. This motivates the requirement for two different modes. If a helical fit is possible RecPack performs the fitting and returns a final fitted helix, within provided measurement errors, with a momentum and charge estimate.

If a helical fit is not possible, denoted as the low momentum case, several different algorithms are used, as discussed in subsection 4.6.4.

The fitting is performed using the Kalman filter algorithm, by using this underlying equation and assuming each measurement point has some error. Each measurement point $\vec{X}$ is related to the next through extrapolation of the helical equation and assuming an error: $\vec{X}_{k+1} = \vec{F}_{k+1,k}\vec{X}_k + \vec{w}_k$. It is in this error term where multiple scattering and energy loss is taken into account. The output is then given as: $\vec{Y}_k = \vec{H}_k\vec{X}_k + \vec{v}_k$. The helical equation goes into forming the matrix F and H.

It should be noted that, in Baby MIND, a helix model is an approximation given that there is no fully encompassing magnetic field and various different materials, iron and scintillator, in the detector. A more correct, but much more complex model would be a helix in the iron with straight line segments in between the non-magnetised air gaps and scintillator modules.

4.6.4 Low momentum algorithms

The force applied to a particle travelling through a magnetic field is given by the Lorentz force:

$$\vec{F} = q\frac{\vec{v}\times\vec{B}}{c} \tag{4.10}$$

where c is the speed of light in vacuum, $\vec{v}$ is the velocity, q the charge and $\vec{B}$ the magnetic field vector.

Using Newton's second law one produces the following differential vector equation.

$$\vec{F} = m\vec{a} = m\dot{\vec{v}} = q\frac{\vec{v} \times \vec{B}}{c} \tag{4.11}$$

The solution to this equation is given by:

$$\vec{p} = m\vec{v} = q\frac{\vec{l} \times \vec{B}}{c} \tag{4.12}$$

where $\vec{p}$ is the momentum of the particle and $\vec{l} = \vec{X} - \vec{X_0}$ is a vector containing the lengths traversed through the magnetic field.

Using the definition of the cross-product, writing this as a scalar equation, using the small angle approximation and writing using S.I. units produces the normally recognisable equation

$$p = 0.3QB_{\perp}\frac{|\vec{l}|}{\theta} = 0.3QB_{\perp}R \tag{4.13}$$

where p is the momentum in MeV/c, the charge Q is in units of e, the electron charge, the magnetic field strength B is in Tesla and the radius of curvature R is in m. This is one of the main equations used for momentum reconstruction in SaRoMaN. The charge is then reconstructed using $p/|p|$.

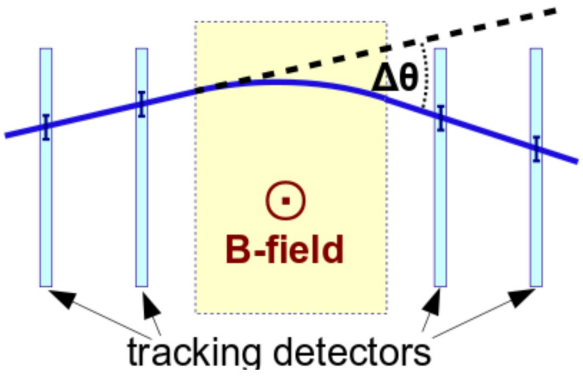

Figure 4.6: Track bending inside a magnetised iron plate, measured by four scintillator detectors [131].

A previous study performed in the collaboration showed that the best best way of evaluating the charge using this method comes from comparing both the first and second bending in the detector, seen in figure 4.6, using two different distributions to handle the scattering.

Assuming the distribution of multiple scattering angles and the notation in figure 4.7, such as $f(\Delta_1|\mu)$ representing the distribution of the measured angle Δ_1 given an assumed charge,

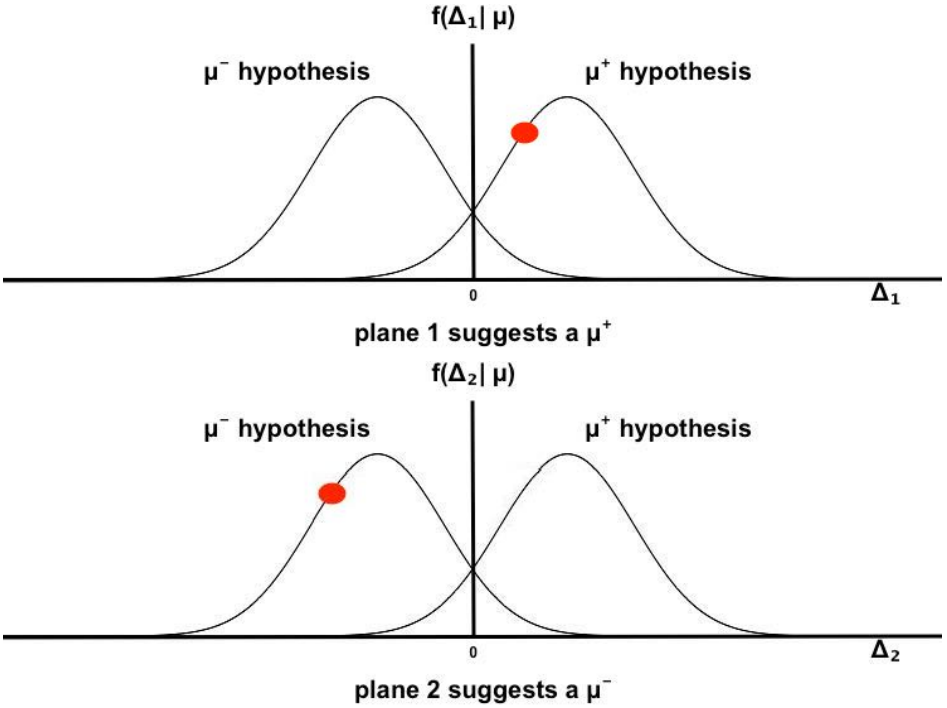

Figure 4.7: Illustration of the angular distributions and criteria for selecting charge.

the choice of charge is given by the ratio of probabilities.

The algorithm returns a μ^- if

$$\frac{f_{\mu^-}(\Delta_1)}{f_{\mu^+}(\Delta_1)} > \frac{f_{\mu^+}(\Delta_2)}{f_{\mu^-}(\Delta_2)} \tag{4.14}$$

and it returns a μ^+ if

$$\frac{f_{\mu^+}(\Delta_1)}{f_{\mu^-}(\Delta_1)} > \frac{f_{\mu^-}(\Delta_2)}{f_{\mu^+}(\Delta_2)} \tag{4.15}$$

The bending angles are calculated from both measurement planes, (or only one if not possible) and tested against a null-hypothesis of having deflection from only multiple scattering [23] given by:

$$\theta_0 = \frac{13.6MeV}{\beta cp} z\sqrt{x/X_0}[1 + 0.038\ln(x/X_0)] \tag{4.16}$$

where βc is the velocity, z is the number of elemetary charges of the incident particle and x/X_0 is the thickness of the scattering medium in radiation lengths.

The probability, using this notation, is given in equation 4.17:

$$P_{\mu^\pm} = \frac{1}{2\pi} e^{-(\theta \pm \Delta)^2/2\theta_0^2} \tag{4.17}$$

Another goal of the reconstruction is to estimate the momentum. Many different methods using the scattering width or fits have been studied to reconstruct this value in a low mo-

mentum region, however the current best approach is to use the continuous slowing down approximation (CSDA). CSDA is based on knowledge of the energy loss in the material before a certain measurement in the detector, assuming the particle deposits an average energy in all materials which it passes. The modular nature of Baby MIND and the varying distance between iron and scintillator planes implies that it has a non-uniform material description. The range of a particle in the detector can be used to extract an initial estimate of the momentum of the particle, and the uncertainty associated with this estimate depends on the number of iron plates between specific scintillator modules. For example, if there are three iron modules between scintillators the error on the momentum is estimated to be approximately $\sqrt{2} \times 90 MeV/c$. Combining information from the CSDA and the angle produces the final momentum and charge estimate.

At low momentum, when tracks do not penetrate into Baby MIND very much, a quadratic fit for the first four hits can be carried out to estimate the momentum.

4.6.5 Performance

During development of SaRoMaN two main metrics were used to evaluate performance, track reconstruction efficiency and charge reconstruction efficiency. These metrics are evaluated by determining how many simulated tracks can be reconstructed compared to the total number of simulated tracks and how many of those reconstructed tracks have the correct charge. This is done for muons of both charges and different momentum values.

Performance will be shown for the initially proposed layout of Baby MIND, for which the software algorithms were designed, the layout implemented for the CERN test beam, and a final study based on the layout used for the WAGASCI detector. The main difference between the initial and test beam layout was to remove the initial measurement plane d0, restructuring a few of the blocks and adding gaps between each of the blocks, as seen in figure 4.8.

The charge identification is however improved when utilizing a measurement point from a neutrino target, the WAGASCI module upstream of Baby MIND; however, this will reduce the lower energy limit of reconstruction since the muons must traverse the material of the WAGASCI.

In figure 4.9 results for the initially proposed geometry can be seen. The plots have been generated by simulating negative and positive muons in the SaRoMaN framework. The results for the slightly changed test beam geometry layout can be seen in figure 4.10.

The main difference between the results are both below 1 GeV/c and in the region above 1 GeV/c and below 2 GeV/c. Below 1 GeV/c the charge reconstruction is slightly worse for the test beam geometry, which can be attributed to the removal of the first scintillating

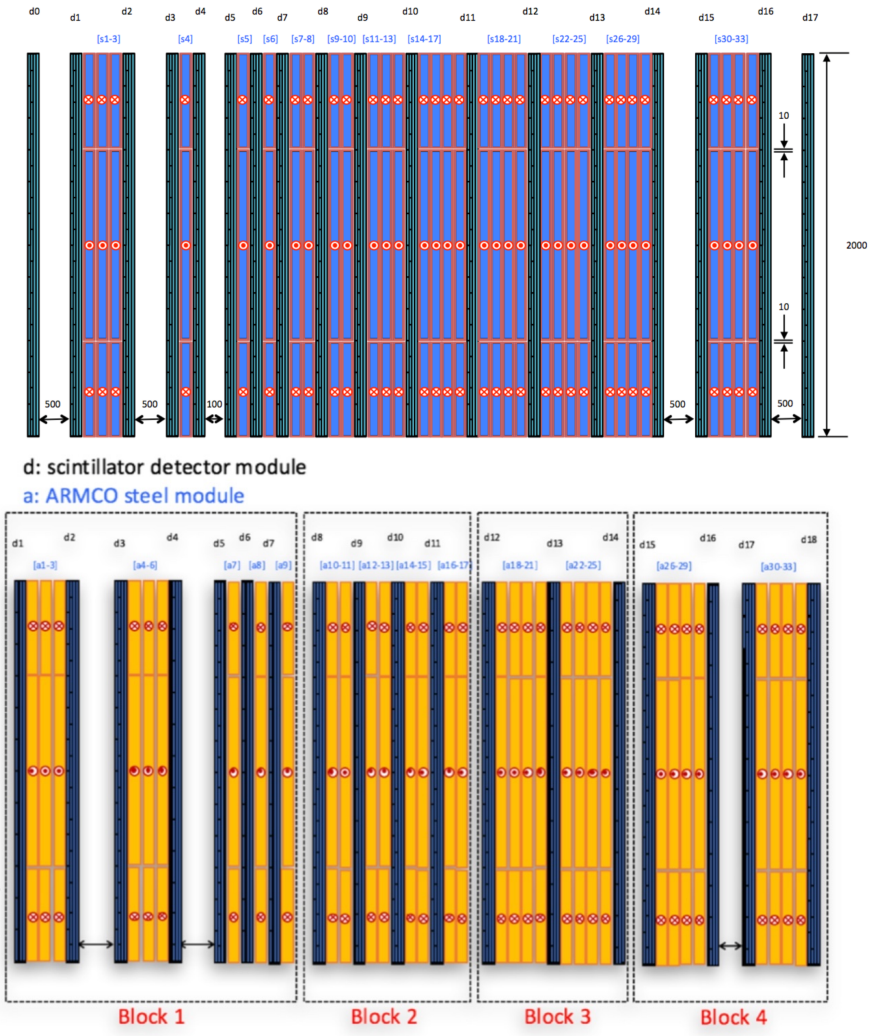

Figure 4.8: (Top) Image of the initial Baby MIND layout. (Bottom) The current Baby MIND layout. The main differences consist of removing the first scintillator plane, a different configuration layout in the middle blocks and removing the final scintillator plane. This was done for constructional reasons to be able to transport the detector from CERN to J-PARC.

plate d0. There is also a slight change in the shape of the reconstruction efficiency above 1 GeV/c and below 2 GeV/c, related to the change of the structure of the detector and additions of gaps providing some drift between measurement positions. For both of the layouts the reconstruction efficiency $> 95\%$ above 0.7 GeV/c and its charge identification efficiency is $> 95\%$ above 0.7 GeV/c. For the full region both reconstruction and charge identification efficiencies are $> 80\%$.

4.6.6 Unpacking of data

Currently data has to be recorded by the front-end board and handled by a test beam computer system. The full data contained in the spills has to be written to disk and then it can be

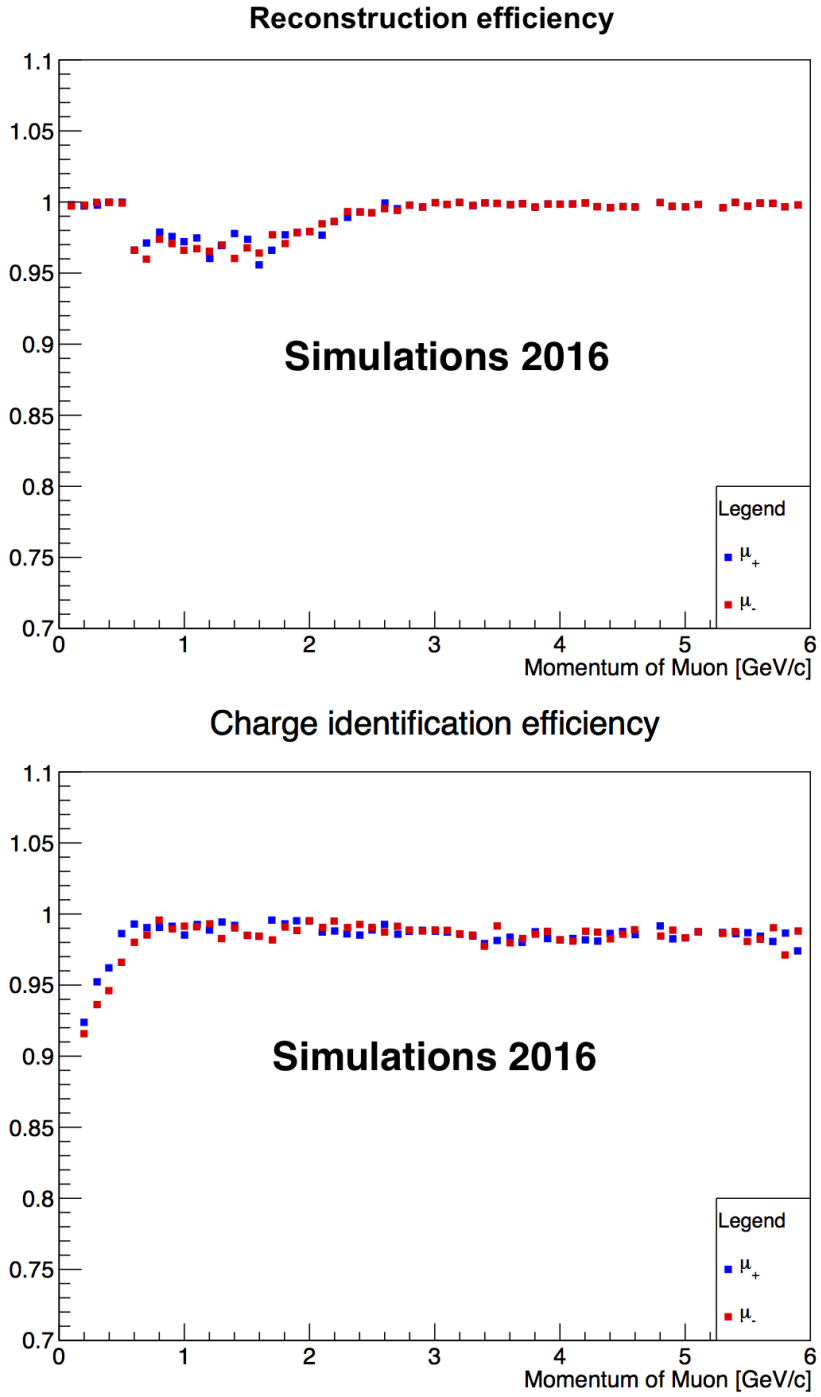

Figure 4.9: Reconstruction efficiency and charge identification efficiency of the initial Baby MIND layout using the SaRoMaN simulation and reconstruction package. The low momentum points in the top figure are based on a different algorithm and definition as they do not require the identification of tracks. Also note that in both figures the points sit on top of each other with red covering blue.

processed off-line after the data taking.

The format consists of a time slot, with a time-division multiplexing index (TDM), containing a spill with several triggers. Each global trigger (GTRIG) contains all of the hit data

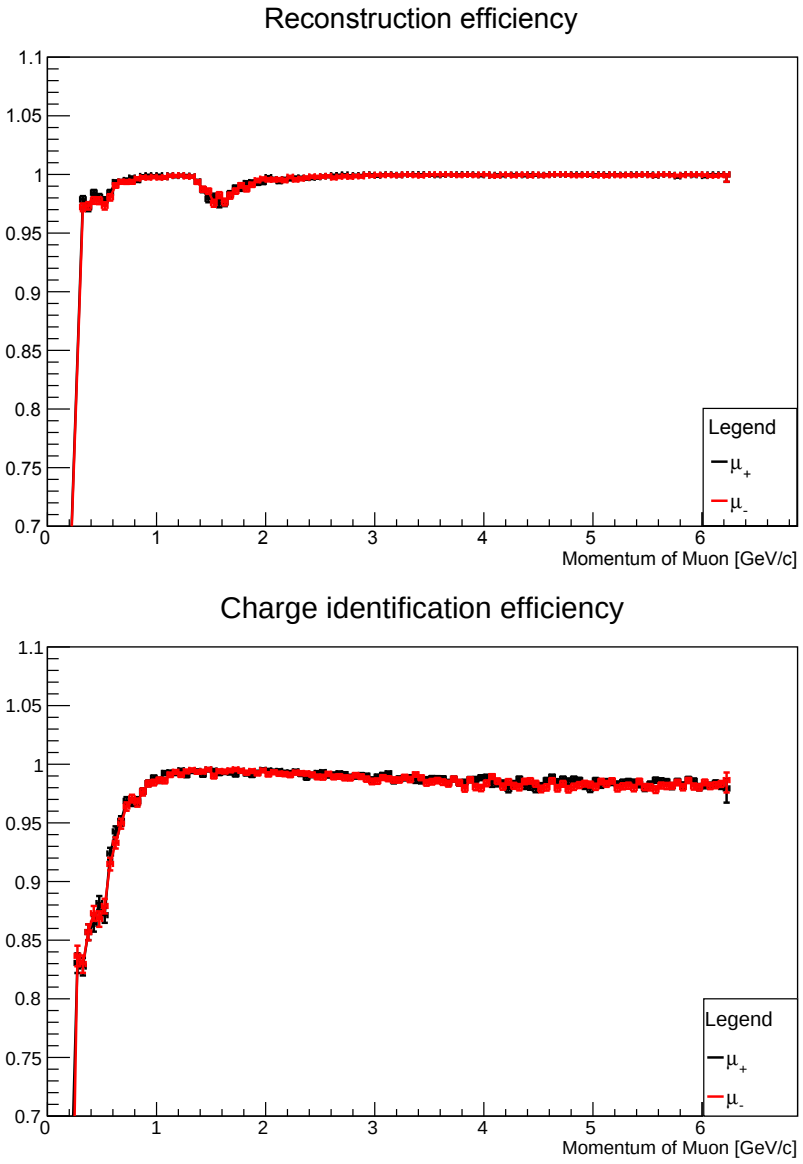

Figure 4.10: Reconstruction efficiency and charge identification efficiency of simulated events for the Baby MIND layout configured for the CERN test beam, using the SaRoMaN simulation and reconstruction package. The dip in the top figure represents the boundary as tracks leave the detector where the algorithm changes.

from the various channels at all the times inside the trigger. Hit data contains amplitude and time measurements with the channel information. Each time measurement comes in steps of 2.5 ns so the system can only distinguish hits on a channel if they happen more than 2.5 ns apart. The triggers come in blocks of 10 μs resulting in at most 4000 events per channel per trigger. The format can be seen in figure 4.11.

Figure 4.11: TDM, GTRIG, spill and data structure for the FEB readout communication. Figure, courtesy of Yannick Favre

4.6.7 Particle identification

Machine learning algorithms are used through the Toolkit for Multivariate Data Analysis with ROOT (TMVA) [132] for particle identification. The main goal of the particle identification is to identify muon tracks from other background events with high efficiency. There are several filters trying to perform particle identification; however, TMVA is needed to further improve this identification. This will be described in chapter 5.

4.7 Future development

Based on the main principles of easily shareable code, using the latest versions and simplicity, a further development of SaRoMaN has already commenced by creating a fully new version based on newer versions of the third party software packages such as GEANT4, GENIE and ROOT. By moving to the latest versions and ensuring that they will be easy to maintain the software becomes “future proof” which is very important for ensuring that the results are making use of the latest physics software. The new framework, following the Lord of the Rings theme [133], has been named SAURON (Simulation And Universal Reconstruction Of Neutrino-like events). SAURON also makes sure to only use open source software and has thus moved from the RecPack Kalman filter to use a Runge-Kutta and Kalman open source fitter known as GENFIT [134]. The change of fitter significantly improved the track reconstruction and momentum reconstruction. The software environment and code can be found

in a docker environment at: `https://hub.docker.com/r/patha325/science/`. The code is hosted at : `https://github.com/patha325/NewSaRoMaN`.

The simulation is based on a generic GEANT4 simulation, which takes in neutrino data simulated with the GENIE open source code used by many. The reconstruction package GENFIT [134], used by several different experiments, takes generic points and uses a Runge-Kutta method to fit the points and calculate the track momentum and charge.

In a similar way to SaRoMaN, the running is handled by a very simple python script which ensures that all software runs coherently with each other. The geometry is handled in a GDML file and read through all different parts to provide one single point of entry for the geometry. To ensure that the code can be used by anyone on different machines without a difficult installation process, the full software is provided in a docker container which means that the code can be run on any operating system.

To be compatible with the DAQ unpacking software developed for Baby MIND, a secondary docker container has been created to handle the specific root version requirement as well as some other minor software requirements which all clash with the SAURON container.

SAURON is currently in a state were it can be seen as a simplified and novel version of SaRoMaN. Bar representation, clustering and pattern recognition is not currently implemented in the reconstruction, these are all handled by using truth information from the simulation or are provided as extra information. None of these are seen to have a major impact on the results, but should be implemented in a future version. In a similar way, the DAQ unpacking is not included, instead the data is assumed to have been processed through it before being passed into the reconstruction. There are currently discussions regarding a unification of the DAQ unpacking and SAURON.

4.7.1 Containers

One of the main issues with scientific software is that they are developed by small teams, often not made publicly available and often the knowledge is only spread through scientific papers. This means that there are many great software solutions and packages which are not used by scientific collaborations, or are misused due to a lack of communication. One could argue that code should be easy to read and that the purpose of a piece of software should be easy to understand, however this assumes that all developers follow some form of coding standard and has/takes the time to develop their code properly which is often not the case. The clear solution to this problem would be to spend more time documenting and cleaning up code as well as sharing it publicly. One problem which may arise is the use of specific third party software versions which make installation quite difficult especially in a climate where documentation is not prioritised and where software is constantly in development.

One proposed solution which solves the problem would be to provide a full runnable coding platform such as a virtual machine. The benefits are numerous, however most of these are further improved by moving to a new software technique known as a container.

4.7.1.1 Container vs Virtual machine

A container is similar to a Virtual machine (VM) but without requiring any abstraction of hardware, they also run on the OS kernel not requiring an added layer. In essence, a container includes an application with the code and all its dependencies without also requiring a full copy of an operating system. This reduces the size of a container compared to a VM and decreases boot time.

4.7.1.2 Container for particle physics simulations

There exist several containers which can be combined for various particle physics simulations. There is currently an official version of the root software in a container `https://root.cern.ch/root-docker-container-alpha-version` as well as various unofficial containers for software such as GEANT4.

During the development of SAURON, early versions of the container provide good tools for running particle physics simulations, without providing the SAURON framework or the neutrino specific parts. There are also early versions which provide the GENIE neutrino generator which provides a good starting point for running neutrino simulations.

4.8 Summary

In this chapter the software framework for Baby MIND has been described, as well as future ongoing developments for improving the software framework. The reconstruction and charge identification efficiencies were evaluated for a series of Baby MIND detector configurations, using the SaRoMaN simulation and reconstruction software, showing that it can deliver high efficiencies over a large momentum range from sub-GeV/c to 10 GeV/c muon momenta.

Chapter 5

Baby MIND test beam at CERN

The Baby MIND collaboration performed an electronics validation using the Totally Active Scintillating Detector (TASD) at the T9 test beam in the PS facility at CERN in 2016. After construction was completed of Baby MIND in 2017, the full Baby MIND was commissioned in the same test beam.

The Baby MIND test beams took place at the T9 beam line at the proton synchrotron (PS) experimental hall. The beam lines are derived from the 24 GeV/c primary proton beam from the PS, which provides 2.4 s cycles of about 400 ms spill duration. The T9 beam is extracted as a secondary beam by firing the proton beam at a 200 mm thick aluminium target which delivers secondary particles up to 15 GeV/c at a production angle of 0 degrees. The line is designed to provide the users with non-separated secondary particles, with positive or negative polarity, as hadron (pion) or muons and the beam momentum can be adjusted by setting the currents for the optical magnets of the beam line. Additional particle identification Cherenkov detectors can be included as part of the T9 beam line but these were not included during the Baby MIND 2016 and 2017 tests.

In this section details will be given on how the data was collected and processed before showing some sample events and then further describing how data is processed in SaRoMaN to provide the results obtained from each of the two test beams.

5.1 TASD test beam

5.1.1 Setup

During June-July 2016 a test beam was performed to characterise the readout system, data acquisition (DAQ) and electronics to be used in the Baby MIND detector. The test beam was at the T9 beam of the East Area, operating at the Proton Synchrotron (PS) at CERN. A

Totally Active Scintillation Detector (TASD) constructed under the AIDA-2020 project (Advanced European Infrastructures for Detectors at Accelerators) was used to test the readout system, electronics, DAQ and reconstruction software. Baby MIND uses the same read out electronics and boards, with some firmware upgrades from this initial test beam.

The TASD detector consisted of horizontal and vertical planes, each plane with 16 scintillator bars, $10 \times 10 \times 1000\ mm^3$, and the configuration can be seen in figures 5.1 and in 5.2. Each bar is read out on both sides by S12571-025C Hamamatsu Multi Pixel Photon Counters (MPPCs). There are a total of twelve planes of either horizontal or vertical type in an alternating vertical, horizontal pattern. The layout is six combined planes providing both vertical and horizontal information with spacing between each. This results in a detector with 96 horizontal and 96 vertical bars read out on both sides using a total of 384 MPPCs and a total detector size of $1\ m^3$. For the test beam only 12 layers of 16×16 bars were instrumented and the total instrumented volume was $0.003\ m^3$.

5.1.2 Data acquisition (DAQ)

Each MPPC is connected to a Front End Board (FEB) which returns data in a specific format. Four FEBs, with 96 MPPC channels each, were fully instrumented for the test beam setup. These FEBs were then all connected via USB3 to a readout personal computer (PC). The readout PCs are controlled via remote connection/ethernet by a computer outside of the beam area in the control room. The data was just recorded to disk, thus all the information from each FEB was merged and analysed offline. This was a consequence of the time available to prepare the test beam and the complexity of unpacking the data consistently.

The data is sent from each of the FEBs in a custom-made data format. The data format combined the data from all of the FEBs; however, it could only work for offline processing as the footers need to be read before any processing can be done.

After the merger of the FEB data, unpacking software is used to translate the format to actual usable data and hits. During the first test beam, conversion between channel and position were hard coded, this was later changed to a database.

5.1.3 Data preprocessing

The data recorded by the DAQ is translated using a database relating the channel number directly to a relative position for the bar as well as passing on the time of the hit. For this initial test beam there was no conversion possible from signal to deposited energy. It was possible for the DAQ to return hits without a time, which were removed before the analysis, also events which were outside the time window with respect to the initial hit were removed.

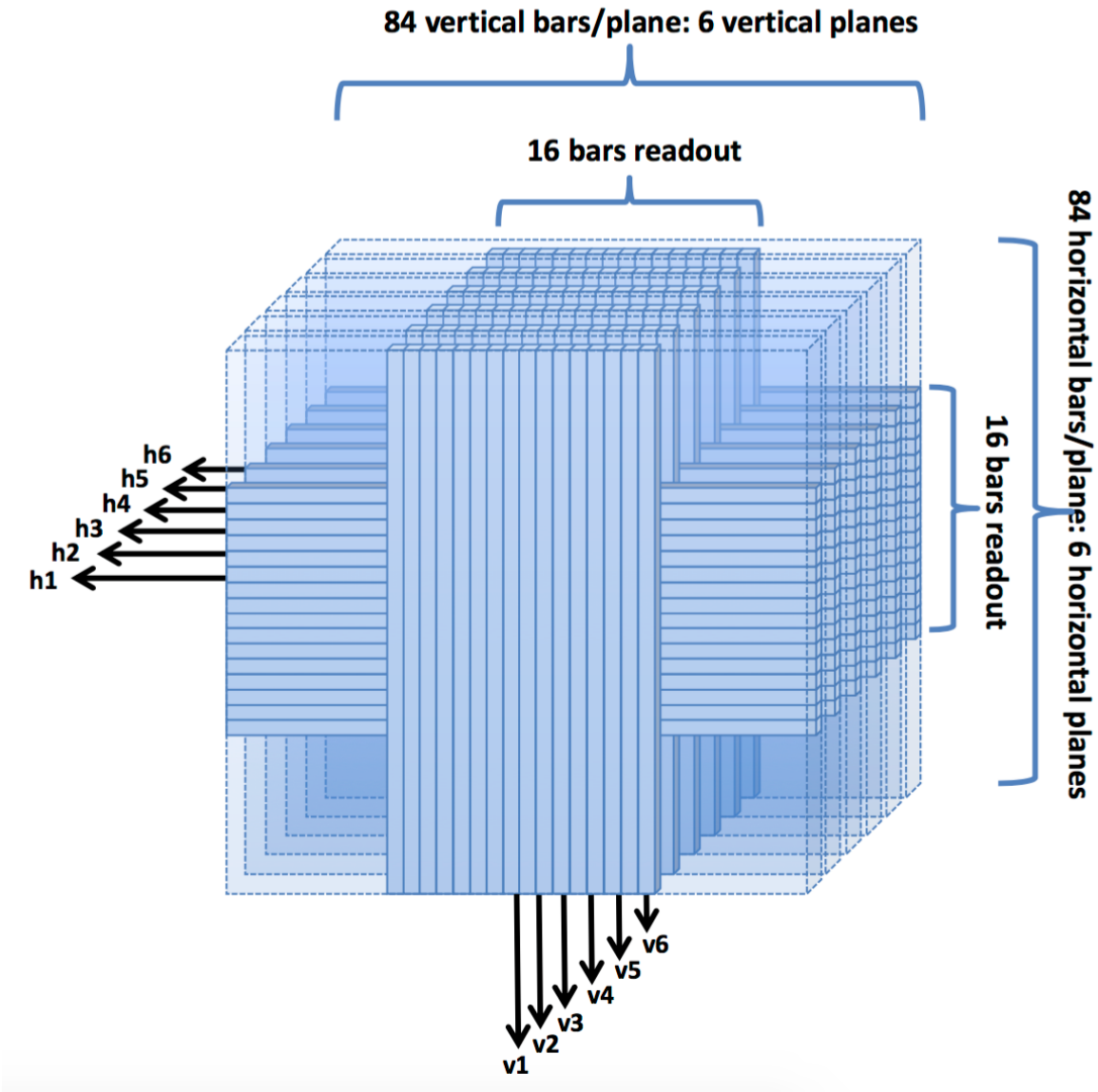

Figure 5.1: The TASD with the instrumented bars visualised.

5.1.4 Results

The main goal of this first test beam was to understand the readout system, electronics, DAQ and reconstruction software. The results can be quite nicely summed up in figure 5.3 and figure 5.4 where the recorded hits have been shown for one specific plane and all recorded hits, seen from the side (figure 5.3). Included in figure 5.4, there is also a combined 3D view and a selected single track. In these figures it can be seen that the TASD was horizontally aligned but the beam was slightly off-center vertically. Detailed studies of the electronics were performed and published in [120].

The plots show that both the electronics and readout system work well, and that the data can be passed through the DAQ into the reconstruction software. Given that the TASD was only 6 planes of scintillator and did not have a magnetic field, the reconstruction software

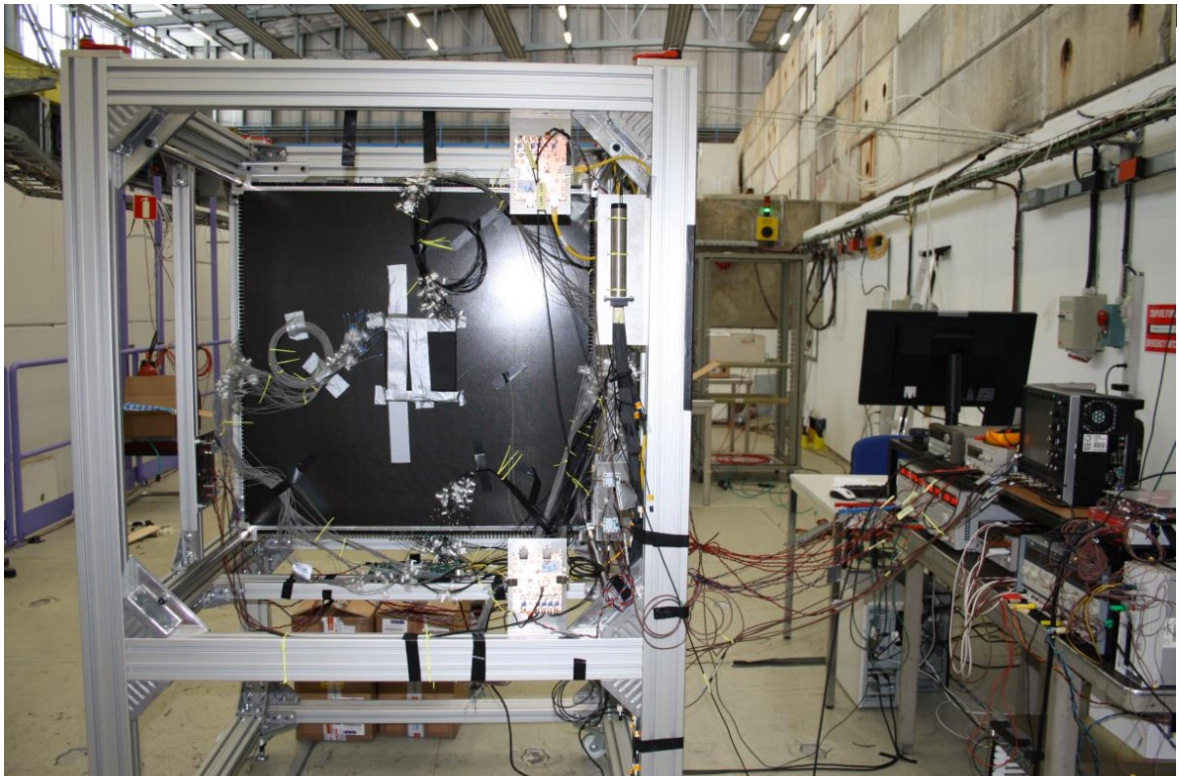

Figure 5.2: The TASD at the T9 CERN test beam with the readout PC.

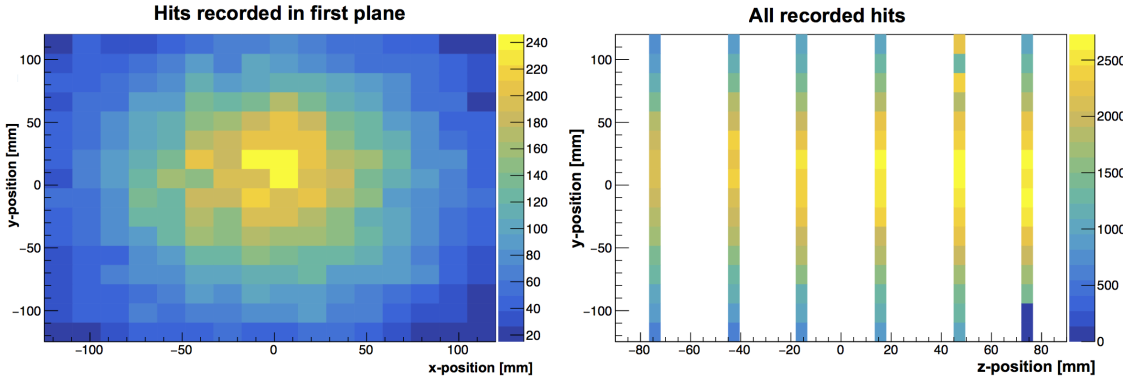

Figure 5.3: (Left) A beam profile in the xy projection as measured by the TASD. The colour code illustrates the number of hits recorded in each bar. (Right) A beam profile in the yz projection as measured by the TASD. A similar colour code illustrates the number of hits recorded.

only combined hits in x and y with the z position to form a final track, without being able to perform any momentum reconstruction. However, it showed that the reconstruction software was operational and could create tracks from these hits.

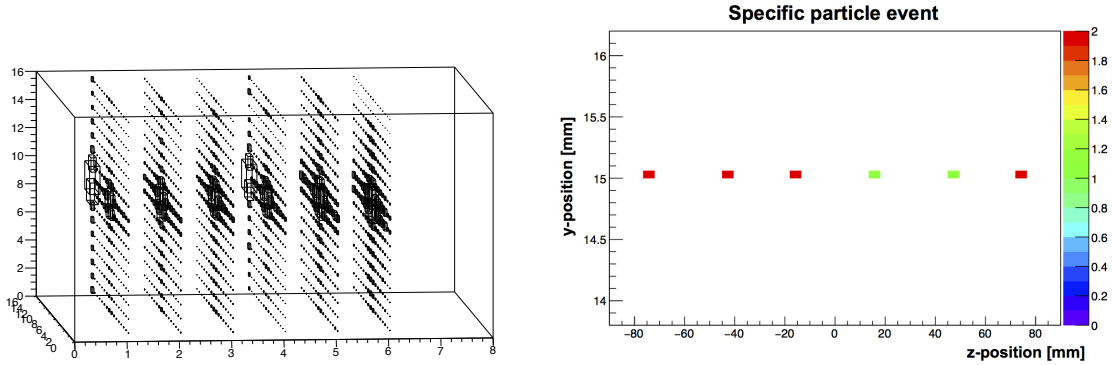

Figure 5.4: (Left) 3D-beam profile measured by the TASD. (Right) Single muon track passing through the detector.

5.2 Baby MIND test beam

The Baby MIND qualification took place at the T9 beam line at the PS experimental hall (East Area), during June - July 2017. A sketch of the layout can be seen in figure 5.5 and a photograph is in figure 5.6.

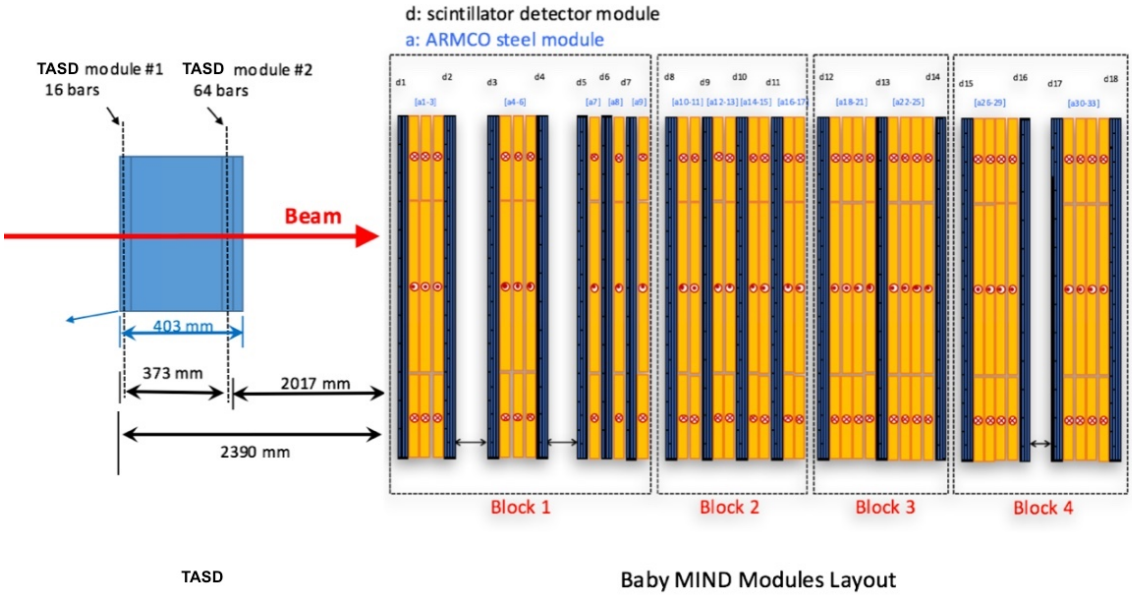

Figure 5.5: A schematic of the layout of the Baby MIND setup at the T9 CERN test beam.

5.2.1 Setup

Four support frames were constructed specifically to support the Baby MIND magnets and scintillator modules mechanically and to meet the transport requirements within CERN and for shipping to J-PARC. The Baby MIND modules were installed in the four frames, as can

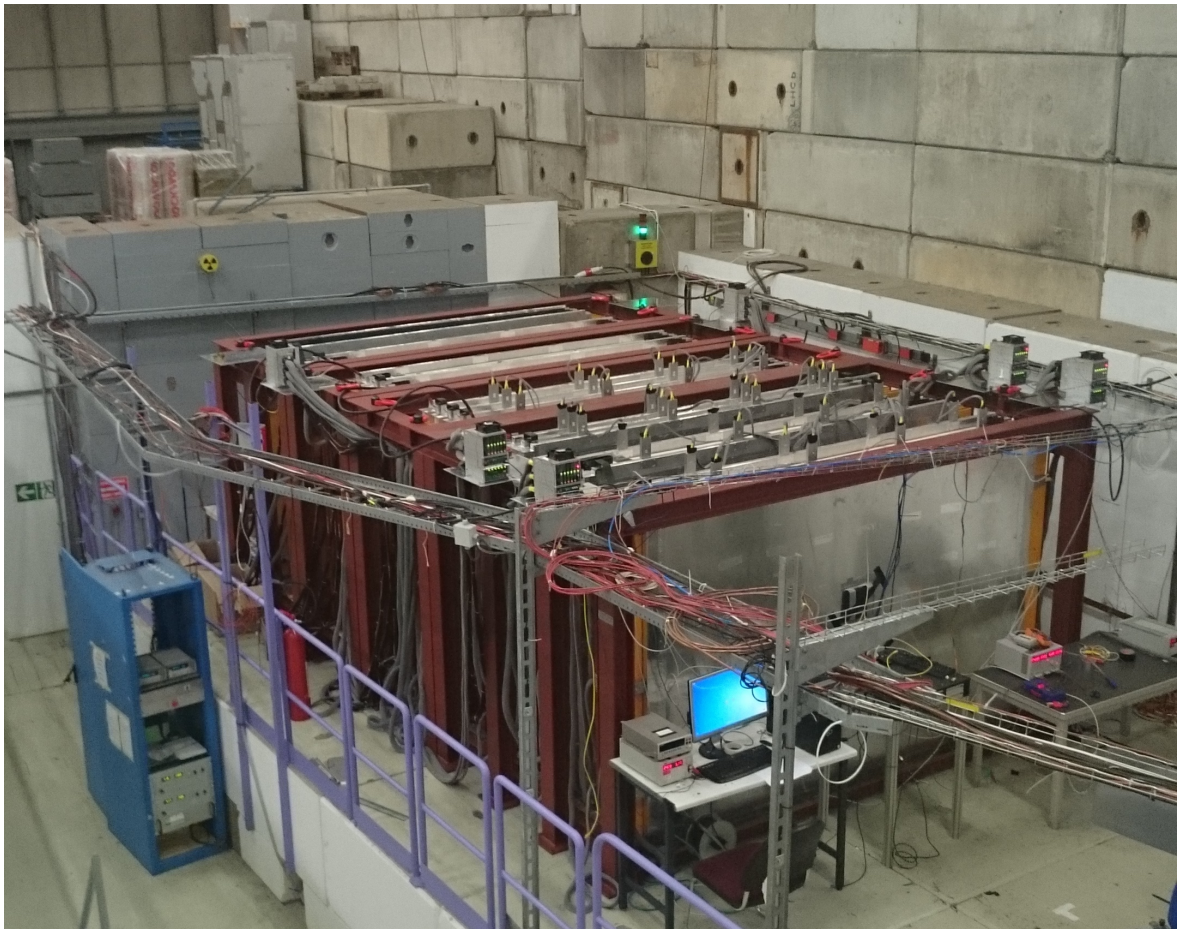

Figure 5.6: A photograph showing the Baby MIND installed at the T9 CERN test beam.

be seen in figure 5.6. The total weight of the detector is around 65 t giving each block a weight of less than 20 tons, which is within the required limits for crane operations at both sites.

For the data taking during the test beam, the TASD AIDA module was placed in front of the Baby MIND to provide initial beam information, both for an angular measurement of the beam and a veto measurement from cosmic rays. It was also used as a trigger to define an event from the spill timing. Only a total of two planes of the TASD were instrumented providing 192 channels.

A total of 44 FEBs mounted on 8 mini crates instrumented the 3996 channels of Baby MIND and took the 192 channels from the TASD. All 44 FEBs were synchronized using the spill signal from the T9 beam line which arrives one second before the arrival of the spill of particles. This signal was fed to a dedicated Master FEB which would generate a reference clock signal for all the other FEBs acquiring data.

5.2.2 Data preprocessing

The data recorded by the DAQ is translated using a database relating the channel number directly to a relative position for the bar as well as passing on the time of the hit. For this initial test beam there was no conversion possible from signal to deposited energy.

It was possible for the DAQ to return hits without a time stamp, which were removed before the analysis. Furthermore, events outside the time window with respect to the initial hit were also removed.

For this test beam, initial filters were used to try to remove possible pion contamination in the event, which produces a hadron shower, such as removing events where on average more than three hits were recorded for the same plane for an event.

Data was taken for a period of two months. Out of the recorded data, verified samples with the best possible settings for the data acquisition were selected for analysis. The samples contained a few hours worth of data taking at different beam momenta for both negative and positive muon beam settings. These samples were all run through the unpacking software required to read out the recorded data before being passed to SaRoMaN. The data was passed directly onto the digitisation for clustering and grouping before being passed into the reconstruction.

5.2.3 Analysis

For the first part of the analysis, the data sample was assumed to be quite clean, containing mostly only muons of either charge. To remove any contribution from outside of the beam, the hits in the TASD were used as a beam trigger to define a 125 ns beam time window after the trigger time within which to accept hits to be used to fit tracks. This time was chosen after carefully optimising the appropriate time to process the data from triggering and to combine hits from the different parts of the detector. To remove any potential showers or noise, any event with less than four hits in Baby MIND or on average more than 10 hits per plane were removed.

Data was run through the SaRoMaN software framework which produced plots of charge reconstruction efficiency and momentum reconstruction, and these were compared to simulations.

In the analysis it was also quite clear that the beam was not pure muons and contained some contamination of other particles. The main contamination seems to be pions. Thus, for a second pass of the analysis, a machine learning algorithm, using the TMVA software package [132] was used to perform particle identification to separate muon and pion events.

5.2.4 Test beam results

Three of the main results provided during the test beam were to commission the detector, showing that all hardware worked to specification, that the reconstruction software was able to reconstruct hits in all the modules and that the magnetisation scheme was able to be used successfully to reconstruct the particle momentum. Results will be presented showing that the detector has been commissioned and showing that the reconstruction framework can read in the data and produce charge and momentum estimates for the beam.

5.2.4.1 Electronics results

Gain plots for all of the 3996 MPPCs installed on Baby MIND are shown in figure 5.7. The gain is evenly distributed around 45 ADC counts per photoelectron, with a variation of ± 5 (figure 5.7, left). The gain variation can be further reduced by optimising the pre-amplifier gain on the FEB for each of the MPPCs. The calibration of the gain for each channel is achieved by fitting the photoelectron distribution for each MPPC to a number of single photoelectron peaks. This is known as the "finger plots", and can be seen in figure 5.7 (right). The average separation between peaks determines the ADC per photoelectron for each channel.

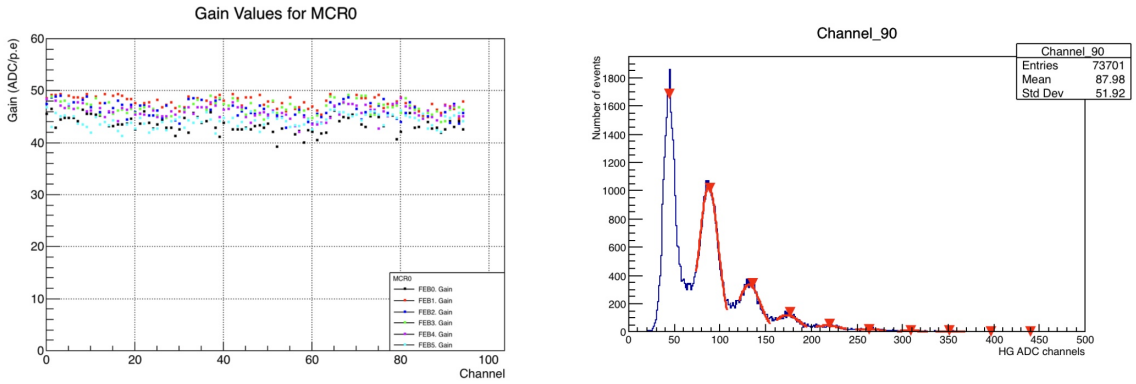

Figure 5.7: Gain for 576 channels (left) and noise spectrum finger plots with 5 viable peaks. for one channel (right). Figure courtesy of Aleksandr Mefodev.

5.2.4.2 Magnet results

The magnet performance was measured at CERN by the CERN magnet team led by Alexey Dudarev, with detailed tests on the first module allowing comparisons for verification of the simulations. The magnet modules reached the design specification of 1.5 T for a current of 140 A. Stray fields were measured at less than 10 mT at a distance of 1 mm from the surface of the magnet modules. The measured power consumption at CERN for the 33 magnet

modules was 11.5 kW. The current and voltage reach stable operating values after several hours, this can be seen in figure 5.8. The ARMCO steel was from three different batches, all with slightly different permeabilities. In the top figure of figure 5.8 measurements of the magnetic field when the coils are powered (B_max) is shown as well as the residual field when the current is off (B_res) for each of the batches. The bottom left figure shows the stability of the power supply when running and the bottom right figure shows how the voltage changes as a function of time due to heating of the coils for a fixed current of 140 A.

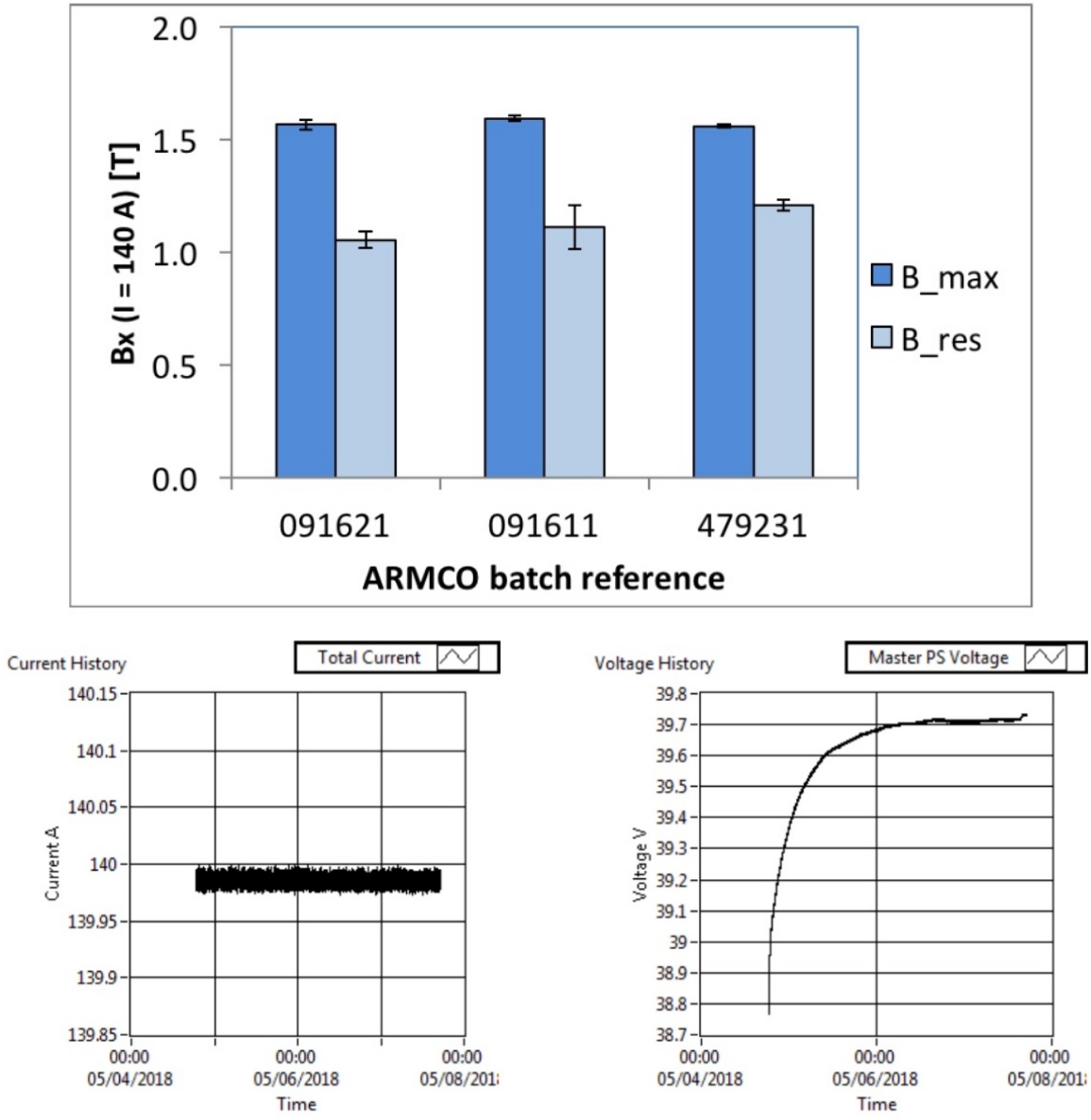

Figure 5.8: Baby MIND magnet measured (at CERN) with field values for 33 modules (top), power supply current (bottom left) and corresponding power supply voltage (bottom right). All of the ARMCO modules had a Bmax of 1.571 ± 0.023 T with the residual field varying between the module types as 1.13 ± 0.08 T. Figures, courtesy of Etam Noah.

5.2.4.3 Hits in SaRoMaN

Using the recorded data, the SaRoMaN reconstruction needed to be verified to see if it could combine the bar data into 3D space points. As can be seen in figure 5.9 the planes show hits along the length of each of the detector planes with no obvious missing hits and a similar filling of hits on all planes.

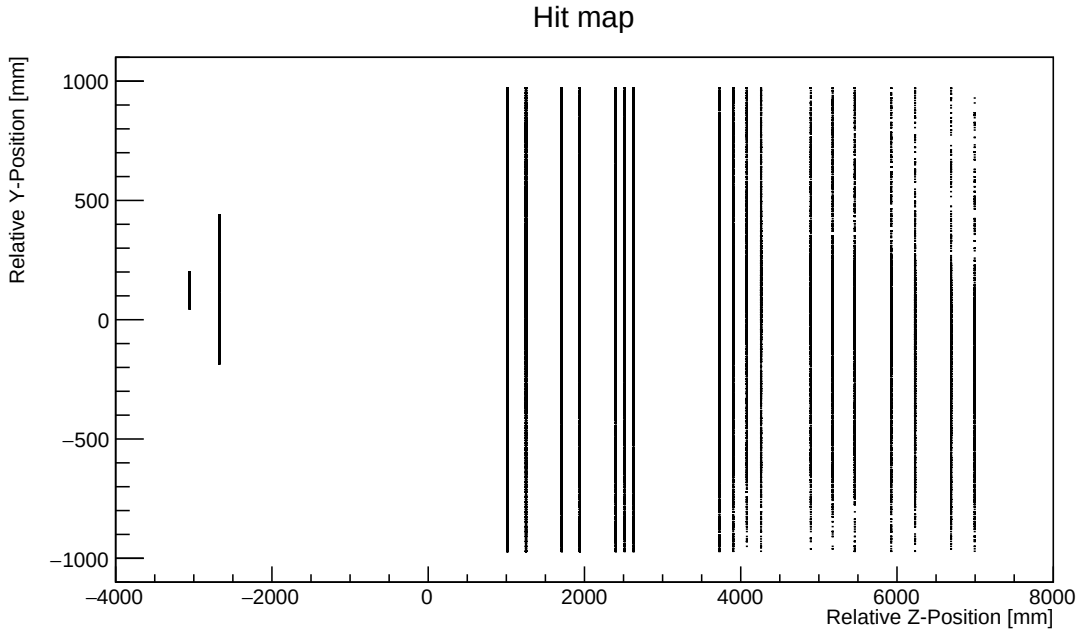

Figure 5.9: All recorded hits for both the two TASD planes and the Baby MIND planes for a run with the 5 GeV/c beam settings.

5.2.4.4 Tracks in SaRoMaN

In a similar way to simulated data, the collected hits are split depending on the time the hits were recorded to build possible tracks, seen in figure 5.10 and figure 5.11. Looking at the track in figure 5.10 and the top track of figure 5.11, it is clear that these look like clean tracks with little showering, with hits in almost all planes and hence they are probably muon tracks. The bottom track in figure 5.11 has a very clear showering pattern after the first three planes and is probably a showering pion. Each of these possible tracks are then filtered to produce the best possible fitted track for those points and some background or noise hits. This can become quite complicated if there are two tracks passing through simultaneously; however, this can be handed by the software even though this phenomenon is rare. Anothe issue is that the momentum may be incorrectly estimated if tracks are missing hits as the curvature will be incorrectly estimated. This means that the electronics efficiency affects the momentum estimate and needs to be studied further.

The main difficulty arises from the framework only being able to reconstruct tracks and not being able to reconstruct shower events. Any track reconstruction of a shower should fail, but sometimes it will attempt to reconstruct a shower as a track and return an incorrect charge and momentum value. This makes it clear that events containing showers need to be removed before any analysis is performed by using pattern recognition to identify showers (non-muons) from muons (non-showers).

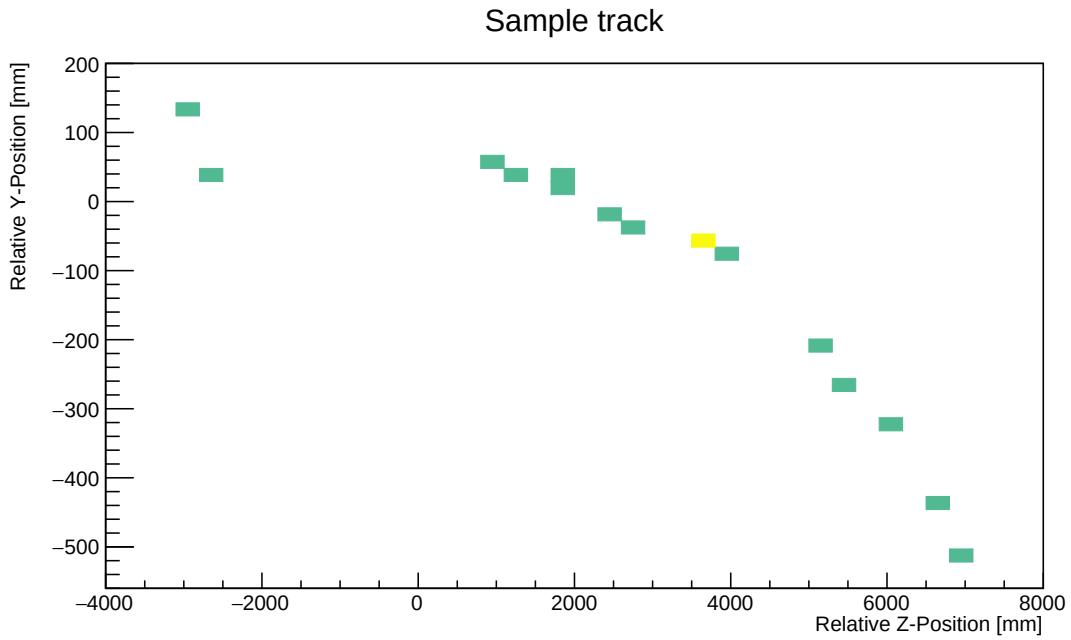

Figure 5.10: A sample track event from the test beam, taking a time cut for the hits for a run with the 5 GeV/c beam settings. Green represents 1 horizontal bar hit and yellow 2 horizontal bars hit within the same time window.

5.2.4.5 Charge identification efficiency

One of the main goals of the Baby MIND detector is to correctly identify the charge of incoming muons. In the test beam it is difficult to estimate the number of muons produced since the beam itself is a mix of mostly muons and pions. As seen above, the reconstruction software can return the number of track-like events against the number of reconstructible tracks. With these reconstructible tracks the charge can then be reconstructed and a charge identification efficiency can be calculated, as seen in figure 5.12. Initial results of this study were shown at NuFact2017 and published in [3].

These plots confirm that the full data analysis chain works, however the results show lower efficiencies than expected from simulations. Looking on an event-by-event basis it became clear that the events are a mix of muons and pions even after an initial pattern recognition to try and isolate muons. This motivated the development of a more advanced pattern recognition algorithm using machine learning. It can be seen that a simulated pion sample, figure

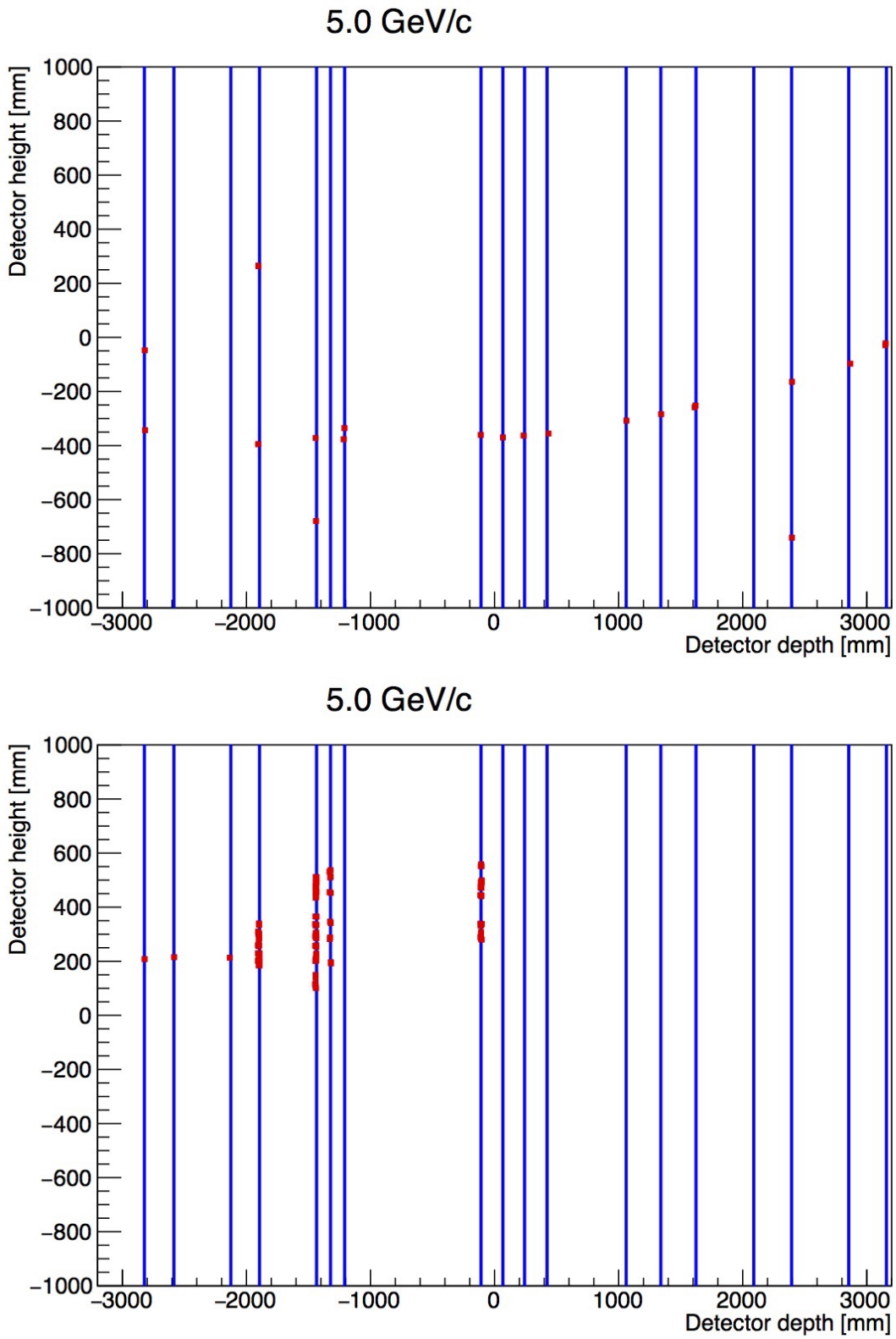

Figure 5.11: Sample events of test beam interactions at a set energy value of 5 GeV/c. The top figure shows a muon-like track and the bottom figure a shower and pion-like track.

5.13, will be very poorly reconstructed and can explain the difference between data and simulation in the mixed test beam. In this poor reconstruction the algorithm falls back to a

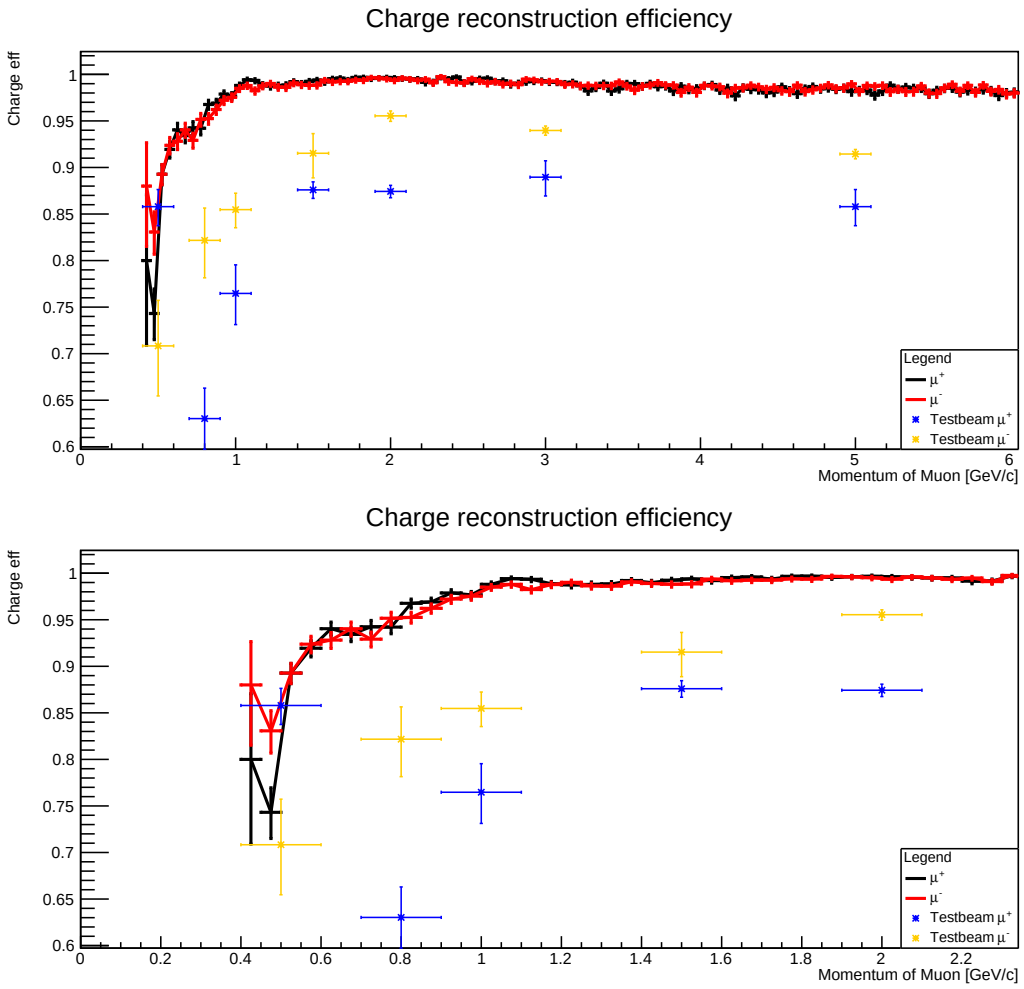

Figure 5.12: Initial charge reconstruction efficiency results for positive and negative muon-like tracks as a function of the nominal momentum of the test beam (the lower plot is just a zoom below 2.3 GeV/c of the top plot).

default estimate, thus over estimating negative charges for the pion samples.

It should be mentioned that for future runs the conversion between photoelectrons to deposited energy will be available and will make the distinction between pions and muons easier.

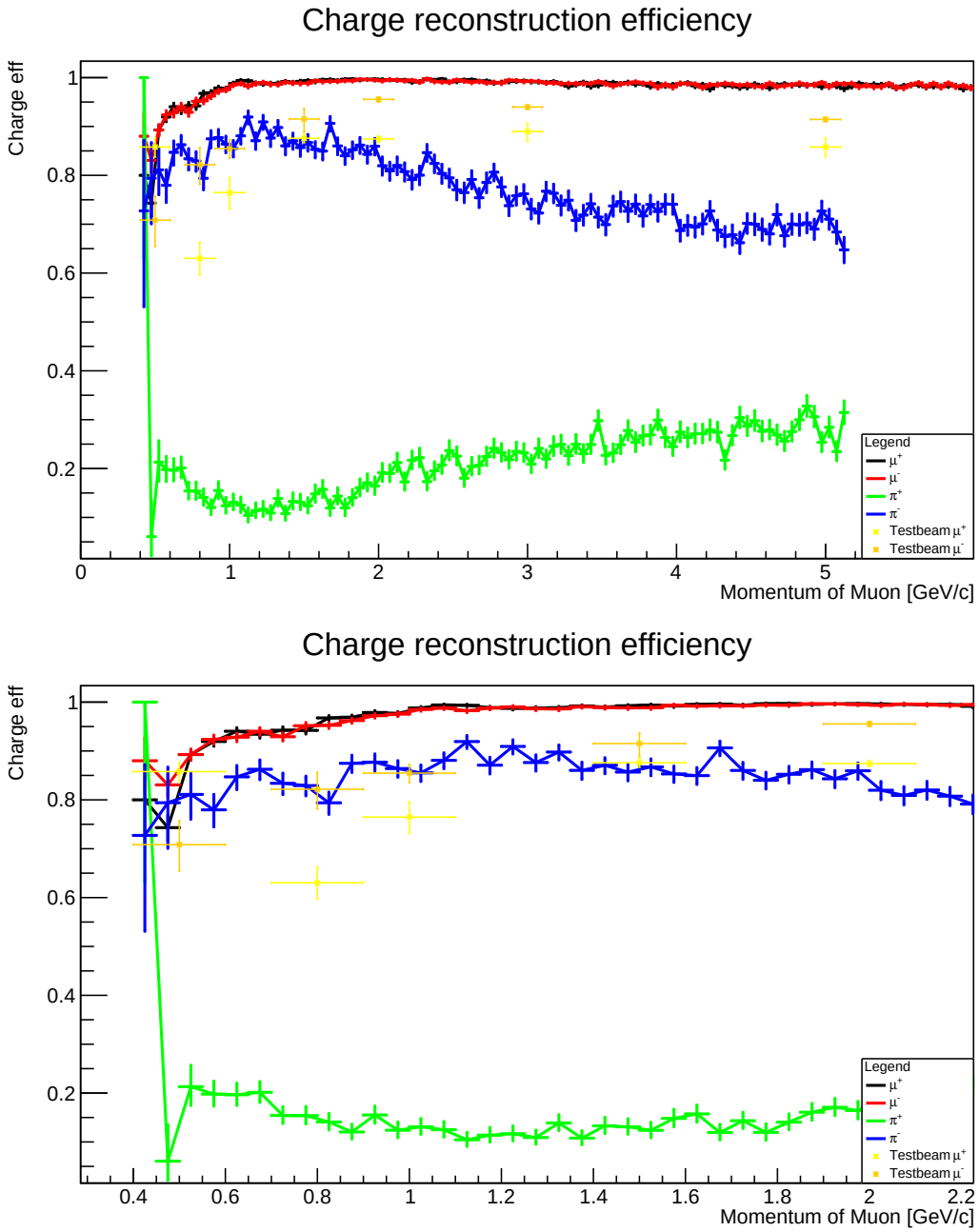

Figure 5.13: Simulated charge reconstruction efficiency results for positive and negative muons and pions as a function of the true momentum of the particle (the lower plot is just a zoom below 2.2 GeV/c of the top plot). The plots are based samples of between 1000 and 10000 events at each energy range.

5.2.4.6 Particle identification

To improve on the previous analysis of charge reconstruction efficiency, a particle identification algorithm was developed using TMVA [132] to classify muons from other events which may still pass through the selection criteria. The model has been developed to be independent of the momentum of the particle, and should be valid over the full momentum range being considered.

Essentially the machine learning algorithm identifies muons in a mixed background. The background particles are not currently identified as being a specific particle. This could be a future study and could be used to identify pions as well. The algorithm is designed to select muon events, so all other particles, such as pions and protons are considered to be background.

The main variables used in the model are the following:

- Number of total hits in the event (Hits),
- Number of used planes to perform the fit (uPlanes),
- Number of hits used in the fit divided by the number of used planes (HPPlanes),
- Average number of hits per plane (AvrHPlanes),
- Maximum distance between hits in an event divided by the distance between the first and last plane in the fit (RL).

The distributions of these variables for signal and background can be seen in figure 5.14 where no pre-selection or cuts have been made to the data before applying the TMVA.

Based on these simulated signal and background samples, TMVA provides a signal efficiency curve based on the various built-in machine learning models, seen in figure 5.15. In this plot is is clear that several models outperform others, however the multilayer perceptron model with a Bayesian Neural Network (MLPBNN) was chosen as the best performing model. The specific performance can be seen in figure 5.16.

Running through this model further it is possible to return the evaluation variable, known as the response, to see how signal and background are classified by TMVA. Figure 5.17 shows that signal and background can be separated and are understood by the algorithm, however there will always be some events which are incorrectly classified as signal or background. In the same figure it can be seen how data points have been added both by the training and testing sample to show that the algorithm has not been over-trained to work for only specific data.

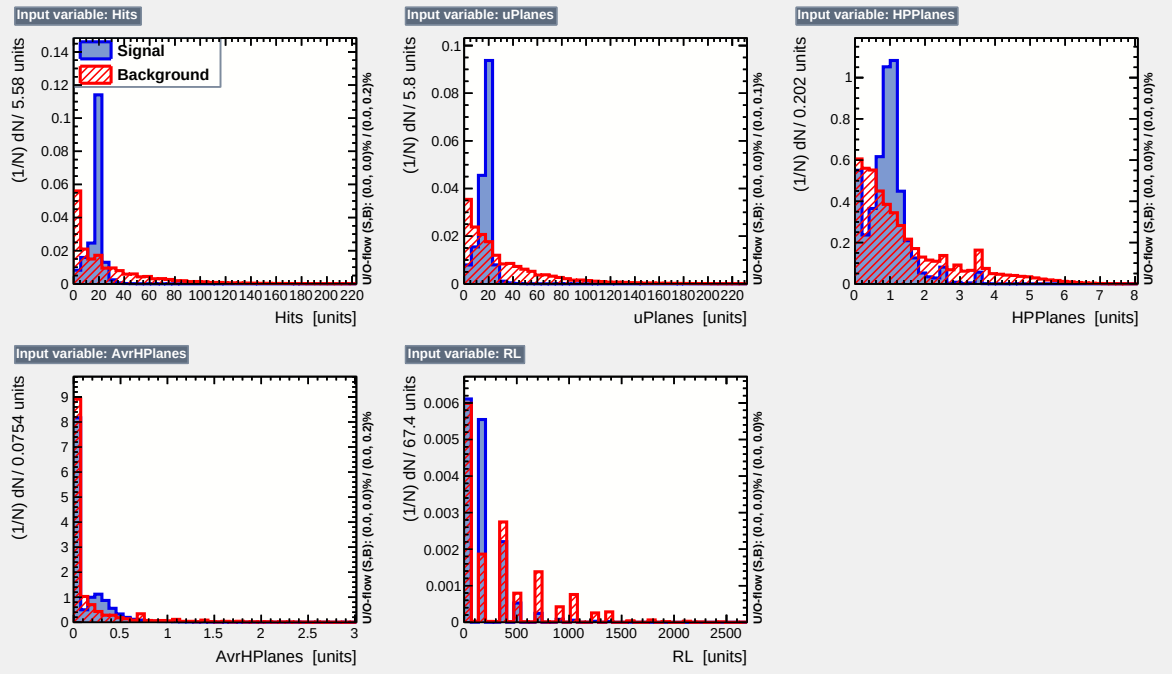

Figure 5.14: Input variables for both signal and background using simulated data.

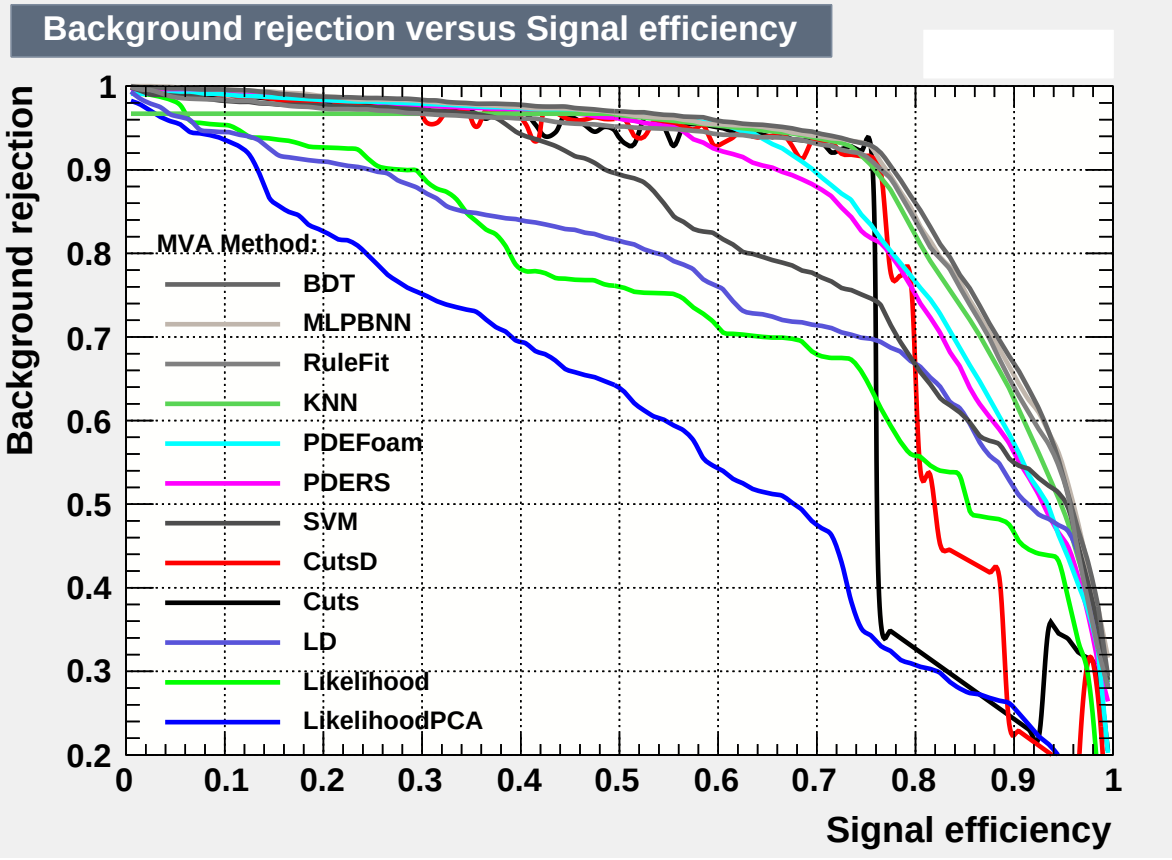

Figure 5.15: Receiver operating characteristic (ROC) curve for various machine learning algorithms.

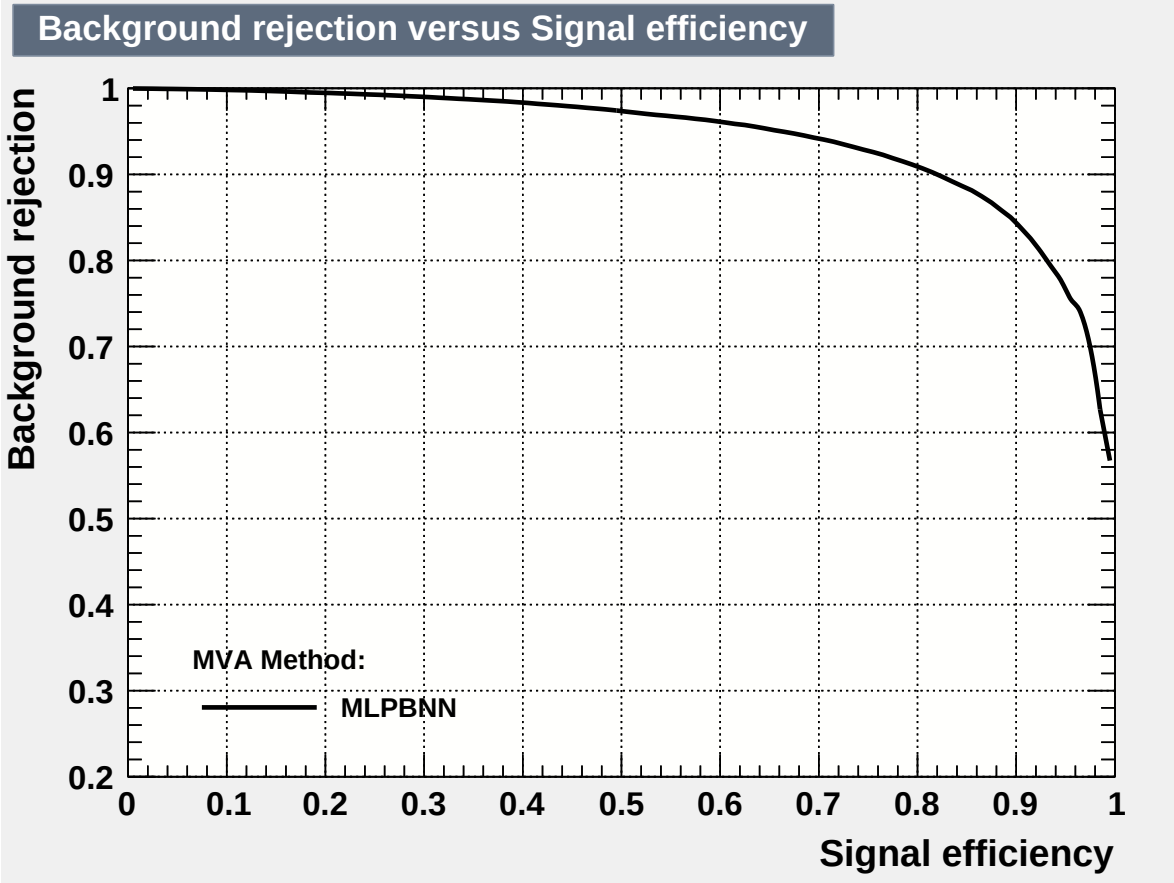

Figure 5.16: Receiver operating characteristic (ROC) curve for the chosen machine learning algorithms.

This translates directly into figure 5.18 showing what value of the response should be used to determine what is signal and background, providing a specific purity, efficiency and significance. The significance is chosen as the possibility to see a signal over the background as $S/\sqrt{S+B}$, where S is the number of signal events and B is the number of background events, which is a figure-of-merit that is often used in particle physics. For this analysis purity is of the most interest as the end goal is to return a data sample with as clean a muon sample as possible. Thus the cut value is chosen as the maximum sensitivity = 0.42, as seen in figure 5.18, and provides 92.3 % of the signal to pass through in a pure sample of signal events and only 11.3 % of background events in a pure background event sample.

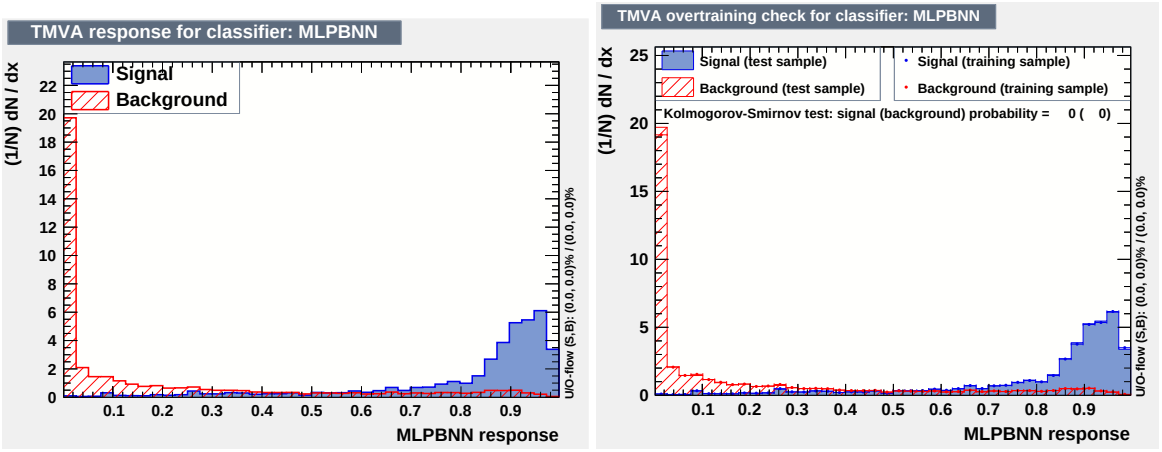

Figure 5.17: Response with and without a check for over-training.

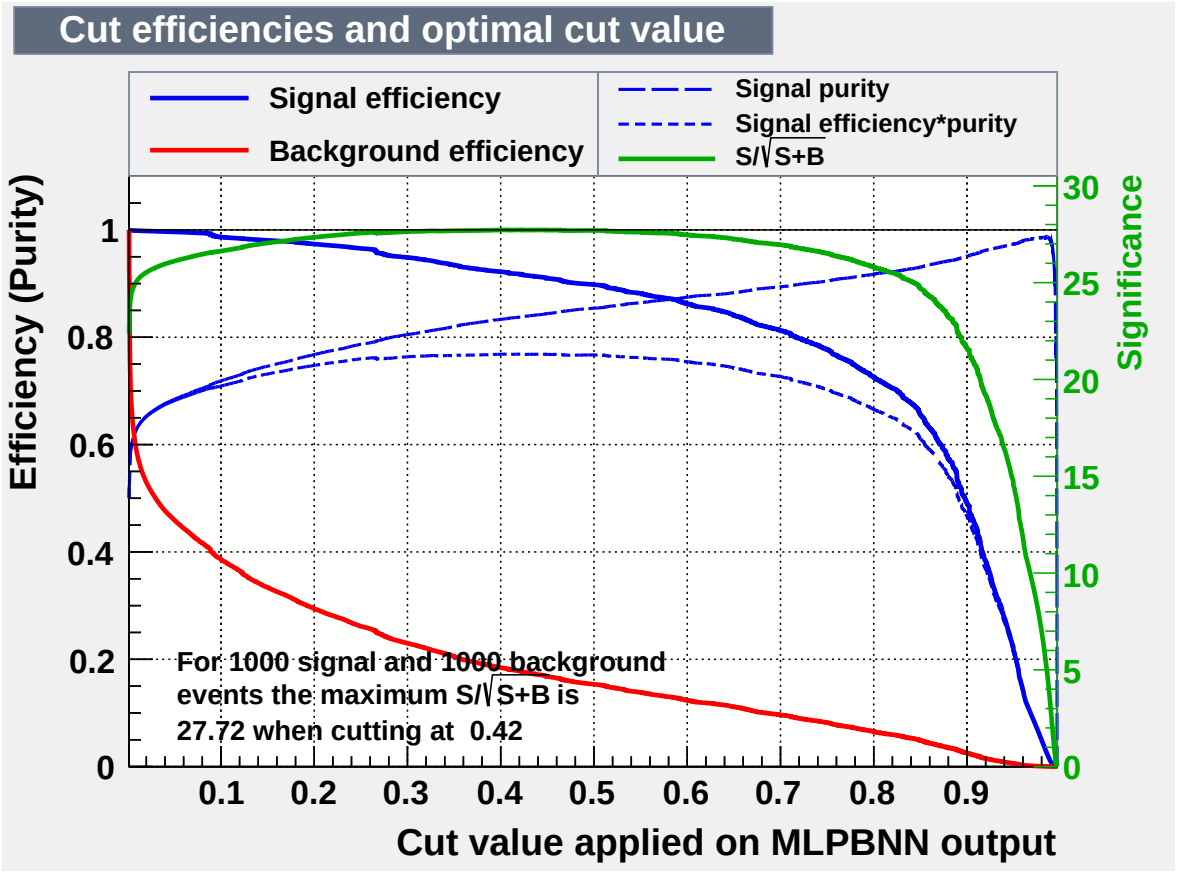

Figure 5.18: Cut efficiency plots.

5.2.4.7 Updated charge identification efficiency

Using the final cleaned sample, with a 81.8% purity, provides the final charge estimates as seen in figure 5.19.

This finally shows that even after improving the purity of the beam to muons to 81.8% there is a discrepancy between the charge reconstruction efficiency of the simulation and the data. This discrepancy is probably due to differences in reconstruction efficiency in real events, due to inefficiencies in the data collection leading to missing hitpoints and shorter fitted tracks, due to the electronics or some timing mismatches between the events. It should also be noted that the momentum values for the data are taken as the momentum selection set by the quadrupole magnets in the beam, which may not yield an accurate momentum value. For instance this may have been an overestimate shifting all data points to the right, where as the real momentum would shift them back to lower momenta. This will require further study and potentially simulations of the entire beamline.

The plots show the potential of using the Baby MIND detector for muon charge reconstruction at lower momenta than had previously been achieved. This is due to the modular nature and careful layout of the detector, with three magnetic modules upstream to perform an initial bend of the particles and gaps between measuring scintillator planes to perform the measurement of the bend. It also shows that for the test beam it was possible to attain a charge identification efficiency of over 70% for the full momentum range (above 400 MeV/c) and above 85% for muons above 1 GeV/c.

5.3 Summary

From the test beam results, it has been shown that the Baby MIND full detector performs as expected and can achieve a high charge reconstruction efficiency for particles with momenta above 400 MeV/c. The electronics and readout systems work within expectation, and the reconstruction programme SaRoMaN can perform reconstruction of tracks, showing that reconstruction of tracks is possible for muons at low momentum. The results show that the Baby MIND detector is ready to be integrated into the WAGASCI experiment as a magnetic spectrometer in the J-PARC neutrino beam.

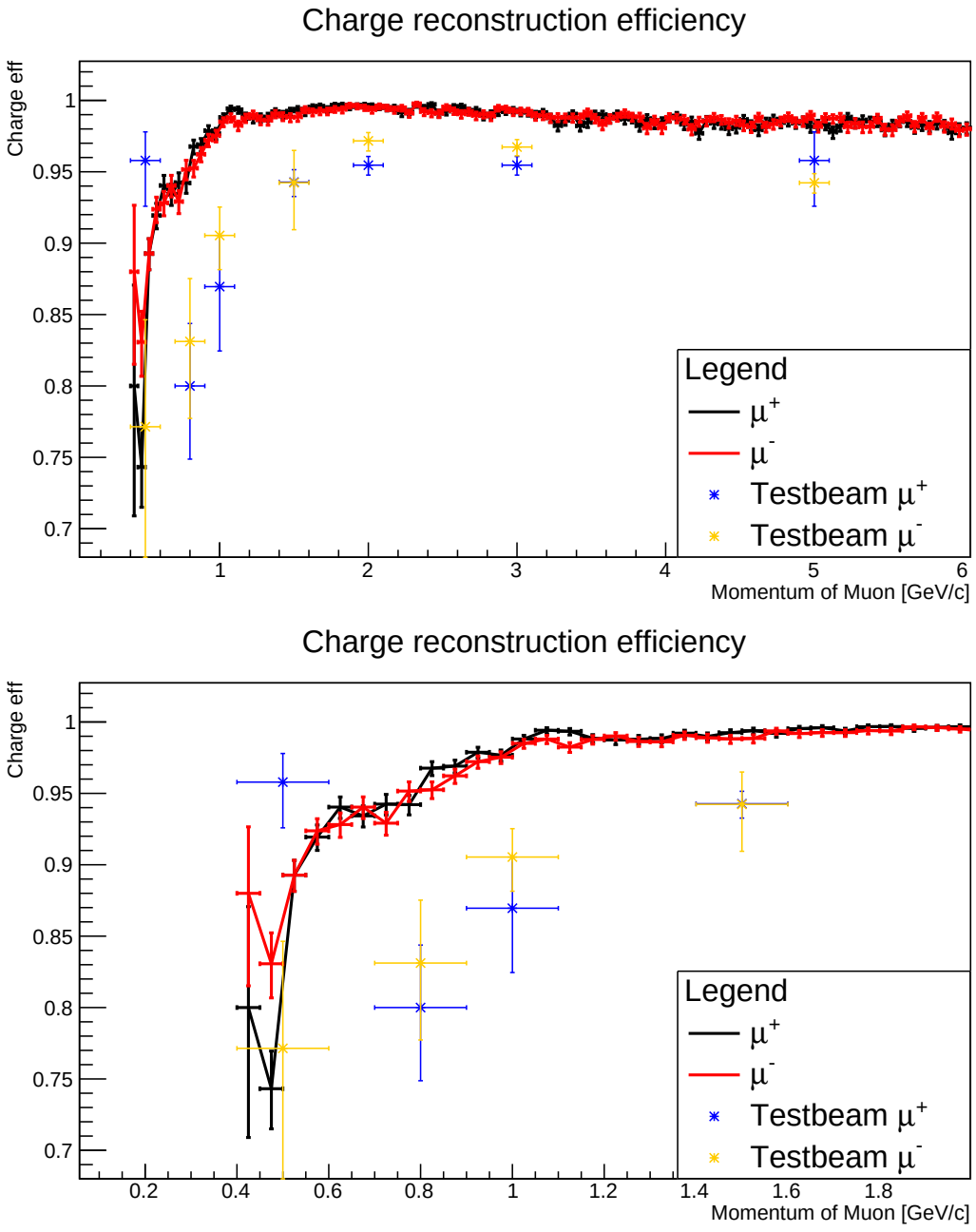

Figure 5.19: Charge reconstruction efficiency plots after adopting the TMVA particle identification algorithm to select a pure sample of muons. The bottom plot is a zoom version of the top plot, with momentum below 2 GeV/c. The discrepancy in rise between data and simulation may be attributed to the difference between known simulated muon momenta and that muon momenta in data is estimated from the beam parameters which may not have been correctly calibrated.

Chapter 6

NuSTORM beam neutrino interaction studies

The Baby MIND detector was built to reconstruct muon tracks passing through the detector. This makes it ideal to be used for muon neutrino reconstruction with an appropriate target. As discussed in subsection 1.4 there are a few interactions which produce a free muon which can then be reconstructed with the Baby MIND. These are the muon neutrino charged current interactions, quasi-elastic (QE) charged current (CC) interactions, deep inelastic scattering (DIS) and resonant single pion interactions (RES) each at various energy ranges as can be seen in figures 6.1 and in 6.2.

The signature for each of these interactions is quite different, as a charged current quasi-elastic interaction will produce a clean proton and muon track, compared to a shower-like pion track or the less clear DIS signature. Baby MIND is designed to operate at a lower energy spectrum, below 5 GeV, meaning that the contribution will be mostly from CCQE and pion interactions. Results from various simulations with the T2K near detector beam spectrum and data recorded from the commissioning will be shown.

6.1 Muon charged current quasi-elastic interactions

Charged current quasi-elastic (CCQE) interactions produce a clear muon track for both neutrinos and antineutrinos, however the interaction only produces a proton track for neutrino interactions as seen below:

$$\nu_\mu + n \rightarrow \mu^- + p \tag{6.1}$$

$$\bar{\nu_\mu} + p \rightarrow \mu^+ + n \tag{6.2}$$

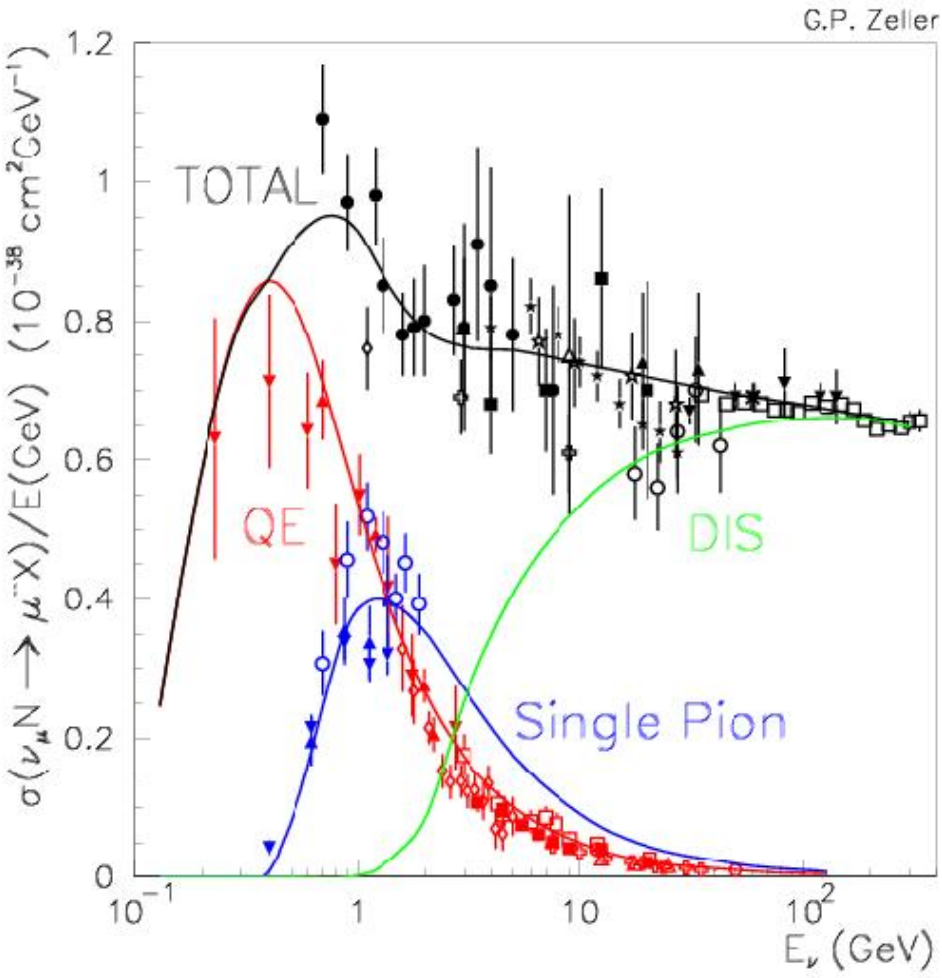

Figure 6.1: Neutrino cross sections, showing the quasi-elastic, deep inelastic and single pion cross sections in the GeV range. Taken from [135], and is modified from the original made by G.P. Zeller [136], containing data points from various experiments.

For the neutrino interactions, this becomes a very clear signature in a fully active target where both a muon and proton track can be identified. For antineutrinos this is not possible since neutron tracks are usually not detectable for most detector types. There have been a lot of interesting articles relating to how to identify neutrino events in argon detectors using machine learning [138] [139]. In a non-active target it becomes very difficult to identify neutrino interactions as pions may decay to muons or they may interact in the material and become indistinguishable from directly produced muons.

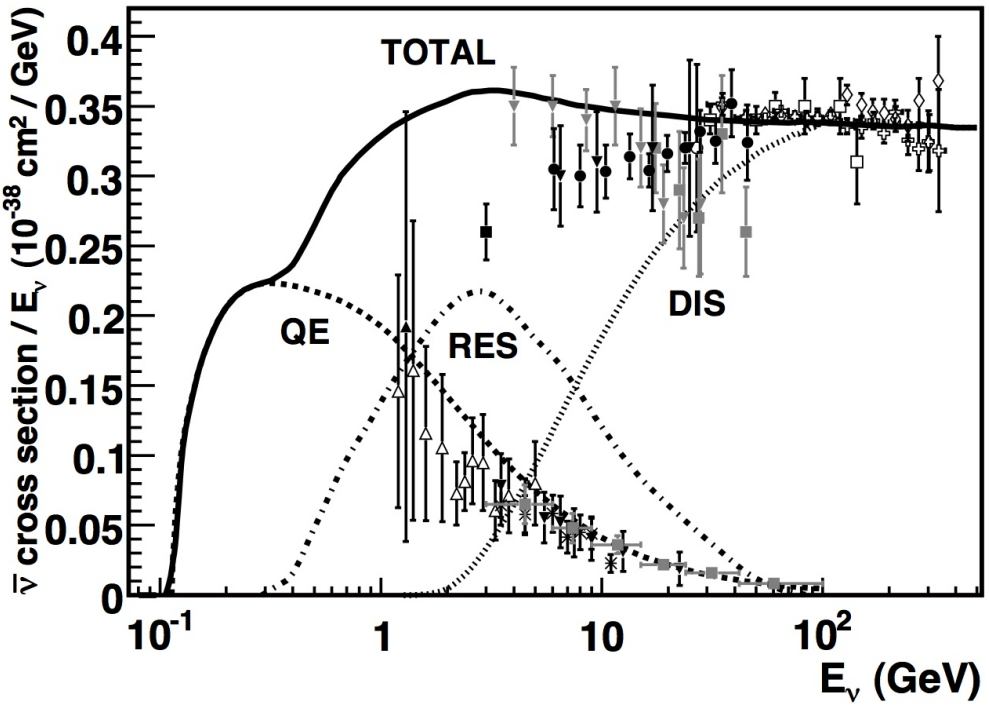

Figure 6.2: Antineutrino cross sections, showing the quasi-elastic, deep inelastic and single pion cross sections in the GeV range [137].

6.2 Neutrino interactions in a TASD and Baby MIND configuration with a NuSTORM beam

As described in subsection 2.7.1, a first stage towards a neutrino factory would contain a storage ring for neutrino and antineutrino production from muon decay. From a muon decay both muon and electron anti-neutrinos will be produced at $\approx 100\%$. In order to evaluate the sensitivity of NuSTORM to the study of neutrino interactions, the TASD and Baby MIND were used as a near detector to measure the interaction type and reconstruction of muon tracks. The main purpose of the study is to see if it is possible to identify muon neutrino CCQE interactions and distinguish them from a background of neutral current interactions and electron anti-neutrino charged current interactions. This study was performed using a TMVA trained algorithm with simulated samples. As part of this study the fitted efficiency and charge identification efficiency of negative and positive muon tracks produced by simulated muon neutrinos and antineutrinos in Baby MIND are shown.

The NuSTORM neutrino energy spectrum from the decay of μ^- has been simulated as can be seen in figure 6.3 for both muon neutrinos and electron anti-neutrinos. This is the spectrum of neutrino flavours observed in a detector at a distance of 50 m from the end of the NuSTORM straight section (as shown in figure 2.40). The main job for any detector will be to identify if the neutrino event is produced from either a ν_μ CC interaction, producing a μ^-, or from

a $\bar{\nu}_e$ interaction, which produces positrons, as well as dealing with the neutral current (NC) background from all neutrinos.

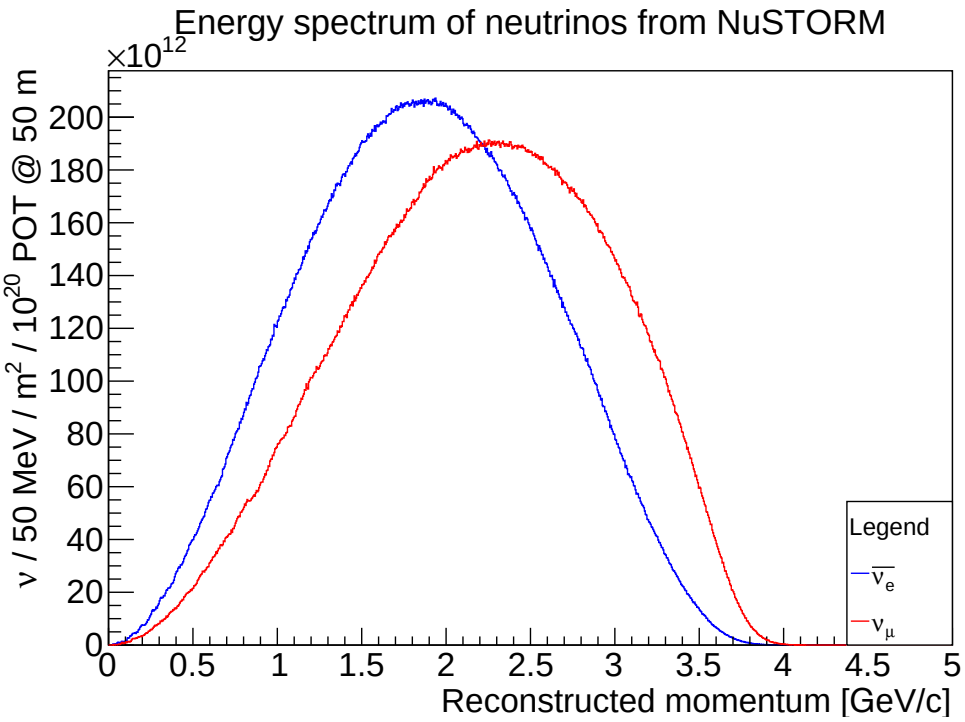

Figure 6.3: Energy spectrum of muon neutrinos and electron anti-neutrinos produced at NuSTORM and recorded at 50 m from the storage ring.

During the construction of Baby MIND, it was proposed to fully instrument the whole TASD, used during the first beam test, and use it as a fully active target to be combined with Baby MIND, illustrated in figure 6.4. This could become a setup for a NuSTORM detector.

Using the SAURON framework, 10^5 muon neutrinos and muon antineutrinos were simulated using the NuSTORM energy spectrum and reconstructed to provide the figures of merit presented below. In figure 6.5 the reconstruction efficiency is presented, figure 6.6 shows the charge efficiency and finally figure 6.7 shows these two multiplied. Each of the plots show different metrics to evaluate the SAURON framework and the detector performance. The reconstruction efficiency is defined as the ratio of reconstructible tracks divided by all the simulated tracks. The charge efficiency is defined as how many of the reconstructible tracks are reconstructed with the correct charge. Multiplying these two results gives the ratio of reconstructed tracks with the correct charge divided by all simulated tracks.

Similarly to the studies carried out in chapter 5 for single muons in the CERN test beam, the charge reconstruction efficiency of muons from neutrino charged current interactions, using the NuSTORM beam, is very high, even at low momenta. The main difference arises from the fact that the neutrinos are produced over a range of angles with respect to the neutrino direction instead of straight on the center of the detector (with some beam size). Muons

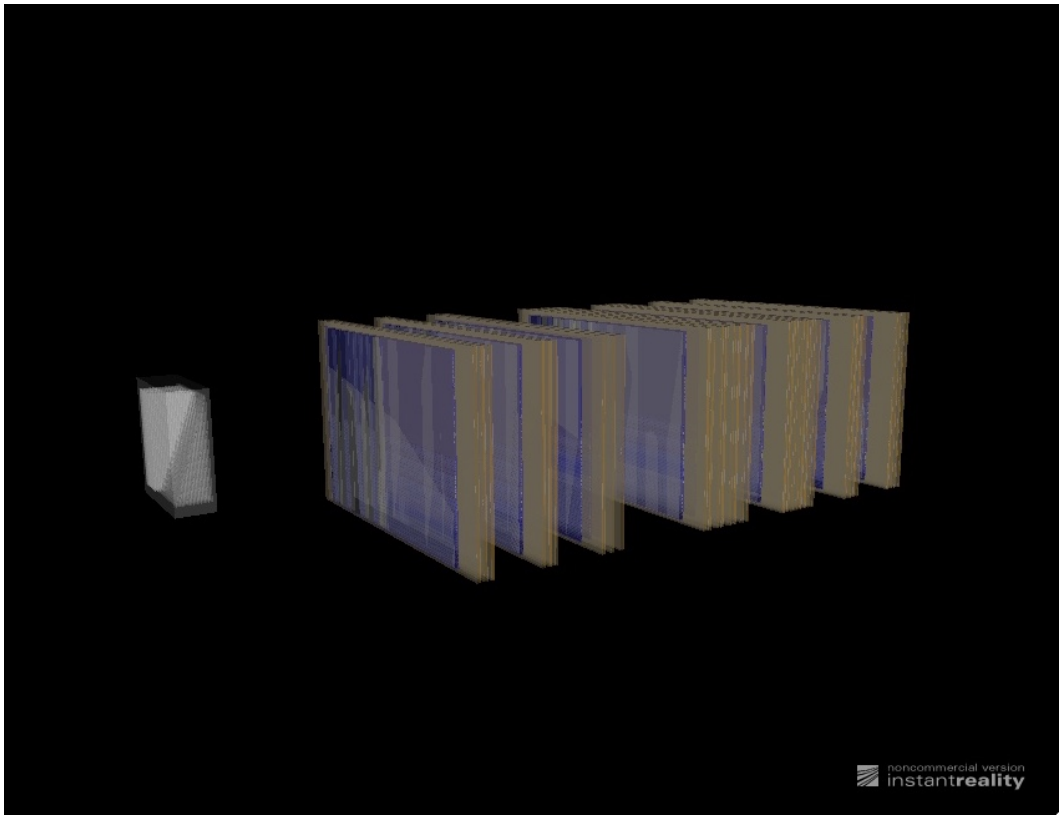

Figure 6.4: An illustrative sketch of the detector setup with the TASD detector in front of Baby MIND.

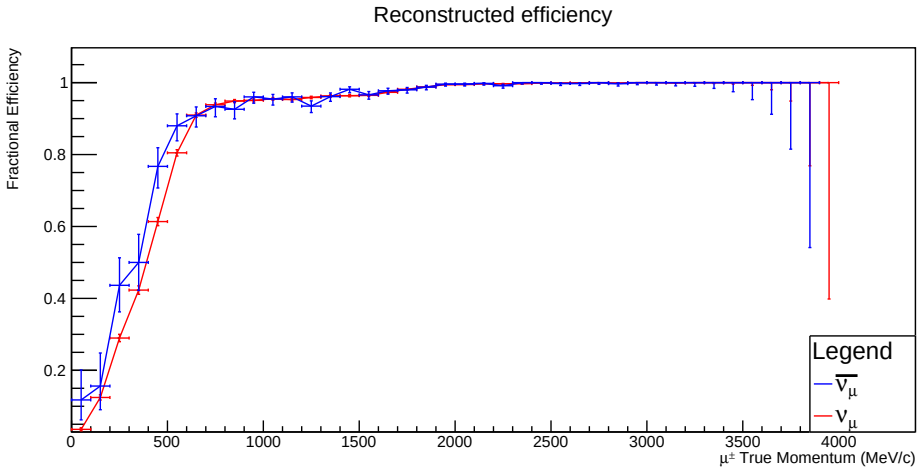

Figure 6.5: The efficiency plot of how well the SAURON algorithm can reconstruct muon tracks from neutrino interactions simulated with the NuSTORM beam as a function of muon momenta.

from neutrinos are produced at different angles depending on the kinematics of the neutrino interaction and neutrino energy.

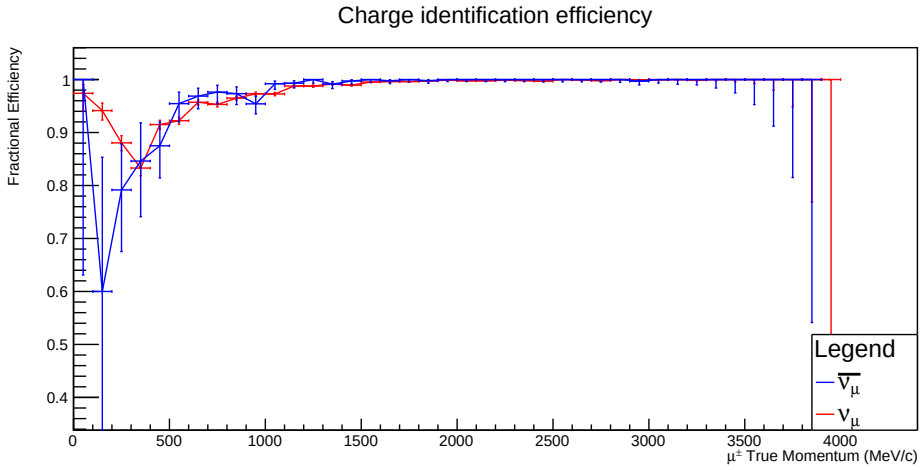

Figure 6.6: The efficiency plot of how well the SAURON algorithm can reconstruct the charge from reconstructed muon tracks from neutrino interactions simulated with the NuSTORM beam as a function of muon momenta.

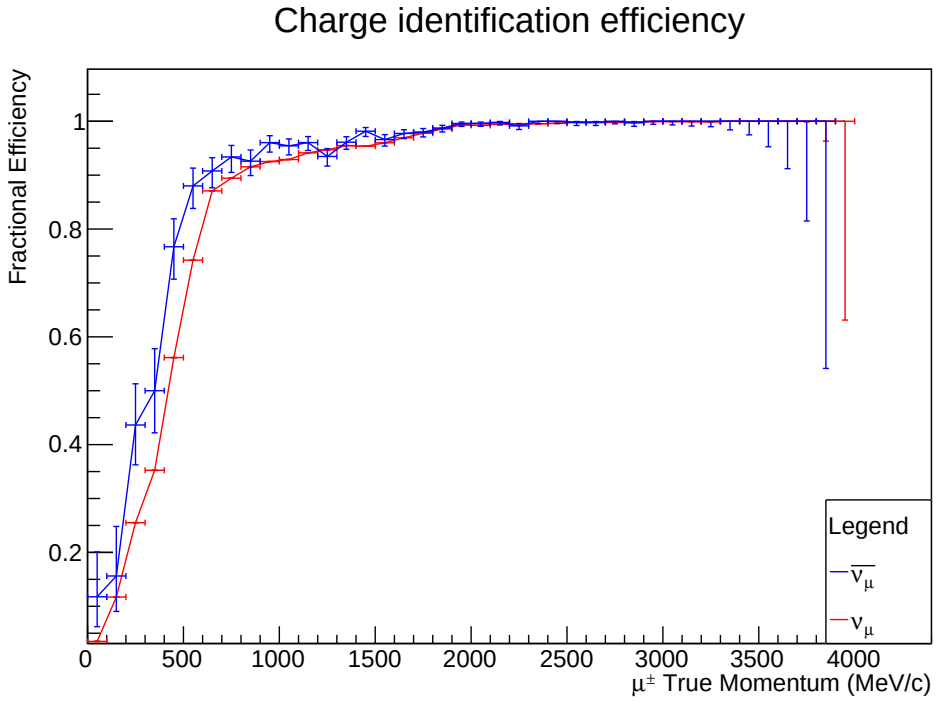

Figure 6.7: The efficiency plot of how well the SAURON algorithm can reconstruct the charge from muon tracks with respect to all the simulated neutrino interactions with the NuSTORM beam as a function of muon momenta. This plot is the multiplication of the efficiencies in figure 6.5 and figure 6.6.

6.3 Neutrino event selection from the NuSTORM beam

The NuSTORM beam produces ν_μ and $\bar{\nu}_e$ neutrinos from the decay of muons, $\mu^- \rightarrow e^- + \nu_\mu + \bar{\nu}_e$ according to the energy distribution in figure 6.3. These neutrinos can produce both CC and NC events in the TASD in front of Baby MIND. It is important to separate the ν_μ CCQE interactions from the NC and $\bar{\nu}_e$ background to perform analysis of CCQE events. A machine learning multi-variate analysis was carried out to perform the event selection, using the TMVA package. The variables used to populate the TMVA algorithm are similar to the particle identification study carried out in chapter 5.

The main variables used in the model are the following:

- Track length for distance between first and last hits in an event (MC_ track_ len),
- Angle of the track compared to the z-axis that defines the length of the detector (MC_ angle),
- Number of total hits in the event (NumberofHits),
- Number of planes hit (NumberofPlanes),
- Average number of hits per plane (AvrHitsPerPlane).

The distributions of these variables for signal and background can be seen in figure 6.8.

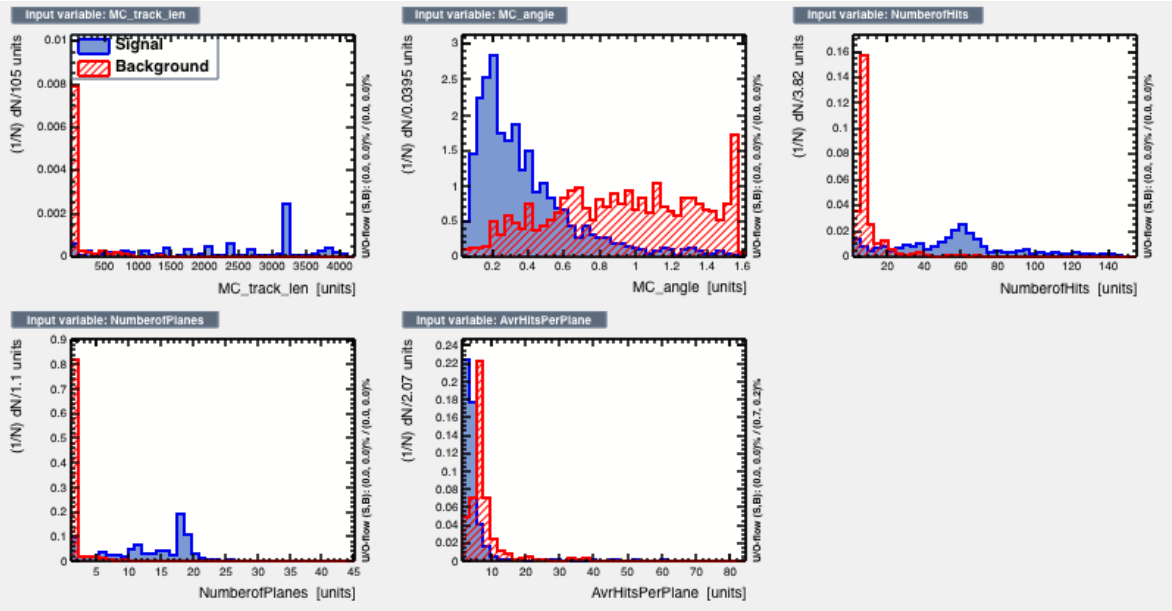

Figure 6.8: Input variables for both signal and background using simulated data.

Based on these simulated signal and background samples, TMVA provides a signal efficiency curve based on the various built-in machine learning models, seen in figure 6.9. In this plot is is clear that several models outperform others; however, the multilayer perceptron with a Bayesian Neural Network (MLPBNN) was chosen as the best performing model. The MLPBNN response can be seen in figure 6.10 and shows a clear distinction between signal and background samples. It is quite clear that any cut between these two distinct peaks will produce the desired outcome, this is plotted in figure 6.11. For this study the significance is chosen as the possibility to see a signal over the background as $S/\sqrt{S+B}$, where S is the number of signal events and B is the number of background events, which is a figure-of-merit often used in particle physics. The background is chosen to be close to the estimated interaction probability. For 1000 ν_μ CC signal events, there are 1000 $\bar{\nu}_e$ CC events and 333 ν_μ NC events and 333 $\bar{\nu}_e$ NC events. This provides a total of 1666 background events for 1000 signal events.

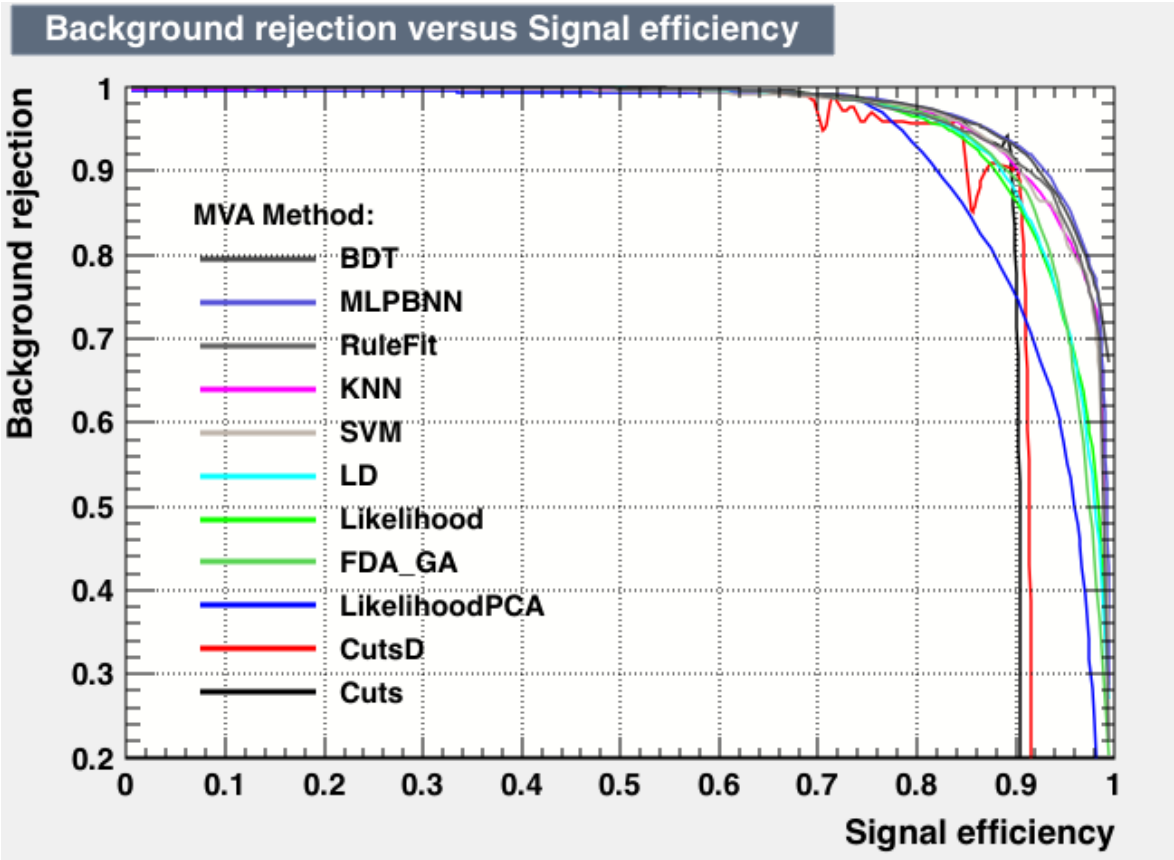

Figure 6.9: Receiver operating characteristic (ROC) curve for various machine learning algorithms. The best method was the MLPBNN however many of the methods gave similar, but only slightly worse, results.

With this trained algorithm the best possible cut value (0.50) allows 91% of the signal events to pass, and only accepts 7.6% of the background.

As with the previous study, this analysis is performed independently of neutrino energy

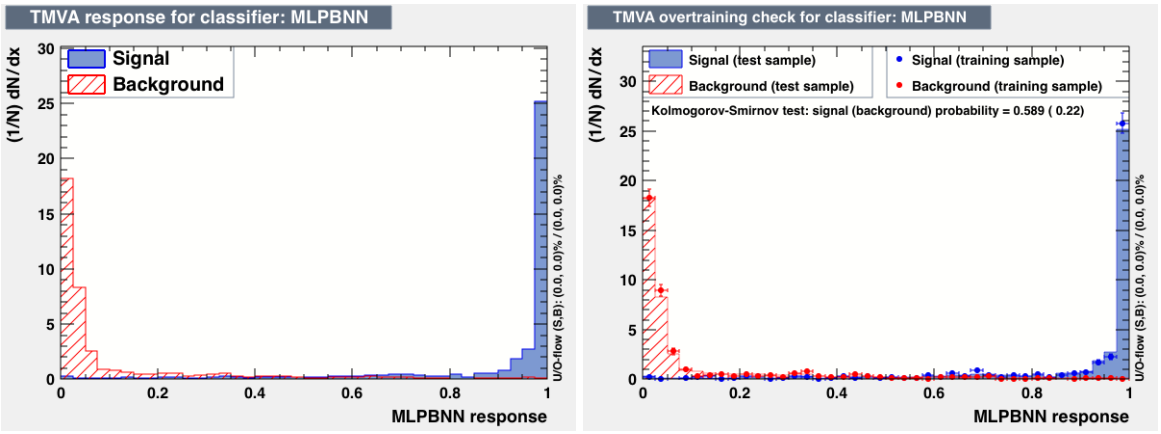

Figure 6.10: Response with and without over-training check.

values. The estimated neutrino energy, through for instance energy deposited into the scintillating bars in the detector, could be used as an extra variable in the TMVA study and could possibly provide improved cuts.

Applying the TMVA algorithm to a mixed sample of electron neutrinos and muon neutrinos produces the neutrino energy spectrum seen in figure 6.13 with the initial spectrum seen in figure 6.12 providing a signal efficiency of 84%.

6.4 Expected neutrino scattering results at the NuSTORM beam

Using the table of event rates for 10^{21} protons-on-target (POT) estimated for a 100 ton detector 50 m from the nuSTORM storage ring discussed in [140] the spectra in figures 6.12 and 6.13 can be converted to number of events. In NuSTORM the following events are expected: 6.1×10^6 ν_μ CC events, 2.5×10^6 $\bar{\nu}_e$ CC events, 2.1×10^6 ν_μ NC events and 1.0×10^6 $\bar{\nu}_e$ NC events in a 100 ton detector for 10^{21} POT. The numbers used were reduced by a factor of 10 to provide an estimate for a 10 ton detector and the final result can be seen in figures 6.14 and 6.15.

The result of the TMVA can be combined to estimate the total statistical and systematic error on the cross-section measurement possible in a NuSTORM beam line.

The CC inclusive cross section is given by the subtraction of the total background from the signal, and dividing by the neutrino flux and the total number of nucleons in the detector. The estimated uncertainty is given by the quadratic sum of the errors for the signal and the total background. By defining the following operation, $a \oplus b = \sqrt{a^2 + b^2}$ and generalising it as $\bigoplus x_i \equiv \sqrt{\sum x_i^2}$, the error is defined through combining each error as $\sigma_{\nu_{\mu CC}} \oplus \sigma_{\bar{\nu}_{eCC}} \oplus \sigma_{\nu_{NC}}$. Using this error estimate combined with the cross-section values from figure 6.1 results in

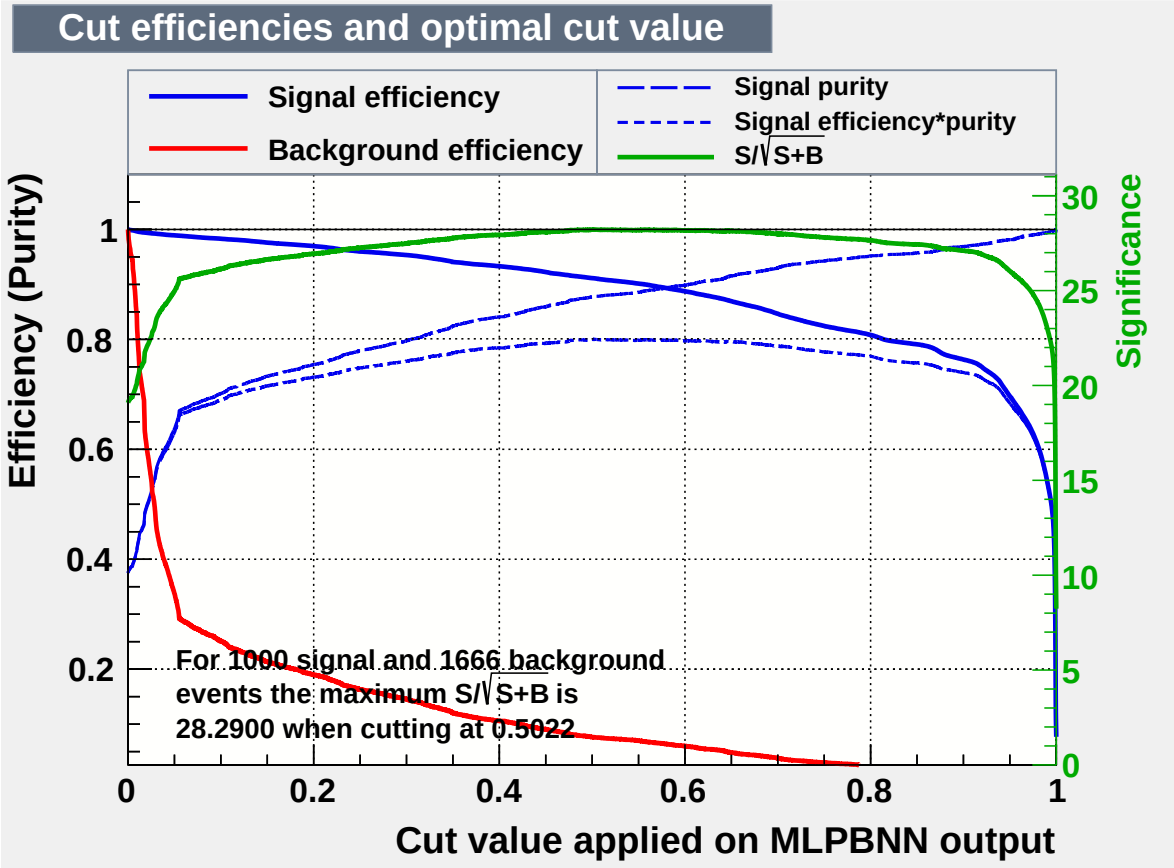

Figure 6.11: Cut efficiency plots expecting the combined background of $\bar{\nu}_{eCC}$ to be at the same number as the signal ($\nu_{\mu_{CC}}$) and $\nu_{\mu_{NC}}$ to be approximately $\frac{2}{3}$ of the number of signal events.

the determination of the ν_μ inclusive CC cross section, as shown in figure 6.16 with the estimated measurement errors included.

The results show that it is possible to measure the neutrino inclusive CC cross section with small statistical errors (of order 3% per bin), for a 10 ton detector in the NuSTORM beam at 10^{21} POT. These errors would decrease with a larger detector mass as well as with more protons on target.

6.5 Summary

From the NuSTORM study carried out in this chapter, a detector configuration consisting of a Totally Active Scintillator Detector (TASD) with a Baby MIND spectrometer downstream would be able to provide charge reconstruction of tracks down to 400 GeV/c with the possibility to identify and distinguish between the $\nu_{\mu_{CC}}$ signal in a background of $\bar{\nu}_{eCC}$, $\nu_{\mu NC}$ and $\bar{\nu}_{eNC}$ from the NuSTORM beam with 84% efficiency and contamination of 7.4%.

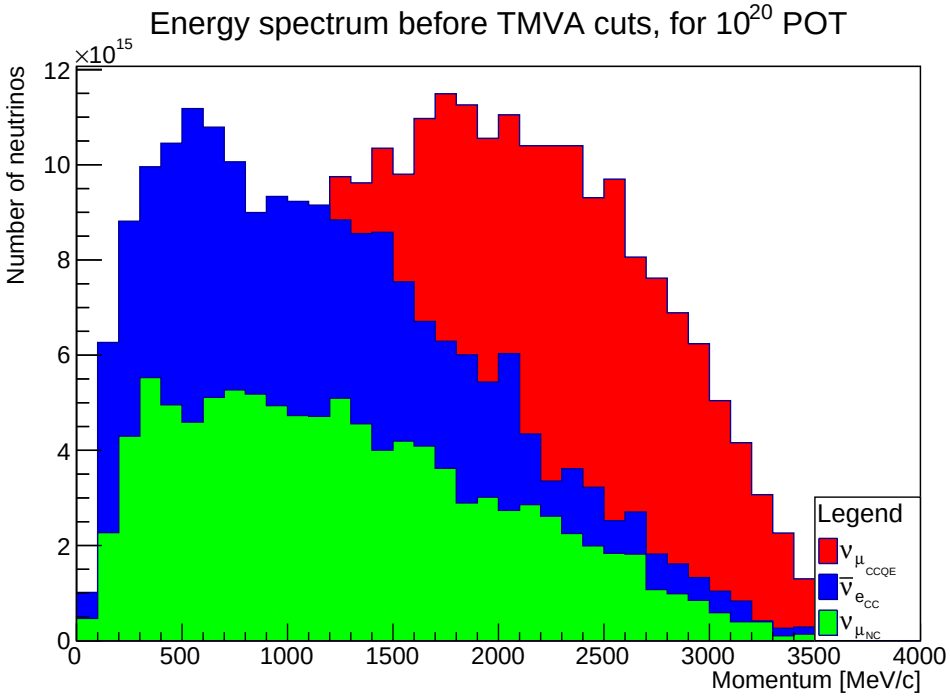

Figure 6.12: Neutrino energy spectrum of $\bar{\nu}_{eCC}$, $\nu_{\mu_{CC}}$ and $\nu_{\mu_{NC}}$ produced from 10^{20} protons-on-target (POT), before passing through the TMVA algorithm.

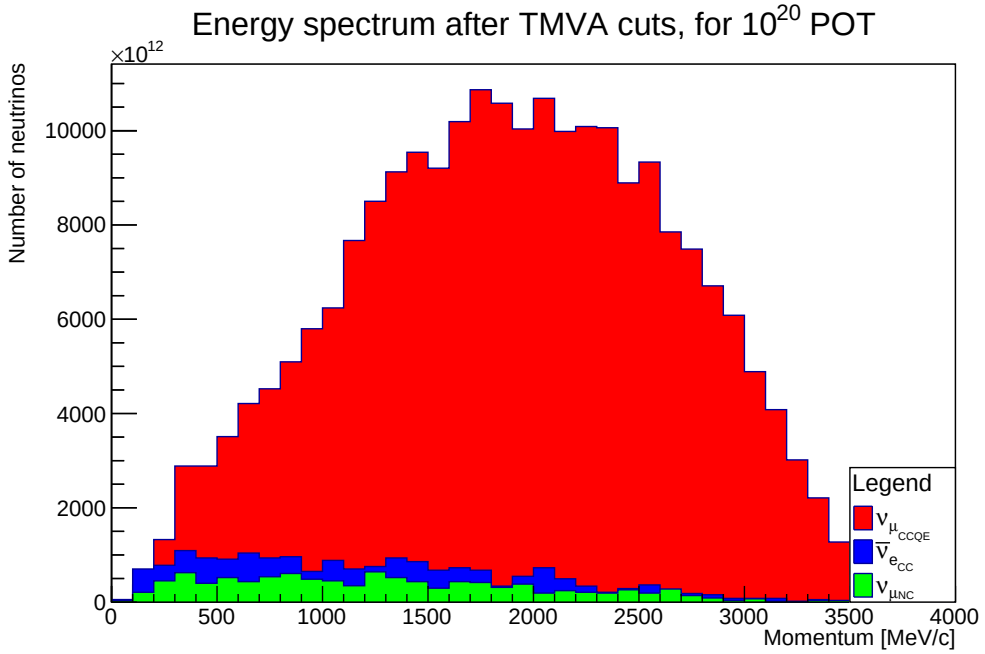

Figure 6.13: Neutrino energy spectrum of $\bar{\nu}_{eCC}$, $\nu_{\mu_{CC}}$and $\nu_{\mu_{NC}}$ produced from 10^{20} protons-on-target (POT), after passing through the TMVA algorithm.

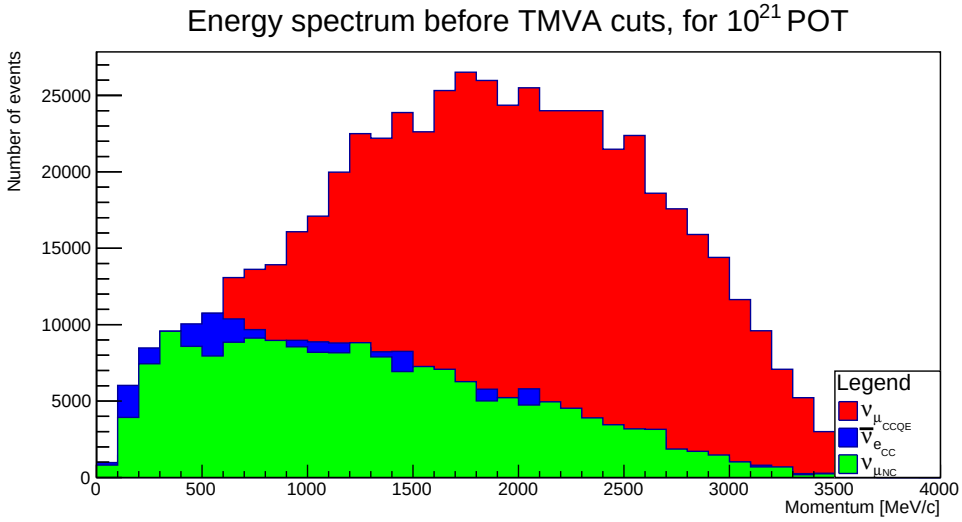

Figure 6.14: Neutrino energy spectrum of $\bar{\nu}_{eCC}$, $\nu_{\mu_{CC}}$ and $\nu_{\mu_{NC}}$ recorded from 10^{21} protons-on-target (POT) in a 10 ton detector at 50 m, before passing through the TMVA algorithm.

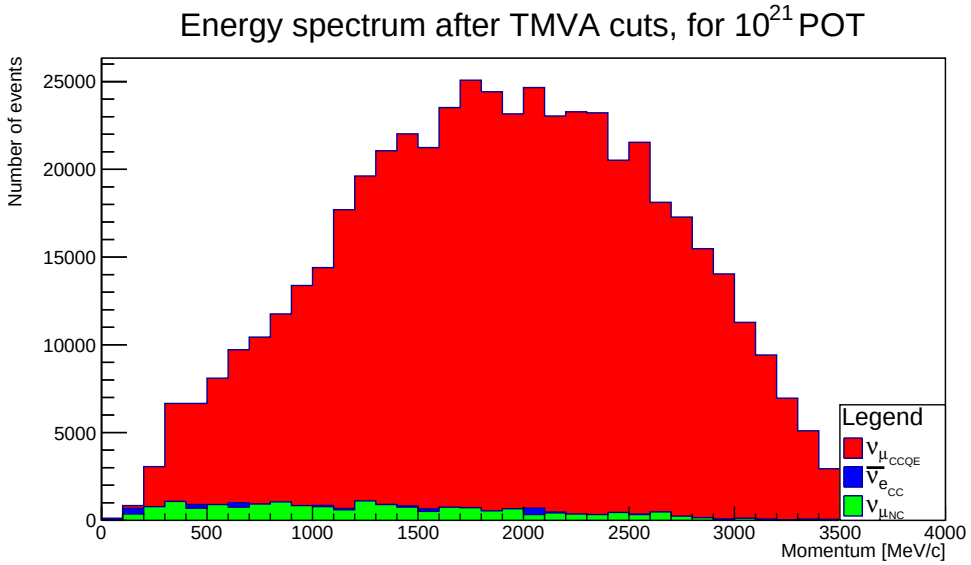

Figure 6.15: Neutrino energy spectrum of $\bar{\nu}_{eCC}$, $\nu_{\mu_{CC}}$and $\nu_{\mu_{NC}}$ recorded from 10^{21} protons-on-target (POT) in a 10 ton detector at 50 m, after passing through the TMVA algorithm.

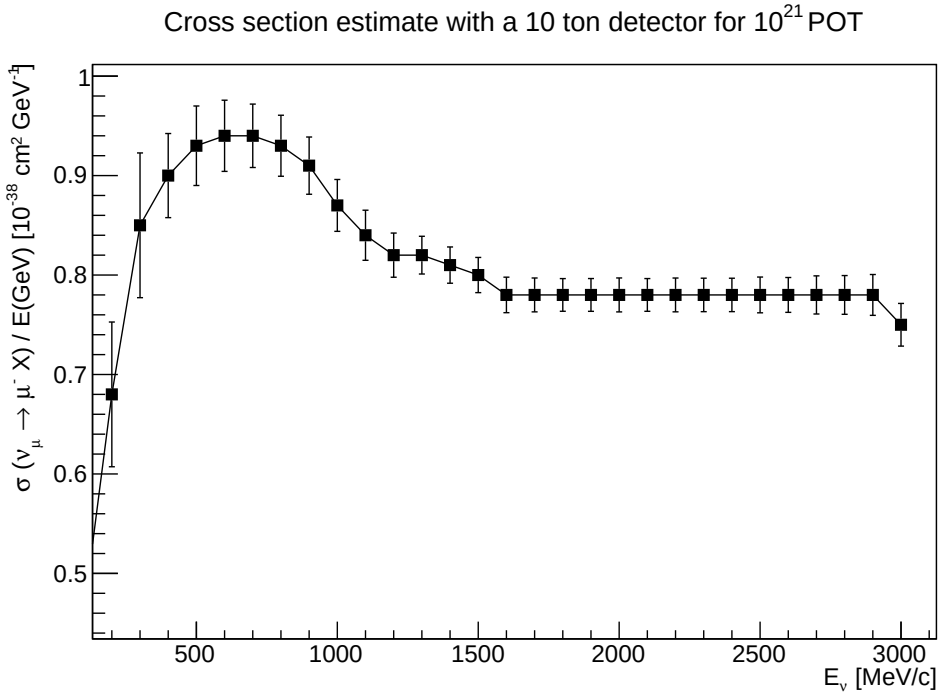

Figure 6.16: Inclusive neutrino CC cross section for a 10 ton detector at a NuSTORM beam with 10^{21} POT. The cross section from figure 6.1 is overlayed with error bars estimated from this study.

Chapter 7

J-PARC beam neutrino interaction studies

7.1 Neutrino interactions in iron in Baby MIND

Neutrinos at T2K are produced from a 30 GeV/c proton beam impinging on a graphite target with three horns to focus the correct polarity of pions that decay to produce neutrinos with the flux spectrum, given by reference [141]. The INGRID on-axis detector [142], performs measurements of the beam direction and on-axis flux.The ND280 experiment uses the beam at a 2.5° off-axis angle at a distance of 280 m which provides a narrower energy spectrum with a shifted energy peak at 600 MeV, as can be seen in figure 7.1. The energy spectrum at the 1.5° off-axis angle for the WAGASCI detector has a peak at a higher energy, 800 MeV, than the peak from the 2.5° off-axis angle of the ND280 detector, as can be seen in figure 7.1.

The goal described in this chapter is to perform the first measurement of neutrino interactions in the iron of Baby MIND. To validate the simulation framework SAURON, simulations will be compared to the recorded data. Data for the study were taken during the commissioning of Baby MIND at J-PARC between March and May 2018 when the beam was operated in reverse horn current mode. This mode produces a majority of muon antineutrinos with a contamination of muon neutrinos.

The reverse horn current neutrino and antineutrino spectrum at 1.5° that the WAGASCI and Baby MIND detectors observed in the run between March and May 2018 can be seen in figure 7.3. The fraction of muon antineutrinos is approximately 92%, with a mean energy of 1.43 GeV, and the fraction of muon neutrinos is approximately 9%, with a mean energy of 0.86 GeV. These spectra were used to perform simulations of neutrino and antineutrino events in WAGASCI and Baby MIND.

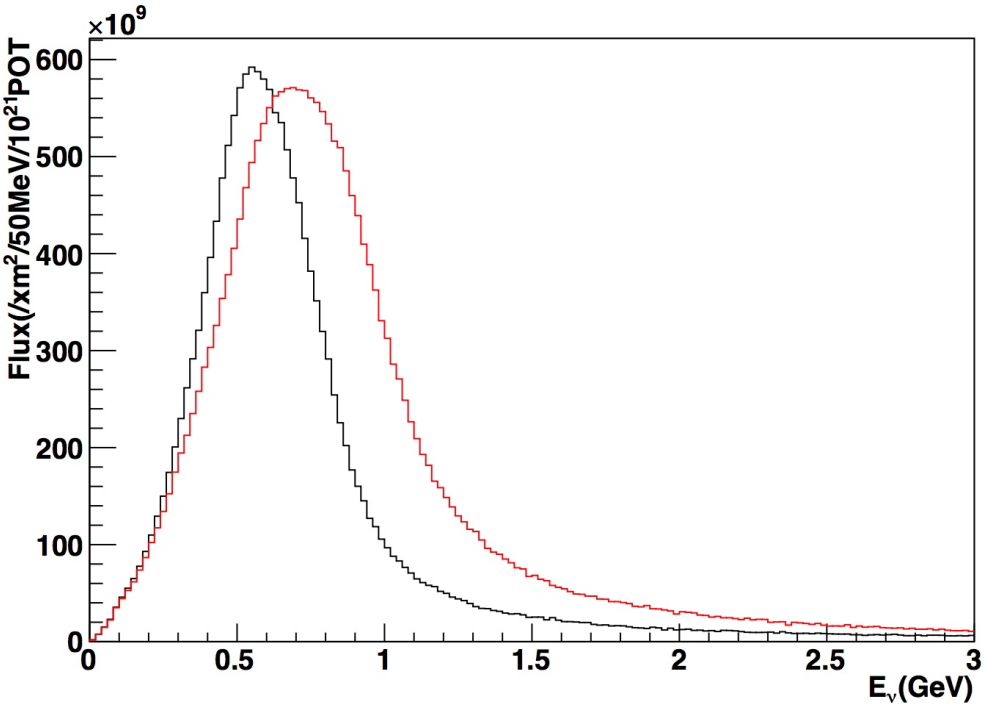

Figure 7.1: Neutrino energy spectrum for WAGASCI (red, off-axis $1.5°$) and ND280 (black, off-axis $2.5°$). The peak energy at $1.5°$ degrees is 800 MeV, with respect to the peak energy of 600 MeV at $2.5°$. Figure, courtesy of Akihiro Minamino.

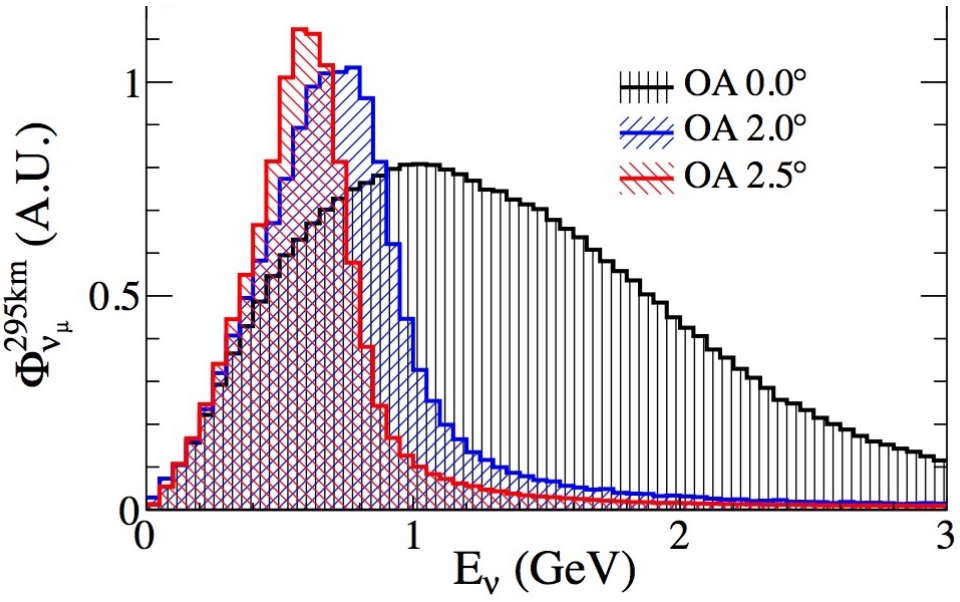

Figure 7.2: Neutrino energy spectrum of the J-PARC neutrino beam extrapolated to 295 km for various off-axis angles in degrees. Figure, courtesy of Akihiro Minamino.

To compare simulations with data taken for the commissioning run, interactions were simulated in the iron of Baby MIND to perform a standalone Baby MIND analysis, independent of the data taken by the WAGASCI detector. The fiducial volume selected includes the first

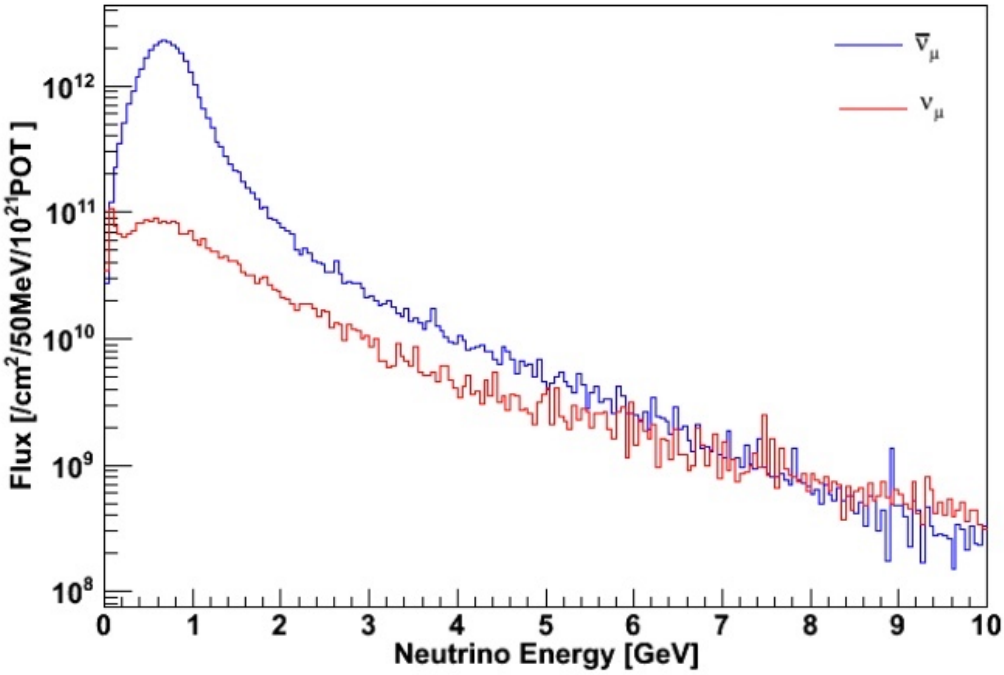

Figure 7.3: The energy spectrum for muon neutrinos and muon antineutrinos in the T2K near detector reverse horn current (RHC) beam. Figure, courtesy of Akihiro Minamino.

three iron plates in the upstream section of Baby MIND (denoted as a1-3 in figure 7.4) and can be seen in detail in figure 7.5. The selected area is 1×1 m^2 around the centre of the Baby MIND detector providing a total weight of 1500 kg of iron and 9.03×10^{29} iron nucleons.

The event selection has been chosen to ensure that only muons from neutrino interactions in the iron are evaluated. Firstly, to remove outside muons the first veto cut requires that there are no hits in the first scintillator module. Secondly to compare to simulations and to reduce muons entering from the side of the detector, at least one hit in each of scintillator module 2, 3 and 4 is required.

7.2 Reconstruction efficiency of neutrino events in Baby MIND

For the simulations the WAGASCI spectrum has been used in the SAURON framework to generate neutrino interactions in the iron, using the event selection previously described. These simulated neutrino events were reconstructed in a similar manner to the interactions in the TASD, detailed in chapter 6. The reconstruction efficiency is defined as the ratio of reconstructible tracks divided by all the simulated tracks. The charge efficiency is defined as the number of tracks with the correct charge divided by the number of reconstructible tracks.

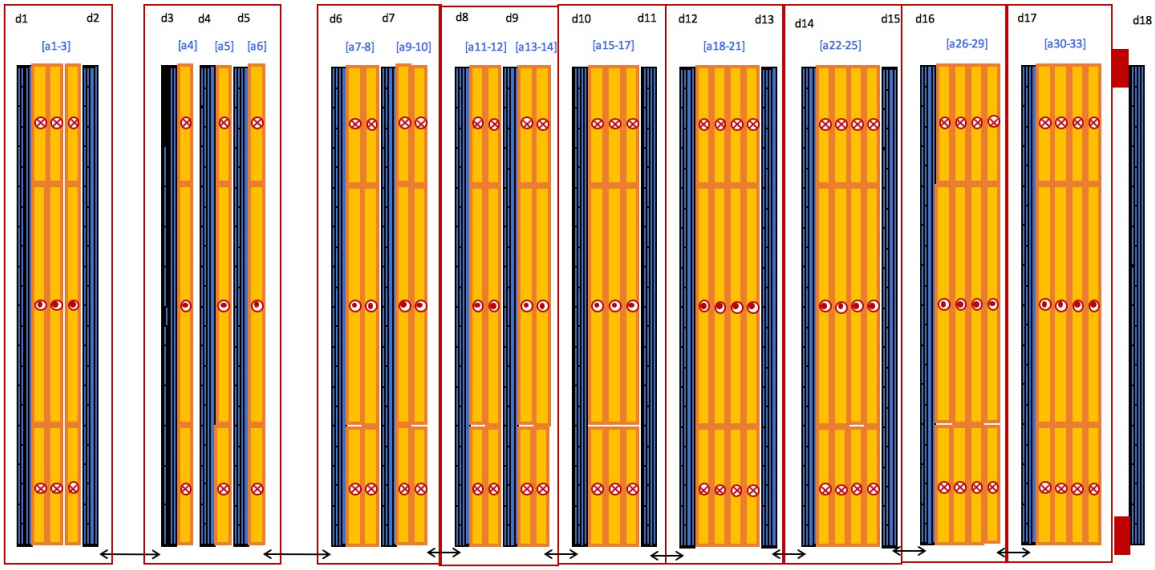

Figure 7.4: The layout of the MIND for the commissioning neutrino run.

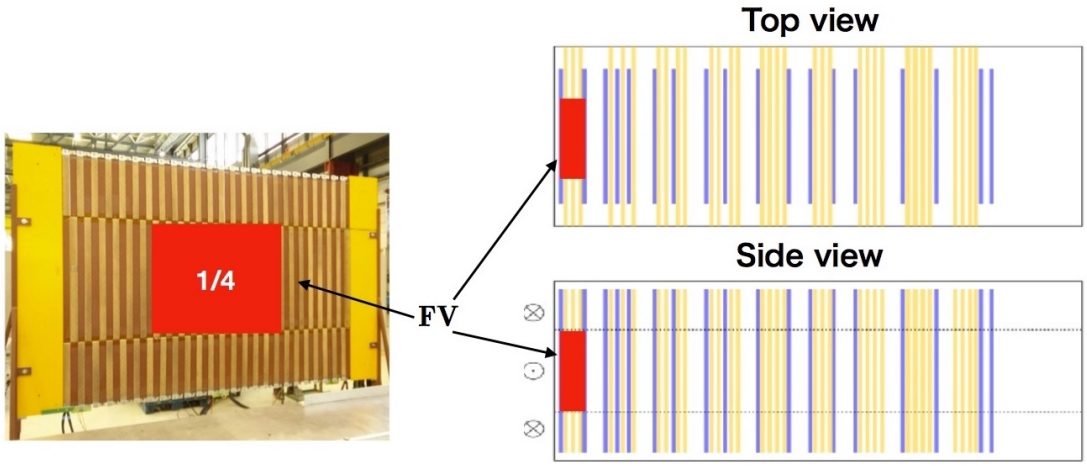

Figure 7.5: Fiducial volume chosen to measure neutrino events in the first module of iron in the Baby MIND detector. Figure, courtesy of Kenji Yasutome.

Multiplying these two results gives the ratio of reconstructed tracks with the correct charge divided by all simulated tracks.

Similarly to the studies carried out in chapter 5 for single muons in the CERN test beam, the charge reconstruction efficiency of muons from neutrino charged current interactions, using the J-PARC neutrino beam, is very high, even at low momenta. The track reconstruction efficiency is shown in figure 7.6 and the charge reconstruction efficiency with respect to the reconstructed track is shown in figure 7.7. The study requires some more investigation as to why there is a difference in the simulations between the reconstructed efficiency for muon neutrinos and antineutrinos.

In figure 7.7 the efficiency for antineutrinos at the lowest momentum does not reach zero as the few tracks which have been fitted can provide a charge. This is seen when multiplying the two plots together as in figure 7.8 with a focus on the low momentum range in figure 7.9.

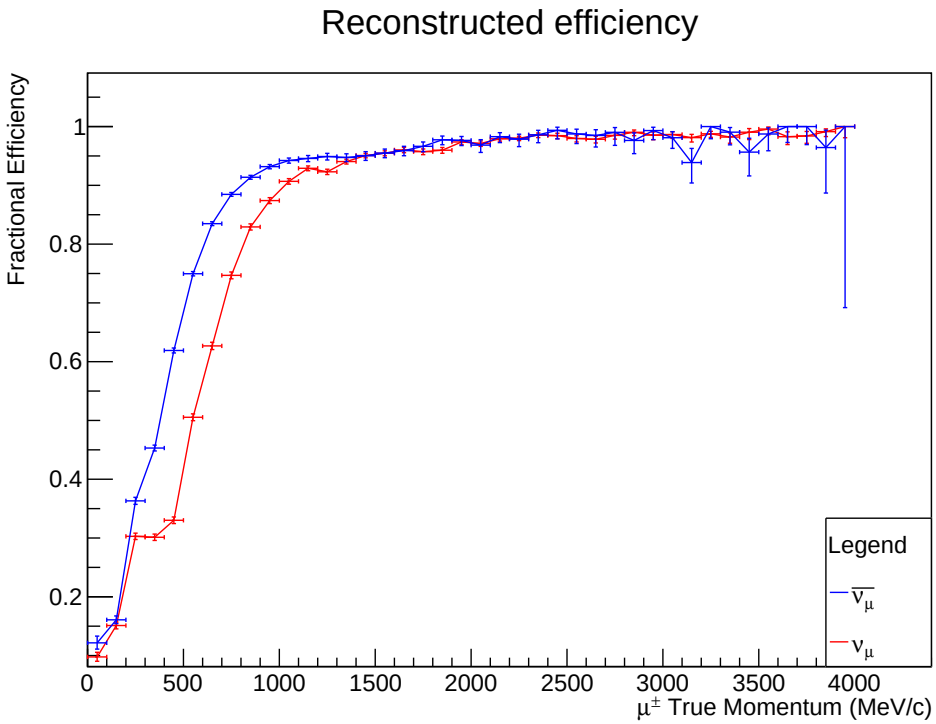

Figure 7.6: Track reconstruction efficiency, showing the probability of reconstructing a simulated neutrino charged current event in the first three modules of iron of Baby MIND as a function of the momentum of the reconstructed muon.

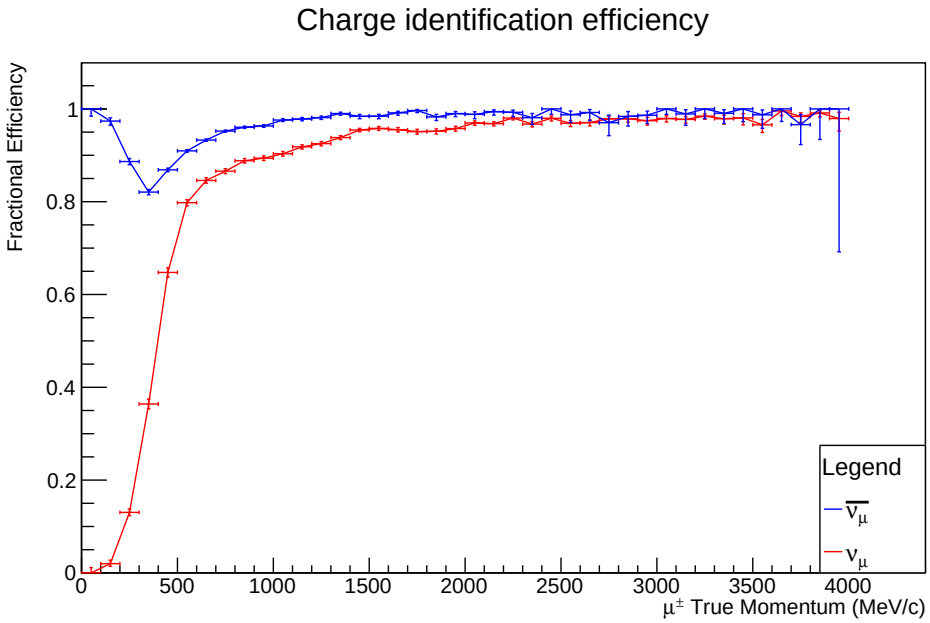

Figure 7.7: Charge reconstruction efficiency showing the efficiency of reconstructing the correct muon charge from a simulated neutrino charged current event in the first three modules of iron of Baby MIND with respect to the reconstructed track, as a function of muon momenta.

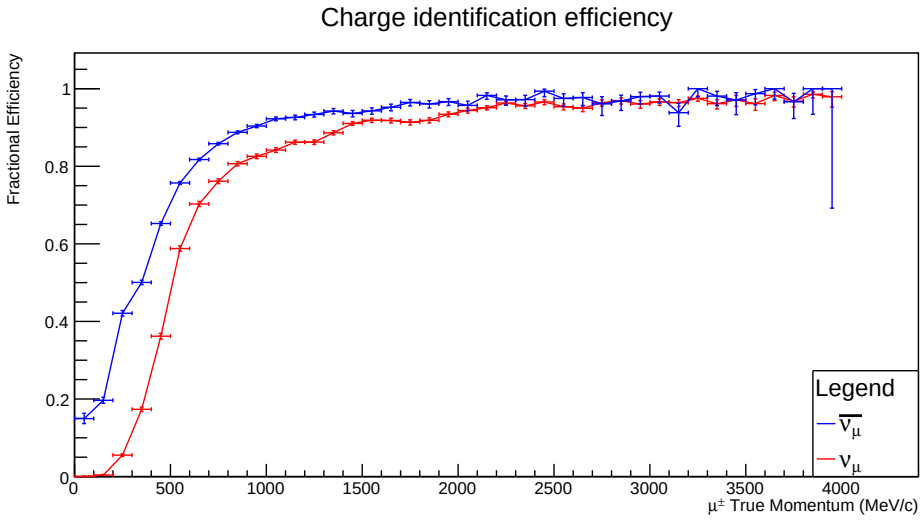

Figure 7.8: Charge reconstruction efficiency with respect to the originally simulated neutrino interaction in the first three modules of Baby MIND, showing the efficiency of reconstructing the correct muon charge with respect to the simulated neutrino charged current event, as a function of muon momenta. This plot is the multiplication of the efficiencies in figures 7.6 and 7.7.

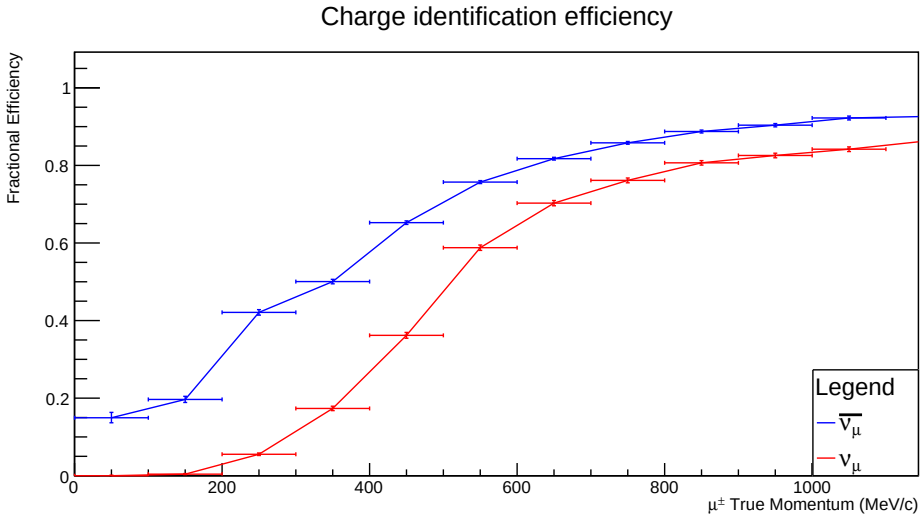

Figure 7.9: Zoom of figure 7.8, showing the charge reconstruction efficiency with respect to the originally simulated neutrino interactions in the first three modules of Baby MIND, in the lower momentum range.

7.3 Comparison of simulations to data

Data was collected during March and May 2018. For this study, data collected between the 24th and 31st of May were used. The data was extracted by the unpacking software for the Baby MIND data, found at `https://github.com/MrMefodij/BabyMINDunpacking`. The unpacking of the data produced 34675 (100%) events which were input into the SAURON framework. From this number of events only 9562 (27.6%) are seen as track-like and were able to be reconstructed. After the events were selected, an angular cut was made requiring the initial track angle with respect to the $z-$axis to be less than 30°, thus reducing the number of events to 4585 (13.2%). The requirement that the momentum was within a range $200\ \mathrm{MeV/c} < p < 10,000\ \mathrm{MeV/c}$, further reduced the number of events to 3899 (11.2%). Events outside of this range are inconsistent with neutrino events and were considered unphysical and rejected. After these cuts there are 2245 tracks reconstructed as having a positive charge and 1654 with negative charge. Further imposing the fiducial cuts such as no hits in the first scintillator plane (to remove neutrino interactions upstream of Baby MIND) reduces this number to 2209 (6.4%) and finally requiring hits in the second, third and fourth scintillator planes provides the final number of events to be 224 (0.6%). Out of this sample, 123 event are reconstructed with positive charge and 101 with negative charge. Based on the number of reconstructed events and using the statistical error the estimated ratio of antineutrino to neutrino events at 1.5° off axis is 1.22 ± 0.15.

To compare data to simulations, two samples of 100000 muon neutrino and antineutrino events each were simulated in the SAURON framework defining the GENIE interaction area to be the same iron plates as described in the fiducial cut. This provided the reconstructed energy spectrum as seen in figure 7.10 with 27926 (27.9%) neutrino and 33681 (33.7%) antineutrinos which survive all the cuts.

The simulated reconstructed energy spectrum needs to be converted to number of events. This is done through the following equation:

$$N_{events} = \int \phi_\nu(E) \times \sigma(E) \times N_{target} dE \tag{7.1}$$

where $\phi(E)$ is the neutrino flux as a function of neutrino energy E, seen in figure 7.11, $\sigma(E)$ is the neutrino and antineutrino total cross sections taken from figures 6.1 and 6.2 and N_{target} is the number of iron nucleons in a 1500 kg mass which is $N_{target} = 9.03 \times 10^{29}$. This provides the total number of neutrino events as 7588 muon neutrinos and 23432 muon antineutrinos for 1500 kg of iron and 10^{21} POT. Combining these results with the reconstruction efficiency provides 2117 muon neutrinos and 7899 muon antineutrinos reconstructed with the correct charge for 1500 kg of iron and 10^{21} POT. The expected ratio of neutinos

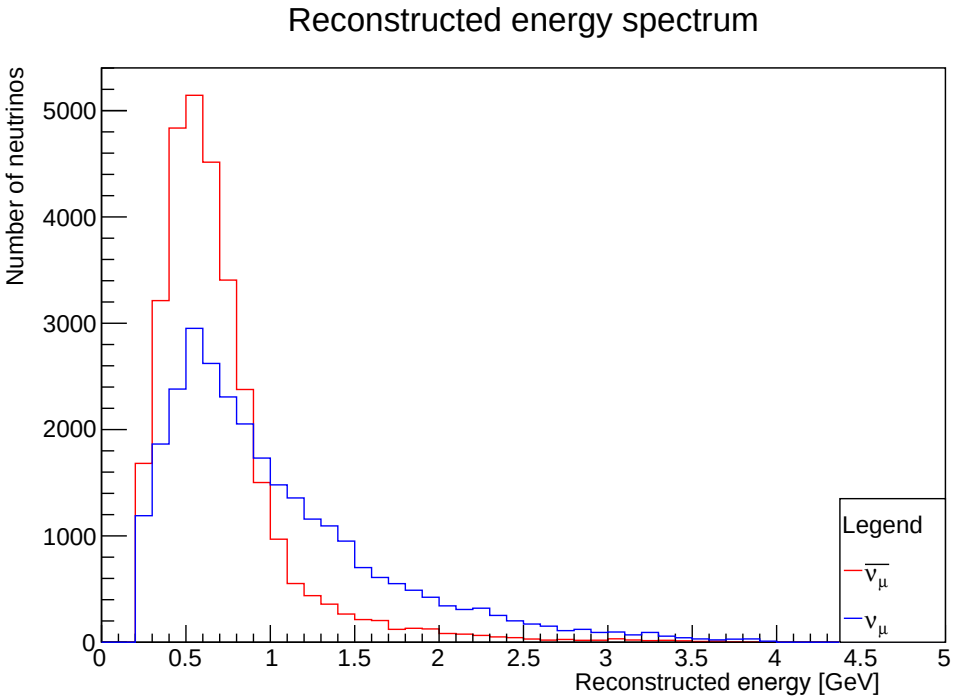

Figure 7.10: The reconstructed energy spectrum for the simulated neutrino events in SAURON.

to antineutrinos is 3.7, which is different to the observed ratio of 1.22 in the data. This discrepancy is under investigation.

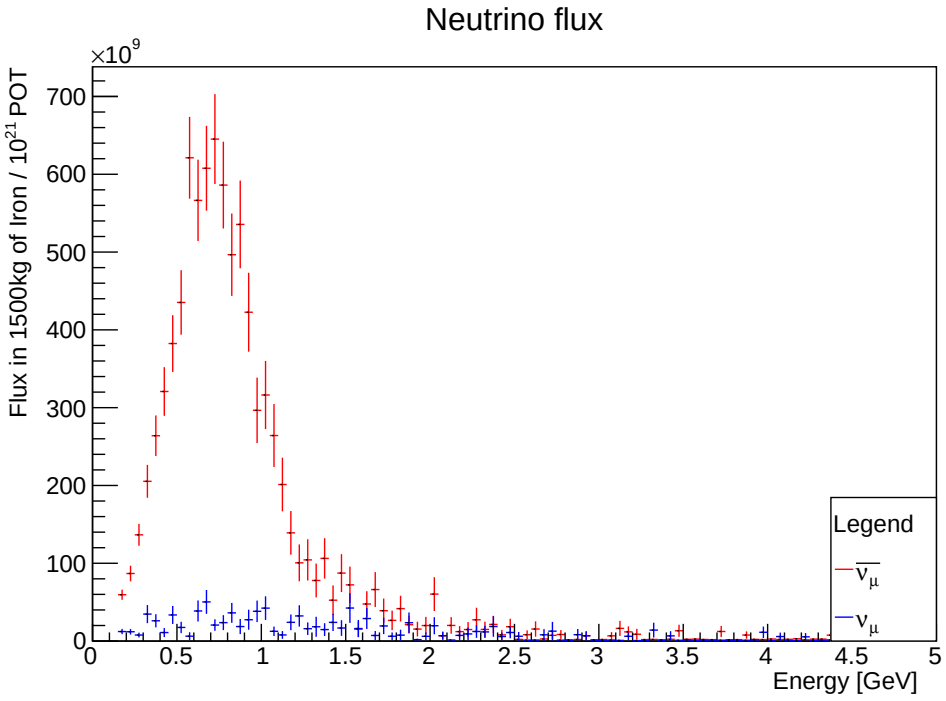

Figure 7.11: The neutrino flux for $\bar{\nu}_\mu$ and ν_μ. Figure, courtesy of Kenji Yasutome.

The reconstructed energy spectra for events which have been classified as muon neutrinos and muon antineutrinos were compared to the simulations. In figure 7.12 and figure 7.13 the simulated (expected) reconstructed energy spectrum is plotted with the recorded data points extracted from the neutrino beam overlayed. Both plots have been normalized to each other to ensure that the number of simulated events have been scaled to match the number of recorded events. The results shown in figure 7.12 show good agreement between data and simulations for muon antineutrino events. The results shown in figure 7.13 show good agreement between data and simulations for muon neutrino events.

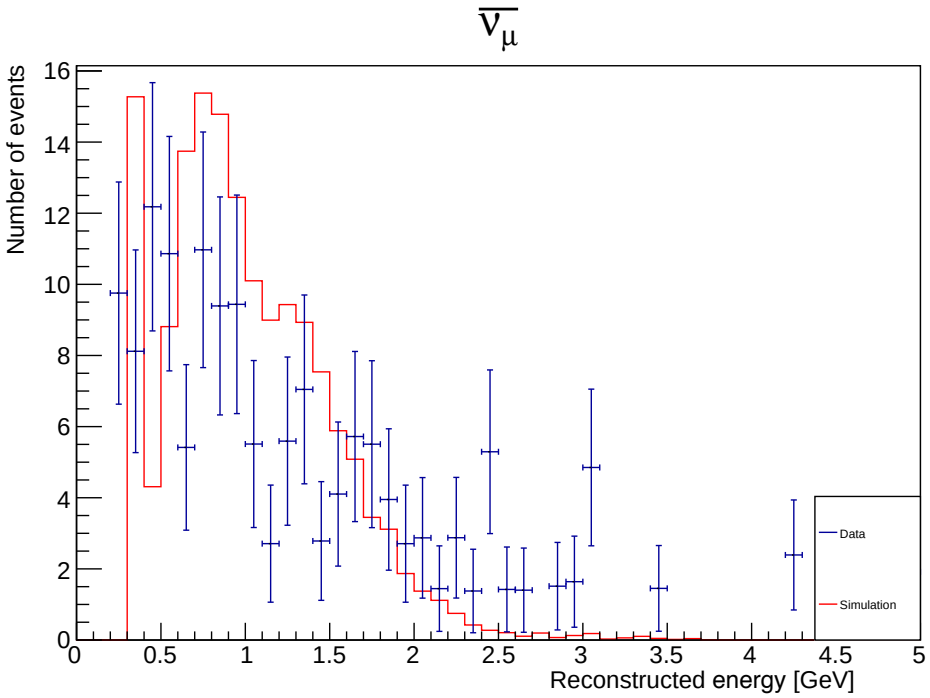

Figure 7.12: Energy spectrum of the reconstructed antineutrino $\bar{\nu}_\mu$ events in data (points with error bars) compared to the simulation (histogram).

7.4 Summary

During commissioning of Baby MIND, it was possible to reconstruct neutrino events during the data taking period in May 2018. A preliminary study was carried out to reconstruct neutrino interactions in the first three iron plates of Baby MIND and measure neutrino and antineutrino events from the Reverse Horn Current beam at a 1.5° off-axis angle. Charge reconstruction was achieved, with momentum measurements down to 400 MeV/c. A total of 224 neutrino and antineutrino events were identified in Baby MIND, which are the first neutrino events observed in this detector.

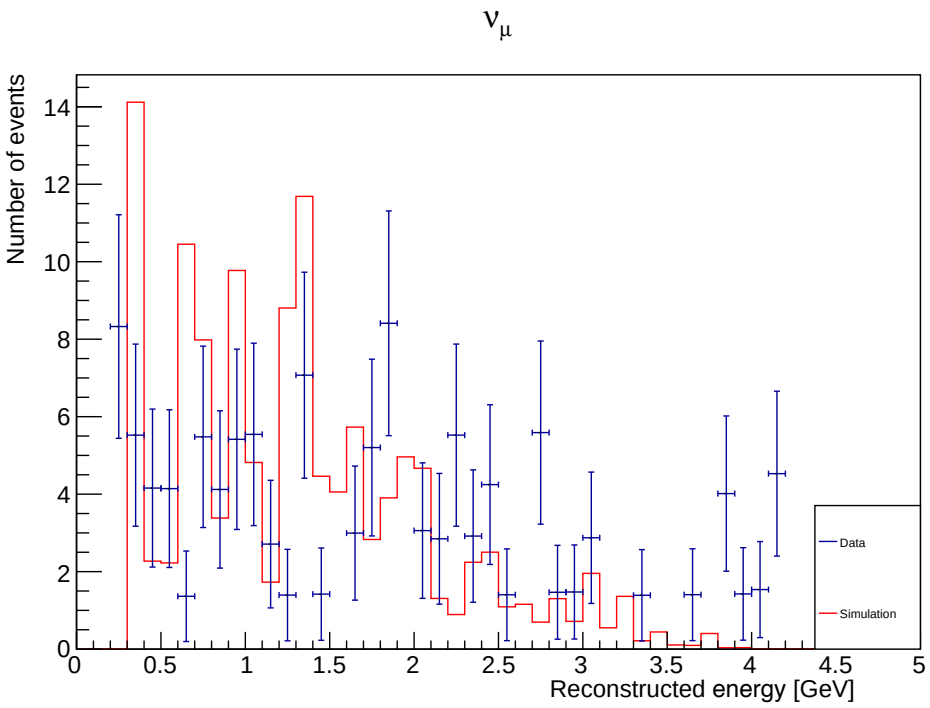

Figure 7.13: Energy spectrum of the reconstructed neutrino ν_μ events in data (points with error bars) compared to the simulation (histogram).

Chapter 8

Conclusions and Outlook

8.1 Conclusions

This thesis summarises the work carried out by the candidate to help build and commission the Baby MIND detector, to supply the simulation and reconstruction software for Baby MIND, to perform track reconstruction and charge identification studies at dedicated commissioning test beams at CERN, and to perform a preliminary measurement of neutrino interactions in the iron of the Baby MIND detector at the J-PARC facility. These tasks were performed as part of a team of collaborators, but responsibility for the reconstruction and the data analysis has been carried out by the candidate. Further work needs to be carried out to fully commission the Baby MIND detector at J-PARC and to integrate it into the WAGASCI and T2K experiments. The future goal of the WAGASCI and Baby MIND collaboration is to measure neutrino and antineutrino cross sections in water and scintillator, in order to reduce the systematic errors for the T2K neutrino oscillation analysis, leading to the potential discovery of CP violation in neutrinos.

Chapter 1 provided a brief introduction into the current theories regarding neutrino interactions as well as highlighting some of the ongoing fundamental questions in neutrino physics. This was followed by chapter 2, in which some past, current and future neutrino experiments were described and how the measurements being carried out are providing a deeper understanding of the properties of neutrinos, with the ultimate goal to determine whether neutrinos observe CP violation.

In chapter 3, the design, layout and technical details of the Baby MIND and WAGASCI detectors were described. Furthermore, the motivation for the design choices were justified in terms of the physics properties that we expect to measure with these detectors.

Chapter 4 describes the two software frameworks which have been developed, SaRoMaN and SAURON. SaRoMaN is a simulation and reconstruction software framework that is able

to unpack the hits in Baby MIND, reconstruct tracks and perform momentum and charge reconstruction of the tracks. The SAURON framework was developed as a new software tool to reduce external dependencies on third-party software packages that limited the evolution of SaRoMaN and reduced its applicability.

Chapter 5 describes the AIDA Totally Active Scintillator Detector (TASD) and the Baby MIND test beams and commissioning at the CERN T9 charged particle beam facility. Results are presented on the reconstruction of positive and negative muon tracks with the Baby MIND detector and comparison of data and simulations. As part of this work, results are also presented on a particle identification machine learning algorithm that can identify muon events from background pion events in the detector.

In chapter 6, a detector configuration consisting of a Totally Active Scintillator Detector (TASD) with a Baby MIND spectrometer downstream was studied in the context of the unique beam of neutrinos that can be achieved using the NuSTORM facility. In this facility, a beam of muon neutrinos and electron antineutrinos from the decay of muons is created and neutrino interactions can be studied with the TASD and Baby MIND configuration. This simulation study was able to show how ν_μ charged current (CC) events can be reconstructed against a background of $\bar{\nu}_e$ CC events and neutral currents (NC) from both ν_μ and $\bar{\nu}_e$. A machine learning algorithm was used to select the signal above the background, and these results were used to estimate the expected sensitivities of this detector configuration at a NuSTORM beam to study neutrino CC cross sections. This chapter also showed the first study performed with the SAURON software. It shows a tendency for the algorithms to produce default values when the charge is difficult to estimate in the very low momentum regime and must be further studied.

Chapter 7 provides results from a study of neutrino interactions in the iron plates of Baby MIND with a comparison to data recorded during the Baby MIND commissioning in the J-PARC neutrino beam between March and May 2018. Baby MIND acts as a spectrometer behind the WAGASCI detector, but this first study was able to isolate neutrino events in the iron of the Baby MIND detector. The first neutrino events were shown and compared to simulations to provide a first analysis of neutrino events in Baby MIND at the 1.5° off-axis location at J-PARC. The simulations in SAURON show a distinction between muon neutrino and anti-neutrino event reconstruction in the iron which must be investigated.

8.2 Outlook

The Baby MIND and WAGASCI experiments will commence full data taking in the J-PARC neutrino beam in 2019. Neutrino interactions will be recorded in the water and scintillator targets of the WAGASCI, where the neutrino events will be identified, and the outgoing

muons from charged current interactions will be reconstructed in the Baby MIND spectrometer downstream of WAGASCI.

To be able to reconstruct full neutrino events in the two detectors, the software frameworks for both WAGASCI and Baby MIND will need to be merged to be able to match hits, vertices and tracks in both detectors. Furthermore, for efficient data taking the Baby MIND data acquisition software will also need to be included in the generic WAGASCI DAQ, so that full event building of both detectors may be carried out. These are the main future software challenges that need to be met in order to be able to perform the WAGASCI and Baby MIND physics programme.

The physics goal for WAGASCI and Baby MIND is to measure the ratio of neutrino and antineutrino cross sections on water and scintillator, to constrain the nuclear effects from neutrino interactions in oxygen and carbon, essential to reduce systematic uncertainties in the T2K neutrino oscillation measurements. The ultimate goal is to reduce the systematic errors in these cross sections by a factor of two, down to 4%, and to enable the measurements of CP violation in the T2K experiment.

Bibliography

[1] M. Antonova et al. "Baby MIND Experiment Construction Status". In: *Proceedings, Prospects in Neutrino Physics (NuPhys2016): London, UK, December 12-14, 2016*. 2017. arXiv: 1704.08917 [physics.ins-det]. URL: https://inspirehep.net/record/1597343/files/arXiv:1704.08917.pdf (cit. on p. 52).

[2] M. Antonova et al. "Baby MIND: A Magnetised Spectrometer for the WAGASCI Experiment". In: *Proceedings, Prospects in Neutrino Physics (NuPhys2016): London, UK, December 12-14, 2016*. 2017. arXiv: 1704.08079 [physics.ins-det]. URL: http://lss.fnal.gov/archive/2017/conf/fermilab-conf-17-270-apc.pdf (cit. on p. 66).

[3] M. Antonova et al. "Baby MIND: A Magnetised Spectrometer for the WAGASCI Experiment". In: *PoS* NuFact2017 (2018), p. 078. DOI: 10.22323/1.295.0078. arXiv: 1704.08079 [physics.ins-det] (cit. on p. 95).

[4] "The β-ray spectrum of radium E". In: *Proceedings of the Royal Society of London A: Mathematical, Physical and Engineering Sciences* 175.960 (1940), pp. 71–87. ISSN: 0080-4630. DOI: 10.1098/rspa.1940.0044. eprint: http://rspa.royalsocietypublishing.org/content/175/960/71.full.pdf. URL: http://rspa.royalsocietypublishing.org/content/175/960/71 (cit. on p. 1).

[5] Wolfgang Pauli. May 2016. URL: https://www.library.ethz.ch/exhibit/pauli/neutrino_e.html (cit. on p. 1).

[6] Fred L. Wilson. "Fermi Theory of Beta Decay". In: *American Journal of Physics* 36.12 (1968), pp. 1150–1160. DOI: http://dx.doi.org/10.1119/1.1974382. URL: http://scitation.aip.org/content/aapt/journal/ajp/36/12/10.1119/1.1974382 (cit. on p. 1).

[7] F. A. Scott. "Energy Spectrum of the Beta-Rays of Radium E". In: *Phys. Rev.* 48 (5 1935), pp. 391–395. DOI: 10.1103/PhysRev.48.391. URL: https://link.aps.org/doi/10.1103/PhysRev.48.391 (cit. on p. 2).

[8] Frederick Reines and Clyde L. Cowan. "The Neutrino". In: *Nature* 178.4531 (Sept. 1956), pp. 446–449. URL: http://dx.doi.org/10.1038/178446a0 (cit. on pp. 2, 22).

[9] G. Danby et al. "Observation of High-Energy Neutrino Reactions and the Existence of Two Kinds of Neutrinos". In: *Phys. Rev. Lett.* 9 (1 1962), pp. 36–44. DOI: 10.1103/PhysRevLett.9.36. URL: http://link.aps.org/doi/10.1103/PhysRevLett.9.36 (cit. on p. 2).

[10] M. L. Perl et al. "Evidence for Anomalous Lepton Production in $e^+ - e^-$ Annihilation". In: *Phys. Rev. Lett.* 35 (22 1975), pp. 1489–1492. DOI: 10.1103/PhysRevLett.35.1489. URL: http://link.aps.org/doi/10.1103/PhysRevLett.35.1489 (cit. on p. 2).

[11] K. Kodama et al. "Observation of tau neutrino interactions". In: *Phys. Lett.* B504 (2001), pp. 218–224. DOI: 10.1016/S0370-2693(01)00307-0. arXiv: hep-ex/0012035 [hep-ex] (cit. on p. 2).

[12] W. E. Burcham and M. Jobes. *Nuclear and Particle Physics*. Second. Pearson education, 1995 (cit. on p. 3).

[13] D. Griffiths. *Introduction to Elementary Particles*. Physics textbook. Wiley, 2008. ISBN: 9783527406012. URL: https://books.google.ch/books?id=w9Dz56myXm8C (cit. on p. 3).

[14] M. Goldhaber, L. Grodzins, and A. W. Sunyar. "Helicity of Neutrinos". In: *Phys. Rev.* 109 (3 1958), pp. 1015–1017. DOI: 10.1103/PhysRev.109.1015. URL: http://link.aps.org/doi/10.1103/PhysRev.109.1015 (cit. on pp. 4, 5).

[15] R. P. Feynman and Murray Gell-Mann. "Theory of Fermi interaction". In: *Phys. Rev.* 109 (1958). [,417(1958)], pp. 193–198. DOI: 10.1103/PhysRev.109.193 (cit. on p. 4).

[16] F. J. Hasert et al. "Observation of Neutrino Like Interactions Without Muon Or Electron in the Gargamelle Neutrino Experiment". In: *Phys. Lett.* B46 (1973). [,5.15(1973)], pp. 138–140. DOI: 10.1016/0370-2693(73)90499-1 (cit. on p. 5).

[17] Steven Weinberg. "A Model of Leptons". In: *Phys. Rev. Lett.* 19 (1967), pp. 1264–1266. DOI: 10.1103/PhysRevLett.19.1264 (cit. on p. 5).

[18] Abdus Salam and John Clive Ward. "Electromagnetic and weak interactions". In: *Phys. Lett.* 13 (1964), pp. 168–171. DOI: 10.1016/0031-9163(64)90711-5 (cit. on p. 5).

[19] S. L. Glashow. "Partial Symmetries of Weak Interactions". In: *Nucl. Phys.* 22 (1961), pp. 579–588. DOI: 10.1016/0029-5582(61)90469-2 (cit. on p. 5).

[20] "The standard model and the neutrino". In: *Massive Neutrinos in Physics and Astrophysics*. 3rd. World Scientific, 2012, pp. 21–41. DOI: 10.1142/9789812562203_0002. eprint: http://www.worldscientific.com/doi/pdf/10.1142/9789812562203_0002. URL: http://www.worldscientific.com/doi/abs/10.1142/9789812562203_0002 (cit. on pp. 5, 16, 18).

[21] F. Englert and R. Brout. "Broken Symmetry and the Mass of Gauge Vector Mesons". In: *Phys. Rev. Lett.* 13 (9 1964), pp. 321–323. DOI: 10.1103/PhysRevLett.13.321. URL: http://link.aps.org/doi/10.1103/PhysRevLett.13.321 (cit. on pp. 5, 6, 8).

[22] Jeffrey Goldstone, Abdus Salam, and Steven Weinberg. "Broken Symmetries". In: *Phys. Rev.* 127 (3 1962), pp. 965–970. DOI: 10.1103/PhysRev.127.965. URL: https://link.aps.org/doi/10.1103/PhysRev.127.965 (cit. on p. 6).

[23] K. A. Olive et al. "Review of Particle Physics". In: *Chin. Phys.* C38 (2014), p. 090001. DOI: 10.1088/1674-1137/38/9/090001 (cit. on pp. 8, 11, 16, 18, 77).

[24] Wikipedia. 2017. URL: http://en.wikipedia.org/wiki/File:Standard_Model_of_Elementary_Particles.svg (cit. on p. 9).

[25] Michael E Peskin and Daniel V Schroeder. *An Introduction to Quantum Field Theory; 1995 ed.* Boulder, CO: Westview, 1995. URL: https://cds.cern.ch/record/257493 (cit. on pp. 9, 10, 19).

[26] Sven-Patrik Hallsjö. "Search for Dark Matter in the Upgraded High Luminosity LHC at CERN : Sensitivity of ATLAS phase II upgrade to dark matter production". MA thesis. Linköping University, Department of Physics, Chemistry and Biology, 2014, p. 79 (cit. on p. 9).

[27] F. J. P Soler, C. D. Froggatt, and Franz. Muheim. *Neutrinos in particle physics, astrophysics and cosmology*. Vol. Scottish graduate series. CRC Press, 2009 (cit. on pp. 13, 20).

[28] Dieter Rein and Lalit M Sehgal. "Neutrino-excitation of baryon resonances and single pion production". In: *Annals of Physics* 133.1 (1981), pp. 79 –153. ISSN: 0003-4916. DOI: https://doi.org/10.1016/0003-4916(81)90242-6. URL: http://www.sciencedirect.com/science/article/pii/0003491681902426 (cit. on p. 14).

[29] J.N. Bahcall. *Neutrino Astrophysics*. Cambridge University Press, 1989. ISBN: 9780521379755. URL: https://books.google.co.uk/books?id=8GIP7uNMhlsC (cit. on pp. 14, 15).

[30] R. Jr. Davis, J. C. Evans, and B. T. Cleveland. *Solar Neutrino Problem*. 1978. URL: http://www.osti.gov/accomplishments/documents/fullText/ACC0068.pdf (cit. on pp. 15, 23, 29).

[31] Nick Jelley, Arthur B. McDonald, and R.G. Hamish Robertson. "The Sudbury Neutrino Observatory". In: *Annual Review of Nuclear and Particle Science* 59.1 (2009), pp. 431–465. DOI: 10.1146/annurev.nucl.55.090704.151550. eprint: http://dx.doi.org/10.1146/annurev.nucl.55.090704.151550. URL: http://dx.doi.org/10.1146/annurev.nucl.55.090704.151550 (cit. on pp. 15, 29, 30).

[32] K. S. Hirata et al. "Observation in the Kamiokande-II detector of the neutrino burst from supernova SN1987A". In: *Phys. Rev. D* 38 (2 1988), pp. 448–458. DOI: 10.1103/PhysRevD.38.448. URL: https://link.aps.org/doi/10.1103/PhysRevD.38.448 (cit. on p. 15).

[33] Y. Fukuda et al. "Evidence for Oscillation of Atmospheric Neutrinos". In: *Phys. Rev. Lett.* 81 (8 1998), pp. 1562–1567. DOI: 10.1103/PhysRevLett.81.1562. URL: http://link.aps.org/doi/10.1103/PhysRevLett.81.1562 (cit. on pp. 15, 23, 26, 27).

[34] B. Pontecorvo. "Neutrino Experiments and the Problem of Conservation of Leptonic Charge". In: *Soviet Journal of Experimental and Theoretical Physics* 26 (May 1968), p. 984 (cit. on p. 15).

[35] Nobel Media AB. 2018. URL: https://www.nobelprize.org/prizes/physics/2015/summary/ (cit. on p. 15).

[36] Ziro Maki, Masami Nakagawa, and Shoichi Sakata. "Remarks on the Unified Model of Elementary Particles". In: *Progress of Theoretical Physics* 28.5 (1962), pp. 870–880. DOI: 10.1143/PTP.28.870. eprint: http://ptp.oxfordjournals.org/content/28/5/870.full.pdf+html. URL: http://ptp.oxfordjournals.org/content/28/5/870.abstract (cit. on p. 15).

[37] K. Abe et al. "Combined Analysis of Neutrino and Antineutrino Oscillations at T2K". In: *Phys. Rev. Lett.* 118.15 (2017), p. 151801. DOI: 10.1103/PhysRevLett.118.151801. arXiv: 1701.00432 [hep-ex] (cit. on p. 18).

[38] Michael Victor Berry. *Principles of cosmology and gravitation*. Bristol: IOP, 1989. URL: https://cds.cern.ch/record/206659 (cit. on p. 19).

[39] M. Aguilar et al. "The Alpha Magnetic Spectrometer (AMS) on the International Space Station: Part I results from the test flight on the space shuttle". In: *Physics Reports* 366.6 (2002), pp. 331 –405. ISSN: 0370-1573. DOI: http://dx.doi.org/10.1016/S0370-1573(02)00013-3. URL: http://www.sciencedirect.com/science/article/pii/S0370157302000133 (cit. on p. 19).

[40] L. Accardo et al. "High Statistics Measurement of the Positron Fraction in Primary Cosmic Rays of 0.5-500 GeV with the Alpha Magnetic Spectrometer on the International Space Station". In: *Phys. Rev. Lett.* 113 (12 2014), p. 121101. DOI: 10.1103/PhysRevLett.113.121101. URL: http://link.aps.org/doi/10.1103/PhysRevLett.113.121101 (cit. on p. 19).

[41] Laurent Canetti, Marco Drewes, and Mikhail Shaposhnikov. "Matter and Antimatter in the Universe". In: *New J. Phys.* 14 (2012), p. 095012. DOI: 10.1088/1367-2630/14/9/095012. arXiv: 1204.4186 [hep-ph] (cit. on p. 19).

[42] M. Fukugita and T. Yanagida. "Baryogenesis Without Grand Unification". In: *Phys. Lett.* B174 (1986), pp. 45–47. DOI: 10.1016/0370-2693(86)91126-3 (cit. on p. 19).

[43] M. C. Gonzalez-Garcia et al. "Global fit to three neutrino mixing: critical look at present precision". In: *JHEP* 12 (2012), p. 123. DOI: 10.1007/JHEP12(2012)123. arXiv: 1209.3023 [hep-ph] (cit. on p. 19).

[44] Andrei D Sakharov. "Violation of CP invariance, C asymmetry, and baryon asymmetry of the universe". In: *Soviet Physics Uspekhi* 34.5 (1991), p. 392. URL: http://stacks.iop.org/0038-5670/34/i=5/a=A08 (cit. on p. 19).

[45] Scott Dodelson and Lawrence M. Widrow. "Sterile-neutrinos as dark matter". In: *Phys. Rev. Lett.* 72 (1994), pp. 17–20. DOI: 10.1103/PhysRevLett.72.17. arXiv: hep-ph/9303287 [hep-ph] (cit. on p. 21).

[46] Gerard Jungman, Marc Kamionkowski, and Kim Griest. "Supersymmetric dark matter". In: *Phys. Rept.* 267 (1996), pp. 195–373. DOI: 10.1016/0370-1573(95)00058-5. arXiv: hep-ph/9506380 [hep-ph] (cit. on p. 21).

[47] J. D. Vergados, H. Ejiri, and F. Simkovic. "Theory of Neutrinoless Double Beta Decay". In: *Rept. Prog. Phys.* 75 (2012), p. 106301. DOI: 10.1088/0034-4885/75/10/106301. arXiv: 1205.0649 [hep-ph] (cit. on p. 21).

[48] C. V. Achar et al. "Detection of muons produced by cosmic ray neutrinos deep underground". In: *Phys. Lett.* 18 (1965), pp. 196–199. DOI: 10.1016/0031-9163(65)90712-2 (cit. on p. 24).

[49] F. Reines et al. “Evidence for high-energy cosmic ray neutrino interactions”. In: *Phys. Rev. Lett.* 15 (1965), pp. 429–433. DOI: 10.1103/PhysRevLett.15.429 (cit. on p. 24).

[50] G. Battistoni et al. “The NUSEX detector”. In: *Nuclear Instruments and Methods in Physics Research Section A: Accelerators, Spectrometers, Detectors and Associated Equipment* 245.2 (1986), pp. 277 –290. ISSN: 0168-9002. DOI: https://doi.org/10.1016/0168-9002(86)91261-1. URL: http://www.sciencedirect.com/science/article/pii/0168900286912611 (cit. on p. 24).

[51] S. Ragazzi et al. “A study of the atmospheric neutrino flux in NUSEX”. In: *Tests of fundamental laws in physics. Proceedings, 9th Moriond Workshop, 24th Rencontres de Moriond, Les Arcs, France, January 21-28, 1989*. 1989, pp. 237–241. URL: http://inspirehep.net/record/292419/files/C89-01-21_237-241.pdf (cit. on p. 24).

[52] K. Arisaka et al. “KAMIOKA Nucleon Decay Experiments; status and performance”. In: *AIP Conf. Proc.* 114 (1984), pp. 54–76. DOI: 10.1063/1.34507 (cit. on pp. 25, 26).

[53] M. Koshiba. “KAMIOKA Nucleon Decay Experiment”. In: *Nuovo Cim.* C9 (1986), pp. 141–158. DOI: 10.1007/BF02514837 (cit. on p. 26).

[54] R. Clark. “The atmospheric neutrino muon-like fraction above 1-GeV”. In: *AIP Conf. Proc.* 412.1 (1997), pp. 958–961. DOI: 10.1063/1.54393 (cit. on p. 26).

[55] K. Abe et al. “Search for Differences in Oscillation Parameters for Atmospheric Neutrinos and Antineutrinos at Super-Kamiokande”. In: *Phys. Rev. Lett.* 107 (24 2011), p. 241801. DOI: 10.1103/PhysRevLett.107.241801. URL: http://link.aps.org/doi/10.1103/PhysRevLett.107.241801 (cit. on p. 26).

[56] MACRO Collaboration et al. “Measurement of the atmospheric neutrino-induced upgoing muon flux using MACRO”. In: *Physics Letters B* 434 (Aug. 1998), pp. 451–457. DOI: 10.1016/S0370-2693(98)00885-5. eprint: hep-ex/9807005 (cit. on p. 28).

[57] M. Ambrosio et al. “The MACRO detector at Gran Sasso”. In: *Nucl. Instrum. Meth.* A486 (2002), pp. 663–707. DOI: 10.1016/S0168-9002(01)02169-6 (cit. on p. 28).

[58] J. P. Cravens et al. “Solar neutrino measurements in Super-Kamiokande-II”. In: *prd* 78.3, 032002 (Aug. 2008), p. 032002. DOI: 10.1103/PhysRevD.78.032002. arXiv: 0803.4312 [hep-ex] (cit. on p. 29).

[59] Q. R. Ahmad et al. "Direct evidence for neutrino flavor transformation from neutral current interactions in the Sudbury Neutrino Observatory". In: *Phys. Rev. Lett.* 89 (2002), p. 011301. DOI: 10.1103/PhysRevLett.89.011301. arXiv: nucl-ex/0204008 [nucl-ex] (cit. on p. 30).

[60] H. M. O'Keeffe, E. O'Sullivan, and M. C. Chen. "Scintillation decay time and pulse shape discrimination in oxygenated and deoxygenated solutions of linear alkylbenzene for the SNO+ experiment". In: *Nucl. Instrum. Meth.* A640 (2011), pp. 119–122. DOI: 10.1016/j.nima.2011.03.027. arXiv: 1102.0797 [physics.ins-det] (cit. on p. 29).

[61] G Ranucci et al. "Overview and accomplishments of the Borexino experiment". In: *Journal of Physics: Conference Series* 675.1 (2016), p. 012036. URL: http://stacks.iop.org/1742-6596/675/i=1/a=012036 (cit. on pp. 30, 31).

[62] F. Dydak et al. "A search for ν_μ oscillations in the Δm^2 range 0.3-90 eV^2". In: *Physics Letters B* 134.3 (1984), pp. 281 –286. ISSN: 0370-2693. DOI: http://dx.doi.org/10.1016/0370-2693(84)90688-9. URL: http://www.sciencedirect.com/science/article/pii/0370269384906889 (cit. on pp. 32, 49).

[63] J. Dorenbosch et al. "Calibration of the charm fine-grained calorimeter". In: *Nuclear Instruments and Methods in Physics Research Section A: Accelerators, Spectrometers, Detectors and Associated Equipment* 253.2 (1987), pp. 203 –221. ISSN: 0168-9002. DOI: https://doi.org/10.1016/0168-9002(87)90708-X. URL: http://www.sciencedirect.com/science/article/pii/016890028790708X (cit. on p. 33).

[64] P. Spentzouris. "Precision electroweak results from neutrino nucleon scattering at CCFR/NuTeV". In: *Nucl. Phys. Proc. Suppl.* 66 (1998). [,112(1998)], pp. 112–115. DOI: 10.1016/S0920-5632(98)00022-X (cit. on p. 33).

[65] Un-Ki Yang et al. "Measurements of F_2 and $xF_3^\nu - xF_3^{\bar{\nu}}$ from CCFR ν_μ−Fe and $\bar{\nu}_\mu$−Fe data in a physics model independent way". In: *Phys. Rev. Lett.* 86 (2001), pp. 2742–2745. DOI: 10.1103/PhysRevLett.86.2742. arXiv: hep-ex/0009041 [hep-ex] (cit. on p. 33).

[66] G. P. Zeller et al. "A Precise determination of electroweak parameters in neutrino nucleon scattering". In: *Phys. Rev. Lett.* 88 (2002). [Erratum: Phys. Rev. Lett.90,239902(2003)], p. 091802. DOI: 10.1103/PhysRevLett.88.091802,10.1103/PhysRevLett.90.239902. arXiv: hep-ex/0110059 [hep-ex] (cit. on p. 33).

[67] J. Altegoer et al. "The NOMAD experiment at the CERN SPS". In: *Nuclear Instruments and Methods in Physics Research Section A: Accelerators, Spectrometers, Detectors and Associated Equipment* 404.1 (1998), pp. 96 –128. ISSN: 0168-9002. DOI: https://doi.org/10.1016/S0168-9002(97)01079-6. URL: http://www.sciencedirect.com/science/article/pii/S0168900297010796 (cit. on p. 33).

[68] P. Astier et al. "Final NOMAD results on on ν_μ to ν_τ and ν_e to ν_τ oscillations including a new search for tau-neutrino appearance using hadronic tau decays". In: *Nucl. Phys.* B611 (2001), pp. 3–39. DOI: 10.1016/S0550-3213(01)00339-X. arXiv: hep-ex/0106102 [hep-ex] (cit. on p. 33).

[69] P. Astier et al. "Search for ν_μ to ν_e oscillations in the NOMAD experiment". In: *Phys. Lett.* B570 (2003), pp. 19–31. DOI: 10.1016/j.physletb.2003.07.029. arXiv: hep-ex/0306037 [hep-ex] (cit. on p. 33).

[70] F Vannucci. "The NOMAD Experiment at CERN". In: *Adv. High Energy Phys.* 2014 (2014), p. 129694. URL: http://cds.cern.ch/record/1666456 (cit. on p. 33).

[71] M. H. Ahn et al. "Measurement of Neutrino Oscillation by the K2K Experiment". In: *Phys. Rev.* D74 (2006), p. 072003. DOI: 10.1103/PhysRevD.74.072003. arXiv: hep-ex/0606032 [hep-ex] (cit. on p. 34).

[72] J. Zalipska. "Neutrino oscillation in the K2K experiment". In: *Acta Phys. Polon.* B37 (2006), pp. 1935–1945 (cit. on p. 34).

[73] A. Habig and E. W. Grashorn. "The MINOS detectors". In: *29th International Cosmic Ray Conference (ICRC 2005) Pune, India, August 3-11, 2005*. [9,319(2005)]. 2005, p. 319. arXiv: hep-ex/0507018 [hep-ex]. URL: http://lss.fnal.gov/cgi-bin/find_paper.pl?conf-05-264-E (cit. on pp. 35, 49).

[74] P. Adamson et al. "The NuMI Neutrino Beam". In: *Nucl. Instrum. Meth.* A806 (2016), pp. 279–306. DOI: 10.1016/j.nima.2015.08.063. arXiv: 1507.06690 [physics.acc-ph] (cit. on p. 35).

[75] P. Adamson et al. "First measurement of electron neutrino appearance in NOvA". In: *Phys. Rev. Lett.* 116.15 (2016), p. 151806. DOI: 10.1103/PhysRevLett.116.151806. arXiv: 1601.05022 [hep-ex] (cit. on p. 35).

[76] M.D. Messier. "First neutrino oscillation measurements in NOvA". In: *Nuclear Physics B* 908 (2016). Neutrino Oscillations: Celebrating the Nobel Prize in Physics 2015, pp. 151 –160. ISSN: 0550-3213. DOI: https://doi.org/10.1016/j.

nuclphysb.2016.04.027. URL: http://www.sciencedirect.com/science/article/pii/S0550321316300657 (cit. on p. 35).

[77] L. Aliaga et al. "Design, Calibration, and Performance of the MINERvA Detector". In: *Nucl. Instrum. Meth.* A743 (2014), pp. 130–159. DOI: 10.1016/j.nima.2013.12.053. arXiv: 1305.5199 [physics.ins-det] (cit. on p. 35).

[78] K. Abe et al. "Measurements of neutrino oscillation in appearance and disappearance channels by the T2K experiment with 6.6x10^{20} protons on target". In: *Phys. Rev.* D91.7 (2015), p. 072010. DOI: 10.1103/PhysRevD.91.072010. arXiv: 1502.01550 [hep-ex] (cit. on pp. 35, 36, 45, 51, 58, 60).

[79] K. Abe et al. "Measurements of the T2K neutrino beam properties using the INGRID on-axis near detector". In: *Nuclear Instruments and Methods in Physics Research A* 694 (Dec. 2012), pp. 211–223. DOI: 10.1016/j.nima.2012.03.023. arXiv: 1111.3119 [physics.ins-det] (cit. on pp. 36, 37).

[80] S. Assylbekov et al. "The T2K ND280 Off-Axis Pi-Zero Detector". In: *Nucl. Instrum. Meth.* A686 (2012), pp. 48–63. DOI: 10.1016/j.nima.2012.05.028. arXiv: 1111.5030 [physics.ins-det] (cit. on pp. 36, 37).

[81] L. Haegel. "The latest T2K neutrino oscillation results". In: *2017 European Physical Society Conference on High Energy Physics (EPS-HEP 2017) Venice, Italy, July 5-12, 2017*. 2017. arXiv: 1709.04180 [hep-ex]. URL: https://inspirehep.net/record/1623206/files/arXiv:1709.04180.pdf (cit. on p. 38).

[82] K. Abe et al. "Combined Analysis of Neutrino and Antineutrino Oscillations at T2K". In: *Phys. Rev. Lett.* 118.15 (2017), p. 151801. DOI: 10.1103/PhysRevLett.118.151801. arXiv: 1701.00432 [hep-ex] (cit. on p. 39).

[83] K. Abe et al. "Neutrino oscillation physics potential of the T2K experiment". In: *PTEP* 2015.4 (2015), p. 043C01. DOI: 10.1093/ptep/ptv031. arXiv: 1409.7469 [hep-ex] (cit. on p. 38).

[84] Carlo Bemporad, Giorgio Gratta, and Petr Vogel. "Reactor based neutrino oscillation experiments". In: *Rev. Mod. Phys.* 74 (2002), p. 297. DOI: 10.1103/RevModPhys.74.297. arXiv: hep-ph/0107277 [hep-ph] (cit. on p. 40).

[85] K. Eguchi et al. "First results from KamLAND: Evidence for reactor antineutrino disappearance". In: *Phys. Rev. Lett.* 90 (2003), p. 021802. DOI: 10.1103/PhysRevLett.90.021802. arXiv: hep-ex/0212021 [hep-ex] (cit. on pp. 40, 41).

[86] A. Gando et al. "Constraints on θ_{13} from A Three-Flavor Oscillation Analysis of Reactor Antineutrinos at KamLAND". In: *Phys. Rev.* D83 (2011), p. 052002. DOI: 10.1103/PhysRevD.83.052002. arXiv: 1009.4771 [hep-ex] (cit. on p. 40).

[87] F. P. An et al. "Observation of electron-antineutrino disappearance at Daya Bay". In: *Phys. Rev. Lett.* 108 (2012), p. 171803. DOI: 10.1103/PhysRevLett.108.171803. arXiv: 1203.1669 [hep-ex] (cit. on pp. 40, 41, 42).

[88] F. P. An et al. "Improved Measurement of Electron Antineutrino Disappearance at Daya Bay". In: *Chin. Phys.* C37 (2013), p. 011001. DOI: 10.1088/1674-1137/37/1/011001. arXiv: 1210.6327 [hep-ex] (cit. on p. 42).

[89] Feng Peng An et al. "Measurement of electron antineutrino oscillation based on 1230 days of operation of the Daya Bay experiment". In: *Phys. Rev.* D95.7 (2017), p. 072006. DOI: 10.1103/PhysRevD.95.072006. arXiv: 1610.04802 [hep-ex] (cit. on p. 42).

[90] J. K. Ahn et al. "Observation of Reactor Electron Antineutrino Disappearance in the RENO Experiment". In: *Phys. Rev. Lett.* 108 (2012), p. 191802. DOI: 10.1103/PhysRevLett.108.191802. arXiv: 1204.0626 [hep-ex] (cit. on p. 43).

[91] J. H. Choi et al. "Observation of Energy and Baseline Dependent Reactor Antineutrino Disappearance in the RENO Experiment". In: *Phys. Rev. Lett.* 116.21 (2016), p. 211801. DOI: 10.1103/PhysRevLett.116.211801. arXiv: 1511.05849 [hep-ex] (cit. on p. 43).

[92] Y. Abe et al. "Indication of Reactor $\bar{\nu}_e$ Disappearance in the Double Chooz Experiment". In: *Phys. Rev. Lett.* 108 (2012), p. 131801. DOI: 10.1103/PhysRevLett.108.131801. arXiv: 1112.6353 [hep-ex] (cit. on p. 43).

[93] Y. Abe et al. "Reactor electron antineutrino disappearance in the Double Chooz experiment". In: *Phys. Rev.* D86 (2012), p. 052008. DOI: 10.1103/PhysRevD.86.052008. arXiv: 1207.6632 [hep-ex] (cit. on p. 43).

[94] F. Ardellier et al. "Double Chooz: A Search for the neutrino mixing angle theta(13)". In: (2006). arXiv: hep-ex/0606025 [hep-ex] (cit. on pp. 43, 44).

[95] N. S. Bowden. "Reactor monitoring and safeguards using antineutrino detectors". In: *J. Phys. Conf. Ser.* 136 (2008), p. 022008. DOI: 10.1088/1742-6596/136/2/022008. arXiv: 0809.2128 [nucl-ex] (cit. on p. 43).

[96] J. I. Crespo-Anadon. "Double Chooz: Latest results". In: *Nucl. Part. Phys. Proc.* 265-266 (2015), pp. 99–104. DOI: 10.1016/j.nuclphysbps.2015.06.025. arXiv: 1412.3698 [hep-ex] (cit. on pp. 43, 44).

[97] C. Jollet. "The JUNO experiment". In: *Nuovo Cim.* C39.4 (2017), p. 318. DOI: 10.1393/ncc/i2016-16318-6 (cit. on pp. 43, 44).

[98] R. Acciarri et al. "Long-Baseline Neutrino Facility (LBNF) and Deep Underground Neutrino Experiment (DUNE) Conceptual Design Report Volume 1: The LBNF and DUNE Projects". In: (2016). arXiv: 1601.05471 [physics.ins-det] (cit. on pp. 44, 45).

[99] R. Acciarri et al. "Long-Baseline Neutrino Facility (LBNF) and Deep Underground Neutrino Experiment (DUNE)". In: (2015). arXiv: 1512.06148 [physics.ins-det] (cit. on p. 45).

[100] K. Abe et al. "Letter of Intent: The Hyper-Kamiokande Experiment — Detector Design and Physics Potential —". In: (2011). arXiv: 1109.3262 [hep-ex] (cit. on pp. 45, 46, 58).

[101] F. J. P. Soler. "Neutrino factories". In: *AIP Conference Proceedings* 1666, 130002 (2015). DOI: http://dx.doi.org/10.1063/1.4915580. URL: http://scitation.aip.org/content/aip/proceeding/aipcp/10.1063/1.4915580 (cit. on pp. 46, 47, 48).

[102] P Gruber et al. "The Study of a European Neutrino Factory Complex". In: CERN-PS-2002-080-PP. CERN-NEUTRINO-FACTORY-NOTE-122. CERN-NUFACT-NOTE-122 (2002), 73 p. URL: http://cds.cern.ch/record/610249 (cit. on pp. 46, 47, 50).

[103] M. Dracos and E. n. S. project. "The ESS neutrino facility for CP violation discovery". In: *Proceedings of the 38th International Conference on High Energy Physics (ICHEP2016). 3-10 August 2016. Chicago, USA.* 2016, p. 460 (cit. on p. 47).

[104] S. Geer. "Muon colliders and neutrino factories". In: *Proceedings, 25th International Linear Accelerator Conference, LINAC2010: Tsukuba, Japan, September 12-17, 2010.* 2011, FR202. arXiv: 1202.2140 [physics.acc-ph]. URL: http://lss.fnal.gov/cgi-bin/find_paper.pl?conf-10-370 (cit. on p. 47).

[105] D. Adey et al. "Overview of the Neutrinos from Stored Muons Facility - nuSTORM". In: *JINST* 12.07 (2017), P07020. DOI: 10.1088/1748-0221/12/07/P07020 (cit. on p. 48).

[106] S. Choubey et al. "International Design Study for the Neutrino Factory, Interim Design Report". In: (2011). arXiv: 1112.2853 [hep-ex] (cit. on p. 49).

[107] The ISS Detector Working Group et al. "International Scoping Study (ISS) for a future neutrino factory and Super-Beam facility. Detectors and flux instrumentation for future neutrino facilities". In: *Journal of Instrumentation* 4.05 (2009), T05001. URL: http://stacks.iop.org/1748-0221/4/i=05/a=T05001 (cit. on p. 49).

[108] A. Bross et al. "Toroidal magnetized iron neutrino detector for a neutrino factory". In: *Phys. Rev. ST Accel. Beams* 16.8 (2013), p. 081002. DOI: 10.1103/PhysRevSTAB.16.081002. arXiv: 1306.5327 [physics.ins-det] (cit. on pp. 49, 66).

[109] Kunihiro Morishima et al. "Discovery of a big void in Khufu's Pyramid by observation of cosmic-ray muons". In: *Nature* 552.7685 (2017), pp. 386–390. DOI: 10.1038/nature24647. arXiv: 1711.01576 [physics.ins-det] (cit. on p. 49).

[110] M. Askins et al. "The Physics and Nuclear Nonproliferation Goals of WATCHMAN: A WAter CHerenkov Monitor for ANtineutrinos". In: (2015). arXiv: 1502.01132 [physics.ins-det] (cit. on p. 49).

[111] Glenn R. Jocher et al. "Theoretical antineutrino detection, direction and ranging at long distances". In: *Phys. Rept.* 527 (2013), pp. 131–204. DOI: 10.1016/j.physrep.2013.01.005. arXiv: 1307.2832 [physics.ins-det] (cit. on p. 49).

[112] E Noah. *Proposal for characterization of muon spectrometers for neutrino beam lines with the Baby MIND*. Tech. rep. CERN-SPSC-2015-031. SPSC-P-353. Geneva: CERN, 2015. URL: http://cds.cern.ch/record/2057587 (cit. on p. 50).

[113] May 2016. URL: https://cenf-baby-mind.web.cern.ch (cit. on p. 50).

[114] S. Agostinelli et al. "Geant4a simulation toolkit". In: *Nuclear Instruments and Methods in Physics Research Section A: Accelerators, Spectrometers, Detectors and Associated Equipment* 506.3 (2003), pp. 250 –303. ISSN: 0168-9002. DOI: http://dx.doi.org/10.1016/S0168-9002(03)01368-8. URL: http://www.sciencedirect.com/science/article/pii/S0168900203013688 (cit. on pp. 51, 66).

[115] AK Steel Corporation. 2018. URL: https://www.aksteel.com/our-products/electrical-steel (cit. on p. 51).

[116] R. Asfandiyarov et al. "Proposal for SPS beam time for the baby MIND and TASD neutrino detector prototypes". In: (2014). arXiv: 1405.6089 [physics.ins-det] (cit. on p. 51).

[117] G. Rolando et al. “New and Optimized Magnetization Scheme for the Baby Magnetized Iron Neutrino Detector at J-PARC”. In: *IEEE Transactions on Magnetics* 53.5 (2017), pp. 1–6. ISSN: 0018-9464. DOI: 10.1109/TMAG.2017.2664053 (cit. on p. 52).

[118] Aleksandr Mefodev. 2016. URL: https://indico.cern.ch/event/573666/contributions/2365530/attachments/1373457/2084345/Scintillator_BabyMIND_update.pdf (cit. on pp. 54, 55).

[119] Stéphane Callier et al. “EASIROC, an Easy & Versatile ReadOut Device for SiPM”. In: *Physics Procedia* 37 (2012). Proceedings of the 2nd International Conference on Technology and Instrumentation in Particle Physics (TIPP 2011), pp. 1569 –1576. ISSN: 1875-3892. DOI: https://doi.org/10.1016/j.phpro.2012.02.486. URL: http://www.sciencedirect.com/science/article/pii/S1875389212018688 (cit. on p. 56).

[120] M. Antonova et al. “Synchronization of the distributed readout frontend electronics of the Baby MIND detector”. In: *2017 XXVI International Scientific Conference Electronics (ET)*. 2017, pp. 1–4. DOI: 10.1109/ET.2017.8124369 (cit. on pp. 57, 87).

[121] T Ovsiannikova et al. “The new experiment WAGASCI for water to hydrocarbon neutrino cross section measurement using the J-PARC beam”. In: *Journal of Physics: Conference Series* 675.1 (2016), p. 012030. URL: http://stacks.iop.org/1742-6596/675/i=1/a=012030 (cit. on pp. 58, 59).

[122] K. Abe et al. “Measurements of the T2K neutrino beam properties using the INGRID on-axis near detector”. In: *Nuclear Instruments and Methods in Physics Research A* 694 (Dec. 2012), pp. 211–223. DOI: 10.1016/j.nima.2012.03.023. arXiv: 1111.3119 [physics.ins-det] (cit. on p. 60).

[123] N. Truong et al. (Baby MIND and WAGASCI collaborations). *Technical Design Report (TDR): Study of neutrino-nucleus interaction at around 1 GeV using cuboid lattice neutrino detector, WAGASCI, muon range detectors and magnetized spectrometer, Baby-MIND, at J-PARC neutrino monitor hall (E69, WAGASCI/Baby-MIND)*. May 2018. URL: https://indico.cern.ch/event/730276/contributions/3009217/attachments/1651510/2641676/wagasci-slash-baby-4.pdf (cit. on p. 61).

[124] Kikawa Tatsuya. Private Communication. kikawa.tatsuya.6e@kyoto-u.ac.jp, 2018 (cit. on p. 62).

[125] N. Seguin-Moreau. "Latest generation of ASICs for photodetector readout". In: *Nucl. Instrum. Meth.* A718 (2013), pp. 173–179. DOI: 10.1016/j.nima.2012.11.134 (cit. on p. 61).

[126] A. Laing. "Optimisation of detectors for the golden channel at a neutrino factory". PhD thesis. University of Glasgow, 2010. URL: http://theses.gla.ac.uk/id/eprint/2216 (cit. on p. 66).

[127] C. Andreopoulos et al. "The GENIE Neutrino Monte Carlo Generator". In: *Nucl. Instrum. Meth.* A614 (2010), pp. 87–104. DOI: 10.1016/j.nima.2009.12.009. arXiv: 0905.2517 [hep-ph] (cit. on p. 66).

[128] A. Cervera-Villanueva, J. J. Gómez-Cadenas, and J. A. Hernando. "RecPack, a general reconstruction toolkit". In: *Astroparticle, Particle, Space Physics and Detectors For Physics Applications - Proceedings of the 13th ICATPP Conference. Edited by Giani Simone et al. Published by World Scientific Publishing Co. Pte. Ltd., 2012. ISBN #9789814405072, pp. 954-960*. Ed. by S. Giani and et al. Aug. 2012, pp. 954–960. DOI: 10.1142/9789814405072_0146 (cit. on pp. 66, 72).

[129] Rene Brun and Fons Rademakers. "ROOT - An Object Oriented Data Analysis Framework". In: *Sep. 1996, Nucl. Inst. & Meth. in Phys. Res. A 389 (1997) 81-86. See also http://root.cern.ch/.* (Cit. on pp. 66, 70).

[130] R. Chytracek et al. "Geometry Description Markup Language for Physics Simulation and Analysis Applications". In: *IEEE Transactions on Nuclear Science* 53.5 (2006), pp. 2892–2896. ISSN: 0018-9499. DOI: 10.1109/TNS.2006.881062 (cit. on p. 69).

[131] Saba Parsa. Oct. 2016. URL: https://indico.cern.ch/event/575040/contributions/2336303/attachments/1353413/2044279/momentum_resolution.pdf (cit. on p. 76).

[132] A. Hoecker et al. "TMVA - Toolkit for Multivariate Data Analysis". In: *ArXiv Physics e-prints* (Mar. 2007). eprint: physics/0703039 (cit. on pp. 82, 91, 99).

[133] J.R.R. Tolkien. *The Lord of the Rings: One Volume*. The Lord of the Rings. Houghton Mifflin Harcourt, 2012. ISBN: 9780547951942. URL: https://books.google.co.uk/books?id=yl4dILkcqm4C (cit. on p. 82).

[134] Johannes Rauch and Tobias Schlter. "GENFIT a Generic Track-Fitting Toolkit". In: *Journal of Physics: Conference Series* 608.1 (2015), p. 012042. URL: http://stacks.iop.org/1742-6596/608/i=1/a=012042 (cit. on pp. 82, 83).

[135] Kevin Scott McFarland. "Neutrino Interactions". In: *Neutrinos in particle physics, astrophysics and cosmology. Proceedings, 61st Scottish Universities Summer School in Physics, SUSSP61, St. Andrews, UK, August 8-23, 2006*. 2008, pp. 65–90. arXiv: 0804.3899 [hep-ex]. URL: http://inspirehep.net/record/784224/files/arXiv:0804.3899.pdf (cit. on p. 106).

[136] G. P. Zeller. "Low-energy neutrino cross-sections: Comparison of various Monte Carlo predictions to experimental data". In: *2nd International Workshop on Neutrino-Nucleus Interactions in the Few GeV Region (NuInt 02) Irvine, California, December 12-15, 2002*. 2003. arXiv: hep-ex/0312061 [hep-ex] (cit. on p. 106).

[137] J. A. Formaggio and G. P. Zeller. "From eV to EeV: Neutrino Cross Sections Across Energy Scales". In: *Rev. Mod. Phys.* 84 (2012), pp. 1307–1341. DOI: 10.1103/RevModPhys.84.1307. arXiv: 1305.7513 [hep-ex] (cit. on p. 107).

[138] Alexander Radovic et al. "Machine learning at the energy and intensity frontiers of particle physics". In: *Nature* 560.7716 (2018), pp. 41–48. ISSN: 1476-4687. DOI: 10.1038/s41586-018-0361-2. URL: https://doi.org/10.1038/s41586-018-0361-2 (cit. on p. 106).

[139] C. Adams et al. "A Deep Neural Network for Pixel-Level Electromagnetic Particle Identification in the MicroBooNE Liquid Argon Time Projection Chamber". In: (2018). arXiv: 1808.07269 [physics.ins-det] (cit. on p. 106).

[140] F. J. P. Soler. "nuSTORM: Neutrinos from Stored Muons". In: *Proceedings, Topical Research Meeting on Prospects in Neutrino Physics (NuPhys2014): London, UK, December 15-17, 2014*. 2015. arXiv: 1507.08836 [physics.ins-det] (cit. on p. 113).

[141] K. Abe et al. "T2K neutrino flux prediction". In: *Phys. Rev.* D87.1 (2013). [Addendum: Phys. Rev.D87,no.1,019902(2013)], p. 012001. DOI: 10.1103/PhysRevD.87.012001,10.1103/PhysRevD.87.019902. arXiv: 1211.0469 [hep-ex] (cit. on p. 118).

[142] K. Abe et al. "Measurements of the T2K neutrino beam properties using the INGRID on-axis near detector". In: *Nucl. Instrum. Meth.* A694 (2012), pp. 211–223. DOI: 10.1016/j.nima.2012.03.023. arXiv: 1111.3119 [physics.ins-det] (cit. on p. 118).